Preparing for LISA Pathfinder operations: characterisation of the optical metrology system

Von der QUEST-Leibniz-Forschungsschule der Gottfried
Wilhelm Leibniz Universität Hannover
zur Erlangung des Grades

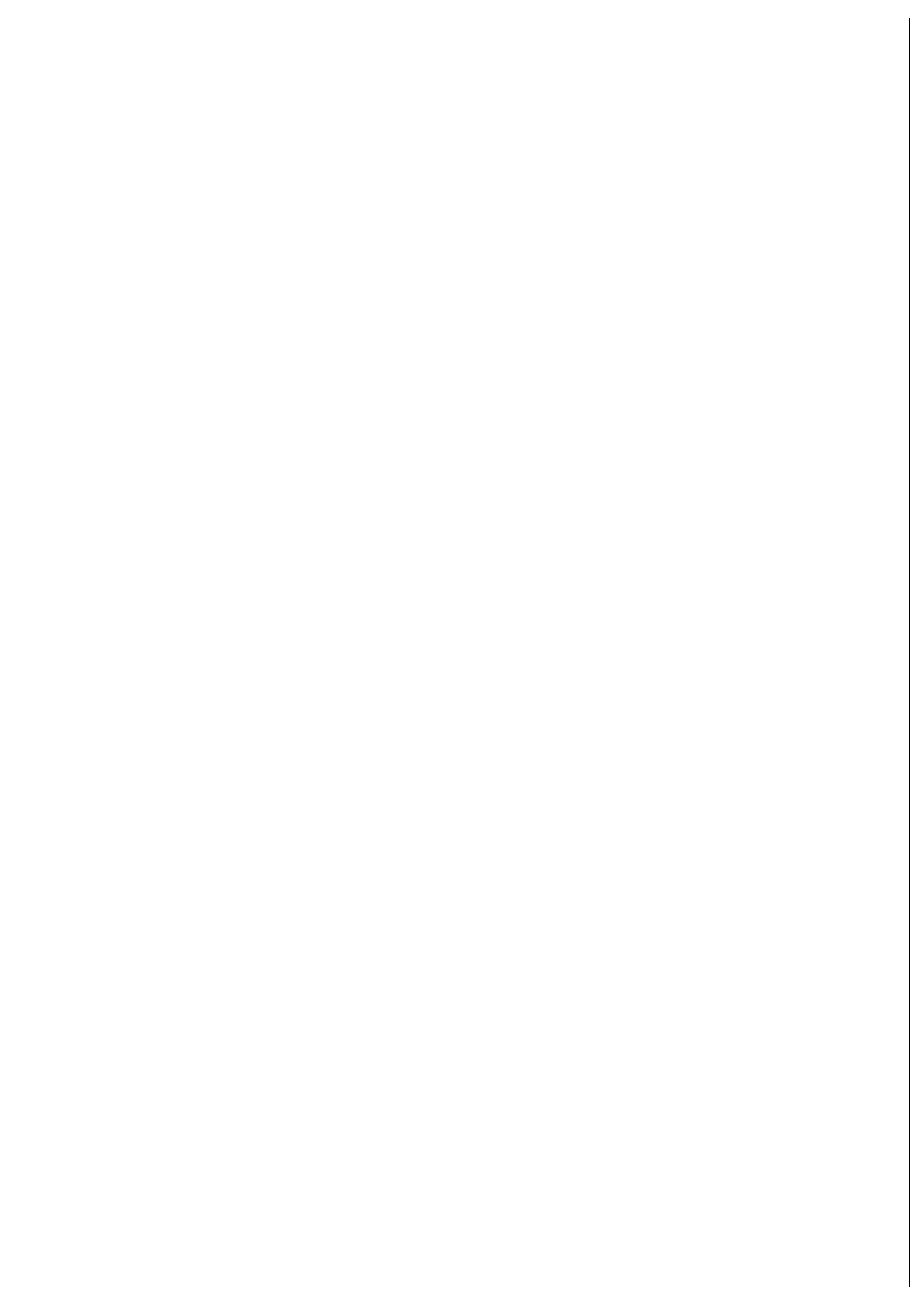**Doktor der Naturwissenschaften**
Dr. rer. nat.

genehmigte Dissertation
von

M.Sci (Hons) Heather E. Audley

geboren am 8. November 1986 in Birmingham, UK

2014

2

Abstract

The LISA Pathfinder mission will demonstrate key technologies required for a future space-based gravitational wave detector such as the evolved Laser Interferometer Space Antenna (eLISA). Specifically, the control of a drag-free test mass using high-precision interferometry and micro-Newton thrusters. At the core of the LISA Pathfinder satellite is the optical metrology system. This comprises the subsystems for the interferometric measurement of the longitudinal and angular fluctuations of the test masses. In order to measure the residual test mass acceleration to the required level, the noise contribution from the optical metrology system must be minimised. This includes interferometric readout noise, and noise that directly couples into test mass acceleration.

There are a number of noise sources inherent in the optical metrology system that contribute to the measurement of the differential test mass displacement. Of these, frequency, optical pathlength difference, and amplitude noise are suppressed by control loops. In order to understand the measured acceleration noise in-flight it is necessary to characterise the contributions of these noise sources, and, if the noise levels are higher than expected, adapt the responses of the control loops accordingly. As such, investigations for characterising the noise sources and control loops in-flight have been designed, in addition to procedures for performing the associated data analysis. The proposed investigations are presented alongside results from the ground-based hardware test campaigns of the optical metrology subsystems. These results provide the best available estimate of the noise from each source, and the overall noise contribution that can be expected in-flight.

In chapter one, LISA Pathfinder is introduced, with focus on the optical metrology subsystems and the interferometric measurement chain. In chapter two, the various noise sources that contribute to the optical metrology system are presented, in addition to a description of the associated control loops. In chapters three, four, and five, the in-flight noise characterisation investigations and analyses, including the results of the ground-based hardware test campaigns, are presented for the frequency noise, optical pathlength difference noise, and amplitude noise respectively. Finally, an overview of the results and investigations is presented, with a breakdown of the situations in which

the various investigations may be performed in-flight.

Zusammenfassung

Die LISA-Pathfinder Mission wird die Schlüsseltechnologien demonstrieren, welche für zukünftige weltraumbasierte Gravitationswellendetektoren, wie eLISA (evolved Laser Interferometer Space Antenna), benötigt werden. Von besonderem Interesse ist hier vor allen Dingen die Kontrolle der frei fallenden Testmassen mit Hilfe von mikro-Newton Schubdüsen (thruster). Im Kern des LISA-Pathfinder Satelliten befindet sich das optische Metrologie-System. Dieses setzt sich aus zwei interferometrischen Teilsystem zusammen, eins für die Messung der longitudinalen Schwankungen zwischen den Testmassen und eins für die Messung der Winkelverschiebungen zwischen diesen. Um die restliche Testmassenbeschleunigung mit der vorausgesetzten Genauigkeit messen zu können müssen alle Rauschbeiträge des optischen Metrologiesystems minimiert werden. Dazu gehören das Rauschen des interferometrischen Ausleseverfahrens sowie alle Rauschquellen welche direkt in die Beschleunigung der Testmassen koppeln. Es existiert eine Vielzahl systemimmanenter Rauschquellen des optischen Metrologie-Systems, welche die Messung der differentiellen Testmassenverschiebung beeinflussen. Zu diesen zählen auch Frequenzrauschen, Amplitudenrauschen sowie Fluktuationen der optischen Weglänge, welche mit Hilfe von aktiven Regelschleifen unterdrückt werden. Um das gemessene Beschleunigungsrauschen, während des Fluges, zu verstehen, ist es notwendig die Beiträge dieser Rauschquellen zu charakterisieren und falls diese größer sein sollten als erwartet, die Regelschleifen gemäß der neuen Anforderungen anzupassen. Für diesen Zweck wurden sowohl Messverfahren entwickelt, um die Rauschquellen der Regelschleifen auch während des Fluges überprüfen zu können, als auch die entsprechenden Verfahren zur Datenauswertung dieser Messmethoden. Die vorgeschlagenen Messverfahren werden hier neben den Ergebnissen der erdbasierten Testkampagne für die Hardware des optischen Metrologiesystems vorgestellt. Diese Ergebnisse liefern die bisher besten Abschätzungen für die Beiträge der einzelnen Rauschquellen und das daraus resultierende Gesamtrauschlevel, das während des Fluges zu erwarten ist.

Im ersten Kapitel wird LISA Pathfinder vorgestellt, wobei vor allem auf die Teilsysteme des optischen Metrologiesystems und den genauen Ablauf des interferometrischen Messverfahrens eingegangen wird. Das zweite Kapitel stellt die verschiedenen Rauschquellen des optischen

Metrologiesystems dar und geht außerdem näher auf die Regelschleifen ein, die zur Unterdrückung dieser Rauschquellen eingesetzt werden sollen. Die Kapitel drei, vier und fünf erklären die Untersuchungen und Auswertungsverfahren zur Rauschcharakterisierung während des Fluges, zusammen mit den erwarteten Rauschbeiträgen für das Frequenzrauschen, das Amplitudenrauschen und die Variationen der optischen Weglänge, welche auf den Ergebnissen der erdbasierten Testkampagne beruhen. Abschließend wird ein Überblick über die Ergebnisse und Untersuchungen präsentiert, in welchem auch ein Einblick gegeben wird, zu welchem Zeitpunkt die verschiedenen Untersuchungen während des Fluges durchgeführt werden könnten.

Schlagworte: LISA Pathfinder, Gravitationswellen, Weltrauminterferometrie, Regelschleifen, Rauschcharakterisierung

Contents

Contents

Acronyms

ADC Analogue to Digital Convertor

AEI Albert Einstein Institute

ao Analysis Object

AOM Acousto-Optic Modulator

APC AstroParticule et Cosmologie, Université Paris Diderot

ASD Astrium Deutschland

ASU Astrium UK

CAD Computer Aided Design

CLG Closed-Loop Gain

CLTF Closed-Loop Transfer Function

CMM Coordinate Measurement Machine

DAC Digital to Analogue Convertor

DC Direct Current

DDS Data Disposition System

DFACS Drag-Free and Attitude Control System

DFT Discrete Fourier transform

DMU Data Management Unit

DRS Disturbance Reduction System

DWS Differential Wavefront Sensing

eLISA Evolved LISA

ELITE European LIsa TEchnology

EM Engineering Model

EMP Experimental Master Plan

ESA European Space Agency

FF Fast Frequency

FFT Fast Fourier transform

FIOS Fibre Injector Optical Sub-Assembly

FM Flight Model

FP Fast Power

FPGA Field Programmable Gate Array

FT Fourier Transform

GUI Graphical User Interface

iABG Industrieanlagen-Betriebsgesellschaft mbH

ICE Instrument Configuration Evaluation

IDL Interferometer Data Log

ifo Interferometer

IGR Institute for Gravitational Research, University of Glasgow

IIR Infinite Impulse Response

KT Kaiser Threde

LA Laser Assembly

LA PFM Laser Assembly Pre-Flight Model

LCA LTP Core Assembly

LCU Laser Control Unit

LISA Laser Interferometer Space Antenna

LMU Laser Modulation Unit

LPF LISA Pathfinder

LTP LISA Technology Package

LTPDA LISA Technology Package Data Analysis

MOC Mission Operations Centre

NASA National Aeronautics and Space Administration

NPRO Non-Planar Ring Oscillator

NTE NTE Sener with IEEC, Barcelona

OB Optical Bench

OBC Onboard Computer

OBI Optical Bench Interferometer

OGSE On-ground Support Equipment

OLG Open-Loop Gain

OLTF Open-Loop Transfer Function

OMS Optical Metrology System

OPD Optical Pathlength Difference

OSTT On-Station Thermal Tests

PD Photodiode

PFM Pre-Flight Model

PT Phase Tracking

PZT Piezo-electric Transducer

QPD Quadrant Photodiode

RAM Random Access Memory

RF Radio Frequency

RIN Relative Intensity Noise

RLU Reference Laser Unit

SBDFT Single-Bin Discrete Fourier Transform

SC Spacecraft

SDP System Data Pool

SEPD Single Element Photodiode

SF Slow Frequency

SID System Identification

SMART-2 Small Missions for Advanced Research in Technology

SNR Signal to Noise Ratio

SP Slow power

SSC Source Sequence Counter

SSM State Space Model

SSMM Solid-state Mass Memory

ST-7 Space Technology-7

STOC Science Technology Operations Centre

TC Telecommand

TIA Trans-Impedance Amplifier

TM Test Mass

TN Technical Note

UOB University of Birmingham

1 Introduction

Contents

1.1 Gravitational waves and their detection

The existence of gravitational waves is a prediction of Einstein's General Theory of Relativity [1]. Simply put, gravitational waves are

1 Introduction

ripples in space-time generated as a result of accelerating mass. They are predicted to propagate as a wave at the speed of light, and exist in two polarisations, commonly referred to as + and ×. In the same way that the coupling between mass and space-time allows moving masses to generate gravitational waves, masses in space-time will be periodically displaced relative to one another by a passing gravitational wave. This effect can be visualised with the aid of a ring of free-floating test particles, as shown in Figure 1.1.
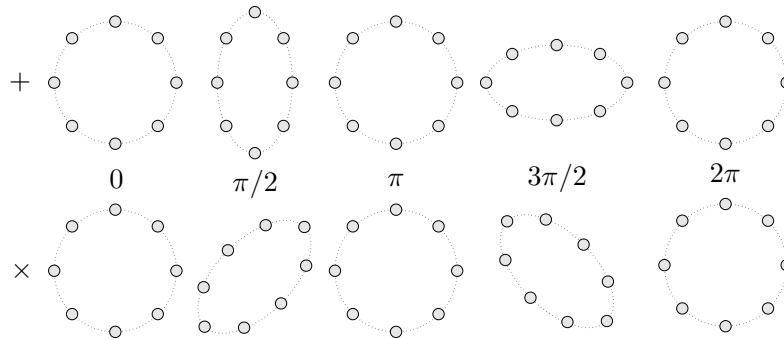
Figure 1.1: The effect of each polarisation, + and ×, of a gravitational wave propagating perpendicular to the page, on a ring of test particles [2].

The magnitude of a gravitational wave is typically defined in terms of the strain amplitude, h, it causes. As the coupling between mass and space-time is weak and the propagation distances large, only very energetic accelerations of high mass objects are able to produce gravitational waves that may be detectable at the Earth. Gravitational waves are expected to be emitted by a wide range of astronomical sources including events such as the collapse of stellar cores, the rotation of asymmetric pulsars, and rotating binary star systems. A gravitational wave background, analogous to the cosmic microwave background, from fundamental processes such as the Big Bang is also predicted [2].

Attempts have been made to experimentally detect gravitational waves since the 1960s [3], but, as yet, only indirect detections have been possible [4] [5]. This is because the required strain sensitivity of a gravitational wave detector is of the order of 10^{-21} [6]. The most sensitive existing gravitational wave detectors are laser interferometers, such as LIGO, VIRGO, and GEO600 [7] [8] [9]. Such detectors are described in detail in [2], [10], and [6]. The frequency range of sources that could be detected by ground-based detectors is limited by gravity gradient

noise, and the achievable sensitivity is restricted by the limits on the interferometer armlengths. In order to detect low-frequency gravitational waves (less than a few Hz), and increase the interferometer armlengths, it is necessary to construct a gravitational wave detector in Space, such as the proposed eLISA mission [11].

1.2 The eLISA mission

The evolved Laser Interferometer Space Antenna (eLISA) is a concept for a space-based gravitational wave observatory. It was recently presented as a strawman mission in 'The Gravitational Universe', a white paper response to the European Space Agency (ESA) Cosmic Vision call for science themes [11]. The mission is a variation on the well established Laser Interferometer Space Antenna (LISA) concept [12] [13]. The mission aims to detect gravitational waves in the $0.1\,\mathrm{mHz}$ to $1\,\mathrm{Hz}$ range, from sources such as compact galactic binaries, coalescing massive black holes, the capture of stellar remnants onto massive black holes, and background gravitational radiation from the early Universe [14].

The eLISA constellation consists of three satellites, a 'mother' and two 'daughters', that form a Michelson interferometer configuration with one million kilometre armlengths, as shown in Figure 1.2. Drag-free test masses at the end of each arm act as the end mirrors of the interferometer. Each test mass follows the local geodesics of space-time, such that a gravitational wave will displace the test masses relative to one another. Due to the large inter-satellite distances, it is not possible to directly measure the relative test mass displacements, so the measurement is made in two parts. Firstly, the displacement of each test mass relative to the local satellite is determined interferometrically. Secondly, the relative displacement of the satellites at either end of the interferometer arm is measured by the detection of a beatnote from the interference of the received laser light from the distant satellite with a local laser. After processing, the relative displacement of the test masses can be calculated.

In order to show that the requirements for the control and readout of drag-free test masses can be achieved, it is necessary to demonstrate the applicable technologies in space. To this end, a technology
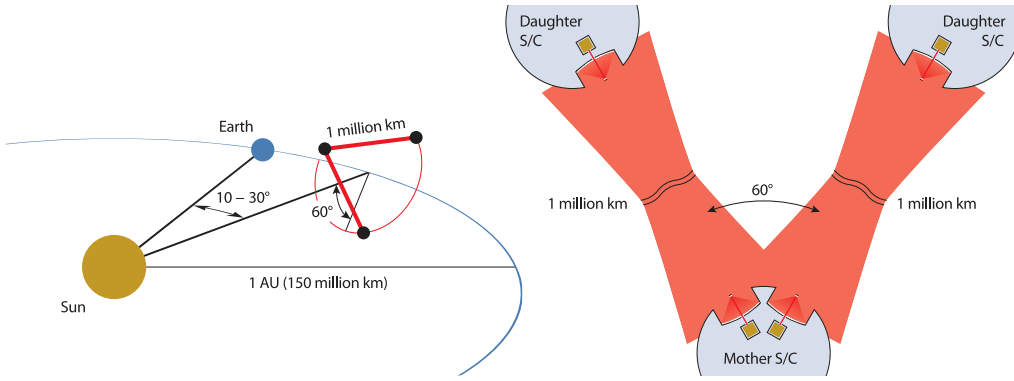
Figure 1.2: A diagram showing: left) The eLISA constellation of three satellites, forming a Michelson laser interferometer configuration with one million kilometre armlengths, and right) the 'mother' and two 'daughter' satellites. A drag-free test mass at the end of each interferometer arm acts as the end mirror [11].

demonstration mission, LISA Pathfinder (LPF), is due for launch in mid-2015.

1.3 LISA Pathfinder

The LISA Pathfinder satellite will demonstrate the key technologies required for a future space-based gravitational wave detector such as Evolved LISA (eLISA), including:

- picometre precision interferometry;

- microNewton thrusters;

- control of a drag-free Test Mass (TM), such that it is only influenced by the local geodesics of space-time.

The goal is to achieve a residual TM acceleration, $\delta\widetilde{a}(f)$, in a $1\,\mathrm{mHz} \leq f \leq 30\,\mathrm{mHz}$ measurement bandwidth, of [15]:

$$\delta\widetilde{a}(f) \leq 3 \times 10^{-14} \left(1 + \left(\frac{f}{3\,\mathrm{mHz}} \right)^2 \right) \frac{\mathrm{m}}{\mathrm{s}^2} \frac{1}{\sqrt{\mathrm{Hz}}} \qquad (1.1)$$

This is a relaxation, in both acceleration and frequency, of one order of magnitude compared to the requirement for the original Laser

Interferometer Space Antenna (LISA) design, and the eLISA design [11].

The LISA Pathfinder satellite can be thought of as a dramatically shortened version of one eLISA arm. Rather than having some several millions of kilometres between the TMs, both TMs are housed in one spacecraft, approximately 30 cm apart. This short armlength means that LISA Pathfinder will be insensitive to gravitational waves.

A highly simplified conceptual diagram of the LPF satellite is depicted in Figure 1.3. It shows the two test masses housed with the satellite. The differential acceleration is measured along the axis joining the two TMs, often referred to as the sensitive axis. The spacecraft is actuated along this axis, and it is therefore only possible to maintain the drag-free condition of one test mass, TM1. The other test mass, TM2, is electrostatically actuated such that it follows TM1. The longitudinal and angular fluctuations of the TMs along the axis between them are measured interferometrically by the Optical Metrology System (OMS).

The displacement of test mass one relative to the satellite, x_1, is measured by the X1 interferometer. The X1 interferometer output is used to provide feedback to the thrusters to adjust the position of the satellite, via a control loop with transfer function T_1. Similarly, the differential displacement of the two test masses, x_{12}, along the sensitive axis is measured by the X12 interferometer. This provides the input to the capacitive actuation control loop which acts on test mass two, with transfer function T_2.

In order to reach the mission requirement for the residual test mass acceleration given in Equation 1.1 the test masses must be isolated from external forces. This depends upon the residual noise levels of the capacitive actuators and the thrusters, as well as the noise level of the interferometric readout systems that provide the input signals.

The main measurement system, the LISA Technology Package (LTP), is shown in Figure 1.4. The two cubic TMs are each positioned in vacuum tanks, and surrounded by an electrode housing. This subsystem is located at the centre of the LPF satellite. The OMS, which performs the interferometric readout of the longitudinal and angular test mass displacements, is a subsystem of the LTP.
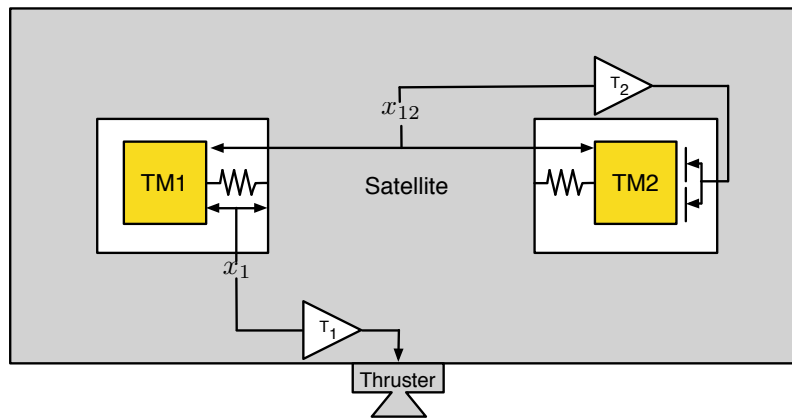
Figure 1.3: A conceptual picture of the LPF satellite showing the X1 interferometer output being fed back to the satellite via the T_1 transfer function, with some noise, $X1_{RO}$. The X12 interferometer output, x_{12}, is fed back to the capacitive actuators around test mass two via a control loop with transfer function T_2 with some noise, $X12_{RO}$. The spring coupling between each test mass and the satellite is also shown.
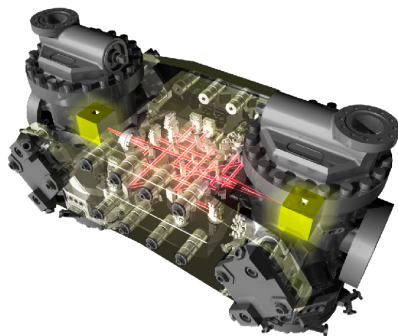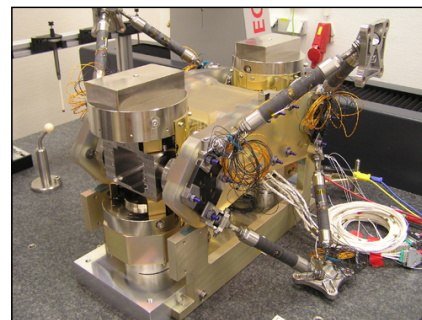
| (a) | (b) |

Figure 1.4: (a) A Computer Aided Design (CAD) diagram of the LISA technology package. The two cubic test masses can be seen, each housed inside a vacuum tank. The optical bench is between the vacuum tanks, with the interferometer beam paths shown in red. This structure is located in the centre of the LPF satellite. Picture courtesy of ESA. (b) A representative version of the LISA Technology package, used in the On-Station Thermal Test (OSTT) campaign (see Section 1.6.3). This version also shows the struts that connect this section to the rest of the satellite. Picture courtesy of ASD.

> **A brief history of the LISA Pathfinder mission**
>
> The LISA Pathfinder mission was first proposed as a precursor to the LISA mission in 1998, under the name European LIsa TEchnology (ELITE), with a launch date in 2002 [16]. The proposal was refined and proposed to the ESA in 2000 as a response to the Small Missions for Advanced Research in Technology (SMART-2) announcement, with a launch date of 2006. This proposal included the LISA Technology Package, a US provided LISA Technology Package, and Darwin Pathfinder, a mission consisting of four to five free-flying spacecraft to search for Earth-like planets around other stars.
>
> After some preliminary studies, the SMART-2 mission was descoped and renamed LISA Pathfinder. This comprised a single satellite containing two payloads: the LTP and the National Aeronautics and Space Administration (NASA) Space Technology-7 (ST-7) Disturbance Reduction System (DRS). The DRS payload was later adapted to use the LTP sensor, due to budget and schedule constraints.

Box 1.1: A brief history of the LISA Pathfinder mission [17].

1.4 The optical metrology system

The Optical Metrology System (OMS) comprises the subsystems required for the interferometric readout of:

- the displacement of TM1 relative to the spacecraft, x_1,

- the displacement of TM2 relative to TM1, x_{12},

- the angular fluctuations of TM1, ϕ_1 and η_1,

- the angular fluctuations of TM2, ϕ_2 and η_2.

These are measured relative to the axis joining the two TMs, as defined in Figure 1.5.

The subsystems that make up the OMS are shown in Figure 1.6. The final Flight Model (FM) versions that will be implemented on the LPF satellite will be described in the following sections. During
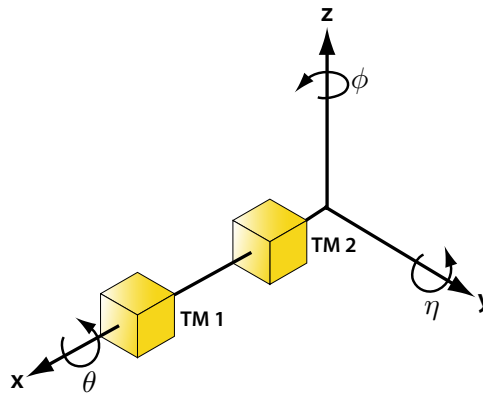
Figure 1.5: A diagram defining the axes for the longitudinal and angular measurements of the test masses by the LTP [18].

hardware test campaigns and laboratory tests, different configurations and versions of hardware were used. These are described in Section 1.6.
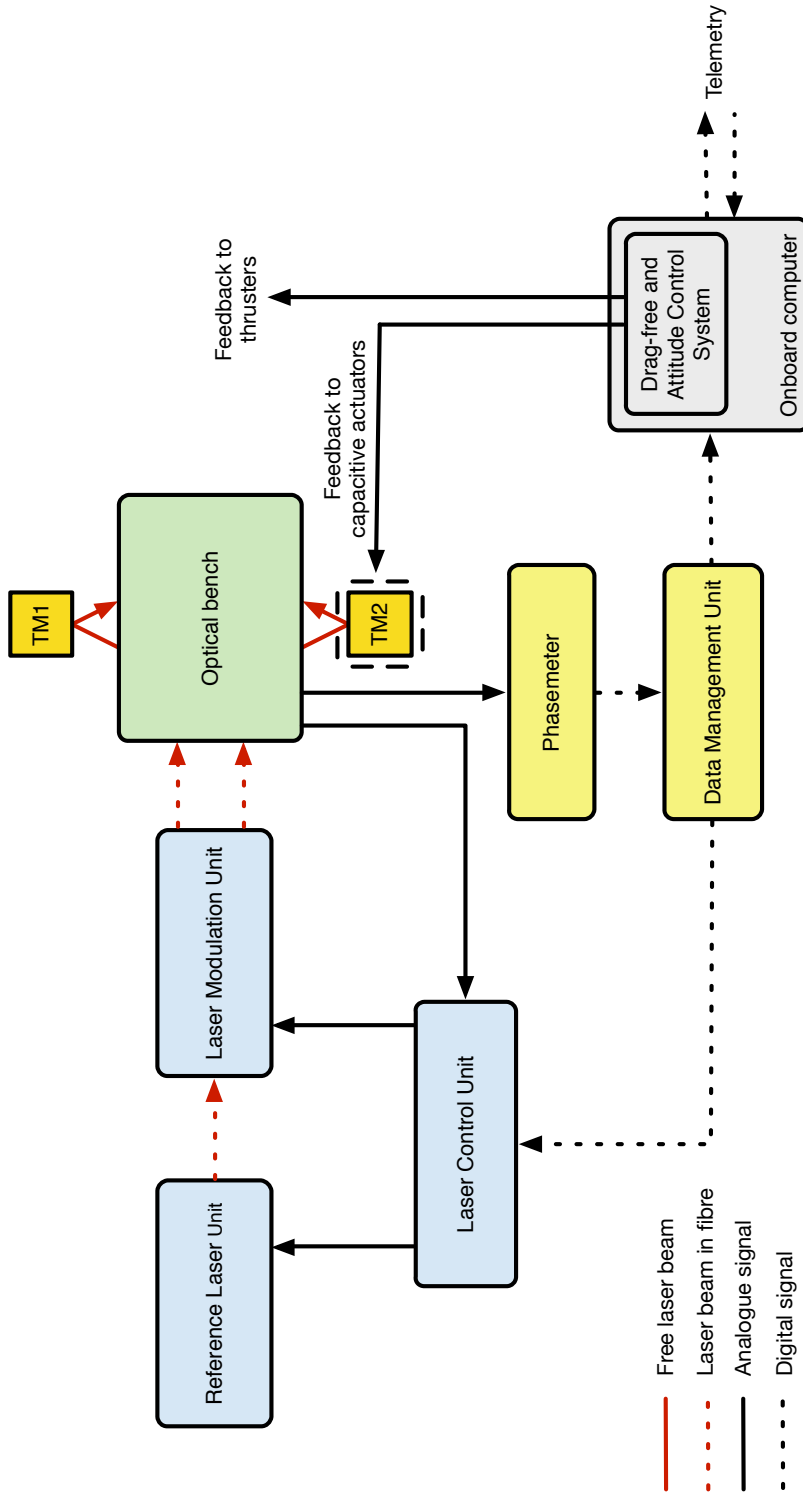
Figure 1.6: A basic block diagram showing subsystems of the optical metrology system in the blue, green, and yellow boxes. The gray boxes show how the signals from the optical metrology system are used as inputs for the Drag-Free and Attitude Control System (DFACS) to maintain the suspended condition of test mass two, and the drag-free condition of test mass one.

1.4.1 Laser assembly

The Laser Assembly (LA) consists of the Reference Laser Unit (RLU), the Laser Modulation Unit (LMU), and the Laser Control Unit (LCU). A block diagram showing only the Laser Assembly (LA) subsystems is shown in Figure 1.7. Photographs of the flight models are shown in Figure 1.8.
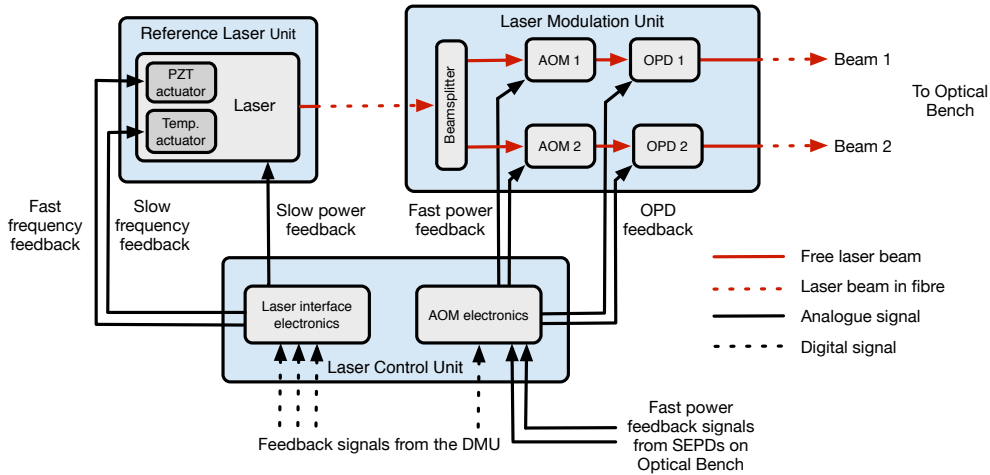
Figure 1.7: A block diagram showing the Laser Assembly subsystems. This diagram shows only the signals relevant to the feedback control systems, a more complete diagram can be found in [18].
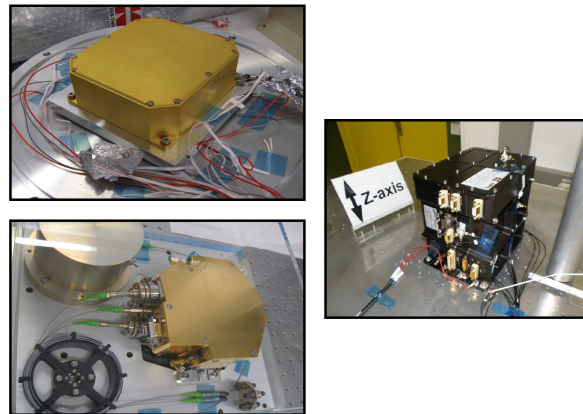
Figure 1.8: The flight models of the RLU (top left), the LMU (bottom left), and the LCU (right). Picture courtesy of ASD and KT.

The laser, housed in the Reference Laser Unit (RLU), is a Non-Planar

Ring Oscillator (NPRO) consisting of a diode-pumped monolithic Nd:YAG crystal. It produces a single transverse TEM_{00} mode at 1064 nm with a linear polarisation [15]. The output power from the laser crystal is approximately 32.5 mW $\pm 30\%$, dependent upon the tuning [19].

The light from the RLU is coupled via an optical fibre with a collimator into the Laser Modulation Unit (LMU) where it propagates as a free beam. This beam is split into two parallel beams of equal intensity and polarisation by a beamsplitter. Each beam passes through an Acousto-Optic Modulator (AOM) where a frequency shift of $+f_{het}/2$ is applied to one beam, and $-f_{het}/2$ to the other (see Box 1.2), where f_{het} is the heterodyne frequency. The result is two beams, with a frequency difference of f_{het}. In-flight, f_{het} is nominally 1 kHz, although this can be changed, if required, via telemetry uploaded to the satellite (500 Hz $< f_{het} <$ 5 kHz). The path of each beam contains an Optical Pathlength Difference (OPD) actuator (see Box 1.3), which adjusts the relative pathlength traversed by the two beams. This is used to suppress differences in the optical pathlengths as well as small vector noise, as described in Section 2.2.2. Each beam is then coupled into a single-mode polarisation-maintaining fibre. The fibre containing beam 1 (often referred to as the measurement beam) is 38 cm longer than the beam 2 (reference beam) fibre.

As well as housing the electronics for the RLU and the LMU, the Laser Control Unit (LCU) also routes the frequency, OPD, and slow amplitude control loops signals from the Data Management Unit (DMU) to the respective actuators, as shown in Figure 1.7. The fast amplitude control loop, described in Section 2.3.3, is implemented inside the LCU. The beam power monitor and RF power monitor signals, as well as the fast amplitude control loop feedback and error signals, are transmitted from the LCU to the DMU.

An introduction to acousto-optic modulators

The AOM consists of a TeO$_2$ crystal with a Piezo-electric Transducer (PZT) bonded to the front face. A Radio Frequency (RF) signal applied to the PZT establishes a propagating acoustic wave inside the crystal. The intensity of the acoustic field changes the refractive index of the crystal, creating a phase grating. A beam passing through the crystal will diffract, and its frequency will be shifted by an amount dependent upon the amplitude of the RF frequency. In LPF, the RF frequency applied to the PZT is 80 MHz $\pm$ f$_{\text{het}}/2$.
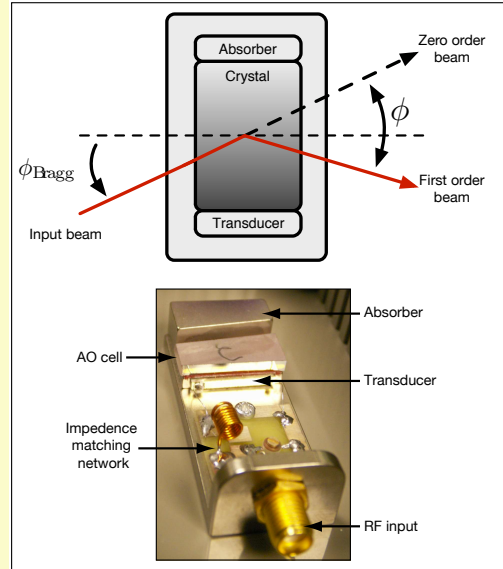
The amount of light diffracted into the first order beam is dependent upon the angle of incidence of the input light, and is maximum at the Bragg angle:

$$\phi_{\text{Bragg}} \approx \frac{\lambda . f_c}{2V_a} \qquad (1.2)$$

where V_a is the acoustic velocity (660 ms^{-1}), f_c is the carrier frequency (80 MHz $\pm$ f$_{\text{het}}/2$), and λ is the optical wavelength (1064 nm) [20].

Changing the RF frequency applied to the crystal changes the efficiency of the phase grating, so applying a lower RF frequency would decrease the power of the first order beam (the power of the zero order beam would increase). This effect is used to control the amplitude of the two beams, as described in Section 2.2.3.

Box 1.2: An overview of the LPF AOMs. The figure shows a conceptual diagram of an AOM, and a photograph of the LPF AOM [21].

The OPD actuators

Each OPD actuator consists of a half wave plate and a fused silica retroreflector mounted on a PZT actuator. The retroreflector can be actuated along the direction of beam propagation to adjust the pathlength travelled by each beam.

The retroreflector is a triple prism, where an incoming beam is reflected from three surfaces, and is output parallel to the original beam. The output beam must later be coupled into a single-mode polarisation maintaining fibre, so the polarisation state and beam quality, i.e., a beam with low phase front distortion and minimal ellipticity, are important. The retroreflector input and output beams will only have the same polarisation state if the input beam is linearly polarised (s- or p-polarisations). Thus, the half wave plate before the retroreflector is used to rotate the polarisation axis of the beam so that all of the incident light is in the s-polarisation state. In this condition, the phase front distortion is small ($\approx \lambda/20$) and there is minimal ellipticity compared to other polarisation states.
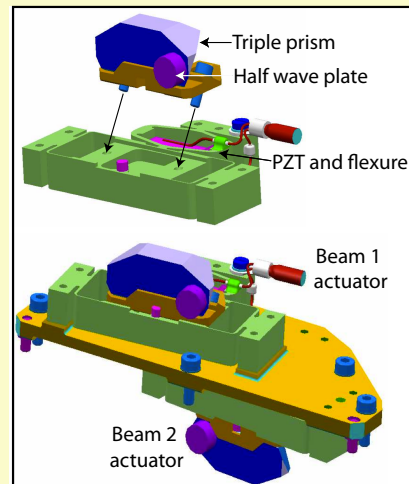
Box 1.3: An overview of the LPF OPD actuator. The figure shows the CAD design of a single actuator (top), and the two actuators on the mounting plate (bottom) [21].

1.4.2 Optical bench and interferometers

The optical bench, as shown in Figures 1.11 and 1.12 and the block diagram in Figure 1.13, consists of a high thermal stability Zerodur® baseplate with hydroxyl-catalysis bonded optics. The light from the two Laser Assembly (LA) fibres is injected onto the optical bench via two Fibre Injector Optical Sub-Assembly (FIOS)s, which are also hydroxyl-catalysis bonded to the baseplate. The beams are often referred to as the measurement beam and the reference beam (not to be confused with the reference interferometer). The beams are then split to form four interferometers:

- **X1**: In the X1 interferometer, shown in Figure 1.14, the measurement beam is reflected off TM1 (having passed through the optical window), while the reference beam remains on the optical bench. The measurement and reference beams recombine and interfere at the beamsplitter marked BS8. This produces two beams, which are read out by the PD1A and PB1B quadrant photodiodes. The measurement beam has a pathlength 38 cm longer, to create an equal armlength interferometer by correcting for the intentional pathlength difference in the optical fibres.

- **X12**: The measurement beam of the X12 interferometer, shown in Figure 1.14 is reflected first from TM1, and then from TM2, while the reference beam remains on the optical bench. The beams recombine and interfere at the BS10 beamsplitter, and are read out by photodiodes PD12A and PD12B. Again, the measurement beam has an extra 38 cm of pathlength to create an equal armlength interferometer by accounting for the difference in the fibres.

- **Frequency**: The frequency interferometer, as shown Figure 1.14, has no moving components, and has an equal armlength on the optical bench. This creates an interferometer with an intentional pathlength mismatch of 38 cm, which amplifies the coupling of laser frequency noise to the interferometer output. This interferometer is used to measure, and provide a feedback signal for the suppression of, laser frequency noise. This is discussed in detail in Section 2.2.1. The measurement and reference beams recombine at beamsplitter BS7, and the resulting beams are readout by photodiodes PDFA and PDFB.

- **Reference**: The reference interferometer, shown in Figure 1.14 has equal armlengths, with an extra 38 cm pathlength difference between the beams on the optical bench to remove the mismatch from the fibres. The processed output from this interferometer is subtracted from the output of the other interferometers in order to subtract the common-mode pathlength fluctuations that occur before the highly stable optical bench (i.e., those originating in the LMU and fibres that connect it to the Optical Bench (OB)). The output from the reference interferometer is also used to provide a feedback signal for the OPD control loop, which suppresses the effect of small vector noise on the output,

as discussed in Section 2.2.2. The measurement and reference beams in the reference interferometer interfere at beamsplitter BS5, and are readout by photodiodes PDRA and PDRB.
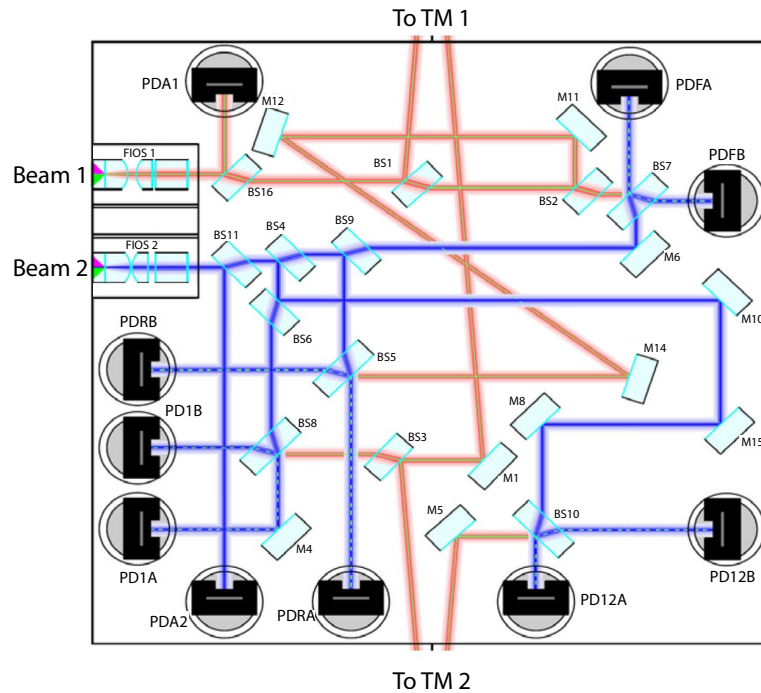
Figure 1.11: A diagram of the optical bench showing the fibre-injectors, the labelled mirrors and beamsplitters, and the photodiodes. Picture courtesy of ASD and IGR.

The principle of optical interference is discussed in detail in Box 1.4.

The photodiodes that detect the interferometric signal after each recombination beamsplitter are InGaS quadrant photodiodes, where 'A' and 'B' are the nominal and redundant photodiodes respectively. They are labelled according to Figure 1.15. The output photocurrent from each photodiode quadrant can be defined according to the convention $I_{i,\hat{j},k}$, where i denotes the interferometer (12, 1, F, or R), $\hat{j}$ the quadrant of the photodiode ($\hat{A}$, $\hat{B}$, $\hat{C}$, or $\hat{D}$), and k defines whether the signal comes from the nominal (A) or redundant (B) photodiode. For example, an output from quadrant A of the nominal X12 interferometer would be labelled $I_{12,A,A}$.

Additionally, the OB has two photodiodes, PDA1 and PDA2, which measure the power in the reflected fraction of each beam after the first beamsplitter. They are used to provide a feedback signal for laser

1 Introduction
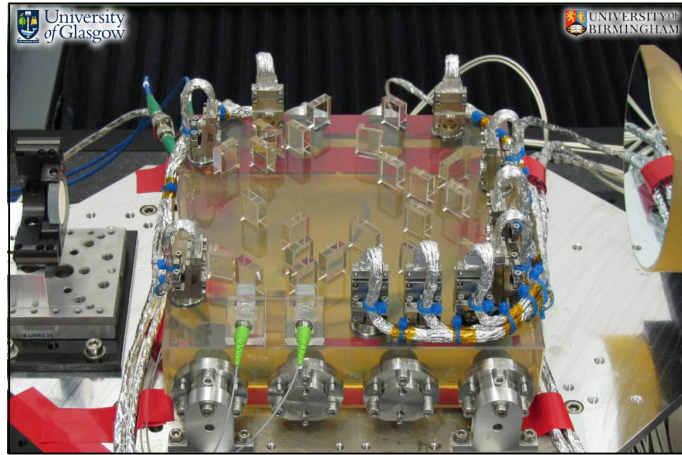
Figure 1.12: A photograph of the flight optical bench, pictured here in a test setup. The FIOSs can be seen near the bottom left of the bench, with green coated fibres inputting light from the Laser Modulation Unit. The bonded optics that form the four interferometers are shown, along with the single-element and quadrant photodiodes located around the edge of the bench with silver coated output cabling. Two mirrors at either side of the optical bench represent the test masses in this setup. Picture courtesy of ASD, IGR and UOB.
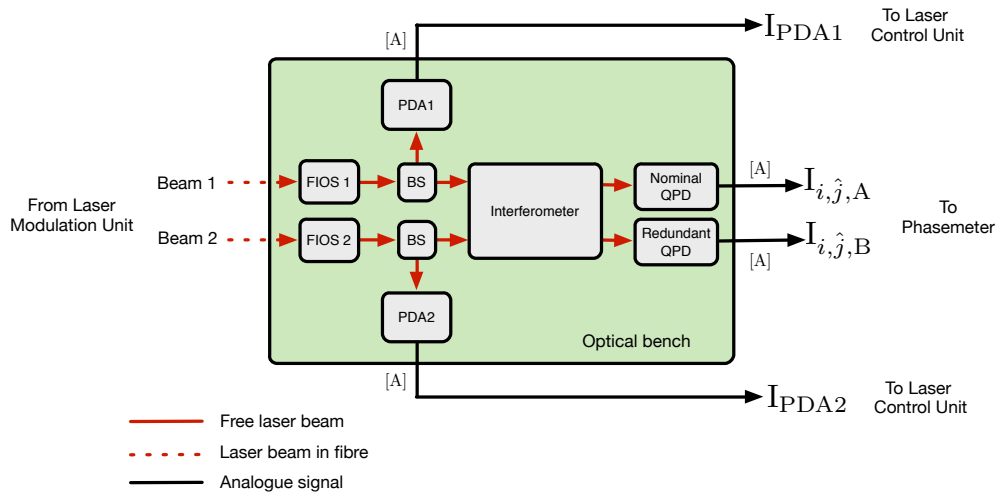
Figure 1.13: A block diagram of the optical bench, showing the two input beams from the Laser Modulation Unit. The two beams are coupled from optical fibres to free beams via the FIOSs and each split at a beamsplitter. The reflected beams, which each contain approximately 8% of the original beam, are read out by single element photodiodes. The transmitted beams form four interferometers, the interference signal of each being readout by two quadrant photodiodes. In this diagram the photocurrent output of just one interferometer is shown, using the $I_{i,\hat{j},k}$ convention for signal labelling, where i denotes the interferometer (12, 1, F, or R), $\hat{j}$ the quadrant of the photodiode ($\hat{A}$, $\hat{B}$, $\hat{C}$, or $\hat{D}$), and k defines whether the signal comes from the nominal (A) or redundant (B) photodiode.
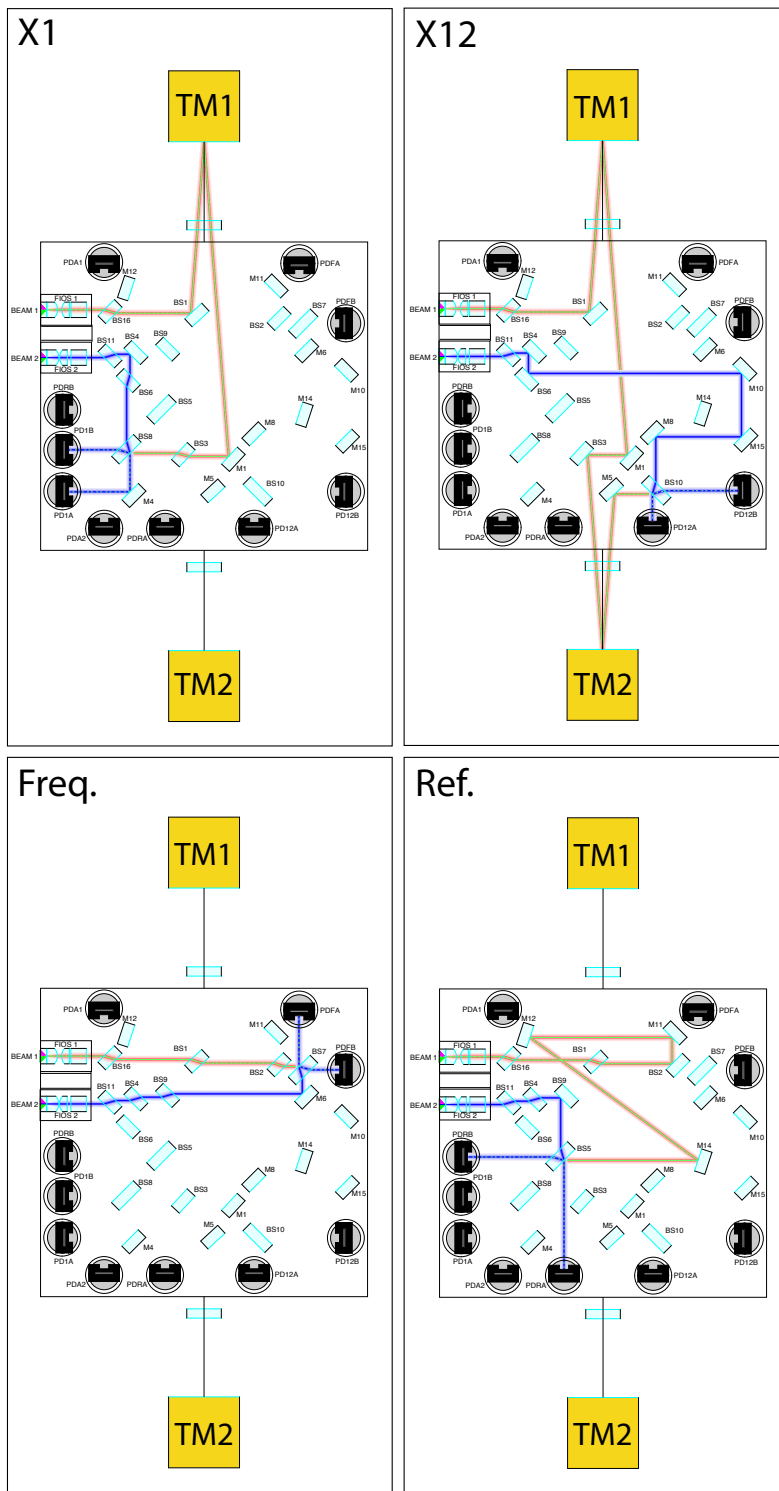
Figure 1.14: Optical diagrams showing the beampaths of the four interferometers on the LPF optical bench with the measurement beam (beam 1) shown in red, and the reference beam (beam 2) shown in blue. Picture courtesy of ASD and IGR.
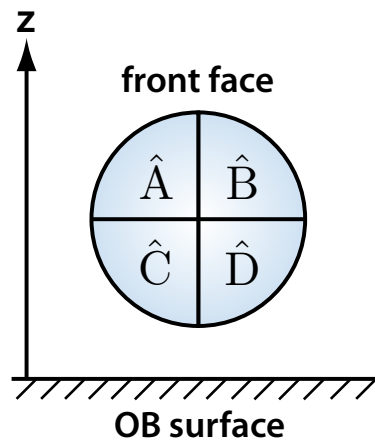
Figure 1.15: The labelling of the quadrant photodiode quadrants, as shown from the front face of the photodiode where the beam is incident [18].

amplitude control, as described in detail in Section 2.2.3. The original intention was for these photodiodes to be single element photodiodes. However, a problem with procurement resulted in them being replaced with InGaS quadrant photodiodes, where the beam is aligned so that all light falls on just one quadrant, and the other quadrants are short circuited [22].

The principle of optical interferometry

A light field at a specific point in space can be described by:

$$E(t) = E_0.e^{i(\omega t + \varphi)} \tag{1.3}$$

where E_0 is the amplitude, $\omega = 2\pi f$ where f is the frequency, t is the time, and φ is the phase.
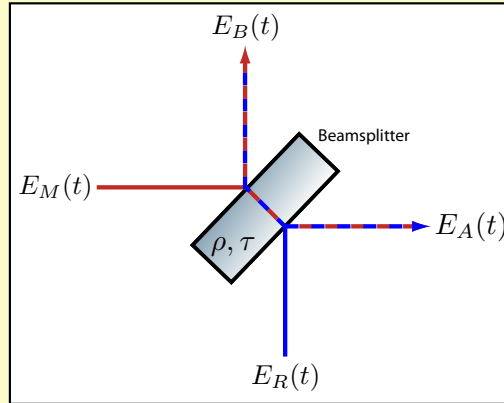
In each of the LISA Pathfinder interferometers two such beams interfere at a recombination beamsplitter, as shown in the above figure. The beamsplitter is ~50:50, such that the coefficients of transmission, τ and reflection, ρ, are equal. The measurement and reference beams, $E_M(t)$ and $E_R(t)$, are described by:

$$E_M(t) = E_{M0}.e^{i(\omega_M t + \varphi_M)} \tag{1.4}$$
$$E_R(t) = E_{R0}.e^{i(\omega_R t + \varphi_R)} \tag{1.5}$$

Continued on next page

1 Introduction

The output beams from the beamsplitter, $E_A(t)$ and $E_B(t)$, are calculated according to the following:

$$
\begin{aligned}
E_A(t) &= i\tau E_M(t) + \rho E_R(t) & (1.6) \\
&= i\tau E_{M0}e^{i(\omega_M t + \varphi_M)} + \rho E_{R0}.e^{i(\omega_R t + \varphi_R)} & (1.7) \\
E_B(t) &= \rho E_M(t) + i\tau E_R(t) & (1.8) \\
&= \rho E_{M0}.e^{i(\omega_M t + \varphi_M)} + i\tau E_{R0}.e^{i(\omega_R t + \varphi_R)} & (1.9)
\end{aligned}
$$

The signal detected at the photodiode is the intensity of the light field, I:

$$\text{I} \propto |E|^2 \tag{1.10}$$

So for $E_A(t)$ the intensity can be calculated according to:

$$
\begin{aligned}
\text{I} &= |E_A(t)|^2 \\
&= |i\tau E_M(t) + \rho E_R(t)|^2 \\
&= \tau^2 E_{M0}^2 + \rho^2 E_{R0}^2 + \\
&\quad i\tau\rho E_{M0}E_{R0}e^{it(\omega_M - \omega_R)+i(\varphi_M - \varphi_R)} - \\
&\quad i\tau\rho E_{M0}E_{R0}e^{it(\omega_R - \omega_M)+i(\varphi_R - \varphi_M)}
\end{aligned}
$$

Using the identities:
$$z - z^* = i2.\text{Im}\{z\}, \tag{1.11}$$

and
$$e^{i\theta} = \cos\theta + i\sin\theta, \tag{1.12}$$

the equation for I can be rewritten as:

$$
\begin{aligned}
\text{I} &= \tau^2 E_{M0}^2 + \rho^2 E_{R0}^2 - \\
&\quad 2\tau\rho E_{M0}E_{R0}\sin((\omega_M - \omega_R)t + (\varphi_M - \varphi_R)). \tag{1.13}
\end{aligned}
$$

So,

$$\text{I} = \tau^2 E_{M0}^2 + \rho^2 E_{R0}^2 - 2\tau\rho E_{M0}E_{R0}\sin(\Delta\omega t + \Delta\varphi) \tag{1.14}$$

Continued on next page

36

where $\Delta\omega = \omega_M - \omega_R$ is the difference in angular frequency of the two beams , and $\Delta\varphi = \varphi_M - \varphi_R$ is the difference in phase. In LPF:

$$\omega_M = 2\pi\left(f_c + \frac{f_{\text{het}}}{2}\right) \tag{1.15}$$

$$\omega_R = 2\pi\left(f_c - \frac{f_{\text{het}}}{2}\right) \tag{1.16}$$

where f_c is the frequency of the carrier, and f_{het} is the heterodyne frequency. The signal incident on the photodiode is therefore a beatnote at the heterodyne frequency:

$$\Delta\omega = \omega_M - \omega_R \tag{1.17}$$

$$= 2\pi\left(f_c + \frac{f_{\text{het}}}{2}\right) - 2\pi\left(f_c - \frac{f_{\text{het}}}{2}\right) \tag{1.18}$$

$$= 2\pi f_{\text{het}} \tag{1.19}$$

Box 1.4: An explanation of the principle of optical interferometry and the photocurrents produced upon the signals detection at a photodiode, with reference to the heterodyne interferometers of LPF [10].

1.4.3 Phasemeter

The LPF satellite contains two 16-channel phasemeters, as shown in Figures 1.16 and 1.17. They take input signals from the nominal and redundant photodiodes respectively. Under normal operating conditions, the output from both phasemeters is used. Each quadrant is treated independently, with each quadrant signal often being referred to as one channel. An overview of the signal processing procedure in the phasemeter is given in Figure 1.18.

The input signal, $I_{i,\hat{j},k}$, from each quadrant is converted to a voltage via a Trans-Impedance Amplifier (TIA) and then low-pass filtered to avoid aliasing. This is then digitised by an Analogue to Digital Convertor (ADC) with a sampling rate, f_s, of $50\,\text{kHz}$. Each channel is now a discretised time-series in the form $V_{i,\hat{j},k}[n]$. The signals

1 Introduction
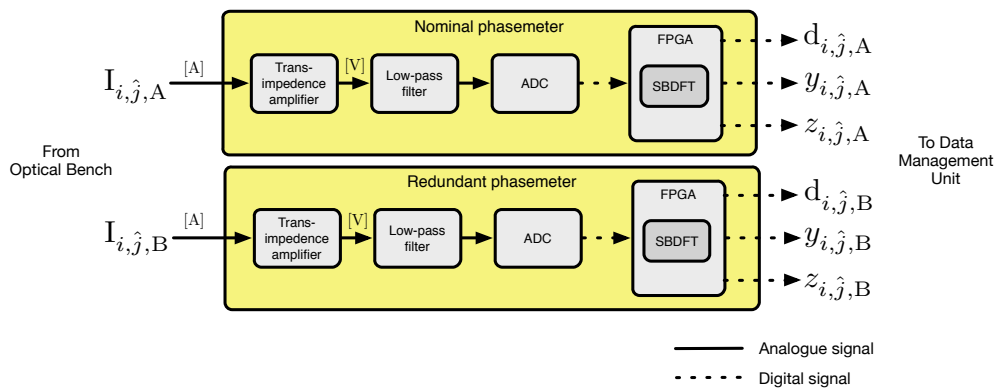
Figure 1.16: A block diagram showing the nominal and redundant phasemeters. Each phasemeter takes in the photocurrent output from each photodiode quadrant, from either the nominal or redundant photodiodes. The photocurrents are converted to a voltage by a trans-impedance amplifier, low-pass filtered, and digitised by an analogue-to-digital convertor. The digital signals are then processed via a single-bin discrete Fourier transform. Each phasemeter outputs the mean DC value and the real and imaginary components of the complex amplitude for each photodiode quadrant.
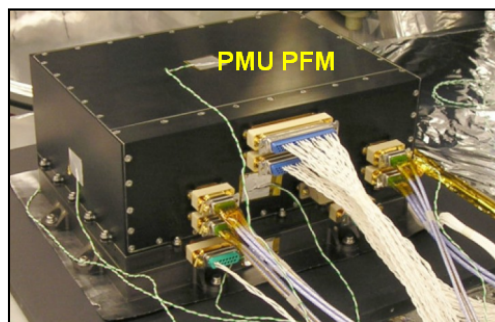
Figure 1.17: A photograph of the flight phasemeter. Picture courtesy of ASD and UOB.

$$\boxed{\mathrm{I}_{i,\hat{j},k}}\ [\mathrm{A}]$$

Convert from current to voltage

$$\boxed{\mathrm{V}_{i,\hat{j},k}}\ [\mathrm{V}]$$

Low-pass filter

Convert from analogue to digital
(scaled to max. ADC voltage range)

$$\boxed{\mathrm{V}_{i,\hat{j},k}[n]}\ [0...1]$$

Single-bin discrete Fourier transform

$$\mathrm{F}(f_{\mathrm{het}}) = z + iy$$

Real component:
$$\mathrm{Re}\{F(f_{het})\} = \sum_{n=0}^{N-1} \mathrm{V}[n].\cos\left(\frac{2\pi f_{het} n}{f_{\mathrm{samp}}}\right)$$

Imaginary component:
$$\mathrm{Im}\{F(f_{het})\} = \sum_{n=0}^{N-1} \mathrm{V}[n].\sin\left(\frac{2\pi f_{het} n}{f_{\mathrm{samp}}}\right)$$

DC (mean) value:
$$d = \sum_{i=0}^{N-1} \mathrm{V}[n]$$

$$\boxed{d_{i,\hat{j},k}} \quad \boxed{y_{i,\hat{j},k}} \quad \boxed{z_{i,\hat{j},k}}$$

[unsigned integer]
(32 bits, 100 Hz)
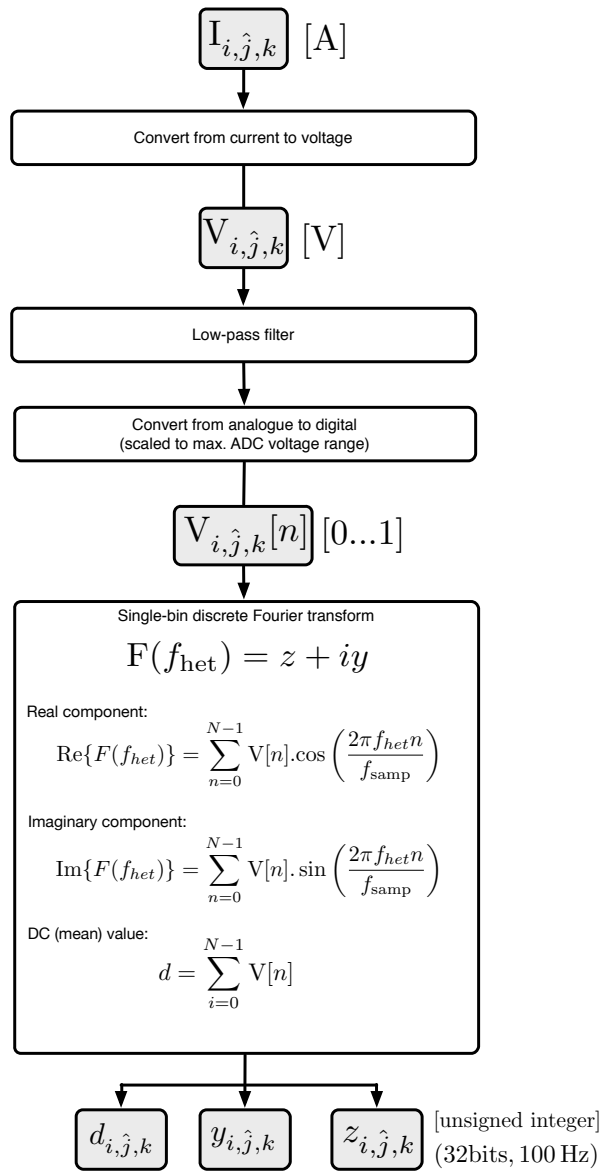
Figure 1.18: A flow chart depicting the signal processing in the phasemeter [23] [18].

are scaled to the voltage range of the ADC such that a value of '1' is the maximum voltage of the ADC. A Single-Bin Discrete Fourier Transform (SBDFT) is performed at the heterodyne frequency, implemented in a Field Programmable Gate Array (FPGA).

The result of the SBDFT is the complex amplitude of the photodiode signal at the heterodyne frequency:

$$\mathrm{F}(f_{\mathrm{het}}) \;=\; z + iy, \tag{1.20}$$

where z is the real component, and y is the imaginary component. One value of $\mathrm{F}(f_{\mathrm{het}})$ is calculated from N samples of $V[n]$. The real and imaginary components of the complex amplitude can be written as:

$$\mathrm{Re}\{\mathrm{F}(f_{\mathrm{het}})\} = \sum_{n=0}^{N-1} V[n].\cos\left(\frac{2\pi f_{\mathrm{het}} n}{f_{\mathrm{samp}}}\right), \tag{1.21}$$

$$\mathrm{Im}\{\mathrm{F}(f_{\mathrm{het}})\} = \sum_{n=0}^{N-1} V[n].\sin\left(\frac{2\pi f_{\mathrm{het}} n}{f_{\mathrm{samp}}}\right). \tag{1.22}$$

Additionally, the total power per quadrant, d, is calculated:

$$d = \sum_{n=0}^{N-1} V[n] \tag{1.23}$$

These signals are 32 bit integers at $100\,\mathrm{Hz}$.

Each channel can be represented by the following:

$$d \;\rightarrow\; d_{i,\hat{j},k} \tag{1.24}$$

$$\mathrm{Re}\{\mathrm{F}\} \;\rightarrow\; z_{i,\hat{j},k} \tag{1.25}$$

$$\mathrm{Im}\{\mathrm{F}\} \;\rightarrow\; y_{i,\hat{j},k} \tag{1.26}$$

where i represents the interferometer (1, 12, F, R), $\hat{j}$ represents the respective photodiode quadrant ($\hat{\mathrm{A}}, \hat{\mathrm{B}}, \hat{\mathrm{C}}$, or $\hat{\mathrm{D}}$), and k is A or B for the nominal or redundant photodiode respectively.

1.4.4 Data management unit

The DMU, shown in Figures 1.19 and 1.20, processes the phasemeter outputs to determine the main OMS measurements via the phasemeter

backend. The calculated values then undergo data preparation, where they are organised into packets at a sampling frequency of 10 Hz. The packets are sent to the Onboard Computer (OBC), and are equivalent to the telemetry packages that are later submitted to ground. In addition, the DMU calculates the feedback signals for the fast and slow frequency control loops, the OPD control loop, and the slow amplitude control loop, which are transmitted to the LCU. An overview of the processing chain is depicted in Figure 1.21. The DMU also houses the LTP master clock, which distributes the clock signals to the other LTP subsystems.

Figure 1.19: A block diagram of the DMU.

Figure 1.20: A photograph of the flight model of the DMU. Picture courtesy of ASD and NTE.

The first step in the DMU processing chain is the conversion of the

1 Introduction

$d_{i,\hat{j},k}$ $y_{i,\hat{j},k}$ $z_{i,\hat{j},k}$ [unsigned integer] (32bits, 100 Hz)

Conversion from integer to floating point numbers

Scaling with c-coefficients:

$$\mathrm{DC}_{i,\hat{j},k} = c^{\mathrm{dc}}_{i,\hat{j},k} \cdot d_{i,\hat{j},k} - c^{\mathrm{offset}}_{i,\hat{j},k}$$

$$\mathrm{Re}\{\mathrm{F}_{i,\hat{j},k}\} = c^{\mathrm{Ry}}_{i,\hat{j},k} \cdot y_{i,\hat{j},k} + c^{\mathrm{Rz}}_{i,\hat{j},k} \cdot z_{i,\hat{j},k} + c^{Rd}_{i,\hat{j},k} \cdot d_{i,\hat{j},k}$$

$$\mathrm{Im}\{\mathrm{F}_{i,\hat{j},k}\} = c^{\mathrm{Iy}}_{i,\hat{j},k} \cdot y_{i,\hat{j},k} + c^{\mathrm{Iz}}_{i,\hat{j},k} \cdot z_{i,\hat{j},k} + c^{Id}_{i,\hat{j},k} \cdot d_{i,\hat{j},k}$$

$\mathrm{DC}_{i,\hat{j},k}$ $\mathrm{Re}\{\mathrm{F}_{i,\hat{j},k}\}$ $\mathrm{Im}\{\mathrm{F}_{i,\hat{j},k}\}$

Quadrant relabelling

$\mathrm{DC}_{i,j,k}$ $\mathrm{Re}\{\mathrm{F}_{i,j,k}\}$ $\mathrm{Im}\{\mathrm{F}_{i,j,k}\}$

Channel selection

$$\mathrm{DC}_{i,j} = \tfrac{1}{2}(\mathrm{DC}_{i,j,\mathrm{A}} + \mathrm{DC}_{i,j,\mathrm{B}}) \qquad \text{A and B ok}$$
$$= \mathrm{DC}_{i,j,\mathrm{A}} \qquad \text{B failure}$$
$$= \mathrm{DC}_{i,j,\mathrm{B}} \qquad \text{A failure}$$
$$= \text{Non-computable} \qquad \text{A and B failure}$$

Channel selection

$$\mathrm{F}_{i,j} = \tfrac{1}{2}(\mathrm{F}_{i,j,\mathrm{A}} + \mathrm{F}_{i,j,\mathrm{B}}) \qquad \text{A and B ok}$$
$$= \mathrm{F}_{i,j,\mathrm{A}} \qquad \text{B failure}$$
$$= \mathrm{F}_{i,j,\mathrm{B}} \qquad \text{A failure}$$
$$= \text{Non-computable} \qquad \text{A and B failure}$$

$\mathrm{DC}_{i,j}$ $\mathrm{F}_{i,j}$

Sum photodiode quadrants

In each interferometer:

$$\Sigma_i = \frac{4}{N_{\mathrm{q}}} \sum_j \mathrm{DC}_{i,j}$$

N_{q} = Number of quadrants used

In other combinations:

$$\Sigma^{\mathrm{left}}_i = \mathrm{DC}_{i,\mathrm{A}} + \mathrm{DC}_{i,\mathrm{C}}$$
$$\Sigma^{\mathrm{right}}_i = \mathrm{DC}_{i,\mathrm{B}} + \mathrm{DC}_{i,\mathrm{D}}$$
$$\Sigma^{\mathrm{up}}_i = \mathrm{DC}_{i,\mathrm{A}} + \mathrm{DC}_{i,\mathrm{B}}$$
$$\Sigma^{\mathrm{down}}_i = \mathrm{DC}_{i,\mathrm{C}} + \mathrm{DC}_{i,\mathrm{D}}$$

Sum photodiode quadrants

In each interferometer:

$$\mathrm{F}_i = \frac{4}{N_{\mathrm{q}}} \sum_j \mathrm{F}_{i,j}$$

N_{q} = Number of quadrants used

In other combinations:

$$\mathrm{F}^{\mathrm{left}}_i = \mathrm{F}_{i,\mathrm{A}} + \mathrm{F}_{i,\mathrm{C}}$$
$$\mathrm{F}^{\mathrm{right}}_i = \mathrm{F}_{i,\mathrm{B}} + \mathrm{F}_{i,\mathrm{D}}$$
$$\mathrm{F}^{\mathrm{up}}_i = \mathrm{F}_{i,\mathrm{A}} + \mathrm{F}_{i,\mathrm{B}}$$
$$\mathrm{F}^{\mathrm{down}}_i = \mathrm{F}_{i,\mathrm{C}} + \mathrm{F}_{i,\mathrm{D}}$$

F_i

Raw Phase with phase tracking

$$\varphi_i = \arg(\mathrm{F}_i) + \mathrm{n}2\pi$$

Processed phase, including subtraction of the reference phase, and phase tracking (PT):

$$\Psi_1 = \mathrm{PT}\left(\arg\frac{\mathrm{F}_1}{\mathrm{F}_{\mathrm{R}}}\right)$$
$$\Psi_{12} = \mathrm{PT}\left(\arg\frac{\mathrm{F}_{12}}{\mathrm{F}_{\mathrm{R}}}\right)$$
$$\Psi_{\mathrm{F}} = \mathrm{PT}\left(\arg\frac{\mathrm{F}_{12}}{\mathrm{F}_{\mathrm{R}}}\right)$$
$$\Psi_{\mathrm{R}} = \mathrm{PT}\left(\arg(\mathrm{F}_{\mathrm{R}})\right)$$

Ψ_i

Amplitude
$$a_i = |\mathrm{F}_i|$$

a_i

Σ_i Σ^{left}_i $\Sigma^{\mathrm{right}}_i$ Σ^{up}_i Σ^{down}_i

$\mathrm{F}^{\mathrm{left}}_i$ $\mathrm{F}^{\mathrm{right}}_i$ $\mathrm{F}^{\mathrm{up}}_i$ $\mathrm{F}^{\mathrm{down}}_i$

Ψ_1 Ψ_{12}

Calculate the normalised DC signals

$$\mathrm{DC}^{\phi}_i = \frac{\Sigma^{\mathrm{left}}_i - \Sigma^{\mathrm{right}}_i}{\Sigma_i}$$
$$\mathrm{DC}^{\eta}_i = \frac{\Sigma^{\mathrm{up}}_i - \Sigma^{\mathrm{down}}_i}{\Sigma_i}$$

Calculate DWS signals

$$\mathrm{DWS}^{\phi}_i = \arg\left(\frac{\mathrm{F}^{\mathrm{left}}_i}{\mathrm{F}^{\mathrm{right}}_i}\right)$$
$$\mathrm{DWS}^{\eta}_i = \arg\left(\frac{\mathrm{F}^{\mathrm{up}}_i}{\mathrm{F}^{\mathrm{down}}_i}\right)$$

Convert from raw phase to pathlength

$$x_1 = \frac{\lambda}{4\pi} \frac{1}{\cos(\alpha)} \cdot \Psi_1$$
$$x_{12} = \frac{\lambda}{4\pi} \frac{1}{\cos(\alpha)} \cdot \Psi_{12}$$

where α = angle of beam incidence on TM

x_1 x_{12} [m]

DC^{ϕ}_i DC^{η}_i [0...1]

DWS^{ϕ}_i DWS^{η}_i

Scale to radians with g-coefficients

$$\phi^{\mathrm{DC}}_1 = g_{11} \cdot \mathrm{DC}^{\phi}_1$$
$$\eta^{\mathrm{DC}}_1 = g_{12} \cdot \mathrm{DC}^{\eta}_1$$
$$\phi^{\mathrm{DC}}_2 = g_{13} \cdot \mathrm{DC}^{\phi}_1 + g_{14} \cdot \mathrm{DC}^{\phi}_{12}$$
$$\eta^{\mathrm{DC}}_2 = g_{15} \cdot \mathrm{DC}^{\eta}_1 + g_{16} \cdot \mathrm{DC}^{\eta}_{12}$$

Scale to radians with g-coefficients

$$\phi^{\mathrm{DWS}}_1 = g_1 \cdot \mathrm{DWS}^{\phi}_1$$
$$\eta^{\mathrm{DWS}}_1 = g_2 \cdot \mathrm{DWS}^{\eta}_1$$
$$\phi^{\mathrm{DWS}}_2 = g_3 \cdot \mathrm{DWS}^{\phi}_1 + g_4 \cdot \mathrm{DWS}^{\phi}_{12}$$
$$\eta^{\mathrm{DWS}}_2 = g_5 \cdot \mathrm{DWS}^{\eta}_1 + g_6 \cdot \mathrm{DWS}^{\eta}_{12}$$

ϕ^{DC}_2 ϕ^{DC}_1 η^{DC}_1 η^{DC}_2 [rad]

ϕ^{DWS}_1 ϕ^{DWS}_2 η^{DWS}_1 η^{DWS}_2 [rad]

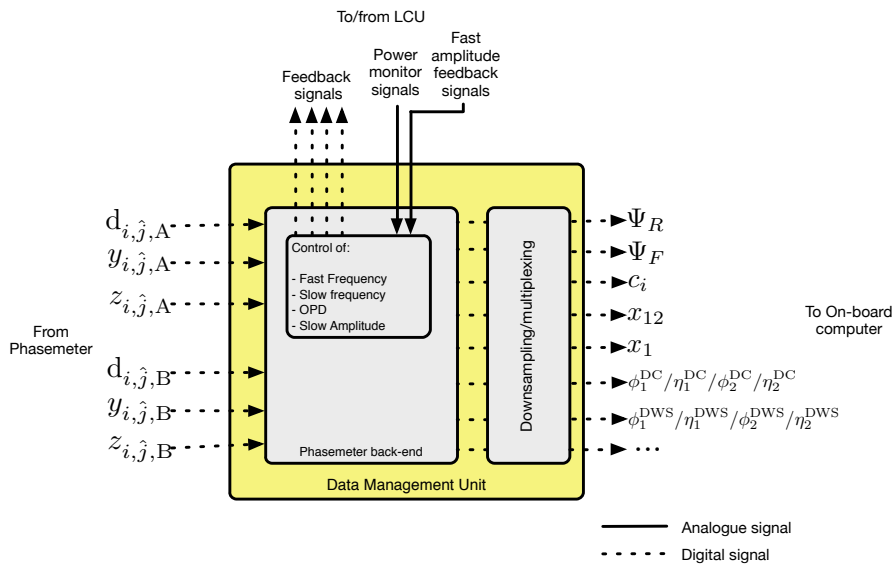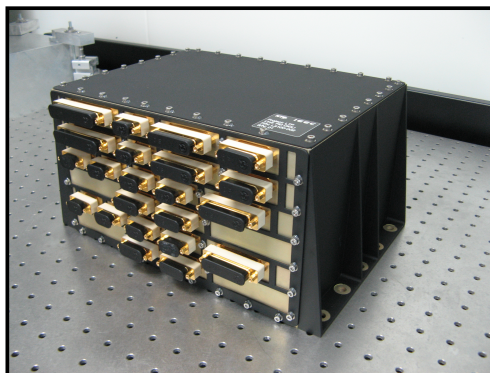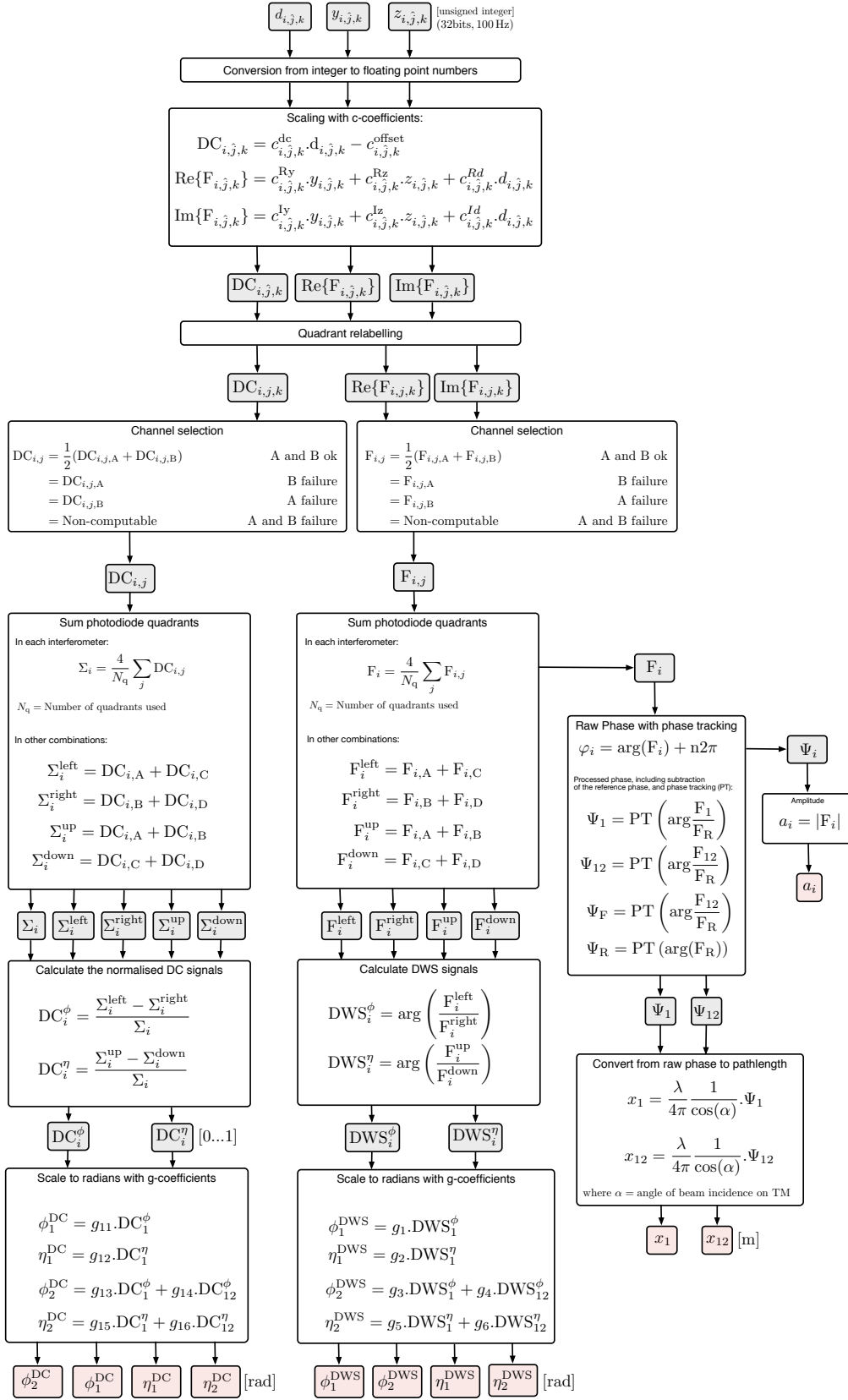**Figure 1.21:** A flow chart depicting the signal processing in the DMU [18] [23].

integer signals from the phasemeter into floating point numbers. The resulting signals are then scaled using c-coefficients, $c_{i,\hat{j},k}$, (see Box 1.6):

$$
\begin{aligned}
\mathrm{DC}_{i,\hat{j},k} &= c_{i,\hat{j},k}^{\mathrm{dc}} . d_{i,\hat{j},k} - c_{i,\hat{j},k}^{\mathrm{offset}} & (1.27) \\
\mathrm{Re}\{\mathrm{F}_{i,\hat{j},k}\} &= c_{i,\hat{j},k}^{\mathrm{Ry}} . y_{i,\hat{j},k} + c_{i,\hat{j},k}^{\mathrm{Rz}} . z_{i,\hat{j},k} + c_{i,\hat{j},k}^{\mathrm{Rd}} . d_{i,\hat{j},k} & (1.28) \\
\mathrm{Im}\{\mathrm{F}_{i,\hat{j},k}\} &= c_{i,\hat{j},k}^{\mathrm{Iy}} . y_{i,\hat{j},k} + c_{i,\hat{j},k}^{\mathrm{Iz}} . z_{i,\hat{j},k} + c_{i,\hat{j},k}^{\mathrm{Id}} . d_{i,\hat{j},k} & (1.29)
\end{aligned}
$$

At this point, the quadrant labelling of the signals needs to be redefined. This ensures that the correct quadrants on the nominal and redundant photodiodes in each interferometer are paired. This only affects the X12 and frequency interferometers, where one of the beams is reflected from a mirror after the recombination beamsplitter. The new labelling scheme is shown in Figure 1.22.
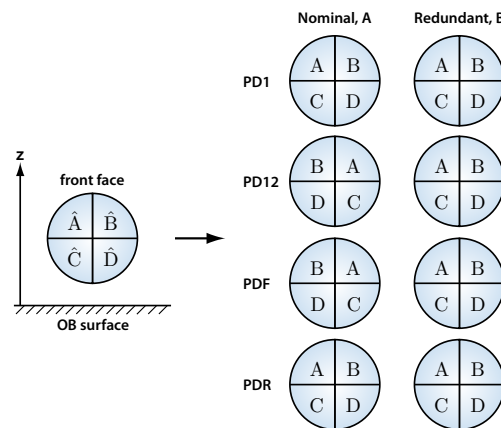

Figure 1.22: A diagram showing the relabelling of the quadrants on the nominal and redundant photodiodes in order to ensure that the correct quadrants are compared during the DMU processing [23].

The next step in the processing chain is the averaging of the photodiode channels. The channels selected from each interferometer depends upon the condition of the data in each quadrant according to the fol-

lowing conditions:

$$\mathrm{DC}_{i,j} = \frac{1}{2}(\mathrm{DC}_{i,j,A} + \mathrm{DC}_{i,j,B}) \text{ A and B ok}$$

$$= \mathrm{DC}_{i,j,A} \text{ B failure}$$

$$= \mathrm{DC}_{i,j,B} \text{ A failure}$$

$$= \text{Non-computable A and B failure}$$

$$\mathrm{F}_{i,j} = \frac{1}{2}(\mathrm{F}_{i,j,A} + \mathrm{F}_{i,j,B}) \text{ A and B ok}$$

$$= \mathrm{F}_{i,j,A} \text{ B failure}$$

$$= \mathrm{F}_{i,j,B} \text{ A failure}$$

$$= \text{Non-computable A and B failure}$$

In this way, a real, imaginary, and a Direct Current (DC) component for each photodiode is determined. By summing the photodiodes channels before calculating the longitudinal test mass displacement and angles, the quadrants with a higher f_{het} amplitude improve the overall Signal to Noise Ratio (SNR).

The next step is to sum the quadrants of each photodiode:

$$\Sigma_i = \frac{4}{N_{\mathrm{q}}} \sum_j \mathrm{DC}_{i,j} \qquad (1.30)$$

$$\mathrm{F}_i = \frac{4}{N_{\mathrm{q}}} \sum_j \mathrm{F}_{i,j} \qquad (1.31)$$

where N_{q} is the number of quadrants used in the calculation, which depends upon the data condition.

Calculation of longitudinal phases and displacements

The amplitude, a_i, and raw phase of the signal, φ_i, can be calculated according to Equations 1.32 and 1.33. A phase tracking algorithm, represented by n2π, has been applied to the phase in order to track test mass displacements larger than λ. This algorithm compares the previously calculated phase value with the current phase value, assumes the difference between the two should be small and adds an

integer number of 2π accordingly.

$$a_i = |F_i| \tag{1.32}$$

$$\varphi_i = \arctan\left(\frac{y_i}{z_i}\right) + n2\pi \tag{1.33}$$

$$= \arg(F_i) + n2\pi. \tag{1.34}$$

Taking into account the subtraction of the reference interferometer to remove common-mode pathlength noise, the processed phase outputs from the four interferometers can be written as:

$$\Psi_1 = PT\left(\arg\frac{F_1}{F_R}\right) \tag{1.35}$$

$$\Psi_{12} = PT\left(\arg\frac{F_{12}}{F_R}\right) \tag{1.36}$$

$$\Psi_F = PT\left(\arg\frac{F_F}{F_R}\right) \tag{1.37}$$

$$\Psi_R = PT\left(\arg(F_R)\right) \tag{1.38}$$

where PT represents the phase tracking algorithm.

The Ψ_1 and Ψ_{12} phase signals are converted to pathlength according to:

$$x_1 = \frac{\lambda}{4\pi}\frac{1}{\cos(\alpha)}.\Psi_1 \tag{1.39}$$

$$x_{12} = \frac{\lambda}{4\pi}\frac{1}{\cos(\alpha)}.\Psi_{12} \tag{1.40}$$

where the $\cos(\alpha)$ scaling converts from an optical pathlength, the distance travelled by the light, into the displacement of the test mass and $\alpha \approx 4.5°$ is the nominal angle of incidence of light on the test mass [22]. This is further explained in Box 1.5.

Conversion from an optical pathlength to an equivalent test mass displacement
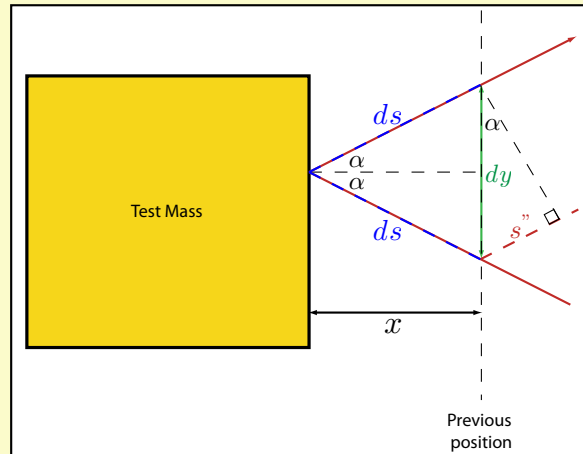
The phase, φ, measured by the interferometer is related to the difference in the optical pathlength between the two interferometer arms, s, according to:

$$s = \frac{\lambda}{2\pi}\varphi \qquad (1.41)$$

where λ is the wavelength of the light. Ideally, the difference in the optical pathlength is due only to the motion of the test mass. The figure above shows the measurement beam reflected from the test mass at an angle, α, where the test mass has been displaced by some longitudinal distance, x. The phase change due to the optical pathlength ds before the reflection is cancelled by the phase change in the opposite direction after reflection. Therefore the phase change measured in the interferometer is due to the s'' optical pathlength. From the diagram, it follows that:

$$
\begin{aligned}
ds &= \frac{x}{\cos\alpha} \\
dy &= 2ds\sin\alpha \\
s'' &= dy\sin\alpha \\
&= 2x\frac{\sin^2\alpha}{\cos\alpha} \\
s &= 2ds + s'' \\
&= 2x\cos\alpha
\end{aligned}
$$

So the displacement, x, is:

$$x = \frac{s}{2 \cos \alpha} \tag{1.42}$$

Using Equation 1.41, the relationship between test mass displacement and interferometric phase is:

$$x = \frac{\lambda}{4\pi \cos \alpha} \varphi \tag{1.43}$$

Box 1.5: An explanation of the conversion from optical pathlength to equivalent test mass displacement [24].

Calculation of angular test mass fluctuations

The main measure of test mass angles is made via Differential Wavefront Sensing (DWS), an additional measurement of beam offsets, the DC, can be used to calculate rough angular estimates:

- **DC:** The DC value estimates the centre of the beam power on the photodiode. These signals provide rough alignment of the beams on the photodiodes as no interference is required, just some light power on the photodiodes. They are used to determine the test mass misalignments:

    - ϕ_i^{DC}: The horizontal misalignment of the test mass, determined by finding the difference in the average power between the left and right side of the photodiode.

    - η_i^{DC}: The vertical DC misalignment of the test mass, determined by finding the difference in the average power between the top and bottom of the photodiode.

- **DWS:** The DWS value determines the tilt of the interfering wavefronts with respect to one another. It is used to provide the

φ and η alignment signals for the test masses to be used as feedback to the Drag-Free and Attitude Control System (DFACS). These signals are also used for precise alignment of the beams of the photodiodes, being approximately ten times more sensitive than the DC signals. They are used to determine the test mass misalignments:

- ϕ_i^{DWS}: The horizontal misalignment of the test mass, found by taking the phase difference between the quadrants on the left and right half of the photodiode.

- η_i^{DWS}: The vertical misalignment of the test mass, found by taking the phase difference between the quadrants on the upper and lower half of the photodiode.

Initially, the complex amplitudes, $\text{F}_{i,j}$, and DC coefficients, $\text{DC}_{i,j}$, are summed to determine the left, right, upper, and lower quadrant combinations for each photodiode:

$$\text{F}_i^{\text{left}} = \text{F}_{i,\text{A}} + \text{F}_{i,\text{C}} \tag{1.44}$$
$$\text{F}_i^{\text{right}} = \text{F}_{i,\text{B}} + \text{F}_{i,\text{D}} \tag{1.45}$$
$$\text{F}_i^{\text{up}} = \text{F}_{i,\text{A}} + \text{F}_{i,\text{B}} \tag{1.46}$$
$$\text{F}_i^{\text{down}} = \text{F}_{i,\text{C}} + \text{F}_{i,\text{D}} \tag{1.47}$$

$$\Sigma_i^{\text{left}} = \text{DC}_{i,\text{A}} + \text{DC}_{i,\text{C}} \tag{1.48}$$
$$\Sigma_i^{\text{right}} = \text{DC}_{i,\text{B}} + \text{DC}_{i,\text{D}} \tag{1.49}$$
$$\Sigma_i^{\text{up}} = \text{DC}_{i,\text{A}} + \text{DC}_{i,\text{B}} \tag{1.50}$$
$$\Sigma_i^{\text{down}} = \text{DC}_{i,\text{C}} + \text{DC}_{i,\text{D}} \tag{1.51}$$

The normalised DC signal is then calculated according to:

$$\text{DC}_i^{\phi} = \frac{\Sigma_i^{\text{left}} - \Sigma_i^{\text{right}}}{\Sigma_i} \tag{1.52}$$

$$\text{DC}_i^{\eta} = \frac{\Sigma_i^{\text{up}} - \Sigma_i^{\text{down}}}{\Sigma_i} \tag{1.53}$$

where Σ_i and F_i are taken from Equations 1.30 and 1.31. These values are scaled to radians by using g-coefficients (see Box 1.7):

$$
\begin{aligned}
\phi_1^{\mathrm{DC}} &= g_{11}.\mathrm{DC}_1^{\phi} & (1.54) \\
\eta_1^{\mathrm{DC}} &= g_{12}.\mathrm{DC}_1^{\eta} & (1.55) \\
\phi_2^{\mathrm{DC}} &= g_{13}.\mathrm{DC}_1^{\phi} + g_{14}.\mathrm{DC}_{12}^{\phi} & (1.56) \\
\eta_2^{\mathrm{DC}} &= g_{15}.\mathrm{DC}_1^{\eta} + g_{16}.\mathrm{DC}_{12}^{\eta} & (1.57)
\end{aligned}
$$

The DWS signals are calculated according to:

$$
\begin{aligned}
\mathrm{DWS}_i^{\phi} &= \arg\left(\frac{\mathrm{F}_i^{\mathrm{left}}}{\mathrm{F}_i^{\mathrm{right}}}\right) & (1.58) \\
\mathrm{DWS}_i^{\eta} &= \arg\left(\frac{F_i^{\mathrm{up}}}{\mathrm{F}_i^{\mathrm{down}}}\right) & (1.59)
\end{aligned}
$$

These give the relative phase difference between the beams as a value between $-\pi$ and $+\pi$. These values are converted into an equivalent geometric TM orientation in radians via the g-coefficients (see Box 1.7):

$$
\begin{aligned}
\phi_1^{\mathrm{DWS}} &= g_1.\mathrm{DWS}_1^{\phi} & (1.60) \\
\eta_1^{\mathrm{DWS}} &= g_2.\mathrm{DWS}_1^{\eta} & (1.61) \\
\phi_2^{\mathrm{DWS}} &= g_3.\mathrm{DWS}_1^{\phi} + g_4.\mathrm{DWS}_{12}^{\phi} & (1.62) \\
\eta_2^{\mathrm{DWS}} &= g_5.\mathrm{DWS}_1^{\eta} + g_6.\mathrm{DWS}_{12}^{\eta} & (1.63)
\end{aligned}
$$

The c-coefficients

Applying the c-coefficients to $d_{i,\hat{j},k}$, and $F_{i,\hat{j},k}$ performs the following:

- Normalisation, so that the nominal value is 1 for the situation where both beams are on and well aligned.

- Removal of the $180°$ phase difference between the nominal and redundant photodiodes.

- DC compensation with $c^{Id}_{i,\hat{j},k}$ and $c^{Rd}_{i,\hat{j},k}$, to remove the DC components of the real and imaginary components of $F_{i,\hat{j}}$ which were added during the unsigned-integer phasemeter processing.

- $c^{dc}_{i,\hat{j},k} = 1/RN$, where N is the SBDFT length, and R is the ADC range. This scales d, as the output from the phasemeter is a fraction of the maximum ADC voltage range.

- Amplitude calibration.

- Phase calibration with $c^{Ry}_{i,\hat{j},k}$ and $c^{Iz}_{i,\hat{j},k}$, which are ideally zero.

- Dark current subtraction with $c^{\text{offset}}_{i,\hat{j},k}$.

- Windowing.

The c-coefficients are pre-computed on-ground.

Box 1.6: A description of the c-coefficients [23] [25].

The g-coeffcients

Assuming no cross-couplings, the physical angular misalignment of each test mass is related to the calculated DC and DWS angular misalignments via a set of k-coefficients, according to:

$$\begin{pmatrix} \mathrm{DWS}_1^\phi \\ \mathrm{DWS}_1^\eta \end{pmatrix} = \begin{pmatrix} k_1 & 0 \\ 0 & k_2 \end{pmatrix} \begin{pmatrix} \phi_1^{\mathrm{DWS}} \\ \eta_1^{\mathrm{DWS}} \end{pmatrix}$$

$$\begin{pmatrix} \mathrm{DWS}_{12}^\phi \\ \mathrm{DWS}_{12}^\eta \end{pmatrix} = \begin{pmatrix} k_3 & 0 \\ 0 & k_5 \end{pmatrix} \begin{pmatrix} \phi_1^{\mathrm{DWS}} \\ \eta_1^{\mathrm{DWS}} \end{pmatrix} + \begin{pmatrix} k_4 & 0 \\ 0 & k_6 \end{pmatrix} \begin{pmatrix} \phi_2^{\mathrm{DWS}} \\ \eta_2^{\mathrm{DWS}} \end{pmatrix}$$

which can also be written as:

$$\begin{aligned} \mathrm{DWS}_1^\phi &= k_1.\phi_1^{\mathrm{DWS}} \\ \mathrm{DWS}_1^\eta &= k_2.\eta_1^{\mathrm{DWS}} \\ \mathrm{DWS}_{12}^\phi &= k_3.\phi_1^{\mathrm{DWS}} + k_4.\phi_2^{\mathrm{DWS}} \\ \mathrm{DWS}_{12}^\eta &= k_5.\eta_1^{\mathrm{DWS}} + k_6.\eta_2^{\mathrm{DWS}} \end{aligned}$$

Similarly for the DC angular misalignments:

$$\begin{pmatrix} \mathrm{DC}_1^\phi \\ \mathrm{DC}_1^\eta \end{pmatrix} = \begin{pmatrix} k_{11} & 0 \\ 0 & k_{12} \end{pmatrix} \begin{pmatrix} \phi_1^{\mathrm{DC}} \\ \eta_1^{\mathrm{DC}} \end{pmatrix}$$

$$\begin{pmatrix} \mathrm{DC}_{12}^\phi \\ \mathrm{DC}_{12}^\eta \end{pmatrix} = \begin{pmatrix} k_{13} & 0 \\ 0 & k_{15} \end{pmatrix} \begin{pmatrix} \phi_1^{\mathrm{DC}} \\ \eta_1^{\mathrm{DC}} \end{pmatrix} + \begin{pmatrix} k_{14} & 0 \\ 0 & k_{16} \end{pmatrix} \begin{pmatrix} \phi_2^{\mathrm{DC}} \\ \eta_2^{\mathrm{DC}} \end{pmatrix}$$

which can be rewritten as:

$$\begin{aligned} \mathrm{DC}_1^\phi &= k_{11}.\phi_1^{\mathrm{DC}} \\ \mathrm{DC}_1^\eta &= k_{12}.\eta_1^{\mathrm{DC}} \\ \mathrm{DC}_{12}^\phi &= k_{13}.\phi_1^{\mathrm{DC}} + k_{14}.\phi_2^{\mathrm{DC}} \\ \mathrm{DC}_{12}^\eta &= k_{15}.\eta_1^{\mathrm{DC}} + k_{16}.\eta_2^{\mathrm{DC}} \end{aligned}$$

The k-coefficients are calculated on-ground by applying a known angular misalignment to each test mass in turn, and recording the output from the DC and DWS [22] [26] [27]. The values for k_1 to k_6 are of the order of a few thousand, and the values for k_{11} to k_{16} are of the order of a few hundred.

Continued on next page

1 Introduction

In-flight it is necessary to convert in the other direction, from the DC and DWS angular misalignments into the physical test mass angular misalignments. This is achieved by applying g-coefficients, which are calculated from the k-coefficients:

$$g_1 = \frac{1}{k_1} \qquad g_{11} = \frac{1}{k_{11}}$$

$$g_2 = \frac{1}{k_2} \qquad g_{12} = \frac{1}{k_{12}}$$

$$g_3 = \frac{k_3}{k_1 . k_4} \qquad g_{13} = \frac{k_{13}}{k_{11} . k_{14}}$$

$$g_4 = \frac{1}{k_4} \qquad g_{14} = \frac{1}{k_{14}}$$

$$g_5 = \frac{k_5}{k_2 . k_6} \qquad g_{15} = \frac{k_{15}}{k_{12} . k_{16}}$$

$$g_6 = \frac{1}{k_6} \qquad g_{16} = \frac{1}{k_{16}}$$

Box 1.7: A description of the g-coefficients, the values used to convert the DWS and DC angular misalignment signals to engineering units [23] [26] [27].

Contrast

The contrast, c_i, of each interferometer is a measure of how well the measurement and reference beams overlap on the photodiode. It is calculated from the ratio of the length of the complex amplitude, F_i, and the DC amplitude, Σ_i. This gives a result between 0 and 1 (although often given as a percentage), where a signal close to 1 is an indication that both the intensities and wavefronts of the interfering beams are well matched.

$$c_i = \frac{|F_i|}{\Sigma_i} \tag{1.64}$$

Feedback signals

The DMU also processes the signals required for the fast and slow frequency, fast and slow Optical Pathlength Difference (OPD), and slow amplitude control loops, as described in Chapter 2:

- **Frequency control loop:** The output from the frequency interferometer (with the reference interferometer signal subtracted), Ψ_F, provides the input signal for the frequency control loop.

- **Optical Pathlength Difference (OPD) control loop:** The output from the reference interferometer, Ψ_R, is used as the input signal to the OPD control loop.

- **Slow amplitude control loop:** The fast amplitude control loop feedback signals are received from the LMU and provide the input signals to the slow amplitude control loop.

These inputs are processed according to the control laws described in Section 2.3, and the resulting feedback signals are transferred to the LCU. Some loop signals are processed and sent to the OBC and can be telemetered to ground (see Section 2.3).

Data preparation

The $100\,\mathrm{Hz}$ data from the phasemeter backend in the DMU is then processed. The way in which it is processed depends upon which telemetry packet it will be sorted into for transmission to ground by the OBC. The LPF telemetry is arranged into packets which contain some combination of parameters (also called channels) defined by a unique System Identification (SID) number.

There are two telemetry packets that contain data relating to the science output of the OMS:

- **128,3:** The main science packet which includes the longitudinal displacement parameters, x_{12} and x_1, and the angular parameters, ϕ_1 and η_1, and ϕ_2 and η_2. This package is non-configurable, and therefore always contains the same parameters. The data

from the DMU is downsampled from $100\,\mathrm{Hz}$ to $10\,\mathrm{Hz}$.

- **128,4:** This packet has numerous related SIDs, so it can be configured to contain parameters specific to a particular experiment. This packet can also be used to transmit up to 36 parameters from the Interferometer Data Log (IDL), see Box 1.8.

The interferometer data log

The IDL provides a means of recording a limited amount of interferometer data at a higher sampling rate. It can be commanded to store up to $256\,\mathrm{kbytes}$ of interferometer data at $100\,\mathrm{Hz}$, $10\,\mathrm{Hz}$, or $1\,\mathrm{Hz}$, without disturbing ongoing OMS calculations. The IDL is organised as a circular buffer, so when the limit of the Random Access Memory (RAM) is reached, the writing continues over the previously recorded information until a stop command is received. This allows a maximum of $18.2\,\mathrm{s}$ of $100\,\mathrm{Hz}$ data to be recorded.

Box 1.8: A description of the IDL [23].

1.4.5 On-board computer

The OBC routes the main science outputs, x_1, x_{12}, ϕ_1^{DWS}, η_1^{DWS}, ϕ_2^{DWS}, and η_2^{DWS} to the DFACS for test mass control. The subsystem also prepares the telemetry for transmission to ground, and processes the information received from Earth for distribution to the appropriate subsystems.

Data is received from all satellite subsystems, but in terms of the OMS, the OBC receives the $10\,\mathrm{Hz}$ 128,3 and 128,4 packets from the DMU, along with housekeeping data. The way in which the data is processed depends upon which telemetry packet it belongs to:

- 128,3: The data from the DMU is unpacked and put into the System Data Pool (SDP) along with the packet generation time. This data can then be directly telemetered to the ground using an OBC housekeeping package (3,25 or 3,26). Alternatively, the data may also be downsampled to $5\,\mathrm{Hz}$, $2\,\mathrm{Hz}$, or $1\,\mathrm{Hz}$ by averaging two, five, or ten parameter values. The sample time is taken directly from the DMU packet generation time.

- 128,4: The 128,4 packet can be processed in two different ways, dependent upon the data it contains:

  - The 128,4 packet can contain 12 parameters which can be taken from any of the SDP parameters, and an additional 24 channels of raw phases. As the form of the data is not known before the package SID is known, the data is unpacked and put into two storage locations, as both a float and an integer. When the required configuration of parameters is defined, the data is extracted from the correct data pool, downsampled as required, and then telemetered via the same housekeeping packet as for the 128,3 (3,25 or 3,26).

  - The 100 Hz IDL data does not require downsampling, and it cannot be filtered by the OBC. The data is sent directly to the packet store to be telemetered to Earth.

1.5 In-flight operations

The LISA Pathfinder mission is planned to last 256 days in total. A breakdown of the mission timeline is shown in Figure 1.23. The phases of the mission, and the data transfer to and from the satellite, are explained in more detail in the following subsections.
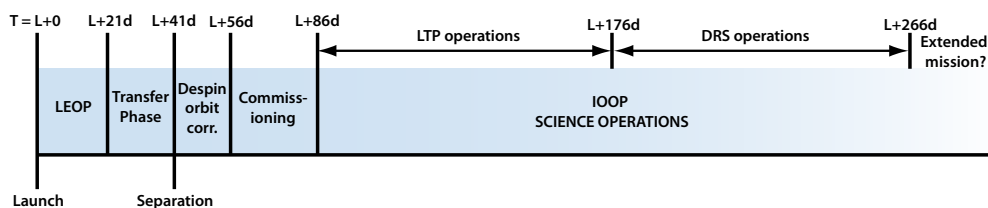
Figure 1.23: An overview of the mission timeline, beginning at launch. Diagram courtesy of ESA.

1.5.1 Launch and orbit

The LISA Pathfinder satellite is due for launch using the European VEGA launcher in mid-2015. The launch will put the satellite and

propulsion module, as shown in Figure 1.24, into a parking orbit with perigee at 200 km, apogee at 1620 km, and an inclination to the equator of 5.3° [28]. After a series of apogee raising manouevres lasting 21 days, the satellite begins the 20 day transfer phase, which takes it to the L1 Earth-Sun Lagrange point. The spin phase, which lasts about 15 days, brings the satellite and propulsion module up to a maximum spin rate of 5° per second. The propulsion module then separates, and the satellite is de-spun using the microNewton thrusters. The final orbit will be a Lissajous orbit around L1. This orbit was selected because it is a thermally stable environment with few eclipses, minimal gravitational and magnetic disturbances, and a distance from Earth between 1.2 and 1.8 million km such that there is no need for very sophisticated telecommunications systems. A diagram showing the different phases is shown in Figure 1.25.

Figure 1.24: A photograph of the satellite and propulsion module. Photo courtesy of ASD.

1.5.2 Operational phase

Once in the L1 orbit, and when a stable zero gravity environment is achieved, the operational phase of the mission begins. Initially 30 days of commissioning activities are performed to check the health of the satellite. Following this, the main scientific operations begin. There are two 90 day segments of experiments planned, one each for the LTP and the DRS respectively.
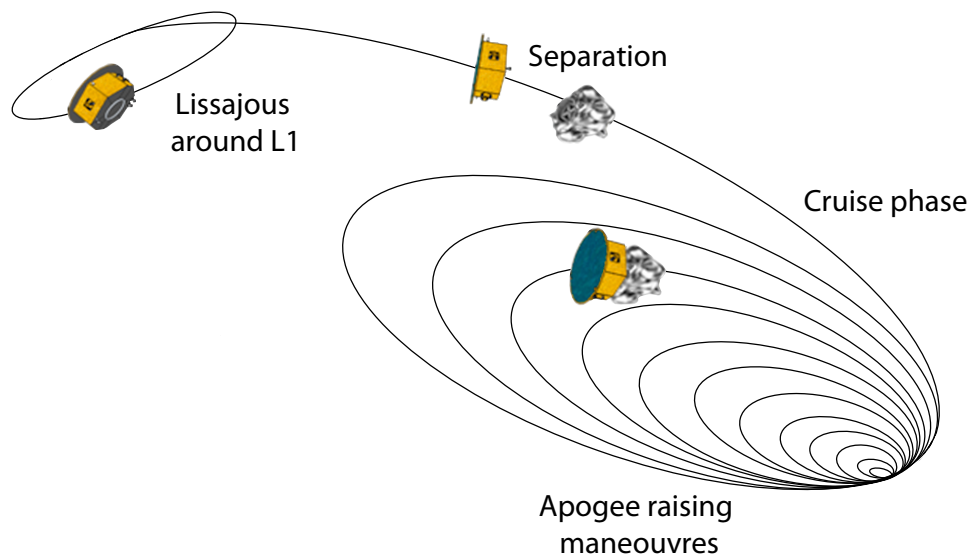
Figure 1.25: A diagram showing the orbital phases of the LISA Pathfinder satellite taken to reach its final Lissajous orbit around the L1 Lagrangian point. Image courtesy of ESA.

The LTP operational timeline is split into defined experiments, which are built from a series of specific and self-contained sequences of instrument operations called 'Runs'. The experiments are organised into 24 hour sets, according to the Experimental Master Plan (EMP). The satellite stores between three and six days of experiments, which are automatically executed. Changes to the mission timeline can be implemented, but only under certain conditions, and with some delay.

1.5.3 Ground segment

A diagram of the data handling setup for the ground segment of the LPF mission is shown in Figure 1.26. The Earth-satellite communications are facilitated by the Cebreros Ground Station for around eight hours per day [28].

Data downlink and uplink

The received telemetry is either live data, in that it is transmitted directly to Earth during a pass, or replay data, which has been stored in
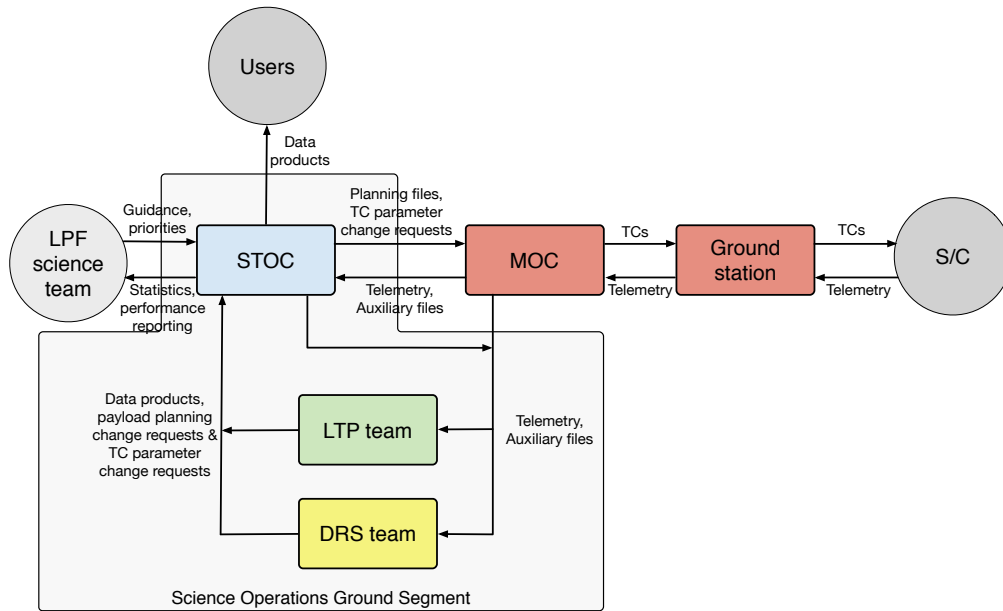
Figure 1.26: A block diagram showing the ground segment for the science operations [28].

the satellite Solid-state Mass Memory (SSMM) until it is commanded to downlink during a Ground Station pass. The telemetry is relayed to the Mission Operations Centre (MOC) from the ground station, where it is stored in the Data Disposition System (DDS). The telemetry and auxiliary files are then retrieved in the form of raw data. They are de-packetised to produce time-series data, and converted from raw data into engineering data using the conversion information stored in the operational database, the data in this form is saved in a dedicated repository. The data can be retrieved by the Science Technology Operations Centre (STOC) for data analysis purposes.

The design for upcoming experiments, and any telecommand parameter change requests are produced by the LTP and DRS teams. These are sent via the STOC to the MOC where they are converted into telecommands. These are transmitted to the satellite via the ground station.

Data analysis

The data analysis is performed by teams of scientists at the STOC, in conjunction with other team members at complementary data centres,

including one at the AstroParticule et Cosmologie, Université Paris Diderot (APC), Paris. The data analysis tasks can be split into two categories:

- Quick look: The Instrument Configuration Evaluation (ICE) data is received at the beginning of the ground station pass, and consists of a reduced number of telemetry parameters, sampled with 1 Hz. These parameters are used to identify potential issues with the satellite, or an experimental run. This can result in a warning being issued to be investigated with the full data, or a request being issued to the MOC to either change a Telecommand (TC) parameter, or immediately command that the LTP be put into standby mode.

- Full data analysis: The full data set is analysed in real-time by the STOC and complementary data centre teams according to the established data analysis pipelines for each experiment.

The data analysis is performed using a custom-designed MATLAB® toolbox, the LISA Technology Package Data Analysis (LTPDA) toolbox.

1.6 Hardware test campaigns

The development of the OMS hardware involved several levels of system manufacture and testing. Following laboratory implementation of the system design, engineering models of the OMS subsystems were produced. They are almost identical in functionality to the flight models, and were successfully tested during the Engineering Model (EM) test campaign. Subsequently the flight models were constructed, and successfully tested during the FM test campaign. The OMS subsystems were then integrated into the main satellite body along with all completed flight hardware for thermal cycling tests in the On-Station Thermal Tests (OSTT) test campaign.

These ground-based tests of the flight hardware provided the only opportunity for pre-launch characterisation of the OMS. The results presented in this thesis focus on the characterisation of three sources of noise that affect the OMS: frequency, OPD, and amplitude noise.

The investigations implemented in these test campaigns provide the basis for the definition of the OMS characterisation investigations that will be performed in-flight.

1.6.1 Engineering model

The EM OMS test campaign took place at the Albert Einstein Institute (AEI) between October 2010 and January 2011, and was performed by Astrium Deutschland (ASD) in collaboration with scientists at the AEI. The campaign successfully verified the end-to-end OMS measurement principle, using the EM hardware [29]. Notable differences to the in-flight LTP configuration are:

- Test masses: the test masses were simulated by either static mirrors, or PZT mounted mirrors.

- Optical windows: no optical windows were used.

- Readout: the OBC was replaced by On-ground Support Equipment (OGSE) which outputs the signals, equivalent to the in-flight telemetry plus some extra data, for analysis.

References: [30], [31], [32], [33], [34], [35] [36].

1.6.2 Flight model

The OMS Pre-Flight Model (PFM) Phase 1, often called the FM, test campaign took place at the AEI between July and mid-September of 2010. It was performed by ASD, with support from the AEI. The campaign successfully demonstrated the end-to-end functionality of the OMS. All completed FM components were used, including the RLU, LMU, LCU, phasemeter, and DMU. There were several differences to what will be the in-flight configuration:

- Optical bench: the EM of the optical bench was used. This bench has the same functionality as the FM bench, but with a slightly different layout.

- Test masses: the test masses were simulated either by fixed mirrors, or by mirrors mounted on PZTs.

- Optical windows: optical windows were not used.

- Readout electronics: instead of the OBC, all of the systems were readout via dedicated OGSE.

- OPD actuator: only one actuator was used.

Note: An additional test campaign, the Laser Assembly Pre-Flight Model (LA PFM) campaign was performed by Kaiser Threde (KT) in mid-2010. This campaign successfully tested only the flight models of the LA subsystems, the same models which were later tested in the FM test campaign.

References: [37], [38], [39], [40], [41], [42], [43] [36].

1.6.3 On-station thermal tests

The OSTT test campaign took place in 2011 at the Industrieanlagen-Betriebsgesellschaft mbH (iABG) facilities. The campaign was led by Astrium (ASD and Astrium UK (ASU)) with cooperation from members of the LPF collaboration. The tests demonstrated system performance, in a thermally representative environment, with all available flight hardware integrated into the main satellite body. In terms of the LTP, there were some differences compared to the final flight hardware:

- Optical bench: the flight optical bench was substituted by the flight spare.

- Photodiodes: the flight spare bench was populated with a combination of InGaS and Si photodiodes.

- Test masses: the flight test masses were substituted by PZT mounted mirrors.

- OPD actuator: only one OPD actuator was used.

1 Introduction

During the test campaign the satellite was inside a large thermal cycling vacuum chamber. Tests were performed under both hot ($30.5°$ C $\pm\,0.5°$C) and cold ($9.5°$ C $\pm\,0.5°$C) conditions.

References: [44], [45], [46], [47].

2 Noise sources

Contents

2.1 Introduction

As presented in Section 1.3, the main mission requirement for the residual differential TM acceleration, $\widetilde{\delta a}(f)$, is:

$$\delta\widetilde{a}(f) \leq 3 \times 10^{-14} \left(1 + \left(\frac{f}{3\,\mathrm{mHz}}\right)^2\right) \frac{\mathrm{m}}{\mathrm{s}^2} \frac{1}{\sqrt{\mathrm{Hz}}} \qquad (2.1)$$

within a measurement bandwidth of $1\,\mathrm{mHz} \leq f \leq 30\,\mathrm{mHz}$ [48]. When discussing the interferometric measurements and the OMS, it can be more intuitive to consider a TM displacement requirement, $\widetilde{\delta x}(f)$:

$$\delta\widetilde{x}(f) \leq 9 \times 10^{-12} \left(1 + \left(\frac{3\,\mathrm{mHz}}{f}\right)^2\right) \frac{\mathrm{m}}{\sqrt{\mathrm{Hz}}} \qquad (2.2)$$

This gives a requirement for the differential test mass displacement, x_{12}, along the sensitive axis of $9\,\mathrm{pm}/\sqrt{\mathrm{Hz}}$, in the measurement bandwidth between 3 and $30\,\mathrm{mHz}$, falling off by $1/f^2$ down to $1\,\mathrm{mHz}$ [18]. The differential test mass displacement is measured by the X12 interferometer, as discussed in Section 1.4.2.

Meeting this requirement is dependent upon the degree to which the test masses are isolated from external forces. This in turn depends upon the residual noise levels of the thrusters and the capacitive actuators, as well as the noise level of the interferometric readout signals that provide the feedback signals to the DFACS. Additionally, a low interferometric readout noise is necessary to enable the small acceleration noise to be observed. It is the noise contribution of the OMS that will be discussed in this thesis.

The conceptual representation of the LPF satellite, originally shown in Figure 1.3, can be reconsidered to show the added noise from the readout of the x_{12} and x_1 interferometers, as shown in Figure 2.1. The interferometric readout noise in the x_1 measurement, $\mathrm{X1_{RO}}$, is processed via transfer function $\mathrm{T_1}$ and adds noise to the thruster feedback. Similarly, noise in the readout of the differential displacement, $\mathrm{X12_{RO}}$, will influence the control of test mass two via the capacitive actuators through the transfer function $\mathrm{T_2}$. There will also be some small contribution due to imperfect common mode rejection, where

the test masses are both displaced by the same amount in the same direction but there is still a measured residual test mass displacement. Additionally, a spring coupling between the test masses and the satellite couples some small component of the X1 measurement into the X12 measurement.
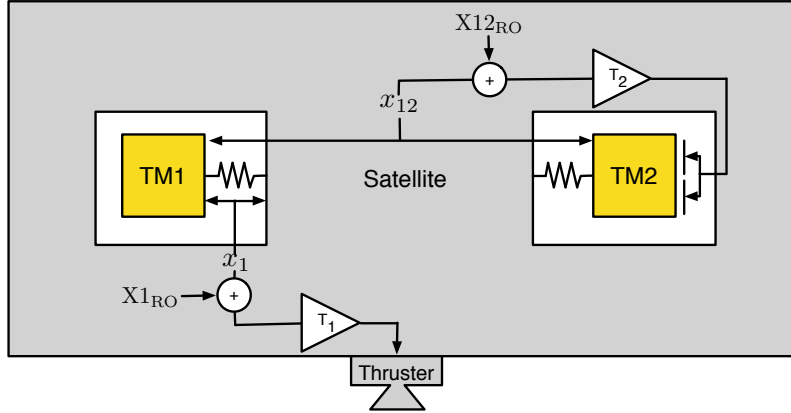

Figure 2.1: A conceptual picture of the LPF satellite showing the X1 interferometer output being fed back to the thrusters via the T_1 transfer function, with some noise, $X1_{RO}$. The X12 interferometer output, x_{12}, is fed back to the capacitive actuators around test mass two via a control loop with transfer function T_2 with some noise, $X12_{RO}$. The spring coupling between each test mass and the satellite is also shown.

An overview of the noise sources that comprise the science requirement defined by Equation 2.2, and their maximum allocated contribution to the requirement, are shown in Figure 2.2 [49].

The allocated contribution from the OMS measurements to the overall allowed noise level in the measurement bandwidth of $1\,\mathrm{mHz} \leq f \leq 30\,\mathrm{mHz}$ is [50]:

$$\delta\widetilde{x}_{12}(f) \leq 6.3 \times 10^{-12} \sqrt{\left(1 + \left(\frac{f}{3\,\mathrm{mHz}}\right)^{-4}\right) \frac{\mathrm{m}}{\sqrt{\mathrm{Hz}}}} \qquad (2.3)$$

The noise from the OMS is therefore a significant contribution in the overall mission noise budget given by Equation 2.2.

This allocation is the sum in quadrature of the allocations from a number of specific noise sources (as well as some margin):
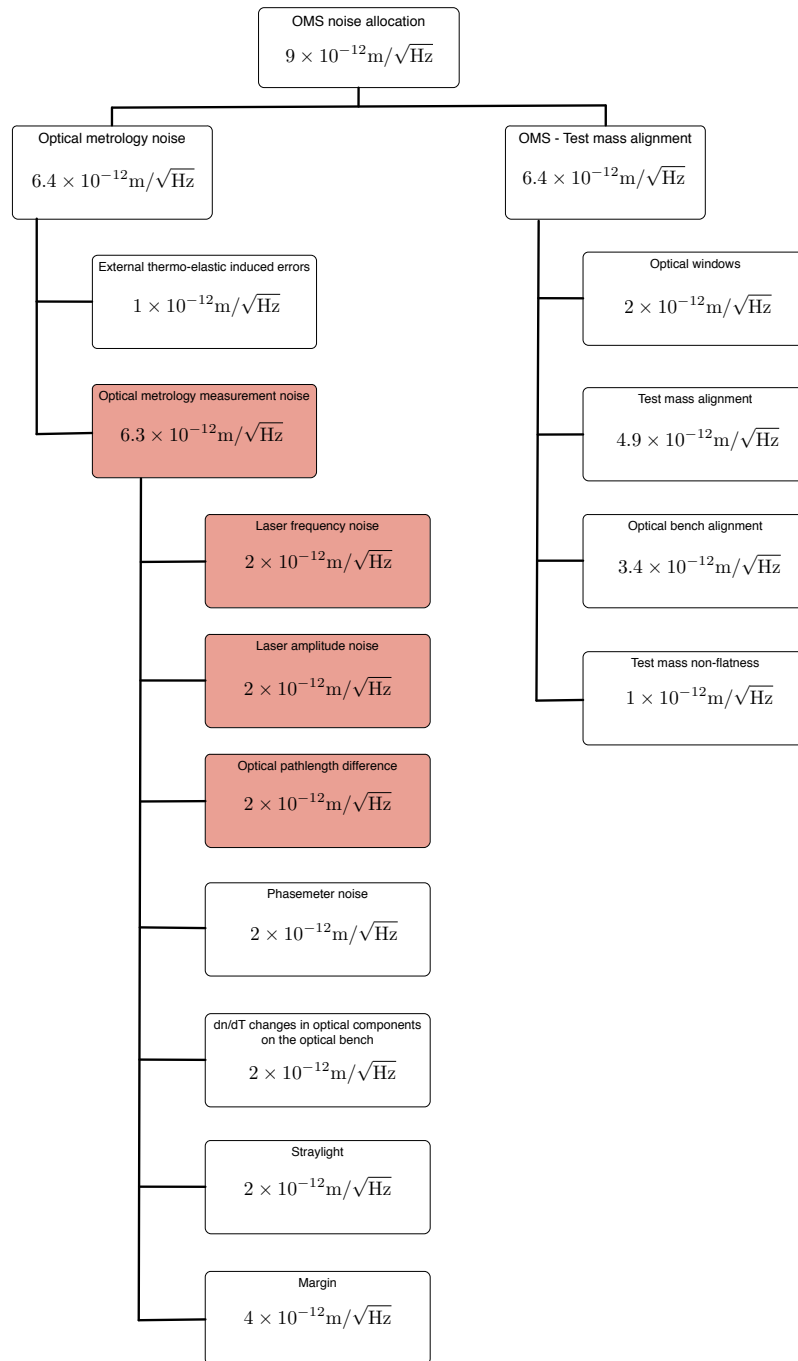
65

2 Noise sources

Figure 2.2: An overview of some of the noise sources that contribute to the overall science requirement for the differential test mass displacement. The allocated values for each noise source are at 30 mHz, and according to the definitions in [49]. The noise contributions highlighted in red are those discussed in this document.

- OMS noise sources requiring active stabilisation:

  - Laser frequency noise;

  - Optical pathlength difference noise;

  - Amplitude noise[1].

- Other OMS noise sources:

  - Phasemeter noise;

  - Thermo-optical noise;

  - Noise due to stray light.

There are other noise sources that affect the OMS readout which are not included in the allocation in Equation 2.3:

- Noise due to the optical windows;

- Residual force noise;

- Beam jitter noise;

- Doppler measurement error.

Understanding the contribution of the noise sources, and their suppression by the associated control loops, is crucial in order to understand the measurement of the residual force noise.

In this thesis, the contribution of the various noise sources to the OMS noise budget are investigated, with focus on those that can be measured in-flight. Where possible the OMS noise is broken down into its component noises, as defined above, and reasonable assumed allocations are defined. In Section 2.4 these values are used to produce a theoretical plot of the contributions of the main noise sources to the overall OMS noise. Subsequently, the investigations necessary for

---

[1]The OMS noise allocation given in Equation 2.3 only includes the contribution from amplitude noise at the heterodyne frequency. However, additional amplitude noise as a result of radiation pressure on the test mass is suppressed by the same control loop. The allocation for each source is presented in detail in Section 2.2.3.

the in-flight characterisation of the noise sources have been defined in Chapters 3, 4, and 5. The noise contributions from the EM, FM, and OSTT hardware test campaigns are also presented. These measurements provide the best estimates for the expected OMS noise contribution to the x_{12} differential displacement measurements in-flight.

2.2 Noise sources and couplings

2.2.1 Frequency noise

Frequency noise originates, as its name suggests, from fluctuations in the frequency of the laser. Such fluctuations can arise at low frequencies due to variations of the laser temperature, and across all frequencies as a result of fluctuations in the intensity of the optical pumping light [51].

When there is a pathlength difference, ΔL, between the arms of a laser interferometer, the frequency noise of the laser, $\delta\nu$, couples into the phase measurement as an equivalent phase fluctuation, $\delta\varphi$, according to [52]:

$$\delta\varphi = \frac{2\pi\Delta L}{c}\delta\nu.$$
(2.4)

In terms of a test mass displacement, δx, this is written as:

$$\delta x = \frac{\lambda\Delta L}{2c\cos\alpha}\delta\nu$$
(2.5)

where α is the angle of incidence of the light on the test mass.

In LTP, static pathlength differences originate from [53]:

- tolerances in the construction of the optical bench;

- tolerances in the connection of the optical bench to the inertial sensor housing;

- mechanical tolerances within the inertial sensor housing;

- the unknown absolute position of the test masses under some operating conditions;

- the imperfect cancellation of fibre pathlength differences by subtraction of the reference interferometer signal.

Accordingly, these pathlength differences will result in frequency noise coupling directly into the observed displacement fluctuations of the test masses, as measured by the X12 and X1 interferometers.

As with most of the OMS noise sources shown in Figure 2.2, the maximum allowable contribution to the differential test mass displacement measurement due to frequency noise, $\delta\widetilde{x}_{12}^{\mathrm{frequency}}$, is [50]:

$$\delta\widetilde{x}_{12}^{\mathrm{frequency}} \leq 2 \times 10^{-12} \sqrt{\left(1 + \left(\frac{f}{3\,\mathrm{mHz}}\right)^{-4}\right)} \frac{\mathrm{m}}{\sqrt{\mathrm{Hz}}} \qquad (2.6)$$

in the measurement bandwidth, $1\,\mathrm{mHz} \leq f \leq 30\,\mathrm{mHz}$. Taking the difference between the interferometric pathlengths in the X12 interferometer to be $\leq 0.01\,\mathrm{m}$, the equivalent allocation for the frequency fluctuations of the laser can be determined [50]:

$$\delta\widetilde{\nu}_{12}^{\mathrm{frequency}} \leq 112 \times 10^{3} \sqrt{\left(1 + \left(\frac{f}{3\,\mathrm{mHz}}\right)^{-4}\right)} \frac{\mathrm{Hz}}{\sqrt{\mathrm{Hz}}} \qquad (2.7)$$

in the measurement bandwidth, $1\,\mathrm{mHz} \leq f \leq 30\,\mathrm{mHz}$. The conversion of the allocation into different units is described in Box 2.1.

In actuality, the mismatch between the interferometer arms on the optical bench is significantly smaller, $< 1 \times 10^{-3}\,\mathrm{m}$ [22], so in-flight this noise source is expected to be below requirements, although it depends upon the final construction and integration of the optical subsystems.

The frequency noise can be measured using the frequency interferometer, as discussed in Section 1.4.2. The frequency interferometer is a fixed armlength interferometer (in that it contains no moving components), with a deliberate mismatch of $\sim 38\,\mathrm{cm}$ between the paths travelled by the measurement beam and the reference beam. With this intentionally large pathlength difference, the effect of the frequency

Chapter 2

noise is amplified. The contribution of the frequency fluctuations is derived using the processed output of the frequency interferometer, Ψ_F, along with Equation 2.4.

The free-running frequency noise of the laser is higher than the allocation, and must therefore be suppressed [52] [53]. This is achieved by using the processed phase measurement from the frequency interferometer[1], Ψ_F, as the input to a feedback control loop, the so-called frequency control loop which is described in Section 2.3.1.

---

[1]The processed phase of the frequency interferometer, Ψ_F, is calculated by subtracting the output of the reference interferometer, φ_R, from the output of the frequency interferometer, φ_F. This removes any common-mode pathlength noise, such that only the pathlength mismatch on the optical bench, the intentional $38\,\mathrm{cm}$, contributes to Ψ_F.

Chapter 2

Conversion of the frequency noise requirement

This box describes how the requirement for the frequency noise contribution to the differential test mass displacement, $\delta\widetilde{x}_{12}^{\text{frequency}}$, can be converted into an equivalent allocation for the frequency noise fluctuations of the laser in units of $\text{Hz}/\sqrt{\text{Hz}}$. This can then be converted into a requirement for the output of the frequency interferometer, in units of $\text{rad}/\sqrt{\text{Hz}}$.
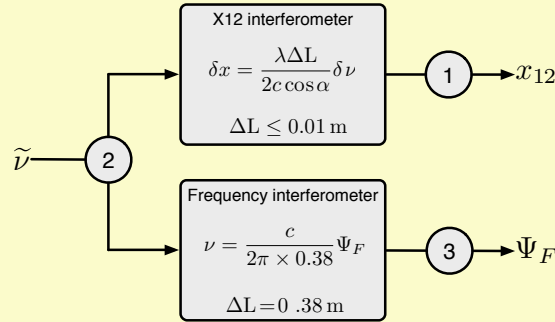
1. The maximum allowable contribution of frequency noise into differential test mass displacement, $\delta\widetilde{x}_{12}^{\text{frequency}}$, is:

$$\delta\widetilde{x}_{12}^{\text{frequency}} \leq 2 \times 10^{-12} \sqrt{\left(1 + \left(\frac{f}{3\,\text{mHz}}\right)^{-4}\right)} \frac{\text{m}}{\sqrt{\text{Hz}}} \qquad (2.8)$$

2. With a maximum armlength mismatch of $0.01\,\text{cm}$ and using Equation 2.5, the allocation for the frequency noise is:

$$\delta\widetilde{\nu} \leq 112 \times 10^3 \sqrt{\left(1 + \left(\frac{f}{3\,\text{mHz}}\right)^{-4}\right)} \frac{\text{Hz}}{\sqrt{\text{Hz}}} \qquad (2.9)$$

3. Knowing that the pathlength mismatch of the frequency interferometer is $38\,\text{cm}$ and using Equation 2.4, the allocation for the frequency interferometer output can be calculated:

$$\delta\widetilde{\Psi}_F \leq 8.91 \times 10^{-4} \sqrt{\left(1 + \left(\frac{f}{3\,\text{mHz}}\right)^{-4}\right)} \frac{\text{rad}}{\sqrt{\text{Hz}}} \qquad (2.10)$$

Box 2.1: Converting the requirement for the contribution of frequency noise to the differential test mass displacement measurement between different units.

2.2.2 Optical pathlength difference noise

OPD noise describes fluctuations in the relative pathlengths of the measurement and reference beams caused by environmental disturbances. They originate before the beams are delivered to the stable optical bench, i.e., from the modulation bench, and the optical fibres that connect it to the optical bench. It has already been shown that the phase output of an interferometer is dependent upon the relative pathlength difference, s, between the interfering measurement and reference beams (see Equation 1.41). Therefore, a phase change due to environmental noise that changes s is indistinguishable from a phase change as a result of residual test mass motion.

In the reference interferometer, as introduced in Section 1.4.2 and shown in Figure 1.14, both the measurement and reference beams are confined to the optical bench, without being incident on either of the test masses, or any moving components. In this way, the phase output, φ_R (interchangeably referred to as Ψ_R), is a measure of the pathlength differences that cause the OPD noise.

This noise is common-mode in all of the interferometers, and can therefore be removed by subtracting the output from the reference interferometer, φ_R, from the raw phase outputs of the other interferometers, φ_1, φ_{12}, and φ_F. The associated calculations in the DMU processing chain are given in Equations 1.35, 1.36 and 1.37 in Section 1.4.4.

However, it was demonstrated that this does not completely cancel all of the measured noise [53]. The remaining noise is the result of imperfect optical pathlength difference subtraction due to electromagnetic cross-talk between the RF signals that drive the two AOMs in the paths of the measurement and reference beams [53] [54] [24].

The crosstalk produces electrical sidebands with small but non-vanishing amplitudes, which couple into optical sidebands on each of the two output beams in the LMU. When the measurement and reference beams interfere, these sidebands will appear in the resulting beat signal, and are therefore detected by the photodiodes. Where the sidebands occur at integer multiples of the heterodyne frequency, e.g., at $\pm f_{het}$ and $\pm 2f_{het}$..., they will also be processed by the SBDFT. In this way, the output phase and amplitude have some components which

are a result of this sideband noise. This is discussed in detail in [53] and [55].

The output signal from the reference interferometer provides the input to the OPD control loop[1], as described in Section 2.3.2. The feedback signal from this loop provides an input to the two[2] OPD actuators which change the pathlength of each beam in the LMU. This will remove any remaining pathlength noise, and will maintain the sideband phase error contribution at a constant DC level, although it cannot be completely removed due to its non-linearity.

Overall the allocation to the OMS budget for the relative longitudinal displacement fluctuations due to OPD noise, $\delta\widetilde{x}_{12}^{\mathrm{OPD}}$, coming from both pathlength fluctuations and sideband contributions in the measurement bandwidth of $1\,\mathrm{mHz} \leq f \leq 30\,\mathrm{mHz}$ is [49]:

$$\delta\widetilde{x}_{12}^{\mathrm{OPD}} \leq 2 \times 10^{-12} \sqrt{\left(1 + \left(\frac{f}{3\,\mathrm{mHz}}\right)^{-4}\right)} \frac{\mathrm{m}}{\sqrt{\mathrm{Hz}}} \qquad (2.11)$$

As the coupling of the noise into the differential test mass displacement is non-linear, this allocation does not directly convert into a requirement on the output from the reference interferometer. Considering the case where the residual pathlength fluctuations and the sideband noise is maximum, the allocation, defined in [49], for the output of the reference interferometer, in the measurement bandwidth of $1\,\mathrm{mHz} \leq f \leq 30\,\mathrm{mHz}$, is:

$$\delta\widetilde{\Psi}_R \leq 1.6 \times 10^{-3} \sqrt{\left(1 + \left(\frac{f}{3\,\mathrm{mHz}}\right)^{-4}\right)} \frac{\mathrm{rad}}{\sqrt{\mathrm{Hz}}} \qquad (2.12)$$

An LTPDA method for analytically determining the contribution of sideband noise from a measured interferometer output is given in [55].

---

[1]If there were no remaining pathlength noise and no sideband noise then the raw phase output from the reference interferometer would be zero.

[2]The two actuators act in a push-pull configuration, so that they each nominally operate using only half of their maximum range. This provides redundancy in the case of a failure.

2.2.3 Amplitude noise

Amplitude noise (often called power noise) describes noise that arises due to power fluctuations in the beams within the interferometers. In LTP this couples into the phase measurement in two ways: at low frequencies in the form of radiation pressure noise which produces test mass displacement, and at the heterodyne frequency as a phase noise.

Note: The radiation pressure noise is not included in the OMS measurement allocation, but rather forms part of the residual force noise requirements given in [49]. It is described here, as it is suppressed by part of the same control loop that suppresses the amplitude noise at the heterodyne frequency.

Noise at the heterodyne frequency

The residual test mass displacements, x_{12} and x_1, are derived from the phase of the interfering measurement and reference beams in the X12 and X1 interferometers at the heterodyne frequency, f_{het}. Therefore, any power noise of the two beams at frequencies around f_{het} will couple directly into the phase measurements. These power fluctuations appear as amplitude modulations on the measurement and reference beams. The contribution to the resulting phase output from the DMU depends on the relative phases of the measurement and reference beams in the interferometer, and the phase of the amplitude modulation. In [53] and [49] a situation is considered where the amplitude noise contribution to the interfered beam at a photodiode is maximum. This signal is processed as it would be in the phasemeter and DMU. The resulting error on the measured phase, φ_i, is given by:

$$\delta\varphi_i = \frac{\delta P}{P} \tag{2.13}$$

where $\delta P/P$ is the ratio of the power fluctuations to the DC power, the Relative Intensity Noise (RIN).

As for all OMS noise sources, the allocation for the differential displacement noise due to the contribution of amplitude noise at the heterodyne frequency, in the measurement bandwidth, $\delta\widetilde{x}_{12}^{f_{\text{het}}\text{RIN}}$, is

[49]:

$$\delta \widetilde{x}_{12}^{f_{\text{het}}\text{RIN}} \leq 2 \times 10^{-12} \sqrt{\left(1 + \left(\frac{f}{3\,\text{mHz}}\right)^{-4}\right)} \frac{\text{m}}{\sqrt{\text{Hz}}} \qquad (2.14)$$

Using Equation 1.43, the equivalent allocation for the RIN of the laser at frequencies around f_{het} can be determined:

$$\frac{\delta \widetilde{P}}{\widetilde{P}} \leq 2.35 \times 10^{-5} \frac{1}{\sqrt{\text{Hz}}} \qquad (2.15)$$

The intensity, and therefore the amplitude fluctuations, of each beam are independently measured using single element photodiodes, PDA1 and PDA2, for the measurement and reference beams respectively. They measure some 8 % of each beam after its delivery onto the optical bench, as shown in Figure 1.11.

In order to meet the requirement for this noise source, the laser amplitude must be stabilised at frequencies around f_{het}. This is achieved with the fast amplitude control loop, as described in Section 2.3.3, which uses the outputs of the single-element photodiodes as its inputs.

Radiation pressure noise

Radiation pressure noise, produced by low frequency RIN, is caused by slow fluctuations in the power of the measurement beam, the beam that is incident on the two test masses. These power fluctuations exert a fluctuating force noise on the test masses, which results in unwanted residual acceleration due to a TM displacement.

A beam of power, P, incident on a surface with a coefficient of reflectivity, ρ, would produce a force, F, due to momentum transfer of the incident photons according to:

$$F = \frac{P}{c}(1 + \rho). \qquad (2.16)$$

This introduces an equivalent TM displacement, $x(f)$, which is dependent upon the Fourier frequency of the power fluctuations, f. For a free mass, this is:

$$x(f) = \frac{P}{mc\omega^2}(1 + \rho) \tag{2.17}$$

where m is the mass of the TM [56]. More accurately, the case should be considered where there is spring coupling between the test mass and the satellite, ω^2_{stiff}:

$$x(f) = \frac{P}{mc(\omega^2 - \omega^2_{\text{stiff}})}(1 + \rho) \tag{2.18}$$

This occurs at frequencies below $1\,\text{mHz}$ [56].

The acceleration noise allocation due to the radiation pressure noise, $\delta a_{12}^{\text{low freq. RIN}}$, is [49]:

$$\widetilde{\delta a}_{12}^{\text{low freq. RIN}} \leq 0.6 \times 10^{-15}\text{ms}^{-2}/\sqrt{\text{Hz}}, \text{ at } 30\,\text{mHz} \tag{2.19}$$

The allocation for the RIN, assuming a power of $4 \times 10^{-3}\,\text{W}$ at test mass one and $m = 1.96\,\text{kg}$, is [49]:

$$\frac{\delta\widetilde{P}}{\widetilde{P}} \leq 1 \times 10^4 \left(1 + \left(\frac{f}{3\,\text{mHz}}\right)^2\right) \tag{2.20}$$

In the laboratory and during test campaigns, this noise source is not present as fixed test masses are used. In-flight the effect of this noise is suppressed by the slow amplitude control loop, as described in Section 2.3.3.

2.2.4 Other OMS noise sources

The following noise sources contribute to the differential displacement measurement. They are each allocated a maximum contribution to the differential displacement of [49]:

$$\delta\widetilde{x}_{12} \leq 2 \times 10^{-12} \sqrt{\left(1 + \left(\frac{f}{3\,\text{mHz}}\right)^{-4}\right)} \frac{\text{m}}{\sqrt{\text{Hz}}} \qquad (2.21)$$

These noise sources will not be investigated in detail in this thesis, but explanations can be found in [49] and [53].

Optical bench thermal noise

Thermal fluctuations of the optical bench and its components can affect the pathlength travelled by the beams. Where this causes a change in the relative pathlength between the measurement and reference beams in an interferometer, there will be an impact on the measured phase of that interferometer. In the case of the X12 interferometer, this will add noise to the readout of the differential test mass displacement. There are three ways in which thermal fluctuations can change the optical pathlength:

- Distortion of the optical components by displacement or rotation;

- Length change of the transmissive optical components;

- Refractive index change of the transmissive optical components.

Stray light

Stray light is caused by the scattering of light from the measurement, reference, or interfered beams by components on or off the optical bench. As the scattered beams potentially have the same frequency as the original measurement and reference beams they can interfere to produce a signal at the heterodyne frequency, f_{het}. This will occur if they are detected on a photodiode and there is a non-vanishing overlap integral with another mode there. This will contribute a spurious phase component to the measured interferometric signal, only in the case where there is a fluctuating amplitude or phase. In the case of

the X12 interferometer, this will add noise to the measured differential displacement.

Phasemeter

The phasemeter processes the outputs from the photodiodes of each interferometer to produce the DC value and the complex amplitude which will later be converted to phase and then pathlength. Accordingly, any noise during this processing will add noise to the output signals. These noise contributions occur due to:

- Conversion of the optical signal to a photocurrent by the photodiode;

- Conversion from photocurrent to voltage in the trans-impedance amplifier;

- Temperature instability in the low-pass filter;

- Digitisation of the signal by the ADC.

These effects are inherent to the processing and cannot be measured during an in-flight investigation.

The phase measurement from each interferometer, φ_i, is determined as a result of a SBDFT at the heterodyne frequency, f_{het}. In order for this calculation to be accurately performed, the f_{het} frequency must be centered in the bin of the SBDFT. This is achieved by selecting f_{het} and the SBDFT parameters. However, fast phase shifts, for example, when there is a fast OPD or test mass position fluctuation, produce an apparent fluctuation in the heterodyne frequency. This is called Doppler noise because the effect is similar to that of the Doppler effect, although it is not caused by the same principle. An LTPDA method to estimate the magnitude of this noise source is described in [55].

2.3 In-flight control loop implementation

In-flight, the frequency and OPD control loops are implemented digitally with an update rate of $100\,\mathrm{Hz}$ within the DMU. The amplitude control loop is implemented with an update rate of $1\,\mathrm{Hz}$. The fast amplitude loop has an analogue implementation in the LCU, and the slow amplitude loop is digital in the DMU. The basic closed-loop control law for each digital loop is generically described by the following:

$$
\begin{aligned}
y_i \;=\;\; & a_0(\Delta x + \delta x_i - x_i) + a_1(\Delta x + \delta x_{i-1} - x_{i-1}) + ... \\
& + a_{n-1}(\Delta x + \delta x_{i-(n-1)} - x_{i-(n-1)}) \\
& + b_1 y_{i-1} + b_2 y_{i-2} + ... + b_n y_{i-n}
\end{aligned}
\tag{2.22}
$$

This describes an Infinite Impulse Response (IIR) filter where the output, y_i, at some time $i\Delta t$ ($\Delta t = 1/f$, where f is the sampling frequency), is the scaled sum of the current and previous inputs ($x_i, x_{i-1}, ..$) and the previous outputs ($y_{i-1}, y_{i-2}, ...$). A constant offset, Δx, can be commanded in addition to a time-dependent offset, δx_i, that can be used as part of a probing function for test inputs. The difference between the current value, x_i, and the offsets, Δx and δx_i, gives an error signal. This is scaled by some coefficients, a_{k-1} and b_k ($1 < k \leq n$), which, along with the sampling time, Δt, define the controller response.

The output, y_i, is a floating point number which is converted to an integer via Equation 2.23 in order to produce an analogue feedback signal. The coefficients, α and β, define the controller output range. This value is clipped between some defined values, y_{min} and y_{max}, in order to prevent it exceeding the actuator limits, and to reduce the duration of transients after large errors. The integer signal is then converted to an analogue signal via a Digital to Analogue Convertor (DAC), which can then be used as input to an actuator:

$$
i_i = \mathrm{round}(\alpha + \beta y_i)
\tag{2.23}
$$

The coefficients, a_{k-1}, b_k, α and β, along with the clipping limits, y_{min} and y_{max}, completely define the controller. Default values of the offsets and coefficients are calculated prior to flight and stored in the DMU SDP, although alternatives can be uploaded in-flight via telecommand [23].

Each loop has several possible states:

- **Inactive**: The loop is open.

- **Fixed output y**: A fixed control output signal y_i is generated from the loop specific parameters defined in the SDP, which is nominally zero. The feedback to the actuator is a constant integer.

- **Variable output y**: A time-dependent probing function is added to the 'fixed output y' signal. This probing function is defined by:

  - Shape: ramp, sine, or triangle.

  - Frequency: 0.001 to 50 Hz, with a resolution of at least 0.0001 Hz.

  - Duration: an integer number of half periods.

  - Amplitude: positive or negative to define the initial slope, with units dependent on the control loop.

  Once the probing function cycles are complete the state returns to 'fixed output y'.

- **Nominal**: Loop is closed, with the optional offset Δx as defined by the telecommand, or the last defined value in the SDP. The value of Δx is initially defined as zero in the SDP.

- **Frozen**: The closed-loop state is suspended, and the last value of y_i is used as the loop feedback signal.

- **Testing offset** Δx: The loop is closed with the parameters defined in the SDP, with a constant offset Δx. In addition, a probing function can also be applied (see the definition in 'variable output y').

- **Frozen for invalid data 1**: When the control loop is in the 'nominal' state and the data quality is noisy or invalid the loop reverts to a frozen state.

- **Frozen for invalid data 2**: When the control loop is in the

'testing offset Δx' state and the data quality is noisy or invalid the loop reverts to a frozen state.

In flight the loop states are defined by a number, as shown in Table 2.1. Achieving a particular loop state requires transition between the states in a defined sequence, as defined in [23].

Loop state	Numerical identifier
Inactive	0
Fixed output y	1
Variable output y	2
Nominal	3
Testing offset Δx	4
Frozen	5
Frozen for invalid data 1	6
Frozen for invalid data 2	7

Table 2.1: A table showing the numerical identifiers associated with each control loop state [23]. These are the values for the states given in the telemetry transmitted from the satellite.

An overview of some key control loop theory is given in Box 2.2, and the specific implementation of the frequency, OPD, and amplitude control loops are described in the following sections.

Control loop theory

A basic block diagram of a control loop, representative of an LTP control loop, is shown below. The loops signals, available via the telemetry, are shown. Ψ_i is the measurement of the noise, ϵ is the loop error signal, and y is the feedback signal. An input to the loop, e.g., a modulation signal, is represented by δx. The response of each loop component is defined by the Laplace transform.
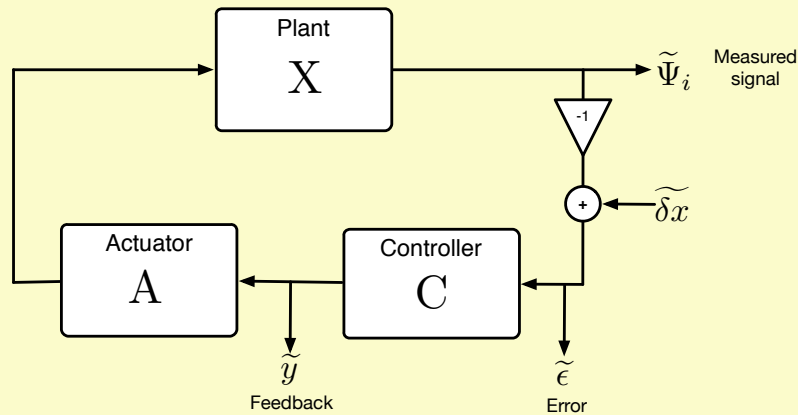
The Open-Loop Transfer Function (OLTF) defines a steady-state response of the loop to a signal that travels once around the loop, and is given by:

$$\text{OLTF}(f) = \frac{\widetilde{\Psi}_i}{\widetilde{\epsilon}} \tag{2.24}$$

$$= -\text{C}(f) \times \text{A}(f) \times \text{X}(f) \tag{2.25}$$

where the tilde represents the Fourier Transform (FT) of the signal. The OLTF allows key characteristics of the loop to be determined:

- **Gain:** The amplitude of the OLTF, more generally referred to as the Open-Loop Gain (OLG), defines the noise suppression at a particular frequency. The unity gain frequency defines frequencies at which the OLG is one. In LTP, the gain is high at low frequencies, and decreases at higher frequencies. Above the unity gain frequency, the loop no longer suppresses the noise. The gain margin is the difference between when the gain is unity, and the gain at the point when the phase is $-180°$. A large gain margin indicates that the loop can remain stable even with large fluctuations in the noise level.

• **Phase margin:** The phase margin is the difference in the phase at the unity gain frequency and $-180°$. In general, a high phase margin indicates that the loop is stable. Where the phase margin is close to zero, it results in a large 'servo bump' in the closed-loop response (see the noise suppression function below). In the limiting case where the phase margin := 0, an oscillation can be sustained within the loop. Typically, the phase margin should be $> 35°$. The phase margin is dependent upon the delay accumulated as the signal passes through the loop. If the delay is too large, then the requirement for the phase margin may be affected.

An example OLTF, in this case based on a model of the OPD control loop, is shown below. The unity gain frequency, gain margin, and phase margin are indicated on the plot. Specific details of the OPD loop can be found in Section 2.3.2, and in Box 2.4.
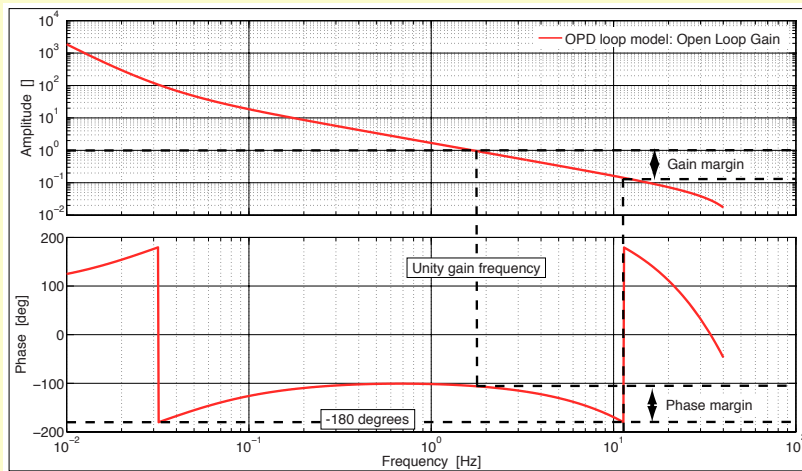
The degree to which the noise is suppressed when the loop is closed is defined by, S, the noise suppression function:

$$S \quad = \quad \frac{\widetilde{\epsilon}}{\widetilde{\delta x}} \tag{2.26}$$

$$= \quad \frac{1}{1 - \text{OLTF}} \tag{2.27}$$

$$= \quad \frac{1}{1 + (\text{C} \times \text{A} \times \text{X})} \tag{2.28}$$

A Bode plot of the amplitude of S, again based on the example of the OPD control loop, is shown below.
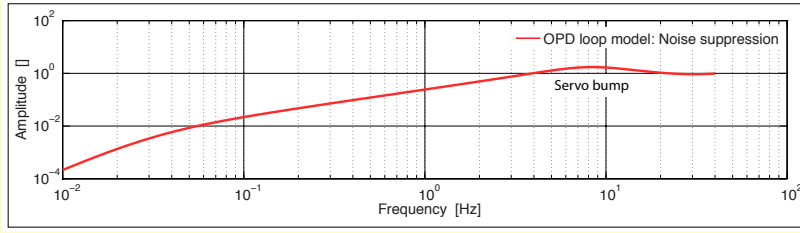
The amplitude of S defines the noise suppression at a particular frequency.

Box 2.2: Basic control loop theory relevant to this thesis. For more information, suggested resources are [51], and [57].

2.3.1 Frequency

A block diagram of the frequency control loop is shown in Figure 2.3. The input to the loop is the output of the frequency interferometer, Ψ_F. The loop is nested, with one part providing 'fast' feedback to the fast frequency actuator, the PZT that acts directly on the laser crystal. The output from this controller provides the input signal to the 'slow' part of the frequency control loop. This controller provides an input signal for the slow frequency actuator, which controls the temperature of the laser crystal. The slow loop controls long term frequency fluctuations, caused by variations in temperature, and ensures that the fast frequency loop remains within its operating range.

The feedback signal for each loop, y^{FF} and y^{SF}, are determined using the generic control law defined in Equation 2.22 with loop coefficients defined in the SDP. The error signals in each loop are given by:

$$\begin{aligned}
\epsilon^{\mathrm{FF}} &= \Delta x^{\mathrm{FF}} + \delta x^{\mathrm{FF}} - \Psi_F \\
\epsilon^{\mathrm{SF}} &= \Delta x^{\mathrm{SF}} + \delta x^{\mathrm{SF}} - y^{\mathrm{FF}}
\end{aligned}$$

where ϵ^{FF} and ϵ^{SF} are the fast and slow error signals, Δx^{FF} and Δx^{SF} are selectively injected DC offsets, δx^{FF} and δx^{SF} are selectively injected probing functions, Ψ_{F} (the processed frequency interferometer

output) is the input to the fast loop, and y^{FF} is the input to the slow loop. These signals are also defined in Figure 2.3.
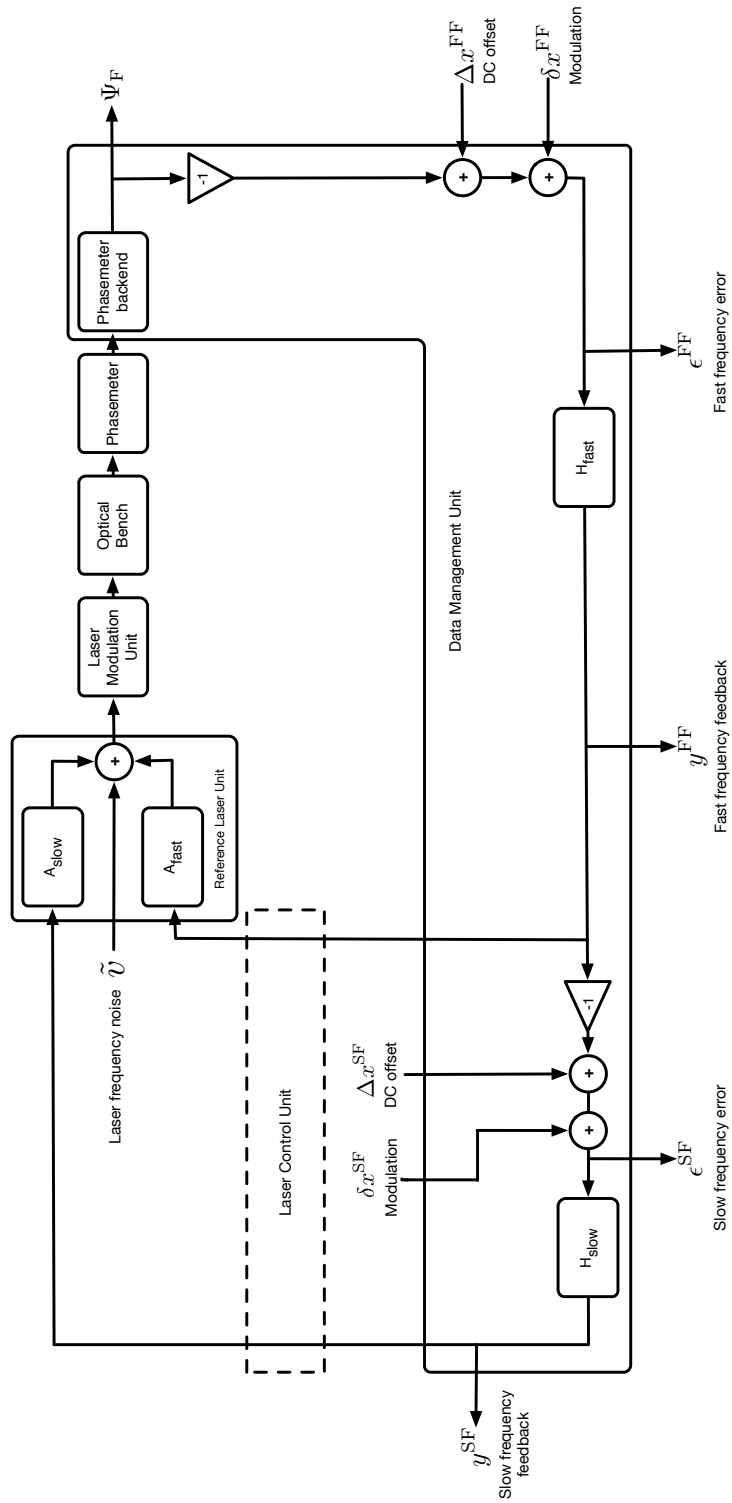
Chapter 2

Figure 2.3: A block diagram of the frequency control loop. The fast and slow controllers are represented by H, and the actuators by A. The input and output signals available via the telemetry are also shown.

In-flight, it is possible to downlink the loop error point and the feedback signals, as well as the loop states for the fast and slow loops, via the 3,25 housekeeping telemetry package. It is also possible to apply a DC offset to the error signal, as well as modulations to both the fast and slow loops via telecommand. An overview of the control loop telemetry is given in Table 2.2, the names associated with this telemetry in the mission database can be found in Appendix 7. If necessary, the telemetry can be recorded at a higher frequency, either 10 Hz or 100 Hz, on request and for a limited duration.

Name	Description
Ψ_F	Processed frequency ifo phase
ϵ^{FF}	Fast frequency loop error
y^{FF}	Fast frequency loop feedback
S^{FF}	Fast frequency loop state
δx^{FF}	Fast frequency loop probing function
Δx^{FF}	Fast frequency loop DC offset
ϵ^{SF}	Slow frequency loop error
y^{SF}	Slow frequency loop feedback
S^{SF}	Slow frequency loop state
δx^{SF}	Slow frequency loop probing function
Δx^{SF}	Slow frequency loop DC offset

Table 2.2: The telemetry parameters available in-flight for the fast and slow frequency control loops. The associated names used in the mission can be found in Appendix 7.

The characteristics of the designed frequency control loop, including the OLTF, defined in [50], are given in Box 2.3. This design provides a starting point for determining the response of the loop components, and the loop as a whole, from test campaign results and later from the results of in-flight investigations.

The design of the frequency control loop

A simplified block diagram of the frequency control loop shown in Figure 2.3, is shown below. The response of each block of the control loop is represented in terms of the associated Laplace transform.
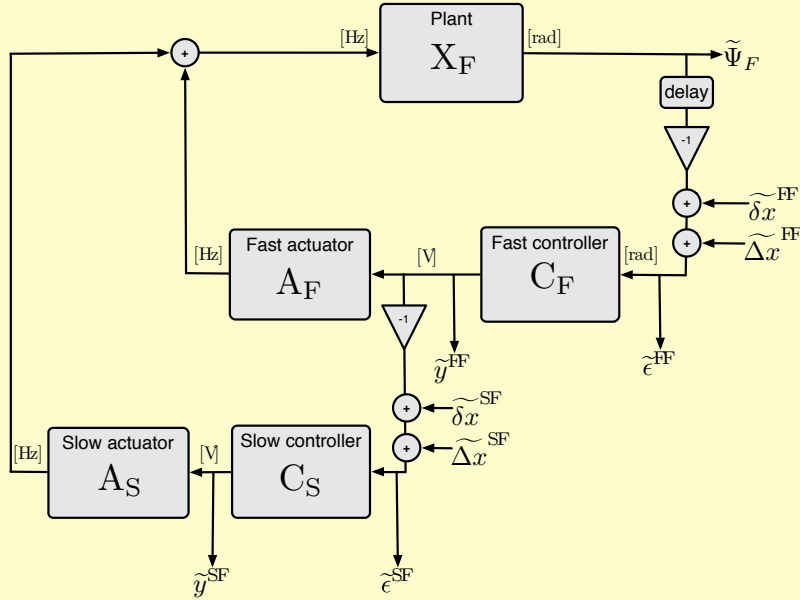

The OLTF of the loop is defined as:

$$\mathrm{OLTF} = \mathrm{C_F.X_F}\left(\mathrm{A_F} + \mathrm{A_S.C_S}\right). \tag{2.29}$$

The noise suppression function, S, is therefore:

$$S = \frac{1}{1 + \mathrm{C_F.X_F}\left(\mathrm{A_F} + \mathrm{A_S.C_S}\right)}. \tag{2.30}$$

A model of the digital implementation of the frequency control loop can be constructed using the design parameters specified in [50]. The diagram below shows a simplified version of the block diagram of the frequency control loop shown in Figure 2.3, including some signal delay.
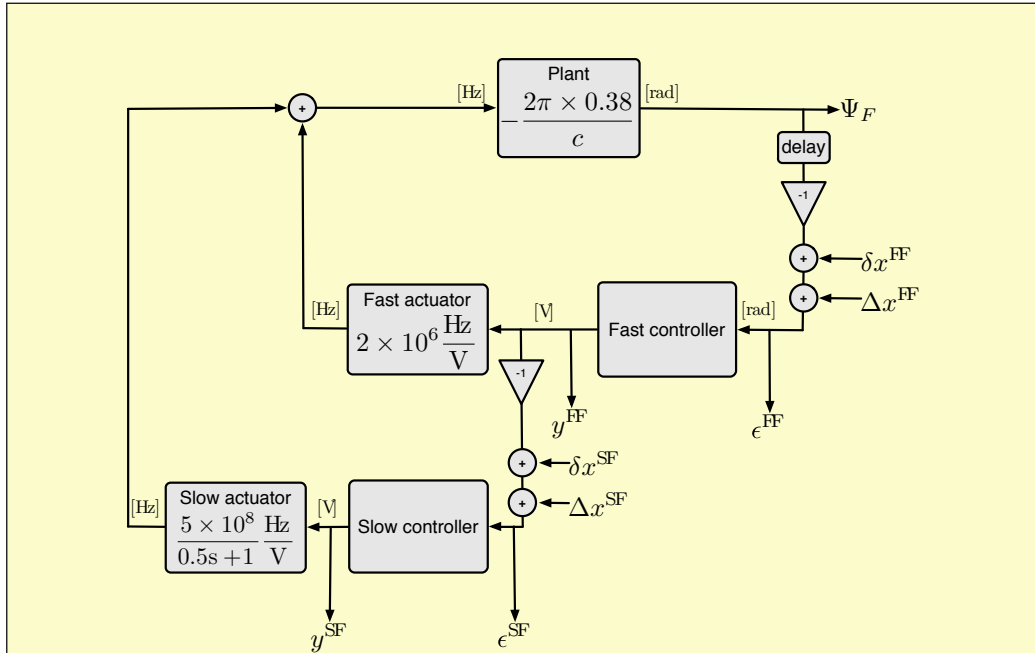
The design values of the plant, the fast actuator, and the slow actuator are shown in the respective blocks. The slow actuator has a gain of $5 \times 10^8/2$ Hz/V with a pole at $f = 2\pi/2$. The response of the fast and slow controllers depends upon the a and b coefficients that define the digital filter (see Section 2.3). The design values for these coefficients are:

Fast controller:

$$a_0 = -1.58 \qquad b_0 = 1$$
$$b_1 = 1$$

Slow controller:

$$a_0 = -5 \times 10^{-5} \qquad b_0 = 1$$
$$b_1 = 1$$

The OLTF of the model, based on the defined loop characteristics along with a delay of 20×10^{-3} s is shown below. The unity gain frequency is at approximately 0.31 Hz. The phase margin is approximately 54°, and the gain margin is approximately 0.97.

Continued on next page
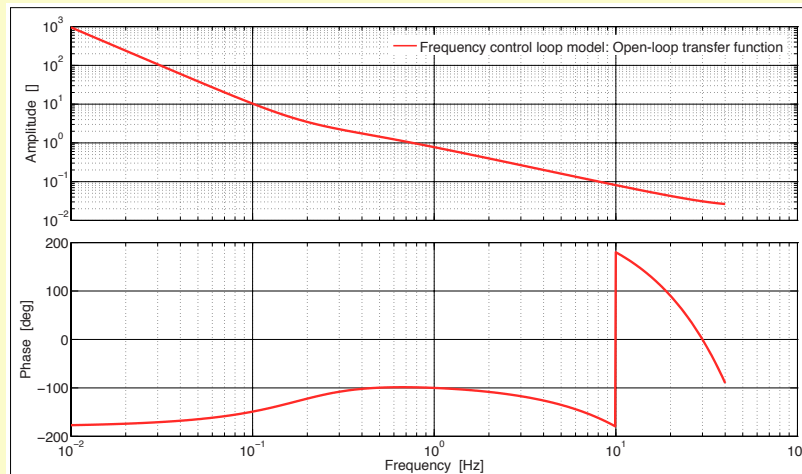
The amplitude of the associated noise suppression is shown below.
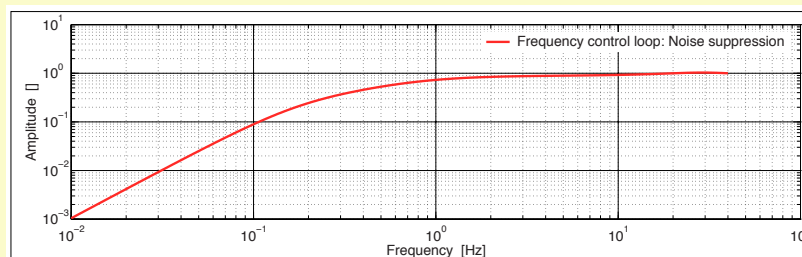
These plots, and the models based on the designed loop components, provide a reference for determining if the control loops have the required characteristics in-flight.

Box 2.3: A model of the frequency control loop, based on the loop design specified in [50].

2.3.2 Optical pathlength difference

The effects of OPD noise are suppressed by the OPD control loop, as shown in Figure 2.4. The loop takes the output from the reference interferometer, Ψ_R, as the loop input. The feedback signal is halved, and applied to the PZT-actuated mirror in each of the beam paths in the LMU (see Section 1.4.1). One actuator receives a positive signal, and the other negative, such that they operate in a push-pull configuration. The use of two actuators provides redundancy, such that if the

function of one actuator is degraded, the feedback signal to the other can be increased to compensate. The actuators have enough range to allow the OPD control loop to operate with only one actuator.

Chapter 2
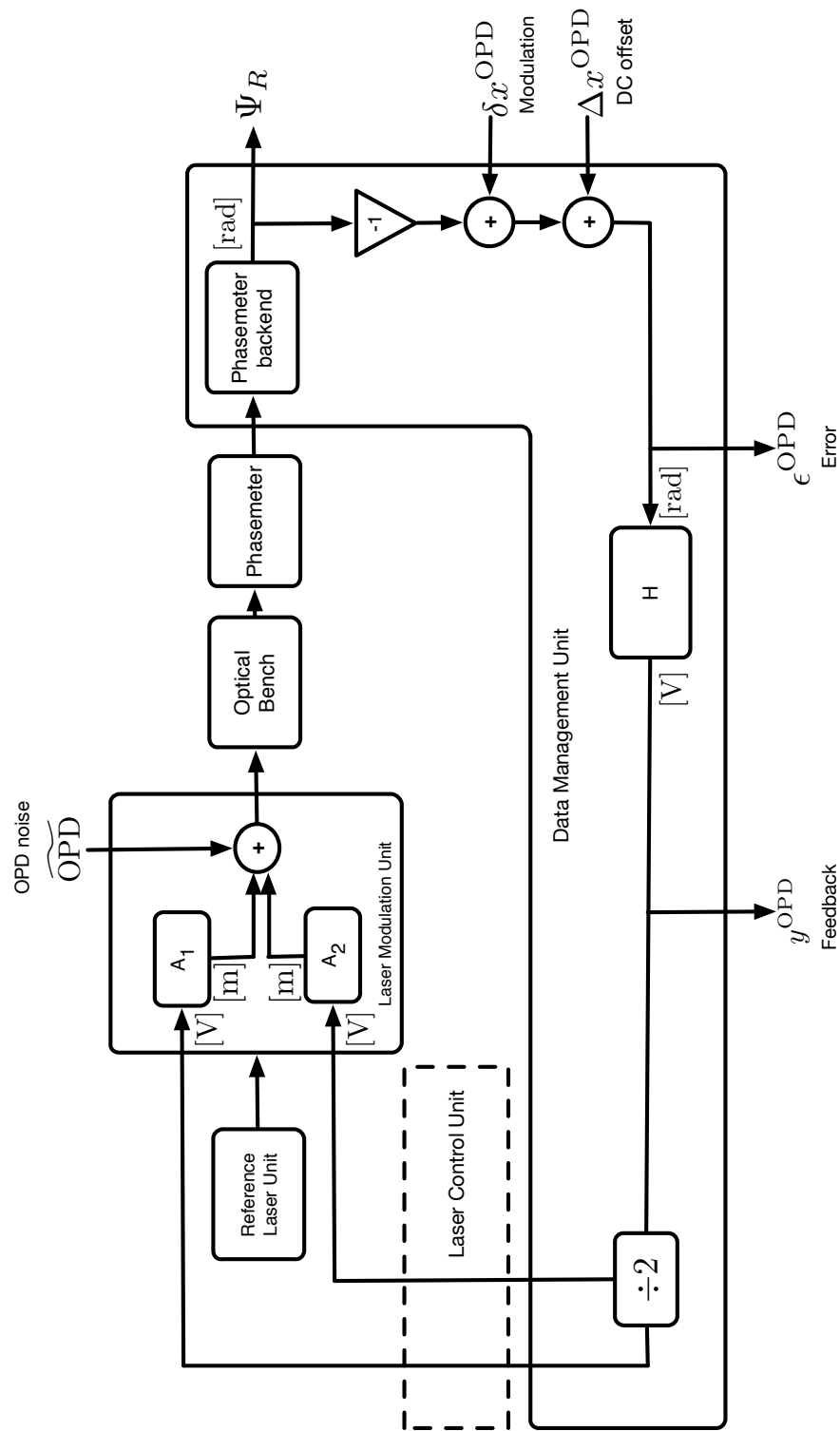
Figure 2.4: A block diagram of the OPD control loop, showing the controller, H, and two actuators, A_1 and A_2. The signals shown are the only outputs and inputs available during flight.

The feedback signal for the loop, y^{OPD}, is determined using the generic control law defined in Equation 2.22 with loop coefficients defined in the SDP. The error signal is given by:

$$\epsilon^{\text{OPD}} \quad = \Delta x^{\text{OPD}} + \delta x^{\text{OPD}} - \Psi_R$$

where ϵ^{OPD} is the error, Δx^{OPD} is a selectively injected DC offset, δx^{OPD} is a selectively injected probing function, and Ψ_{R} is the input to the loop. These signals are also defined in Figure 2.4.

In-flight, it is possible to downlink the loop error point, the loop state, and the feedback signal, via the 3,25 telemetry package. It is also possible to apply a DC offset, as well as modulations to the loop via telecommand. An overview of the control loop telemetry is given in Table 2.3. The associated parameter names for both the test campaign data, and the flight telemetry can be found in Appendix 7.

Name	Description
Ψ_R	Reference ifo. output
ϵ^{OPD}	OPD loop error
y^{OPD}	OPD loop feedback
S^{OPD}	OPD loop state
δx^{OPD}	OPD loop probing function
Δx^{OPD}	OPD loop DC offset

Table 2.3: Table of the telemetry associated with the OPD control loop.

A model of the control loop, based on the original design parameters given in [50], is described in Box 2.4. This model provides a starting point for modelling the loop, and the loop components, during the analysis of the test campaign data, and can also be used as a reference for the analysis of in-flight control loop characterisation investigations.

The design of the OPD control loop

A theoretical model of the digital OPD control loop can be constructed using the design parameters specified in [50]. The diagram below shows a simplified version of the block diagram of the OPD control loop shown in Figure 2.4, including some signal delay. The plant represents the reference interferometer and the processing of the phase output by the phasemeter and the phasemeter backend in the DMU.
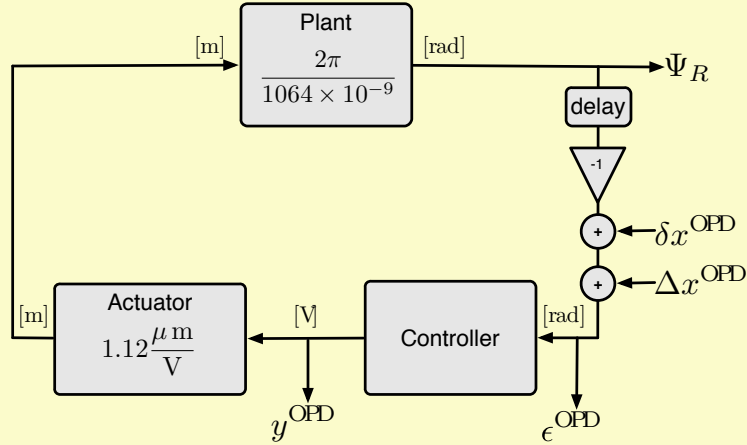

The design values of the plant and actuator (for both OPD actuators combined) are shown in the respective blocks on the diagram. The gain of the controller depends upon the a and b coefficients of the digital filter (see Equation 2.22). The design values for these coefficients are:

$$
\begin{array}{ll}
a_0 = 2.004 \times 10^2 & b_0 = 1 \\
a_1 = -1.996 \times 10^2 & b_1 = 3.0 \\
a_2 = -2.004 \times 10^2 & b_2 = -3.0 \\
a_3 = 1.996 \times 10^2 & b_3 = 1.0 \\
a_4 = 0 & b_4 = 0 \\
a_5 = 0 & b_5 = 0
\end{array}
$$

The OLTF and noise suppression function, S, for this model are shown below. It should be noted that the signs of the above a and b coefficients were switched in order to correctly implement the model.

Continued on next page
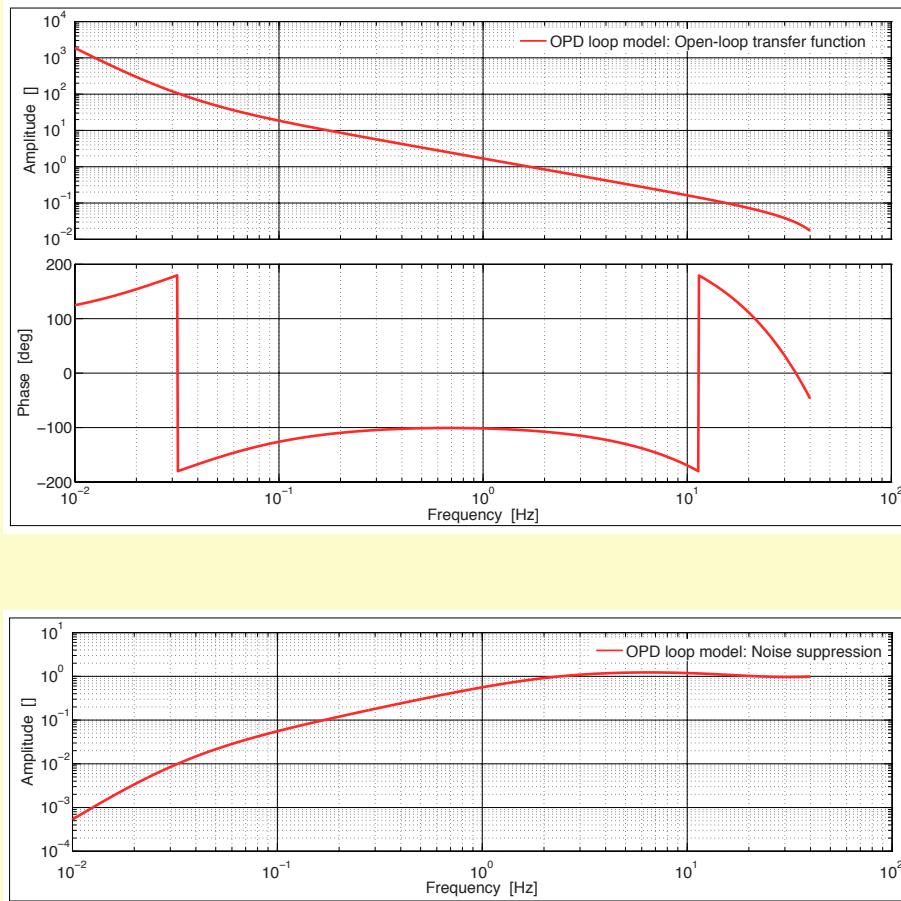
In-flight, the OLTF and the noise suppression function, can be calculated according to:

$$
\begin{aligned}
\mathrm{OLTF} &= \frac{\widetilde{\Psi}_R}{\widetilde{\epsilon}^{\mathrm{OPD}}} \\
S &= \frac{\widetilde{\epsilon}^{\mathrm{OPD}}}{\widetilde{\delta x}^{\mathrm{OPD}}}
\end{aligned}
$$

where the tilde represents the Fourier transform of the signal.
The derivation of these equations has already been shown in Box 2.2.

Box 2.4: A model of the OPD control loop based on the original loop design given in [50].

2.3.3 Amplitude

The effects of amplitude noise are suppressed by the amplitude control loop, as depicted in Figure 2.5. The loop is nested, and consists of two fast amplitude loops with analogue implementation, and a slow amplitude loop operated digitally at an update rate of 1 Hz.

Each fast amplitude control loop acts to stabilise the power in one of the beams. As such, the fast control loop for the measurement beam (beam one) takes the PDA1 Single Element Photodiode (SEPD) signal, Mon_1^{FP}, as the input. Similarly, the fast control loop for the reference beam (beam two) takes the PDA2 SEPD signal, Mon_2^{FP}, as the input. The photodiode outputs are routed to the LCU and are subtracted from a defined setpoint, to give two error signals, ϵ_1^{FP} and ϵ_2^{FP}, which are input into the AOM control electronics for AOM1 and AOM2 respectively. The feedback signals, F^1 and F^2, control the RF power that drives each AOM, thereby changing the beam power by changing the fraction of the input beam diffracted into the first order beam (see Box 1.2). The RF power can be monitored via two signals, $\text{RF\_Mon}_1^{\text{FP}}$ and $\text{RF\_Mon}_2^{\text{FP}}$.

The F^1 and F^2 feedback signals are also transmitted from the LCU to the DMU where they are averaged to provide an input signal for the slow amplitude control loop. This provides a feedback signal which is input into the RLU to control the DC output power of the laser. The feedback signal for the slow control loop, y^{SP}, is defined by the generic control law shown in Equation 2.22, with loop coefficients stored in the SDP. The error signal for the slow loop, ϵ^{SP}, is given by:

$$\epsilon^{\text{SP}} = \Delta x^{\text{SP}} + \delta x^{\text{SP}} - \tfrac{1}{2}(F^1 + F^2)$$

where Δx^{SP} and δx^{SP} are a selectively injected DC offset and probing function respectively. These signals are also defined in Figure 2.5.

In-flight, it is possible to download the two beam power monitors, two errors signals, two feedback signals, and two RF monitoring signals from the fast loops as well as a loop state, S^{FP}, which are down-sampled and routed via the DMU. For the slow power control loop the error signal, the feedback signal, and the loop state can be down-loaded. It is also possible to command a DC offset and a modulation
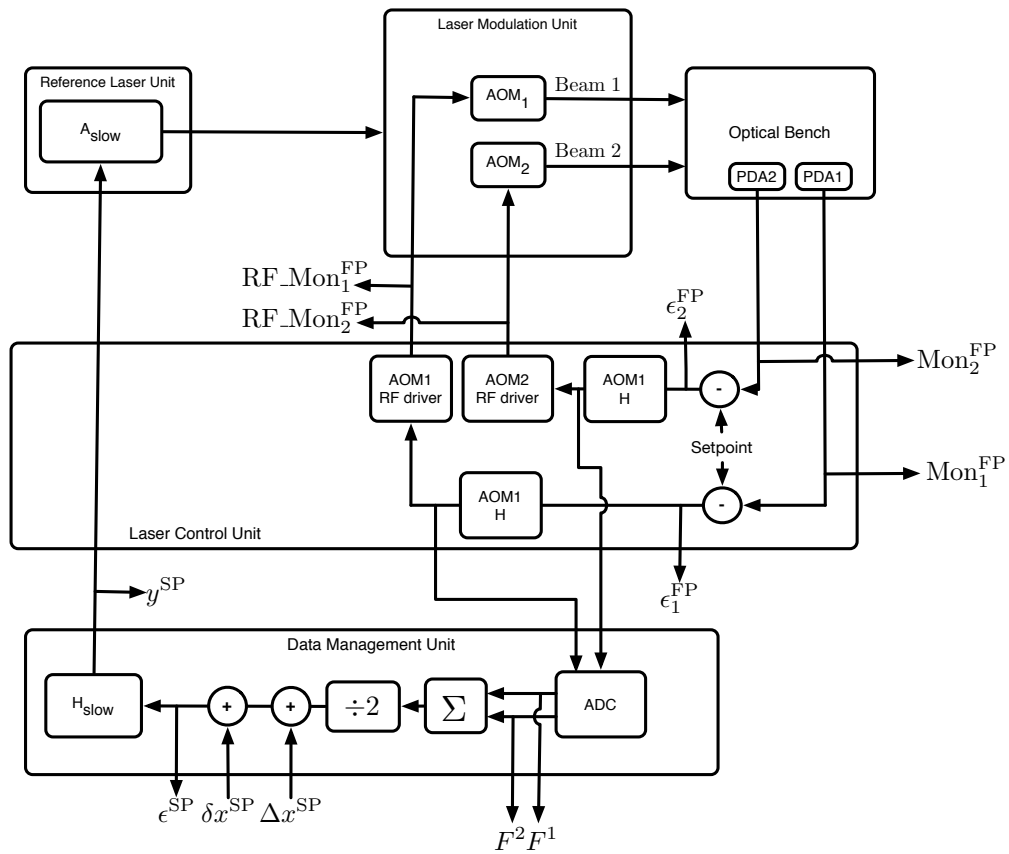
Figure 2.5: Block diagram of the amplitude control loop. In this diagram, the telemetry signals are shown from their point of origin. In actuality, they are routed through the DMU and converted to digital signals before being sent to the OBC.

to the slow error signal, defined via telecommand. An overview of the control loop telemetry and variable parameters is given in Table 2.4.

	Name	Description
Fast power	$\mathrm{Mon}_1^{\mathrm{FP}}$	Beam one power monitor
	$\mathrm{Mon}_2^{\mathrm{FP}}$	Beam two power monitor
	ϵ_1^{FP}	Beam one error
	ϵ_2^{FP}	Beam two error
	F^1	Beam one feedback
	F^2	Beam two feedback
	$\mathrm{RF\_Mon}_1^{\mathrm{FP}}$	Beam one RF power monitor
	$\mathrm{RF\_Mon}_2^{\mathrm{FP}}$	Beam two RF power monitor
Slow power	S^{SP}	Slow power loop state
	ϵ^{SP}	Feedback
	Δ^{SP}	DC offset
	δ^{SP}	Probing function
	y^{SP}	Feedback

Table 2.4: Table of the telemetry associated with the amplitude control loop.

A model, based on the design parameters of the control loop defined in [50], is shown in Box 2.5.

Important note: The design of the slow amplitude control loop has been included in this description for completeness. However, it has been demonstrated during the ground-based test campaigns that the slow amplitude control loop does not function as required. As the two fast amplitude control loops have sufficient gain, it is not necessary to use the slow control loop, and it was not used during the ground-based tests.

The design of the slow amplitude control loop

A simplified model of the slow amplitude control loop was made based on the design given in [50]. The input from the fast amplitude control loops are represented by a gain of -0.923 and a delay of 0.42 s. The controller is defined by the coefficients a and b which are:

$$a_0 = 0.000228882 \qquad b_0 = 1$$
$$a_1 = -0.000076294 \qquad b_1 = 1.0$$

The actuator is a pole-zero model with a gain of 30, and poles and zeros at the following frequencies:

Poles	1	26.7176	220.5	960	795
Zeroes	0	-4.8×10^{-7}	6.4×10^{-4}	-7.2×10^{-1}	796

The OLTF and the noise suppression function are shown below.
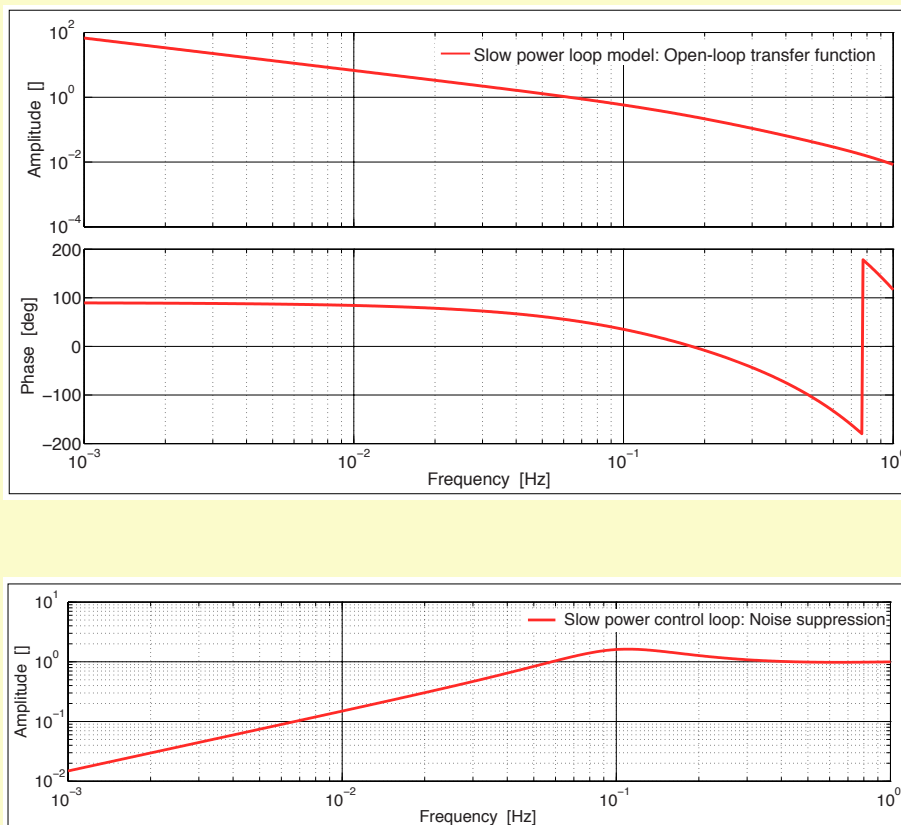
Box 2.5: A model of the slow power loop, based on the design given in [50].

2.4 Theoretical noise projections

The LISA Pathfinder LTP is implemented in the LTPDA toolbox as State Space Models (SSMs), in the form of built-in models. These models represent parts of the satellite, and consist of inputs, states, and outputs. The different blocks can be put together, via corresponding inputs and outputs, to model different parts of the system. A simplified diagram representing the built-in models of the LTP is shown in Figure 2.6. More detailed information regarding the use of the LTP State Space Model (SSM)s can be found in the LTPDA toolbox training sessions, available in the LTPDA section of the MATLAB® help. In this document, all methods refer to the associated LTPDA method.
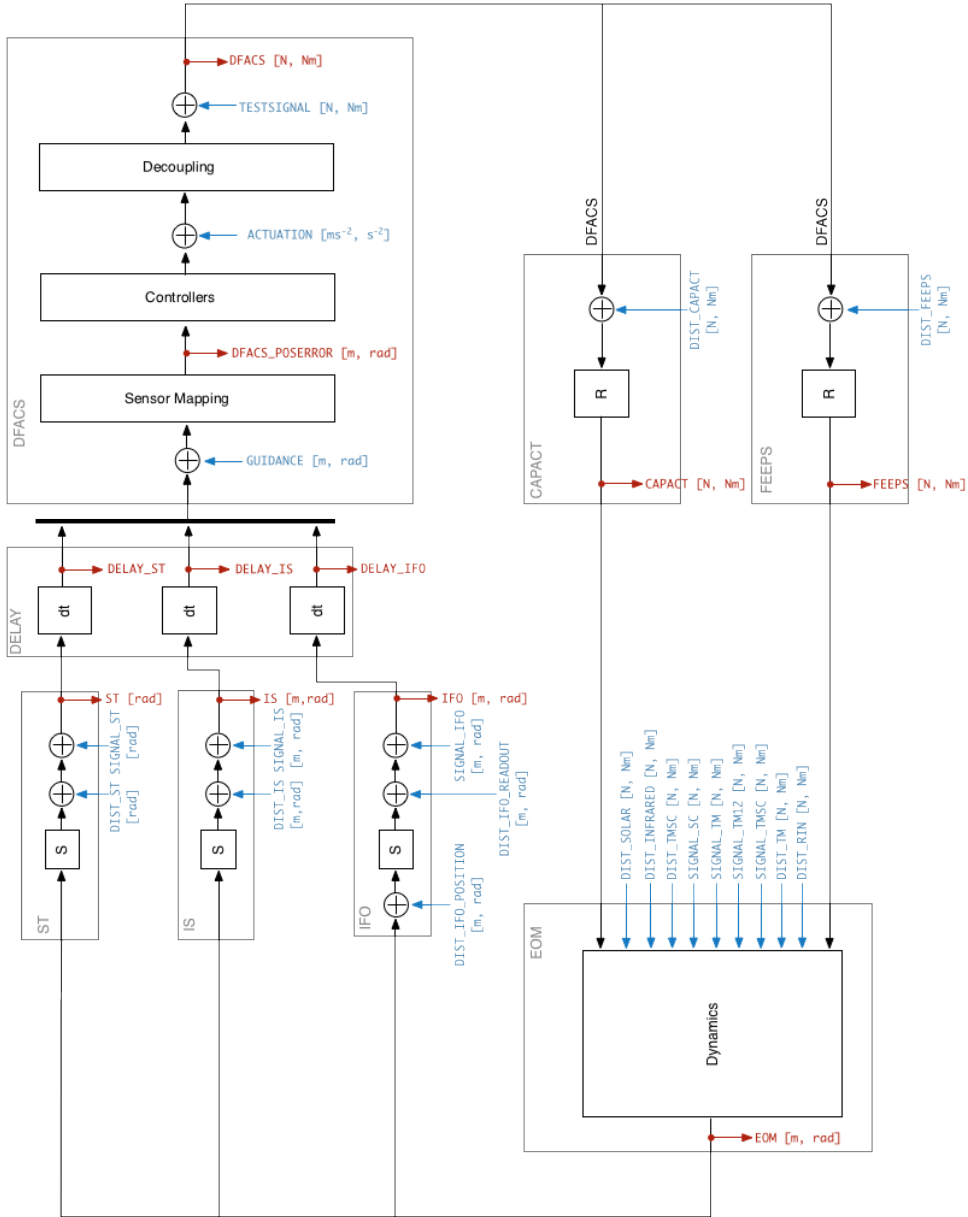
Figure 2.6: An overview of the LTPDA toolbox built-in state space models of the LISA technology package. Inputs are shown in blue, and outputs in red. Image courtesy of M. Hewitson.

A theoretical noise budget, showing the contribution of each OMS noise source to the differential test mass displacement measurement, x_{12}, can be created by injecting some representative noise into the appropriate block of the LTP state-space model. In this thesis, the focus is on the noise sources that can be evaluated through in-flight experiments, which are:

- Frequency noise;

- OPD noise;

- Amplitude noise;

    - RIN at f_{het};

    - RIN at low frequencies (radiation pressure noise).

The allocations for these noise sources, shown in Table 2.5, provide the maximum allowed contribution of each noise source to the differential test mass displacement measurement at $30\,\text{mHz}$. In order to make a theoretical projection of the noise budget, some input value and frequency dependence for each noise source must be adopted. These input spectra should meet the requirement at $30\,\text{mHz}$.

Noise source	Requirement $(\text{m}/\sqrt{\text{Hz}})$
Frequency	2×10^{-12}
OPD	2×10^{-12}
RIN at f_{het}	2×10^{-12}
RIN at low freq.	3.87×10^{-12}

Table 2.5: A summary of the requirements for the noise sources that affect the differential displacement measurement.

Table 2.6 gives the noise source and the appropriate input for its injection into the LTP SSM. It should be noted that in this model the radiation pressure noise is applied to just one test mass, but with the sum total of the beam powers on both test masses. This provides the equivalent differential displacement due to the radiation pressure noise as when calculated separately for each test mass.

Noise source	Input
Frequency noise	DIST_IFO_POSITION.x12
OPD noise	DIST_IFO_POSITION.x12
RIN at f_{het}: beam 1	TESTSIGNAL.tm1_x
RIN at f_{het}: beam 2	TESTSIGNAL.tm2_x
RIN at low freq.	DIST_IFO_POSITION.x1

Table 2.6: The SSM input names for each noise source used in creating the theoretical projection of the OMS noise budget.

The output from the SSM for the differential test mass displacement is DELAY_IFO.x12. The transfer functions from the inputs defined in Table 2.6 to this output are shown in Figures 2.7 and 2.8.

The inputs for each noise source are shown in Table 2.7. They are based on reasonable values and are given a flat frequency response.

Noise source	Value	Units
Frequency noise	1.7×10^{-12}	$\text{m}/\sqrt{\text{Hz}}$
OPD noise	2×10^{-12}	$\text{m}/\sqrt{\text{Hz}}$
RIN at f_{het}: beam 1	$(3 \times 10^{-5})(2 \times 10^{-3})$	$\text{W}/\sqrt{\text{Hz}}$
RIN at f_{het}: beam 2	$(3 \times 10^{-5})(1 \times 10^{-3})$	$\text{W}/\sqrt{\text{Hz}}$
RIN at low freq.	2.2×10^{-12}	$\text{m}/\sqrt{\text{Hz}}$

Table 2.7: The SSM input values for each noise source used in creating the theoretical projection of the OMS noise budget.

Figure 2.9 shows the theoretical X12 noise budget created using the values for each of the noise source given in Table 2.7. The aim of the in-flight noise characterisation experiments described in Chapters 3, 4, and 5 is to allow these projections to be replaced with the real satellite data. As a first step, the results from the EM, FM, and OSTT test campaigns have been analysed to determine the noise contributions in each setup.

Chapter 2
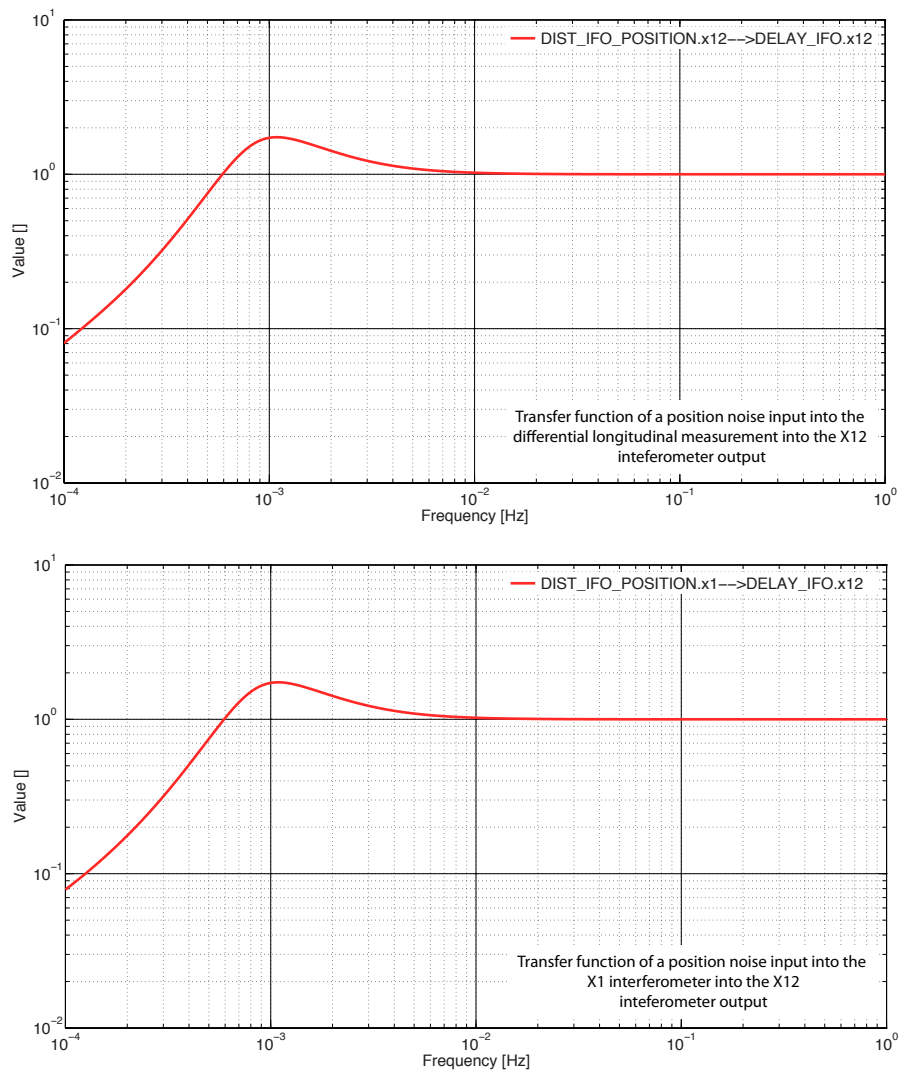
Figure 2.7: Transfer functions for the DIST_IFO_POSITION.x12 (top), and DIST_IFO_POSITION.x1 (bottom) inputs into the DELAY_IFO.x12 output.
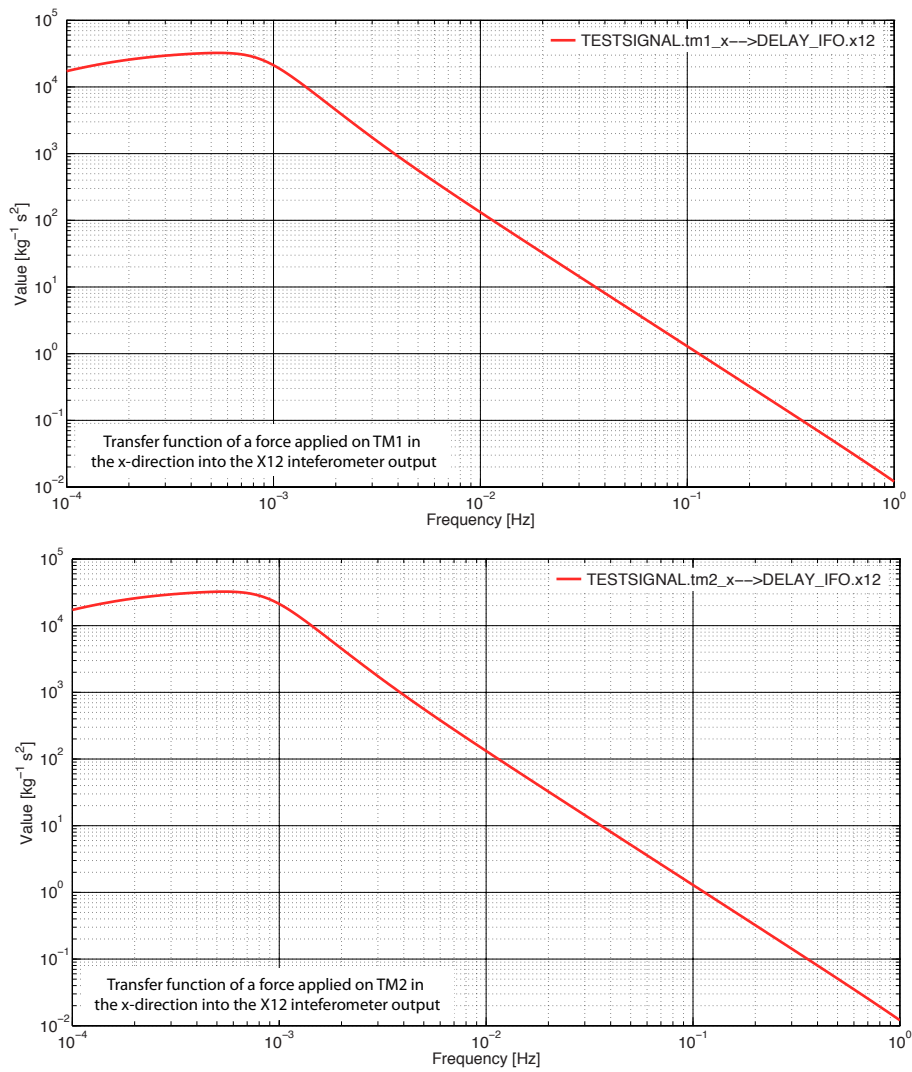
Figure 2.8: Transfer functions for the TESTSIGNAL.tm1_x (top), and TESTSIGNAL.tm2_x (bottom) inputs into the DELAY_IFO.x12 output.
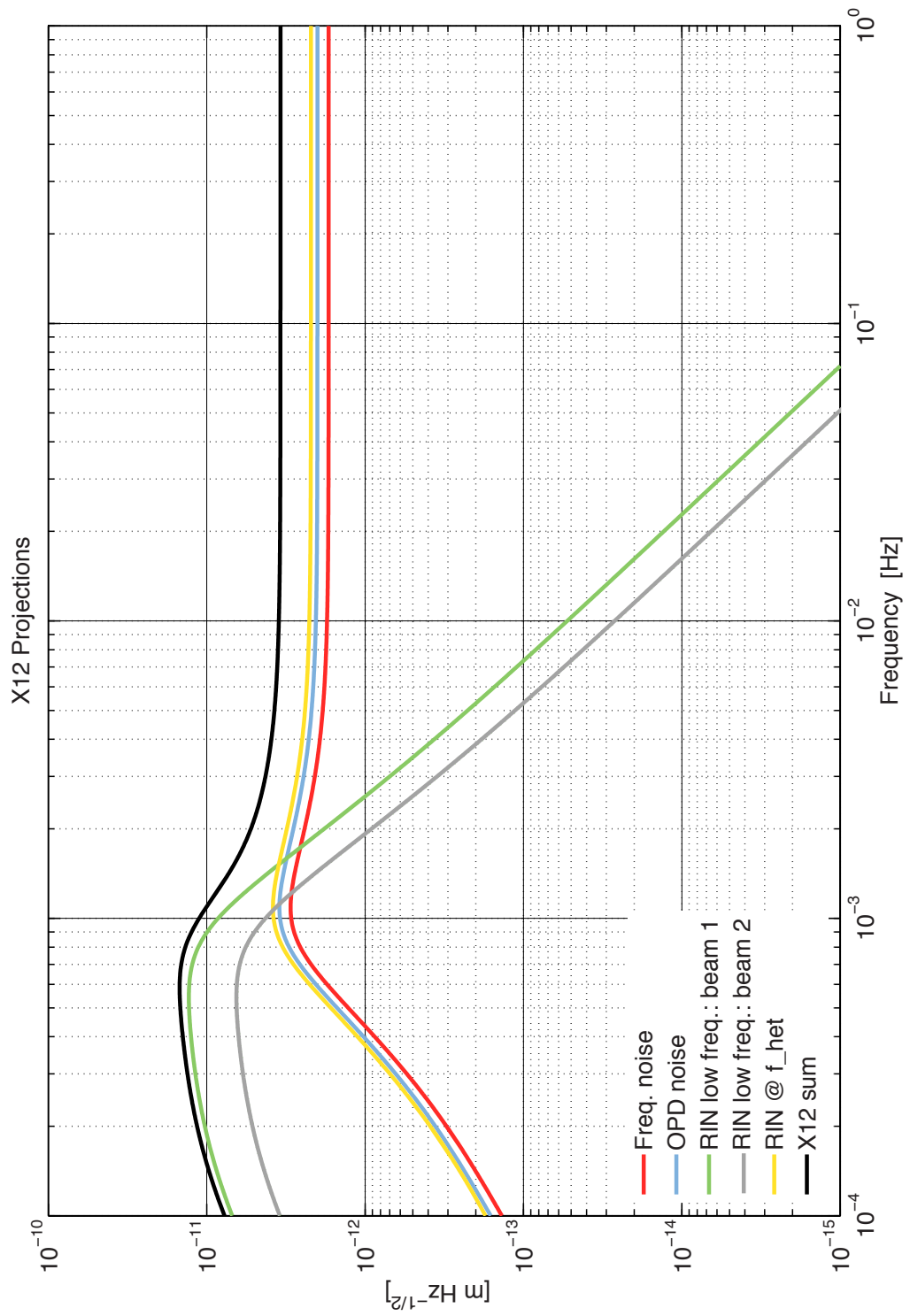
Figure 2.9: A plot showing the theoretical noise projections of the main OMS noise sources that can be measured in flight.

3 Frequency noise characterisation

Contents

The aims of this set of investigations are to measure the frequency noise, both free-running and closed-loop; determine the coupling into the measurement of the differential test mass displacement; and characterise the control loops. The investigations can be split into the following:

- Measurement of the free-running frequency noise:

  - Calculation of the free-running frequency noise spectrum;

  - Determination of a broadband coupling coefficient for frequency noise into differential test mass displacement.

- Characterisation of the fast and slow frequency control loops:

  - Fast controller characterisation;

  - Slow controller characterisation;

  - Calibration of the fast and slow actuators;

  - Calculation of the OLTF and noise suppression function;

  - Determination of a coupling coefficient via injected modulations.

- Projection of the frequency noise component of the differential test mass displacement during a closed-loop measurement.

The motivation for each investigation is presented, along with the results of applicable investigations performed during the ground-based hardware test campaigns. The procedure for performing the investigation in-flight, as well as a suggested procedure for the associated data analysis, is also presented.

3.1 Free-running frequency noise

A free-running noise measurement characterises the frequency noise when it is not stabilised by the frequency control loop. Such an investigation is necessary to determine the magnitude of the free-running frequency noise. An additional result is that a broadband coupling coefficient for frequency noise into the x_{12} differential displacement measurement can be determined.

Free-running frequency noise magnitude

The main goal of the free-running frequency noise investigations is to determine the inherent frequency noise of the OMS. This noise level is dependent upon the characteristics of the laser, and as it is possible that such a laser could be used in future missions, such an investigation provides useful information.

The spectrum of the frequency noise is determined by calculating the amplitude spectral density of the processed phase of the frequency interferometer, Ψ_F[1]. This spectrum provides a reference level which can be compared with the closed loop measurement of the frequency noise.
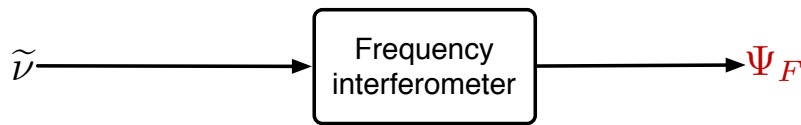
The measured free-running frequency noise, converted to $\mathrm{Hz}/\sqrt{\mathrm{Hz}}$, along with the equivalent allocation for the closed-loop frequency noise defined in Section 2.2.1, allows the gain required by the frequency control loop to be calculated. The calculation is described in Box 3.1.

The results of the ground based hardware tests, particularly the FM and OSTT test campaigns when the flight laser was used, are the best estimates of the frequency noise level that can be expected in-flight.

---

[1] The Ψ_F output from the DMU has units of radians. As a frequency fluctuation is being considered, this can be more logically represented in units of Hz using the conversion described in Box 2.1. The amplitude spectral density of the free-running frequency noise will therefore be in units of $\mathrm{Hz}/\sqrt{\mathrm{Hz}}$.

The allocation for the frequency noise is:

$$\delta\widetilde{\Psi}_F \leq 112 \times 10^3 \sqrt{1 + \left(\frac{f}{3\,\mathrm{mHz}}\right)^{-4}}\,\frac{\mathrm{Hz}}{\sqrt{\mathrm{Hz}}} \qquad (3.1)$$

in the measurement bandwidth of $1\,\mathrm{mHz} \leq f \leq 30\,\mathrm{mHz}$, as discussed in Section 2.2.1.

In order to meet this requirement, the free-running frequency noise, Ψ_F^{fr}, must be suppressed by the frequency control loop. The gain required to achieve this level of suppression is defined by:

$$\mathrm{OLG}(f) \geq 20 \log\left(\frac{\widetilde{\Psi}_F^{\mathrm{fr}}}{\widetilde{\Psi}_F}\right)\,\mathrm{dB} \qquad (3.2)$$

The value of Ψ_F^{fr} is the result of the free-running frequency noise investigation.

Box 3.1: Calculation of the gain required to suppress the measured free-running frequency noise [32].

Broadband coupling of frequency noise

Any differences in the optical pathlengths of the measurement and reference beams of the X12 interferometer will result in the coupling of frequency noise into the differential displacement measurement, x_{12}, as described in Section 2.2.1. The higher level of frequency noise across all frequencies during a free-running measurement, compared to a closed-loop measurement, can be exploited to determine a broadband coupling coefficient.
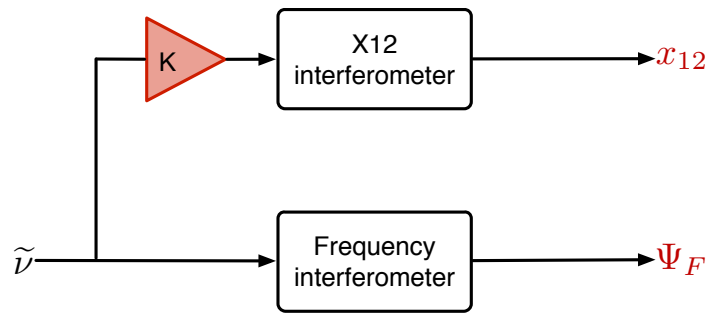
Figure 3.1: A simplified block diagram showing a conceptual representation of the coupling of the frequency noise, $\widetilde{\nu}$, measured by the frequency interferometer via Ψ_F, into the x_{12} measurement via the coupling coefficient, K.

The coupling coefficient, K, in units of m/rad, can be determined by calculating the transfer function from the Ψ_F channel to the x_{12} channel[2]. The coefficient can then be used to make a projection of the frequency noise component onto the differential test mass displacement measurement.

Additionally, the coupling coefficient can be used to calculate an upper limit of the optical pathlength difference between the measurement and reference beams in the x_{12} interferometer. The calculation is explained in detail in Box 3.3.

Note: The accuracy of the coupling coefficient calculated from the free-running frequency noise analysis is low. This is because the magnitude of the frequency noise is such that it doesn't produce large signals in x_{12}. A more accurate coupling coefficient can be calculated as part of the control loop characterisation investigation, described in Section 3.2. Nevertheless, this analysis can be performed easily on the results of the free-running frequency noise investigation, and as such it can be used to provide a rough estimate of the coupling coefficient.

---

[2]The coefficient is represented in units of m/rad as the output from the frequency interferometer that measures the frequency noise is in radians. It would also be possible to convert K to an equivalent coefficient with units of m/Hz using Equation 2.5 defined in Section 2.2.1.

3.1.1 Test campaign results

Free-running frequency noise measurements were made during all three test campaigns. The information relating to the investigation dates and times, as well as the specific details of the analyses can be found in Appendix 8, Tables 8.1, 8.2, and 8.3, for the EM, FM, and OSTT campaigns respectively. The same initial processing of the telemetry channels was performed for both analyses, as described under 'Overview of the analysis'. The analyses of the free-running frequency noise, and the broadband frequency noise coupling are then described under the associated headings.

Overview of the analysis

The telemetry used in these analyses is given in Table 3.1. The equivalent names used in the LTPDA repositories can be found in Appendix 7. The initial processing can be summarised as follows:

Parameter	Description	Frequency [Hz]	ID
S^{FF}	Fast freq. loop state	1 Hz	LST17361
S^{SF}	Slow freq. loop state	1 Hz	LST17364
S^{OPD}	OPD loop state	1 Hz	LST17367
S^{SP}	Slow power loop state	1 Hz	LST17358
y^{FF}	Fast freq. loop feedback	1 Hz	LST17340
		10 Hz	
y^{SF}	Slow freq. loop feedback	1 Hz	LST17345
		10 Hz	
y^{OPD}	OPD loop feedback	1 Hz	LST17350
		10 Hz	
y^{SP}	Slow power loop feedback	1 Hz	LST17357
		10 Hz	
Ψ_F	Freq. ifo. output	10 Hz	LST12406
x_{12}	X12 ifo. output	10 Hz	LST10130
SSC	Source sequence counter	10 Hz	SCT70388

Table 3.1: The telemetry parameters used in the analysis of the EM, FM, and OSTT test campaign free-running frequency noise investigations.

1. The data for the times specified in the test campaign reports were downloaded [32] [43] [44].

2. The data was split to leave the times where the fast and slow frequency control loops were open (state = 1, feedback = 0), and the other control loops were in a stable operating state. As an example, a plot of the loop states from the EM test campaign is shown in Appendix 8, Figure 8.1.

3. The essential channels, Ψ_F and x_{12}, were checked for data quality issues and glitches and repaired accordingly. The data repair method is discussed in Appendix 9.

4. The x_{12} and Ψ_F channels were detrended with order three. This removed any DC offset, and subtracted any linear, quadratic, or cubic trend. The original and detrended timeseries of the Ψ_F and x_{12} channels from the EM, FM, and OSTT test campaigns are shown in Appendix 8, Figures 8.2, 8.3, and 8.4 respectively.

Free-running frequency noise

1. The Ψ_F channel was converted from radians to Hz (see Box 2.1):

$$\Psi_F^{\mathrm{Hz}} = \frac{c}{2\pi \times 0.38} \Psi_F^{\mathrm{rad}} \qquad (3.3)$$

2. The spectrum of the free-running frequency noise was determined from the amplitude spectral density of the converted Ψ_F channel. The results for the three test campaigns are shown in Figure 3.2.

   Note: The amplitude spectral density was calculated using the default Hanning windowing function, which has a default overlap of 50%, and 16 averages.
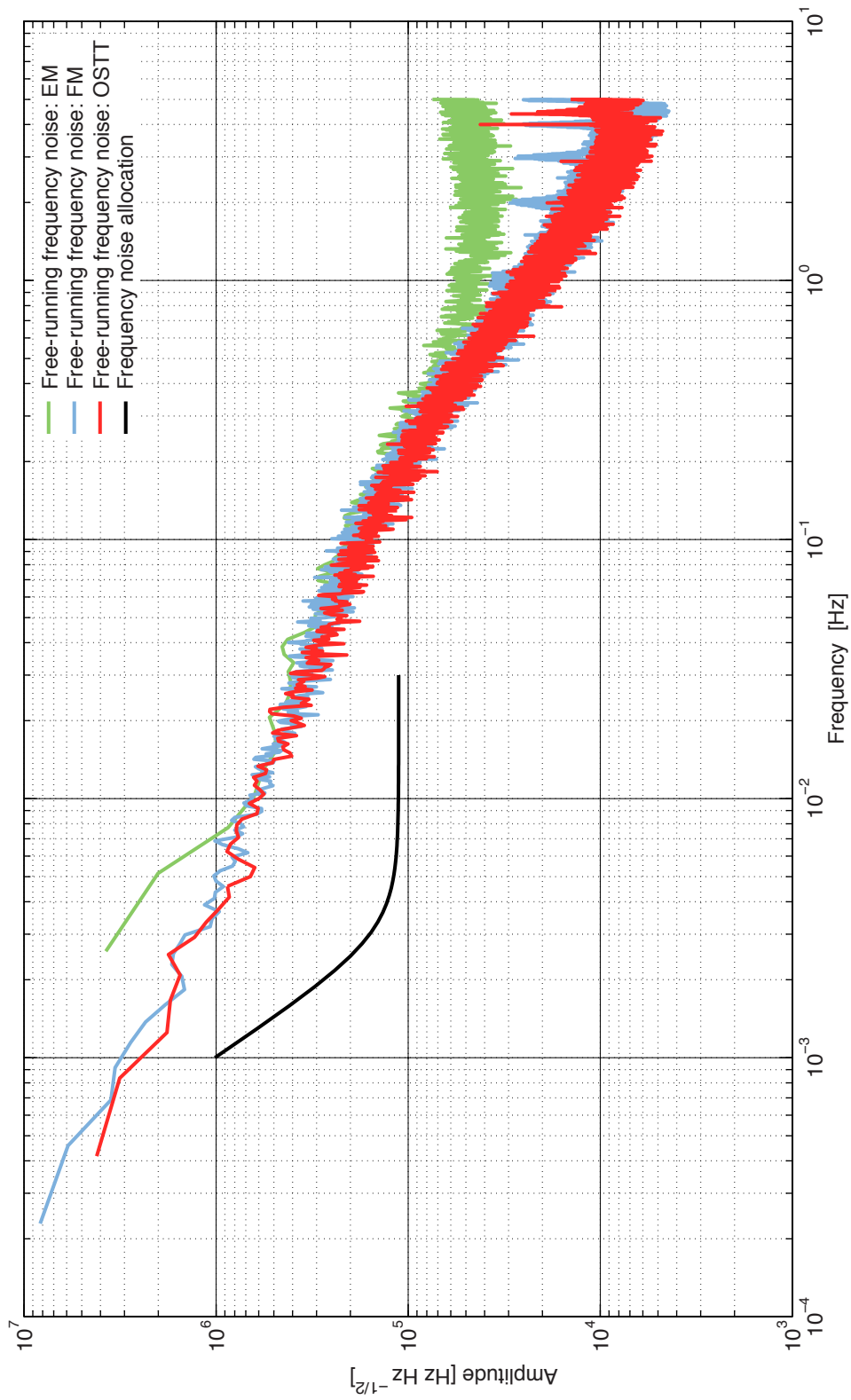
Figure 3.2: The free-running frequency noise for the EM campaign (green), the FM campaign (blue), and the OSTT campaign (red). The allocation for the frequency noise in the measurement bandwidth is also shown in black.

From the spectra of the free-running frequency noise, the gain required by the frequency control loop was calculated, as discussed in Box 3.1. The results are shown in Table 3.2.

	Frequency noise $[\mathrm{Hz}/\sqrt{\mathrm{Hz}}]$	Suppression required	Gain $[\mathrm{dB}]$
EM	4.20×10^5	3.75	11.48
FM	4.05×10^5	3.62	11.16
OSTT	3.21×10^5	2.87	9.14

Table 3.2: The value of the free-running frequency noise at $30\,\mathrm{mHz}$, with the suppression and minimum gain required for the frequency control loop to suppress the frequency noise to the allocated level.

The spectra of the free-running frequency noise in both the FM and OSTT campaigns give very similar results. This is as expected, since the FM laser was tested in both cases. Therefore, this noise level is the best prediction of the free-running frequency noise that can be expected in-flight.

Broadband coupling of frequency noise

1. The x_{12} and Ψ_F channels were detrended with order three. This removed any DC offset, and subtracted a linear, a quadratic, and a cubic fit.

2. A transfer function of the Ψ_F channel into the x_{12} channel, as well as the coherence, was estimated, both with 60 averages. The transfer function and coherence estimates for the EM, FM, and OSTT campaigns can be found in Figures 3.3, 3.4, and 3.5.

3. A frequency range was selected where, ideally, the transfer function had a flat response, the errors were small, and the coherence was high. It can be seen from the plots of the transfer functions and associated coherences, that the selection of such a region was not simple, because the coupling of frequency noise into the x_{12} channel was small.

   In the EM campaign, the only reasonably flat region of the transfer function was selected. Some comments relating to the high
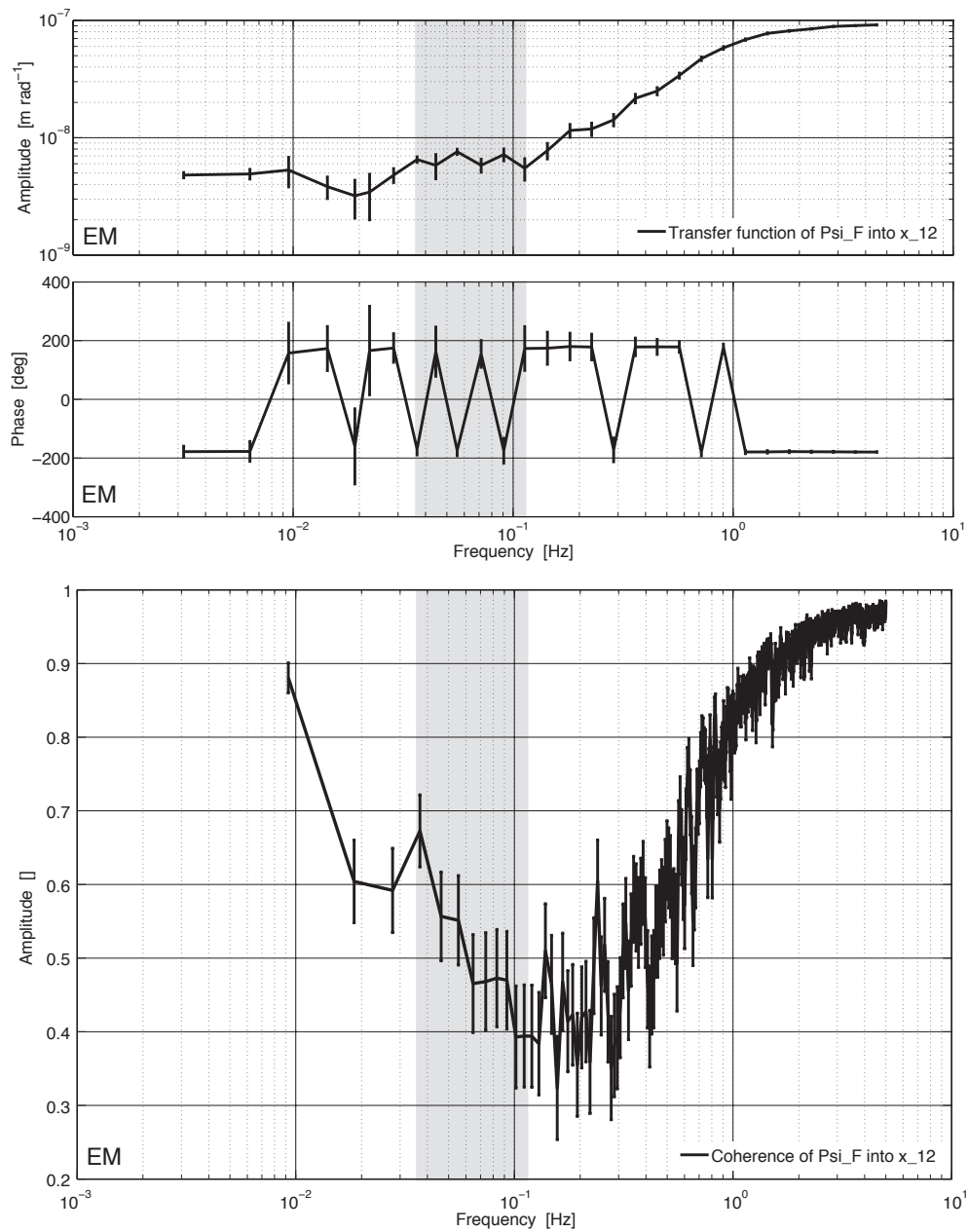
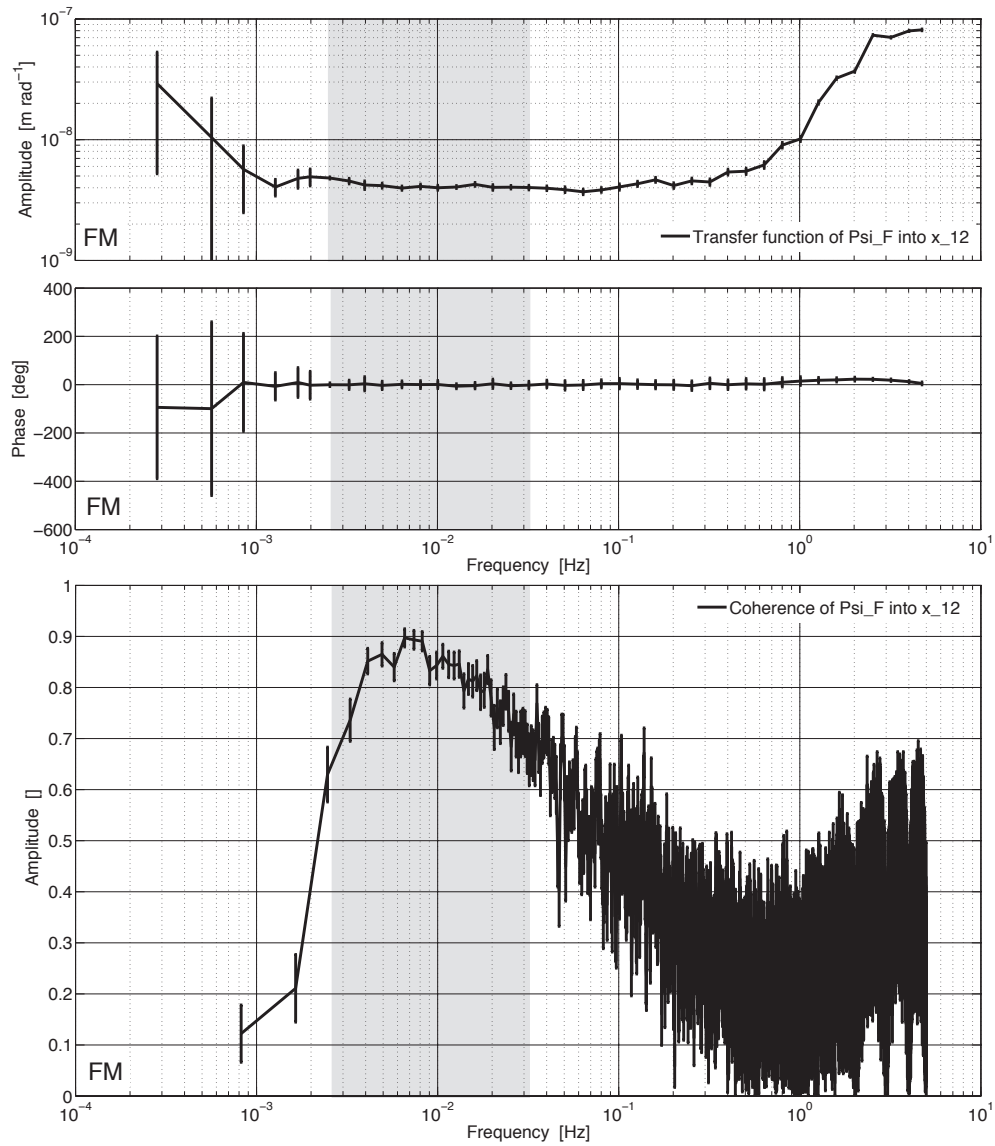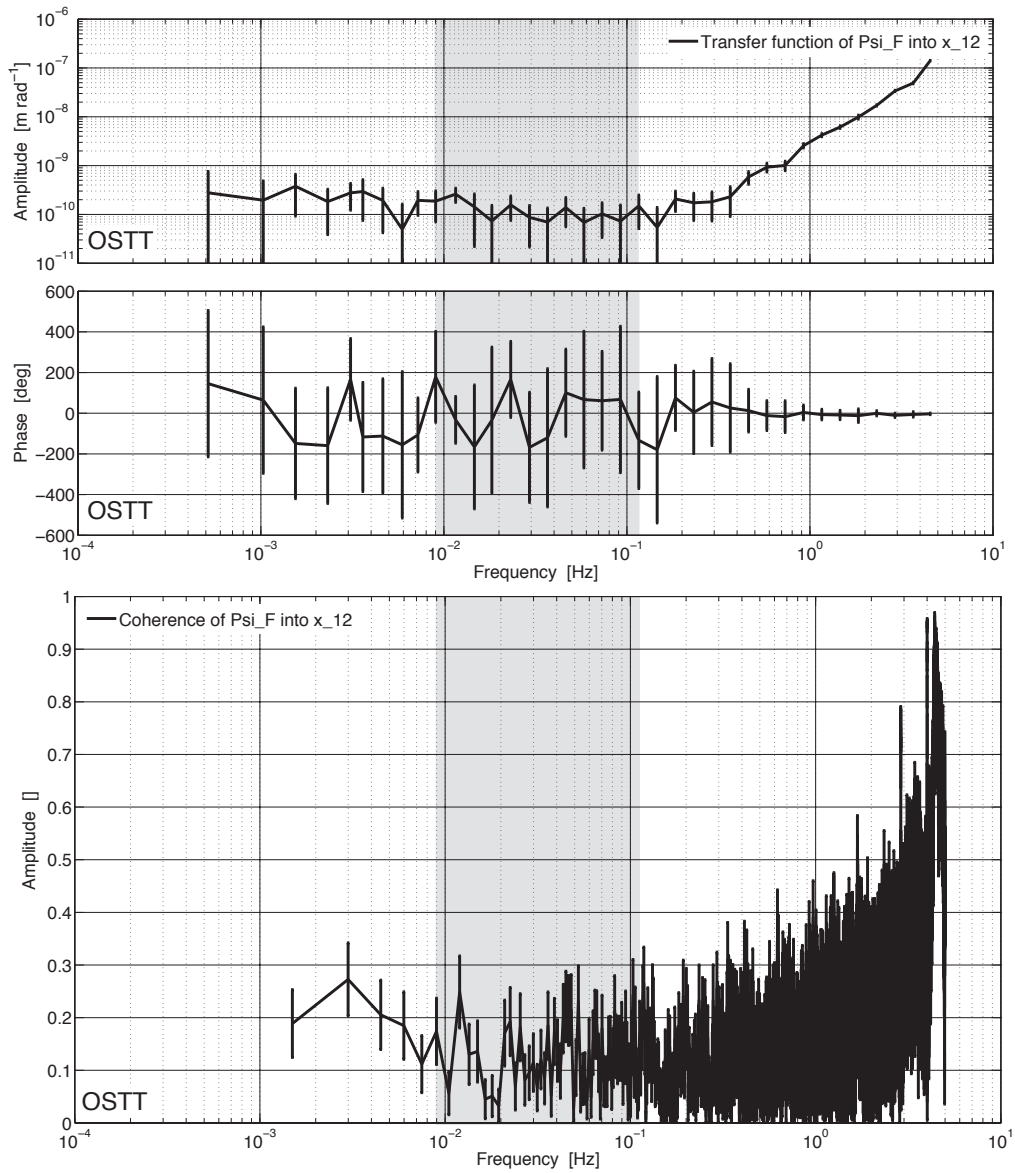# 3 Frequency noise characterisation

Figure 3.3: Plots of the transfer function and coherence of Ψ_F and x_{12} for the EM test campaign investigation of the free-running frequency noise. The grey shaded area represents the frequency region used to determine the coupling coefficient for frequency noise into differential displacement. A discussion of the high coherence of the channels at high frequencies can be found in Box 3.2.

Figure 3.4: Plots of the transfer function and coherence of Ψ_F and x_{12} for the FM test campaign investigation of the free-running frequency noise. The grey shaded area represents the frequency region used to determine the coupling coefficient for frequency noise into differential displacement.

Figure 3.5: Plots of the transfer function and coherence of Ψ_F and x_{12} for the OSTT test campaign investigation of the free-running frequency noise. The grey shaded area represents the frequency region used to determine the coupling coefficient for frequency noise into differential displacement.

coherence of the EM channels at frequencies above $1\,\text{Hz}$ can be found in Box 3.2. The transfer function for the FM campaign contained a wide flat region, and frequencies were selected where the coherence was highest. The coupling and the coherence in the OSTT campaign was negligible, and a frequency range was selected where both the transfer function and the coherence levels were relatively flat.

Note: The transfer function was binned such that each point is the average of ten bins per decade of the original transfer function. The smoothed transfer function provided a better statistical estimate of the error.

4. The mean value of the transfer function in the selected frequency range was calculated, giving an estimate of the coupling coefficient for frequency noise into differential test mass displacement for each test campaign setup. The results are shown in Table 3.3. The coupling is small in the EM and FM test campaigns, and can be considered to be zero in the OSTT campaign.

Campaign	Coefficient [m/rad]		Error [m/rad]
EM	Segment 1:	6.24×10^{-9}	7.23×10^{-10}
	Segment 2:	4.90×10^{-9}	3.77×10^{-10}
FM	4.11×10^{-9}		7.72×10^{-11}
OSTT	2.85×10^{-11}		4.06×10^{-11}

Table 3.3: The values of the coupling coefficient for frequency noise into differential displacement, as calculated from the results of the free-running frequency noise investigations. The data for the EM test campaign contained glitches, and was therefore split into two segments which were analysed separately. All of the values are low, and the value for the OSTT is negligible.

5. The coupling coefficient values in each test campaign were used to calculate the upper limit of the optical pathlength difference between the measurement and reference beams in the x_{12} interferometer. The results are shown in Table 3.4. The associated calculation is explained in Box 3.3.

The coupling coefficient for the frequency noise into the differential displacement measurement in the most representative setup, during the OSTT test campaign, is smaller than the error. The frequency

Campaign	Pathlength mismatch [m]		Error [m]
EM	Segment 1:	27.86×10^{-3}	3.23×10^{-3}
	Segment 2:	22.88×10^{-3}	1.68×10^{-3}
FM	18.35×10^{-3}		3.43×10^{-4}
OSTT	2.07×10^{-4}		2.94×10^{-4}

Table 3.4: The calculated values of the maximum optical pathlength mismatch between the measurement and reference beams of the x_{12} interferometer. The results were calculated from the coupling coefficients shown in Table 3.3 along with the calculations shown in Box 3.3.

noise component of the x_{12} measurement can therefore be considered to be equivalent to zero. It is therefore expected that the contribution of the frequency noise to the differential displacement in-flight will be negligible, although this should be experimentally verified. This was also shown by the x_{12} spectrum for the OSTT measurement in Figure 3.6 almost meeting the allocated noise level for the OMS measurement, even with the frequency noise free-running.

The estimated values for the optical pathlength mismatch in the x_{12} interferometer are reasonable, although perhaps slightly higher than the expected pathlength mismatch for the EM optical bench. No quoted value was found, but an estimate of $\sim 1\,\mathrm{cm}$ is reasonable. The differences between the calculated pathlength mismatches in the EM and FM campaigns where the same optical bench was tested, could be attributed, in part, to the difference in the position of the test mass dummies. The remaining difference was from an unknown source, but these results will be compared to the results from the calculation of the coupling coefficients via injected modulations. The results for the OSTT optical bench, were consistent with the requirement of a pathlength mismatch of $\leq 1 \times 10^{-3}\,\mathrm{m}$.

**Frequency noise component of the differential test mass displacement**

1. The calculated coupling coefficient was multiplied by the Ψ_F data, and the amplitude spectral density of the result plotted with the amplitude spectral density of the x_{12} channel. The

result is a projection of the free-running frequency noise onto the differential displacement. The calculated projections are shown in Figure 3.6.

Note: The amplitude spectral density was calculated using the default Hanning windowing function with $50\,\%$ overlap, 16 averages, and detrending of order one.

Discussion of the high coherence of Ψ_F and x_{12} at high frequencies

The transfer function and coherence plots of the Ψ_F channel into the x_{12} channel for the EM test campaign (see Figure 3.3) show high coherence at frequencies above $1\,\mathrm{Hz}$. Initially, the number of averages in calculating the coherence was changed to check that the effect was not an artifact of the calculation. However, the effect remained. This is not believed to be a result of frequency noise, as the frequency noise transfer function is expected to be flat across the frequency range. It is likely that there is some other noise source coupling into both the Ψ_F and the x_{12} channels. The diagram below shows the frequency noise coupling into the X12 interferometer via the calculated coupling coefficient, K. The unknown noise source, $\widetilde{n}$, couples into both channels and is therefore indistinguishable from frequency noise in the analysis of the free-running frequency noise investigation.
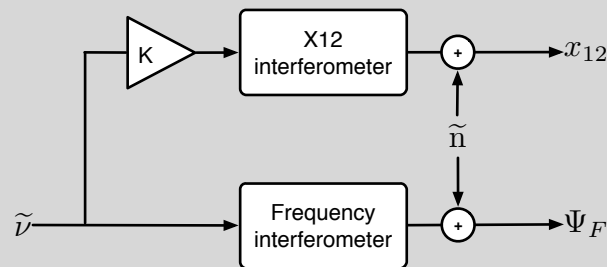
Box 3.2: Comments on the high coherence between the Ψ_F and x_{12} channels at high frequency, as observed during the EM test campaign investigation of the free-running frequency noise.
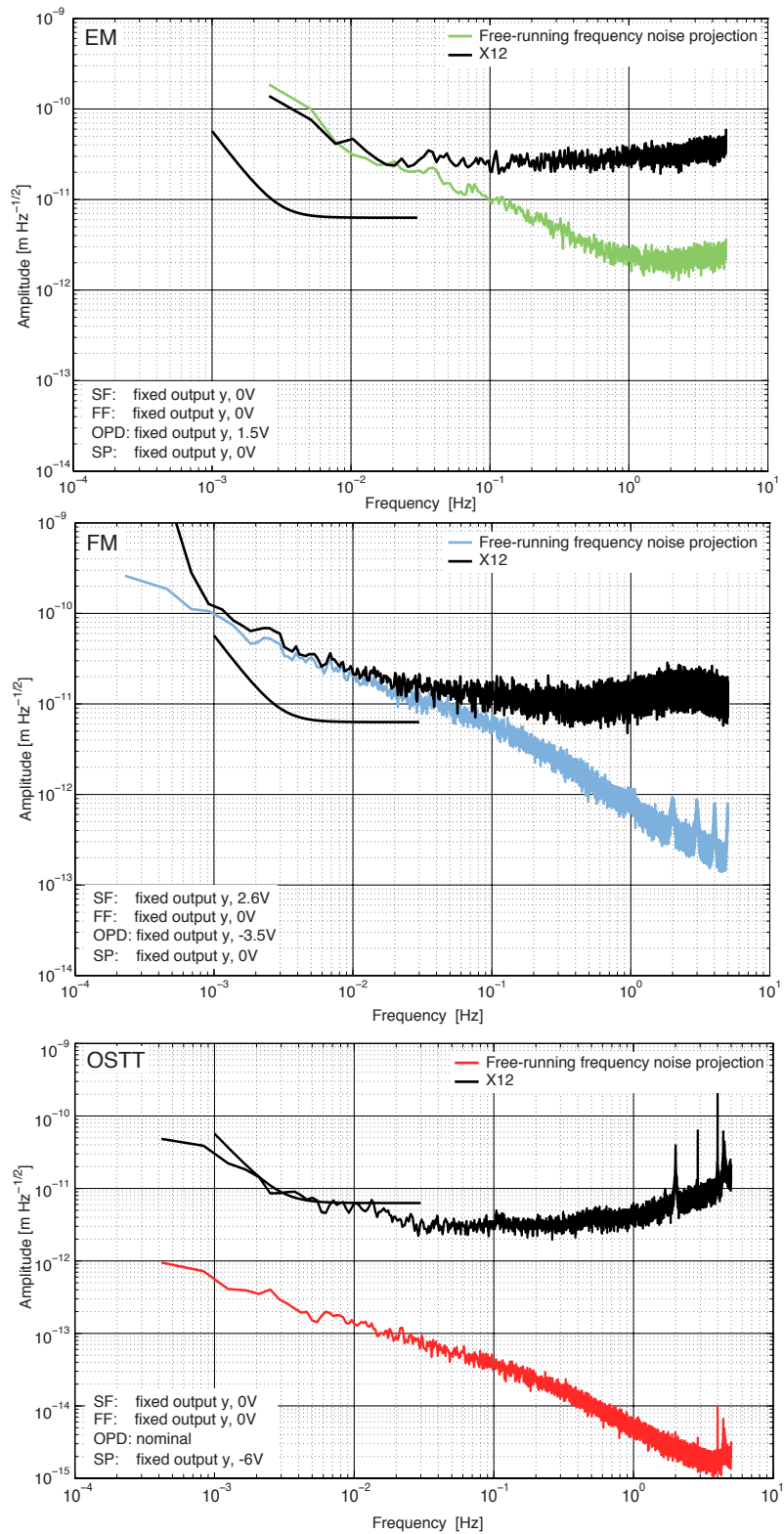
Figure 3.6: Plots of the free-running frequency noise projected onto the x_{12} measurement for the EM (top), FM (middle), and OSTT (bottom), plotted with the allocation for the OMS measurement noise in the measurement bandwidth.

A coupling coefficient for frequency noise into differential displacement, Ψ_F/x_{12}, can be used to calculate an upper estimate of the static optical pathlength difference between the measurement and reference beam of the x_{12} interferometer, ΔL.

The output from the frequency interferometer is:

$$\Psi_F = \frac{0.38 \times 2\pi}{c} \delta\nu \tag{3.4}$$

The output from the x_{12} interferometer is:

$$x_{12} = \frac{\lambda\Delta\text{L}}{2c\cos\alpha} \delta\nu \tag{3.5}$$

Therefore,

$$\begin{aligned} \frac{x_{12}}{\Psi_F} &= \frac{\lambda}{0.38 \times 4\pi\cos\alpha}\Delta\text{L} \tag{3.6} \\ &= 2.24 \times 10^{-7}\Delta\text{L} \tag{3.7} \end{aligned}$$

The percentage error on ΔL is equivalent to the percentage error on the coupling coefficient, x_{12}/Ψ_F.

Each coupling coefficient also has a phase component which determines the sign of the coefficient and the sign of the calculated value of ΔL. This could be used to determine whether the reference beam or the measurement beam is longer in the X12 interferometer. However, this would require knowledge of which beam on the optical bench is longer. A good example of the phase difference between the same injected signal seen in the Ψ_F and x_{12} channels can be seen in the plots below. They show the timeseries of an injected frequency modulation as seen in the Ψ_F and x_{12} channels, for the EM and FM test campaign investigations to calculate the OLTF.
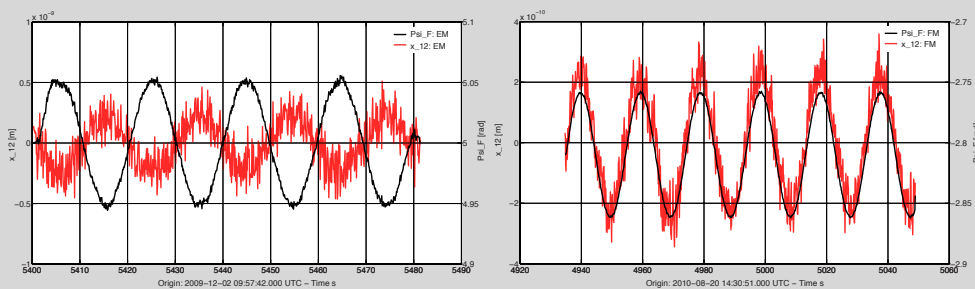
Box 3.3: Determination of an upper limit for the static optical pathlength mismatch between the measurement and reference beams in the X12 interferometer.

123

3.1.2 In-flight investigation

The in-flight measurement of the free-running frequency noise is relatively uncomplicated, and the associated procedure is shown in Figure 3.7. Test mass one is maintained in a drag-free condition and test mass two follows test mass one by electrostatic suspension via DFACS mode 1.2. Both the fast and slow frequency control loops are open, i.e., not providing a feedback signal, while the other control loops operate in the nominal state. The measurement is run for 10 hours. This measurement length was selected in order to ensure that a segment of at least 10000 s was available for analysis, taking into account that there may be glitches in the data. An overview of the experimental setup required, as well as the necessary telemetry, is given in Table 3.5.

An overview of the procedure for the analysis of the investigation is given in Figure 3.8. The analysis comprises several sub-analyses, each indicated by a specific colour. They are:

- Data preparation, indicated in grey, and described in detail in Figure 3.9.

- Determination of the free-running frequency noise level, indicated in red, and detailed in Figure 3.10a.

- Calculation of a coupling coefficient for frequency noise into differential test mass displacement, indicated in blue, and detailed in Figure 3.10b.

- Use of the coupling coefficient to determine the maximum optical pathlength mismatch of the X12 interferometer arms, indicated in green, and detailed in Figure 3.11a.

- Use of the calculated coupling coefficient to determine a projection of the frequency noise component of the x_{12} measurement, indicated in yellow, and detailed in Figure 3.11b.

Where an input is required from a previous analysis, it is indicated in the colour of the original analysis. The procedures were created considering the LTPDA toolbox methods, and some suggestions for setting parameter values for some steps have been given. The code for performing each step has not been provided, as the LTPDA tool-

box evolves over time. The latest version of the handbook should be consulted for the exact implementation of specific methods.

Investigation	Free-running frequency noise		
OMS state	TMs drag-free		
Loop states	SF	Fixed output y	
	FF	Fixed output y	
	OPD	Nominal	
	SP	Nominal	
	FP	Nominal	
Telemetry required	128,3	x_{12}	LST10130
		Ψ_F	LST12406
	128,4	SF feedback	LST17345
		FF feedback	LST17340
		OPD feedback	LST17350
		SP feedback	LST17357
	3,25	SF state	LST17364
		FF state	LST17361
		OPD state	LST17367
		FP state	LST17358
		SSC	SCT70388
Length	10 hours		

Table 3.5: An overview of the key information relating to the experiment for measuring the free-running frequency noise. For the telemetry names associated with each parameter refer to Appendix 7.
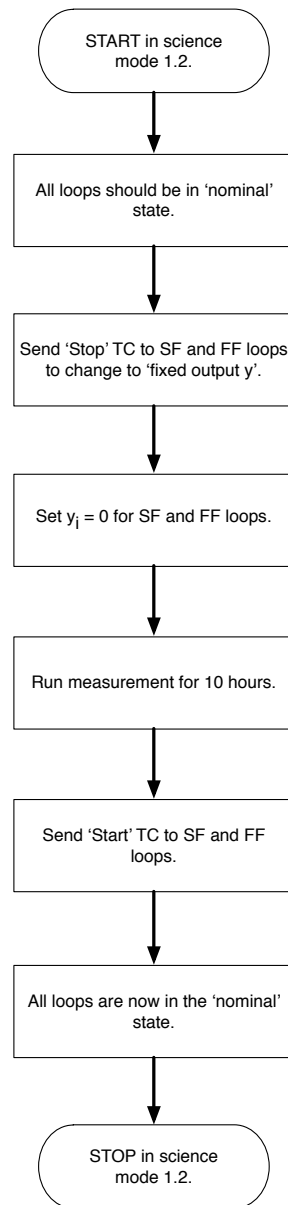
Figure 3.7: The procedure for performing the free-running frequency noise experiment in-flight.
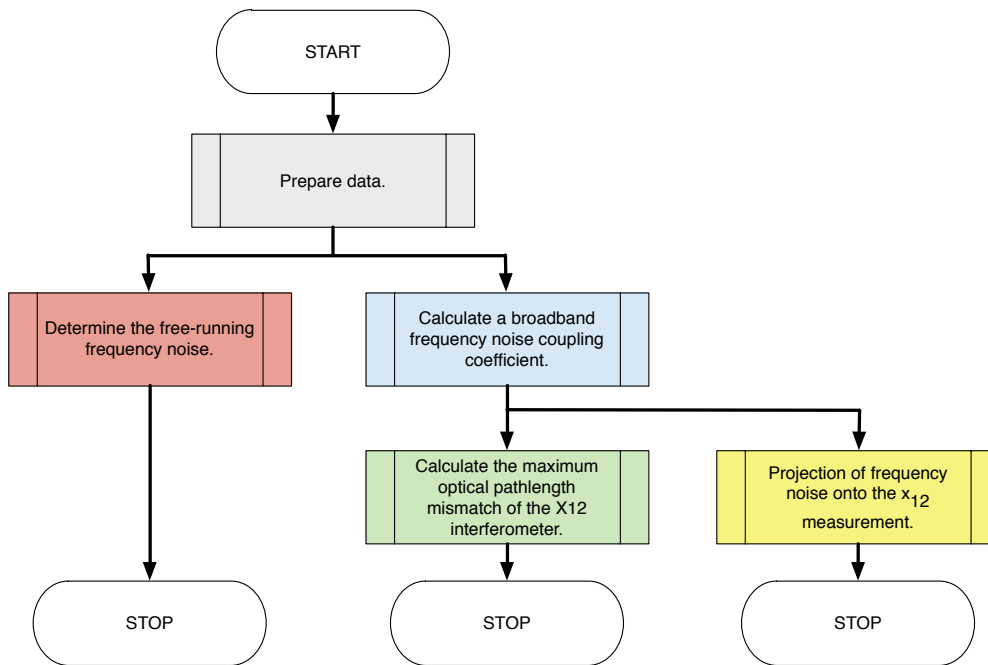
Figure 3.8: An overview of the suggested in-flight analysis procedure for the free-running frequency noise investigation. The analysis comprises several stages, which are identified by a particular colour. The analysis procedure for each of these sub-analyses is indicated in its own flow diagram.
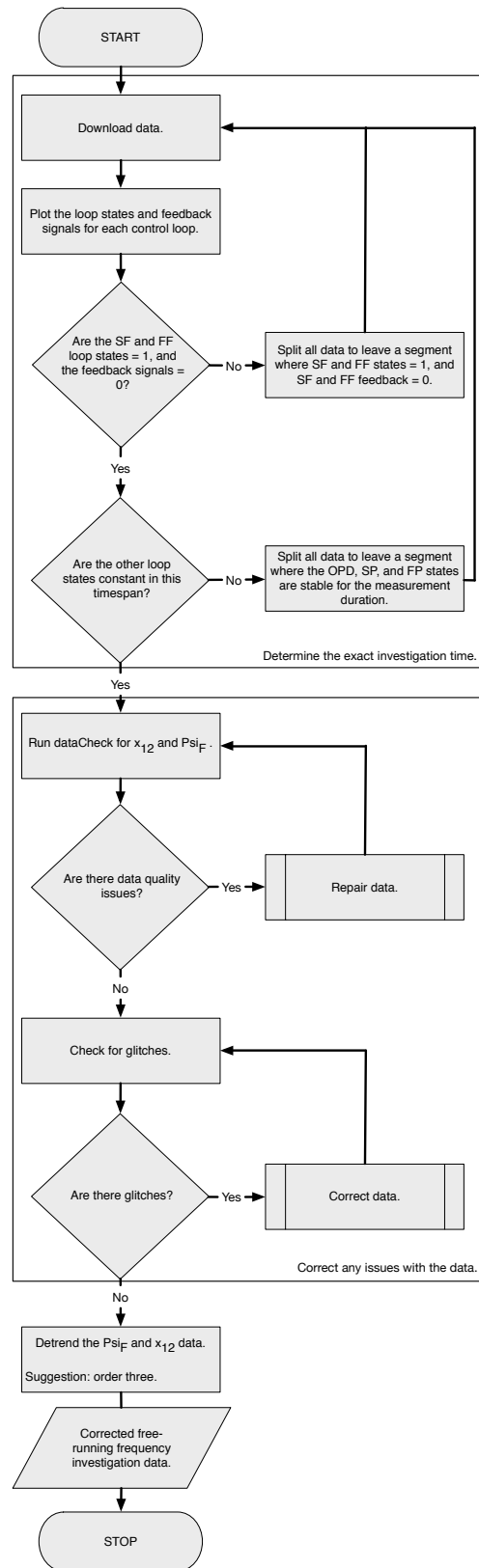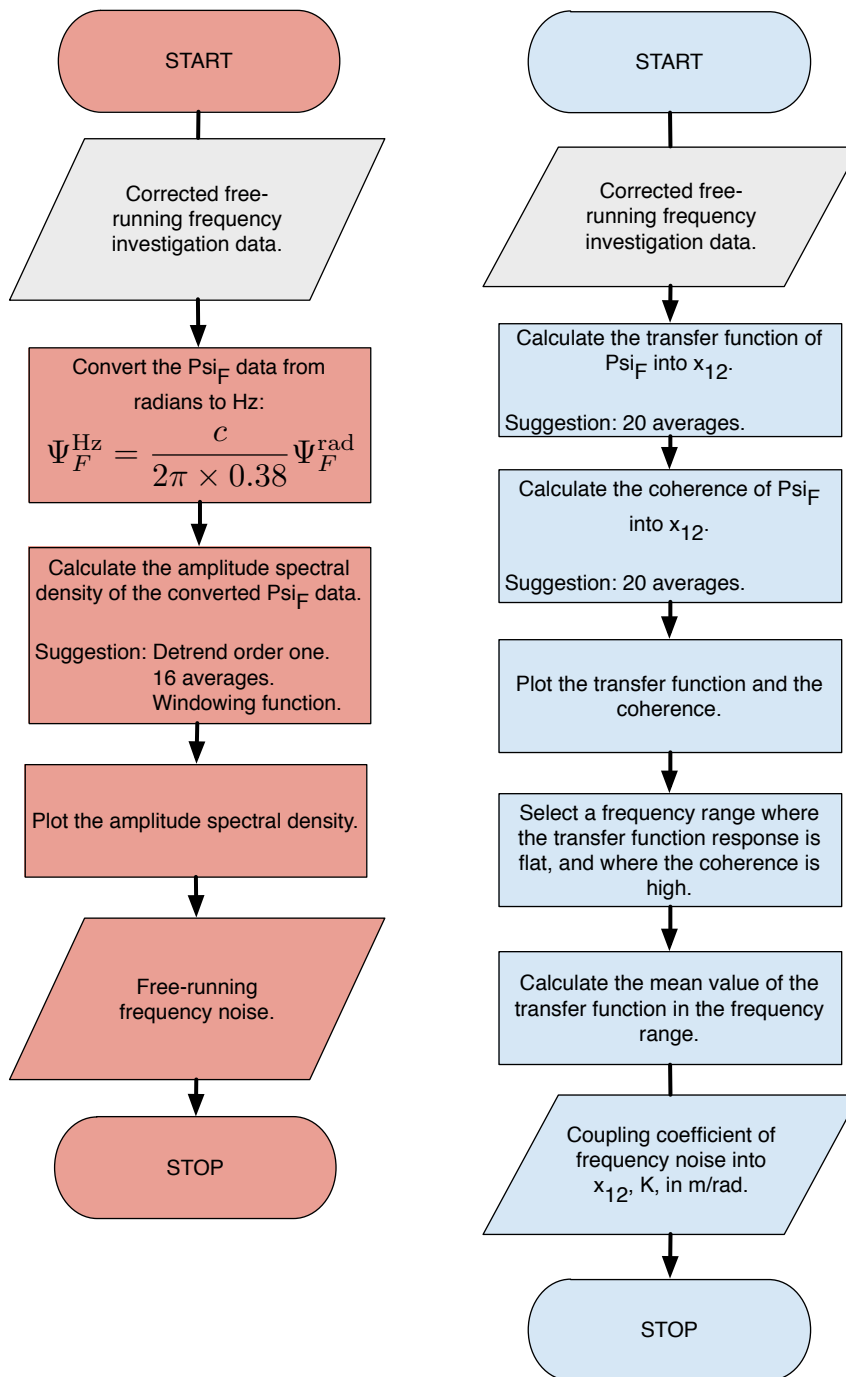
3 Frequency noise characterisation

Figure 3.9: An overview of the data preparation step of the free-running frequency noise analysis procedure.

(a) An overview of the free-running frequency noise analysis procedure.

(b) An overview of the procedure for calculating the coupling coefficient of frequency noise into differential test mass displacement.

Figure 3.10

129
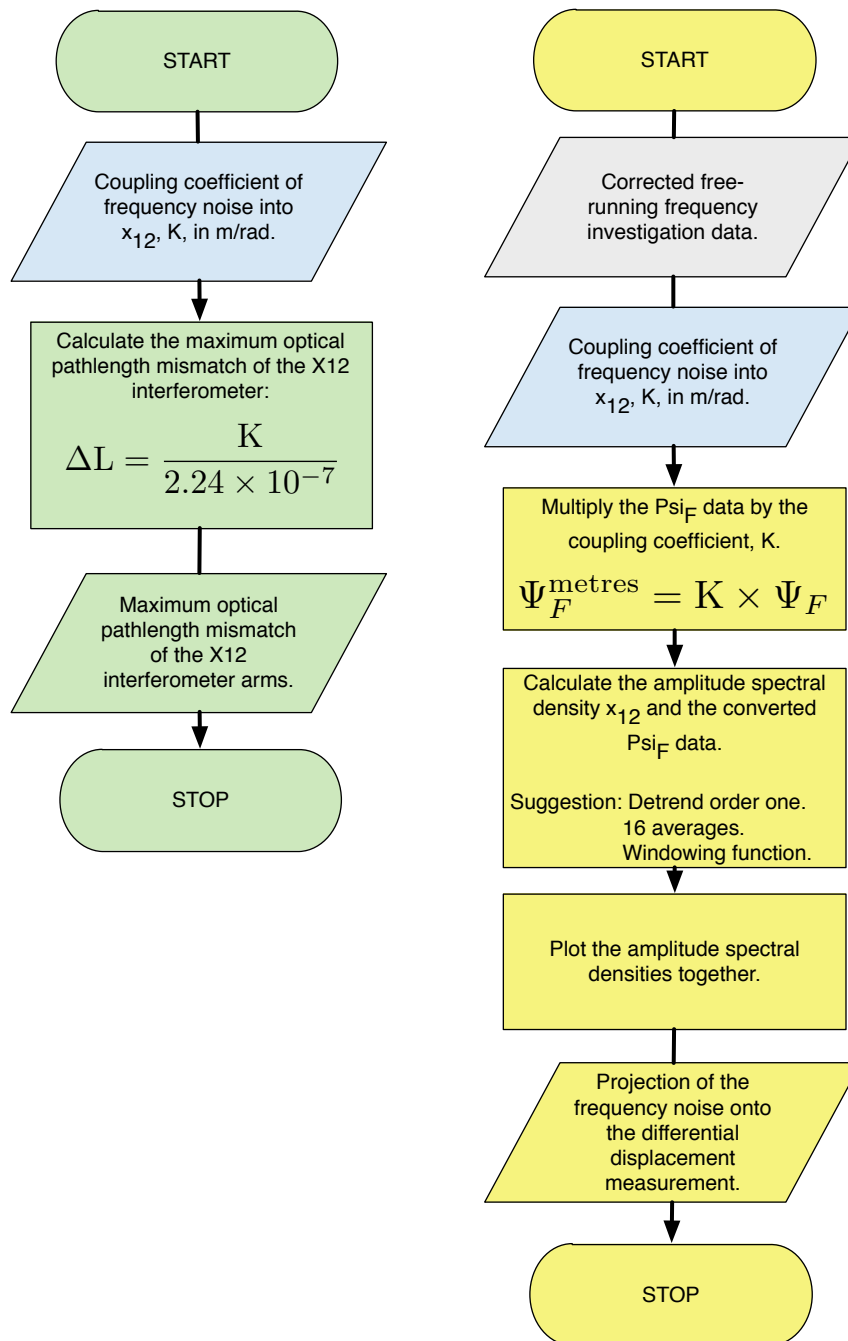
(a) An overview of the procedure for the determining the maximum optical pathlength mismatch of the x_{12} interferometer from the results of the free-running frequency noise analysis.

(b) An overview of the procedure for the projection of the frequency noise component onto the differential displacement measurement.

Figure 3.11

3.2 Control loop characterisation

The in-flight characterisation of the frequency control loop is necessary for several reasons:

- to ensure the loop is functioning as expected;

- to determine whether the response of the control loop needs to be redefined via the fast and slow controller coefficients, a and b.

Original plans for in-flight control loop characterisation involved several individual investigations [58] [59]. They included the calibration of both the fast and the slow frequency actuators, as well as a separate investigation to determine the OLTF. This section describes a single investigation that can be performed to encompass the full loop characterisation[1].

Such an investigation requires known modulation signals to be input into the fast frequency control loop via the δx^{FF} input, while the slow control loop is operating under nominal conditions. The advantage of implementing a single experiment is that more input modulations, at a larger number of frequencies, can be applied in a shorter time period than applying fewer modulations in each of several investigations. This will also improve the accuracy with which the various characteristics of the loop are determined. The investigation can be separated into the following components:

- fast controller characterisation;

- slow controller characterisation;

- fast and slow loop actuator calibration;

- determination of the OLTF and noise suppression function;

---

[1] A single investigation is only possible when the essential telemetry required for downlink to ground is within the limits imposed by the telemetry packets. This depends upon the number of channels required and the sampling frequency of the data. The proposed investigation meets these requirements, but this should be taken into account if the investigation is modified.

and the additional result:

- calculation of a coupling coefficient for frequency noise into the differential displacement via injected modulations.

Each of these analyses is based on determining the transfer function between different combinations of available loop parameters. Two methods were used to determine the transfer functions when analysing the results of the ground-based test campaigns. The first being the calculation of the transfer function between time-series data. The second method involved splitting the data into sections containing a modulation at a single frequency. A Discrete Fourier transform (DFT) at the modulation frequency was determined, and the ratio of the required channels gave the equivalent transfer function at that particular frequency.

The motivation for performing each of the above listed characterisations are described in the following subsections. The relevant results of the ground-based hardware test campaigns are then presented, followed by a description of the procedures for performing and analysing the in-flight investigation.

Fast controller characterisation

The analysis of the fast frequency controller response should provide confirmation that the digital control law implemented in the DMU software matches the ground-based model. The controller response is defined by the a and b coefficients, as described in Section 2.3. The coefficients are defined by values in the SDP, but can be changed if necessary via telecommand. Along with the slow controller coefficients, they are the only means of changing the response of the control loop in-flight.
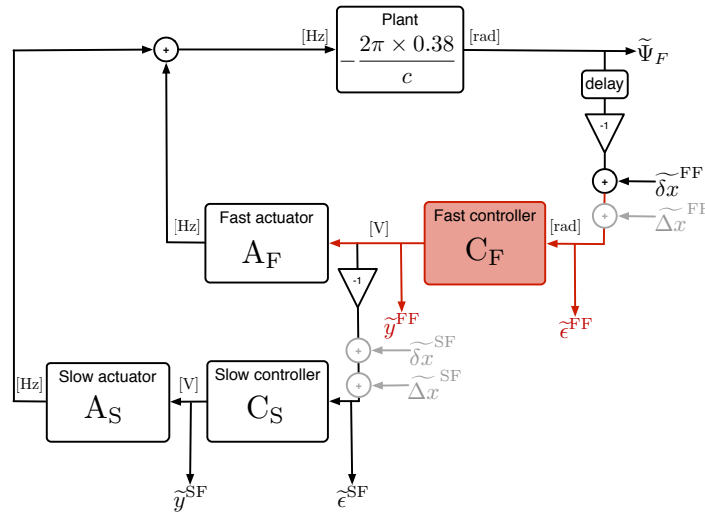
Figure 3.12: A simplified block diagram of the frequency control loop with the components and signals of interest for the fast controller characterisation highlighted in red. The loop components are labelled in terms of the associated Laplace transform.

Both the fast frequency error signal, ϵ^{FF}, and the fast frequency feedback signal, y^{FF}, of the fast frequency control loop are available via the telemetry. It is therefore possible to characterise the steady-state controller response according to:

$$\mathrm{C_F}(f) = \frac{\widetilde{y}^{\mathrm{FF}}}{\widetilde{\epsilon}^{\mathrm{FF}}} \tag{3.8}$$

where the tilde represents the FT of the signal. The result can be compared to a model defined by the a and b values expected to have been implemented in the controller (see Box 2.3), along with some delay. This should provide confirmation that the expected controller coefficients have been implemented. If the model and the result do not match, then fitting the model to the results would allow the actual loop coefficients to be determined.

Slow controller characterisation

In the same way as for the fast frequency controller, the slow frequency controller characteristics are defined by the a and b coefficients of the digital control law given in Section 2.3.
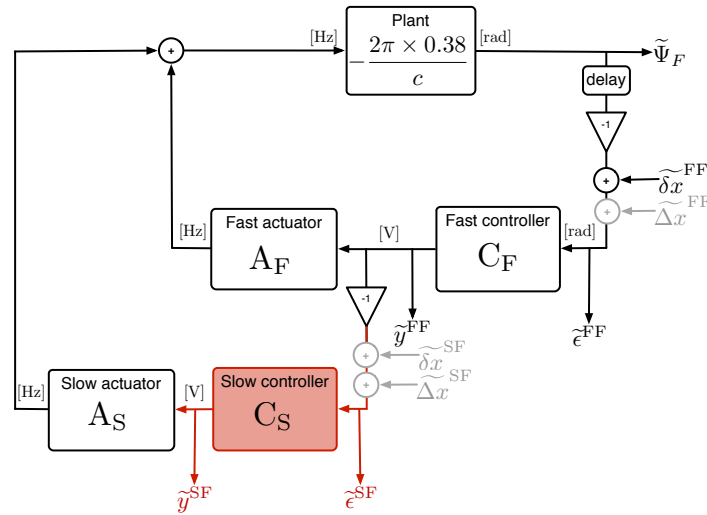
Figure 3.13: A simplified block diagram of the frequency control loop with the components and signals of interest for the slow controller characterisation highlighted in red. The loop components are labelled in terms of the associated Laplace transform.

The steady-state response of the slow loop controller can be determined in-flight via the slow loop error and feedback signals, ϵ^{SF} and y^{SF}, according to:

$$\mathrm{C_S}(f) = \frac{\widetilde{y}^{\mathrm{SF}}}{\widetilde{\epsilon}^{\mathrm{SF}}} \tag{3.9}$$

where the tilde represents the FT of the signal.

A check that the controller coefficients have been applied as expected is made by comparing the result to a model based on the design coefficients (see Box 2.3) along with some delay. If the model and the result do not correspond, then fitting the model to the results would allow the actual loop coefficients to be determined.

Fast and slow actuator calibration

It is necessary to calculate the response of the fast and slow frequency loop actuators to ensure that they are functioning as required. Particularly important is the gain of each actuator. If the gain is different to the actuator design, e.g., if an actuator is damaged in some way, the loop will no longer function to suppress the frequency noise as required. This would require that the a and b coefficients of the digital

filter that defines the response of the fast and slow controllers to be redefined to compensate accordingly.
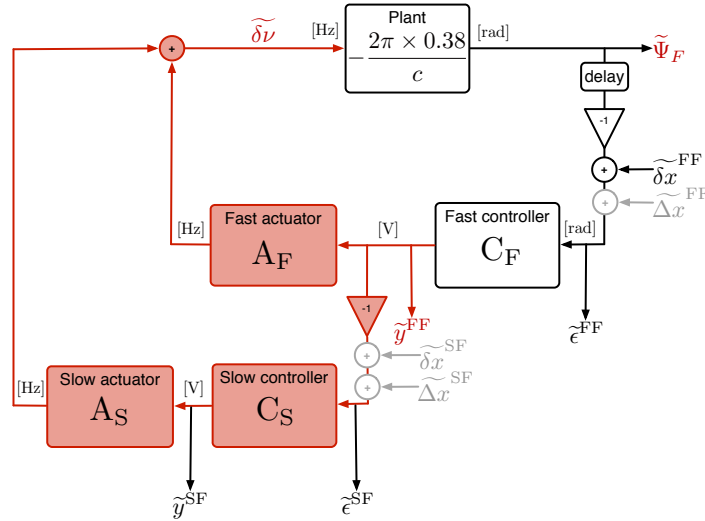

Figure 3.14: A simplified block diagram of the frequency control loop with the components and signals of interest for the characterisation of the fast and slow frequency actuators highlighted in red. Each loop component is represented by the associated Laplace transform.

When both the fast and slow frequency control loops are operating, the frequency of the laser is simultaneously controlled by both the fast and slow actuators. The change in the frequency, referred to here as the frequency fluctuation, can be observed via the output from the frequency interferometer, Ψ_F. This frequency fluctuation, $\delta\nu$, is not an available loop output, but can be calculated using the known relationship between Ψ_F and $\delta\nu$:

$$\delta\nu = -\frac{c}{2\pi\Delta\text{L}}\Psi_F \tag{3.10}$$

where $\Delta\text{L} = 38\,\text{cm}$. This can be rewritten to define a constant for conversion from Ψ_F, measured in rads, into $\delta\nu$, measured in Hz:

$$\frac{\delta\nu}{\Psi_F} = -125.64 \times 10^6 \frac{\text{Hz}}{\text{rad}} \tag{3.11}$$

The frequency fluctuation contains contributions at low frequencies from the slow frequency control loop, and from the fast frequency control loop at high frequencies, such that the combined steady-state response is:

$$(\text{A}_\text{F}(f) - \text{C}_\text{S}(f)\text{A}_\text{S}(f)) = \frac{\widetilde{\delta\nu}}{\widetilde{y}^{\text{FF}}} \tag{3.12}$$

135

where the tilde represents the FT of the signal. This is the definition of the transfer function between $\delta\nu$ and y^{FF}. By fitting a model, M, based on the known frequency control loop design (see description in Box 2.3) to this transfer function the gain of the slow and the fast actuators, G_{F} and G_{S}, in Hz/V, can be determined, as well as any delay, τ, that occurs due to the actuators and the slow controller:

$$M(s, G, \tau) = \text{A}_{\text{F}}(s, G_{\text{F}}, \tau) - \text{A}_{\text{S}}(s, G_{\text{S}}, \tau) \qquad (3.13)$$

Open loop transfer function and noise suppression

The calculation of the OLTF of the frequency control loop is necessary in order to:

- determine if the loop is able to suppress the frequency noise to the meet the specified allocation, i.e., whether the loop has enough gain. The allocation for the frequency noise is $112 \times 10^3 \, \text{Hz}/\sqrt{\text{Hz}}$ at $30 \, \text{mHz}$ (see Section 2.2.1). The required gain will depend upon the level of the free-running frequency noise, as measured by the investigation described in Section 3.1. The gain requirements based on the results of the ground-based hardware test campaigns are shown in Table 3.2;

- determine whether the loop is stable, i.e., whether the phase and gain margin of the loop are sufficiently large.

If the OLTF of the loop is shown not to meet the required gain and/or stability requirements, then it would be necessary to redefine the digital control law coefficients of the fast and slow controllers.
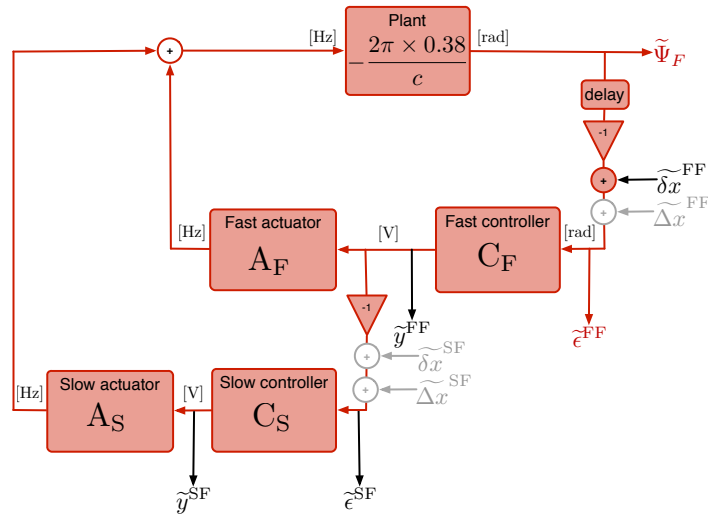
Figure 3.15: A simplified block diagram showing the frequency control loop with the components and signals of interest in the open-loop transfer function investigation. Each loop component is represented by the associated Laplace transform.

The steady-state OLTF of the frequency control loop can be calculated from the available telemetry according to:

$$
\begin{aligned}
\text{OLTF}(f) &= \text{C}_\text{F}(f).\text{X}_\text{F}(f)(\text{A}_\text{F}(f) + \text{A}_\text{F}(f).\text{C}_\text{S}(f)) \quad (3.14) \\
&= \frac{\widetilde{\Psi}_F}{\widetilde{\epsilon}^{\text{FF}}} \quad (3.15)
\end{aligned}
$$

where the tilde represents the FT of the signal.

A Bode plot of the OLTF will allow the key characteristics of the control loop to be determined:

- **Loop gain**: The amplitude of the OLTF Bode plot determines the gain of the control loop.

- **Phase and gain margin**: The amount of phase between the phase at the unity gain frequency and $-180°$ defines the phase margin. The gain margin is the difference in amplitude between unity and the frequency at which the phase reaches $-180°$.

- **Loop delay**: The delay of the whole loop can be determined from the phase of the Bode plot of the OLTF.

An additional measure of the amount of suppression achieved by the control loop is from a bode plot of the noise suppression function, S,

defined by:

$$S = \frac{1}{1 + \text{OLTF}} \qquad (3.16)$$

The amplitude of the corresponding Bode plot gives the amount of suppression achieved by the loop at a particular frequency.

Coupling of frequency noise via an applied modulation

Any differences in the optical pathlengths of the beams in the x_{12} interferometer will result in frequency noise, measured via the Ψ_F channel, coupling into the measurement of the differential displacement (see Section 2.2.1).
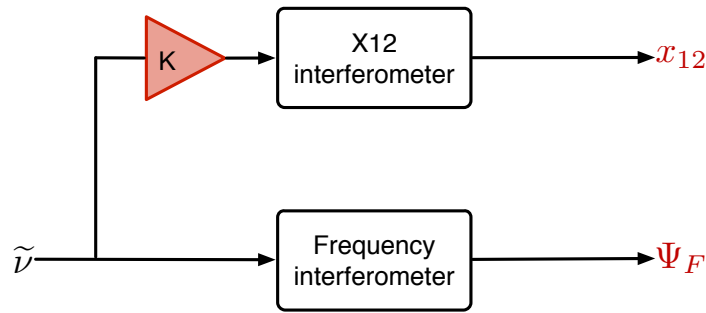

Figure 3.16: A simplified block diagram showing the coupling of the frequency noise, $\widetilde{\nu}$, measured by the frequency interferometer via Ψ_F, into the x_{12} measurement via a coupling coefficient, K.

An investigation where modulations are input into the frequency control loop provides the means to determine a coupling coefficient. As the frequency is modulated with a larger amplitude than the level of the free-running noise, the calculated coupling coefficient should be both easier to determine, and more accurate than the value found as a result of the free-running frequency investigation described in Section 3.1.

The coupling coefficient, K, in units of m/rad, is defined according to:

$$\text{K} = \frac{\widetilde{x}_{12}}{\widetilde{\Psi}_F} \qquad (3.17)$$

where the tilde represents the FT of the signal.

This coefficient can be used to project the frequency noise component onto the differential test mass displacement measurement, as described in Sections 3.1, and 3.3.

Additionally, the coupling coefficient can be used to calculate an upper limit for the optical pathlength difference between the measurement and reference beams in the x_{12} interferometer. The calculation is explained in detail in Box 3.3.

3.2.1 Test campaign results

During the EM and FM test campaigns specific investigations to calculate the response of the fast actuator were performed using a single injected triangular waveform [32] [43]. No such investigation was performed during the OSTT test campaign. As these investigations are not representative of the planned in-flight investigation, the analysis of the results are not presented in this document. No specific investigation of the response of the slow actuators, or the fast and slow controllers was performed. However, modulations were input into the fast frequency control loop via the δx^{FF} input during the OLTF investigation in the EM and FM test campaigns. No equivalent investigation was performed during the OSTT test campaign. It is possible to use the results of these investigations to determine the response of the fast and slow loop controllers and actuators, in addition to the OLTF and noise suppression function, and a coupling coefficient for frequency noise into differential test mass displacement.

The following sections describe the analysis of the results of the EM and FM test campaigns. Initially all channels were pre-processed in the same manner. Subsequently, the two methods for determining the transfer function between the particular combination of parameters, the transfer function method and the DFT method, were applied.

The data pre-processing and an overview of the two analysis methods are described in the 'Overview of the analysis' subsection below. The analyses and results of each individual characterisation are then more completely described in the associated sections.

3 Frequency noise characterisation

Overview of the analysis

The telemetry used in the following analyses is given in Table 3.6 and the equivalent names used in the LTPDA data repositories can be found in Appendix 7.

The processing of the data from both the EM and FM OLTF investigations was performed as follows:

1. The data, as defined in Table 3.6, was downloaded according to the dates and times defined in the EM and FM test reports [32] [43]. The related information can be found in Appendix 8, Tables 8.4 and 8.6.

2. The loop states and feedback signals were checked to ensure that the loops were in the expected states:

    - Fast frequency: switching between 'nominal' and 'testing offset Δx' or 'variable output y' (state 3, and states 4 or 2);

    - Slow frequency: 'nominal' (state 3);

    - OPD and slow power: either 'nominal' or 'fixed output y', with a constant feedback signal, and remaining in that state for the duration of the investigation (states 3 or 1).

    As an example, the associated plots for the EM analysis are shown in Appendix 8, Figure 8.5.

3. The timeseries of each channel, with the exception of the loop states, was detrended with order three to subtract any DC offsets, and linear, quadratic, or cubic drifts. The timeseries of the original and detrended data are given in Appendix 8 as a reference for the expected timeseries from an equivalent in-flight investigation.

    Note: The Ψ_F data required in the analysis of the fast and slow actuator response was processed to determine the applied frequency fluctuation before detrending. This is described in more detail under the associated heading.

Parameter	Description	Frequency [Hz]	ID
S^{FF}	Fast freq. loop state	1 Hz	LST17361
S^{SF}	Slow freq. loop state	1 Hz	LST17364
S^{OPD}	OPD loop state	1 Hz	LST17367
S^{SP}	Slow power loop state	1 Hz	LST17358
y^{FF}	Fast freq. loop feedback	1 Hz	LST17340
		10 Hz	
		100 Hz	LST18338
y^{SF}	Slow freq. loop feedback	1 Hz	LST17345
		10 Hz	
		100 Hz	LST18345
y^{OPD}	OPD loop feedback	1 Hz	LST17350
		10 Hz	
y^{SP}	Slow power loop feedback	1 Hz	LST17357
		10 Hz	
δx^{FF}	Input modulation	10 Hz	LST17338
		100 Hz	
ϵ^{FF}	Fast frequency error	1 Hz	LST17339
		10 Hz	
		100 Hz	LST18339
ϵ^{SF}	Slow frequency error	1 Hz	LST17344
		10 Hz	
		100 Hz	LS18344
Ψ_F	Freq. ifo. output	10 Hz	LST12406
		100 Hz	LST18645
x_{12}	X12 ifo. output	10 Hz	LST10130
		100 Hz	LST15644
SSC	Source sequence counter	10 Hz	SCT70388

Table 3.6: The telemetry parameters used in the analyses of the EM and FM test campaign frequency control loop characterisation investigations.

141

3 Frequency noise characterisation

From this point in each analysis, two methods were used to determine the required output:

- **Transfer function method**: Only the 10 Hz and 1 Hz data was suitable for determining the transfer function. The 100 Hz data from the IDL was unsuitable as it contained gaps between each modulation.

  1. The 10 Hz data contained gaps where the frequencies above 1 Hz were applied and recorded via the IDL. The data was split to leave a time period where there were no large gaps. The times of the split are given in Appendix 8, Tables 8.5 and 8.7 for the EM and FM analyses respectively.

     Note: In the EM test campaign, some modulations were incorrectly applied, so the waveforms in all channels were distorted. This affected the calculation of the transfer functions and coherences, and so the split times for the 10 Hz data in the EM campaign also removed these modulations.

  2. The 1 Hz data had no gaps between modulations, but the sampling frequency was too low to accurately sample the high frequency modulations[1]. An example of this, using the fast frequency feedback signal from the EM campaign, is shown in Figure 3.17 alongside the applied δx^{FF} modulation signal. The timeseries were split to remove data where aliasing was apparent.

  3. The transfer function of the required channels was calculated with 20 averages and using the Hanning windowing function with 50 % overlap. The results for each analysis are given under the respective heading.

  4. The coherence was also calculated for both the 1 Hz and the 10 Hz data, using 20 averages, to show the frequency regions where the transfer functions are most representative.

---

[1]The 1 Hz data from the test campaigns is unfiltered housekeeping data. In-flight, this data should be filtered, such that there will not be an issue with aliasing.

- **DFT method**

    1. Although some information regarding the start and stop times of the modulations was available from the test campaign reports, it was necessary to determine the times at which the modulations started and stopped by hand. The times were initially ascertained from the δx^{FF} channel, at both $10\,\mathrm{Hz}$ and $100\,\mathrm{Hz}$, which shows the applied modulation signal.

    2. All channels were split according to the determined start and stop times to produce segments, each containing a modulation at a single frequency.

        Note: In the EM and FM test campaigns some modulations were incorrectly applied in the first instance, and were applied repeatedly until correct. The issues with the applied modulation can be seen visually in the loop signals. The incorrectly applied modulations were not used in the analysis.

    3. The modulation segments for each channel were plotted.

    4. The segment was checked to ensure that it contained only the modulation, without any large jumps or transients. Due to response of the loop, the modulation can appear at slightly different times, and with some transient effects, in each channel. The effect of transients and non-modulation signals on the DFT calculations was an increased error on the calculated result.

    5. The channels were split again based on the shortest time segments determined from the previous step.

        Note: The channels could also be split using times specific to each channel. For ease, the times were selected such that they removed transients in all channels. The difference in the times in each channel is small, so using this method is not removing a significant amount of information.

    6. A Fast Fourier transform (FFT) was performed on each segment of the δx^{FF} input modulation to determine the fre-

143

quency of the applied modulation. The peak of the result gave an estimate of the frequency, which could be checked against the known applied frequencies from the test campaign reports, to determine the modulation frequency of each segment [32] [43].

7. To check that the frequency was correct, each timeseries segment of δx^{FF} was heterodyned with a sinusoid at the calculated frequency. This is described in Box 3.4.

8. A DFT was performed on each segment at the determined modulation frequency.

9. The ratios of the DFTs of the required channels for each applied modulation were then calculated for each analysis, as described under the following headings.

Note: Further steps were taken in the analysis of the coupling of frequency noise into differential displacement. They are described in more detail under the associated heading.
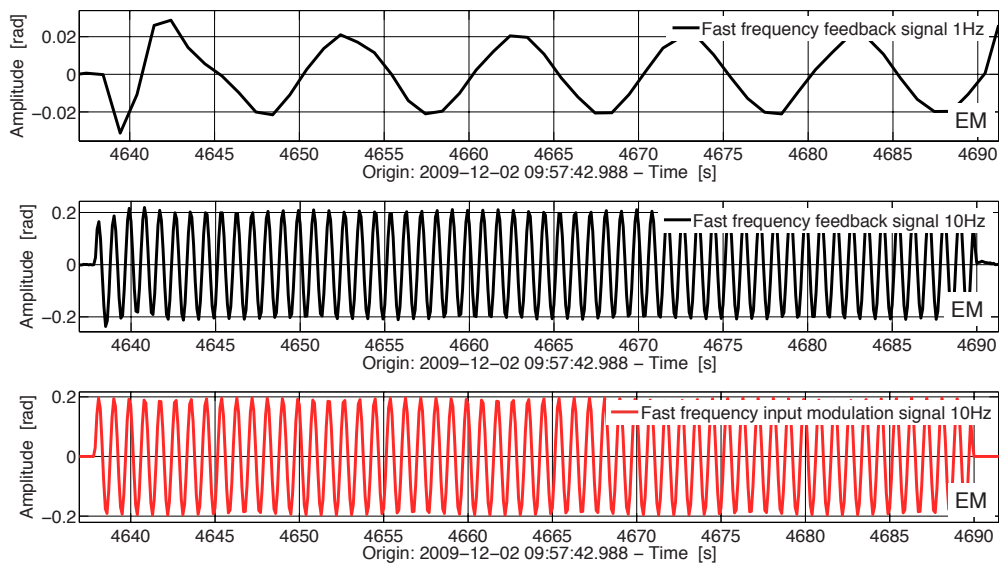
Figure 3.17: An example, from the analysis of the EM OLTF investigation, showing the aliasing of high frequency signals in the 1 Hz channels. In this example the 1 Hz feedback signal from the fast frequency loop is shown alongside the same signal at 10 Hz and the applied modulation at 10 Hz.

Fast controller characterisation

The split timeseries plots of the 10 Hz data for the y^{FF} and ϵ^{FF} channels are shown in Appendix 8, Figures 8.6 and 8.10, for the EM and FM test campaigns respectively.

The transfer function of the EM test campaign fast feedback and the fast error signals were calculated using both the split 1 Hz and 10 Hz timeseries data. The ratio of the DFTs for each modulation split from the 10 Hz and 100 Hz data were also calculated. A model, based on the known digital filter coefficients shown in Table 3.7, was also calculated. The results are shown in Figure 3.18.

	EM	FM
a	-1.58	-1.58
b0	1	1
b1[1]	-1.0	-1.0

Table 3.7: The documented fast frequency controller coefficients used in the EM and FM test campaigns [32] [43].

No 1 Hz data for the error and feedback signals was available for the FM test campaign, so the transfer function and coherence was calculated using only the split 10 Hz channels. In the same manner as for the EM campaign, the DFT ratios and a controller model were calculated. The results are shown in Figure 3.19.

The results from the transfer functions and the DFT results in both the EM and FM test campaigns correspond within errors. In both campaigns the models corresponded to the results of the DFT measurements, so there was no need to fit the model to determine the a and b coefficients.

---

[1] The value of the b1 coefficient is 1.0 in the parameter definition files. However, in the test campaign reports it was noted that it was necessary to invert the coefficient and so the inverted value was used to make the model. It is important that this observation is carried forward to the planning of in-flight operations.
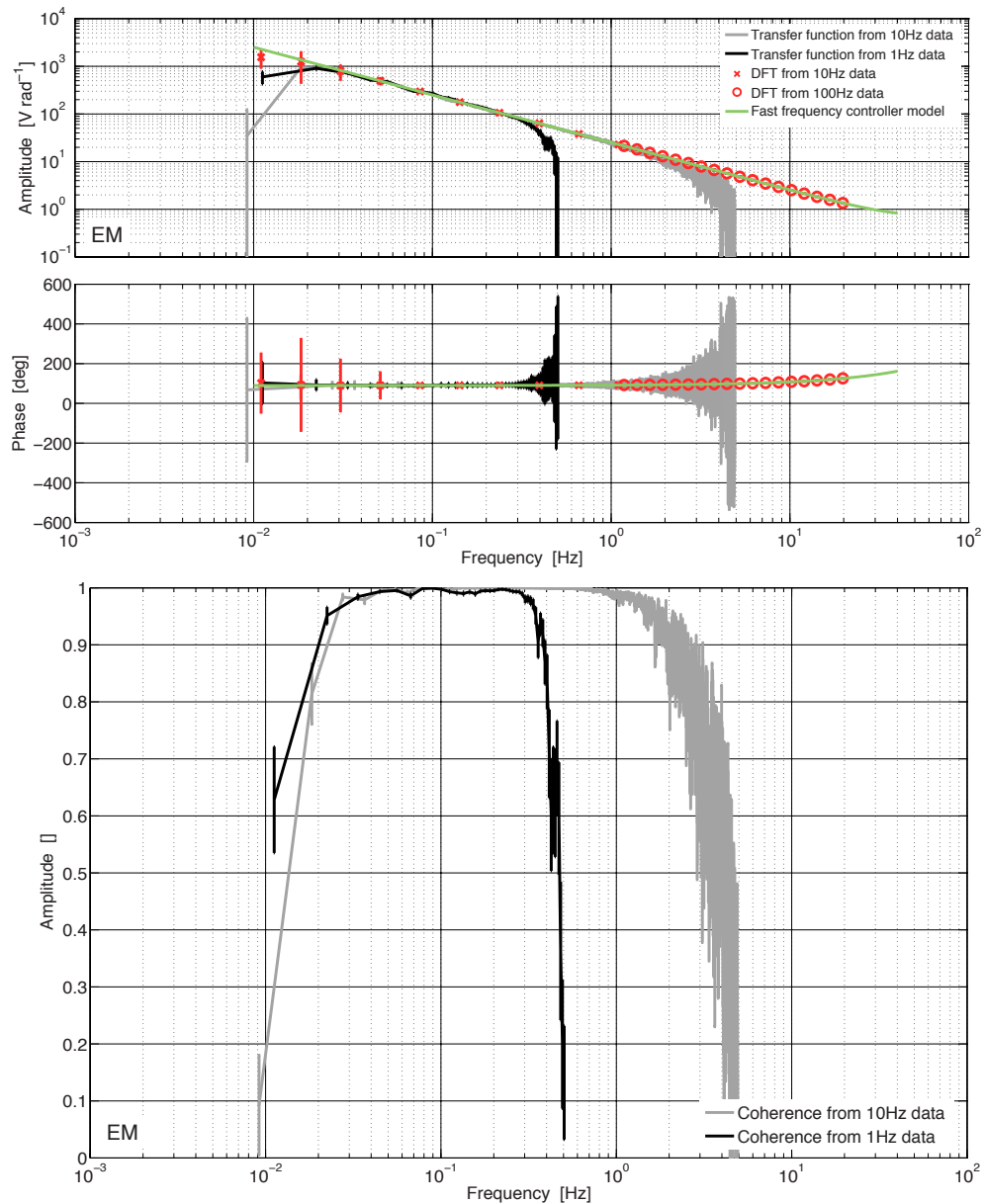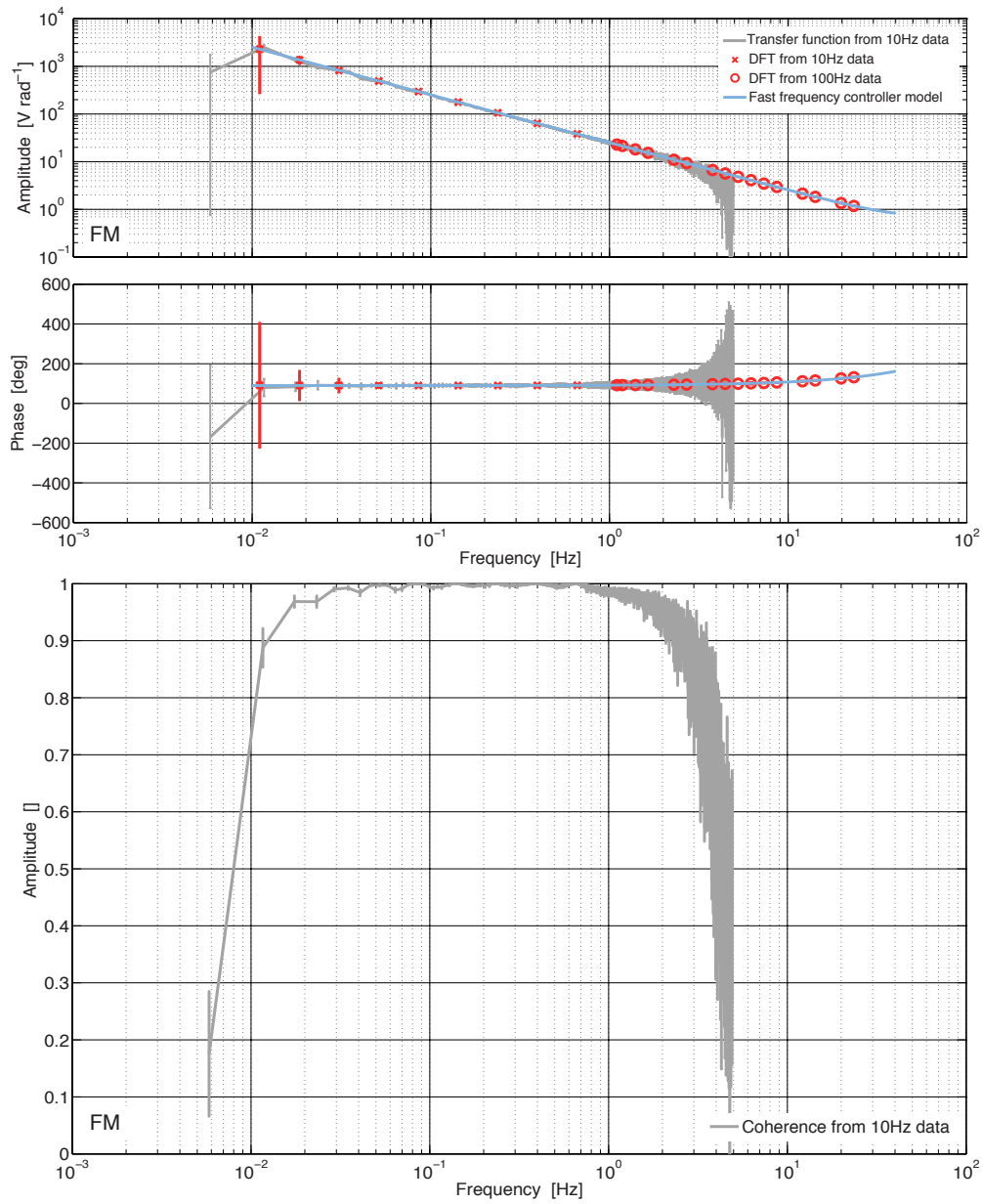
Figure 3.18: The calculated fast frequency controller response for the EM test campaign. The transfer functions calculated from the 1 Hz and 10 Hz detrended timeseries are shown in gray and black, along with the corresponding coherences. The results from the DFT ratios from the 10 Hz and 100 Hz data are shown in red. A model of the controller based on the applied loop coefficients is shown in green.

Figure 3.19: The calculated fast frequency controller response for the FM test campaign. The transfer functions calculated from the 10 Hz detrended timeseries is shown in gray, along with the corresponding coherence. The results from the DFT ratios from the 10 Hz and 100 Hz data are shown in red. A model of the controller based on the applied loop coefficients is shown in blue.

3 Frequency noise characterisation

Slow controller characterisation

The split timeseries plots of the 10 Hz data for the y^{SF} and ϵ^{SF} channels are shown in Appendix 8, Figures 8.7 and 8.11, for the EM and FM test campaigns respectively.

The transfer function and the coherence of the slow feedback and error signals were calculated using both the 1 Hz and the 10 Hz data. The DFT ratios for each applied modulation, using both the 10 Hz and the 100 Hz data were also calculated. A model, based on the loop coefficients given in Table 3.8 was also determined. The results are shown in Figure 3.20.

	EM	FM
a	-5×10^{-5}	-5×10^{-5}
b0	1	1
b1^2	-1.0	-1.0

Table 3.8: The coefficients of the slow frequency controller digital filter used in the EM and FM test campaigns [32] [43].

Similarly, the results for the corresponding FM test campaign analysis are given in Figure 3.21. In this case, no 1 Hz data was available. The coefficients of the calculated controller response model are shown in Table 3.8.

The results from both the EM and FM test campaigns showed that the transfer function and DFT results matched. The model produced the same result, demonstrating that the loop coefficients were implemented as expected.

Fast and slow actuator calibration

Both the original and detrended timeseries of the 10 Hz Ψ_F channel are shown in Appendix 8, Figures 8.8 and 8.12, for the EM and FM

---

[2]As mentioned in the fast controller characterisation analysis, the loop coefficient files from the EM and FM test campaigns apply a positive value of 1.0 for the b1 coefficient. However, the response from the loop shows that the actual required, and implemented, value is -1.0. This should be carried forward in planning the in-flight experiments.
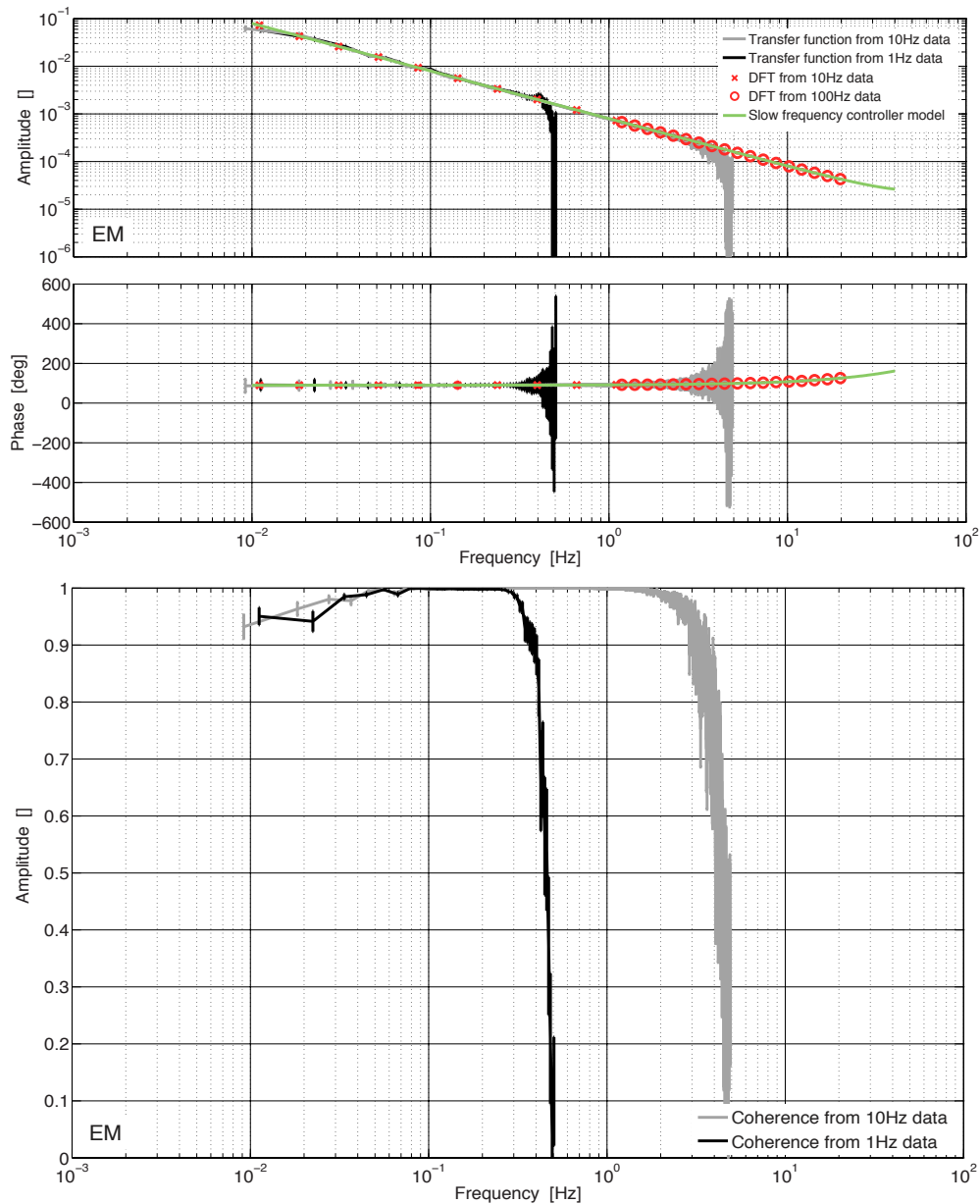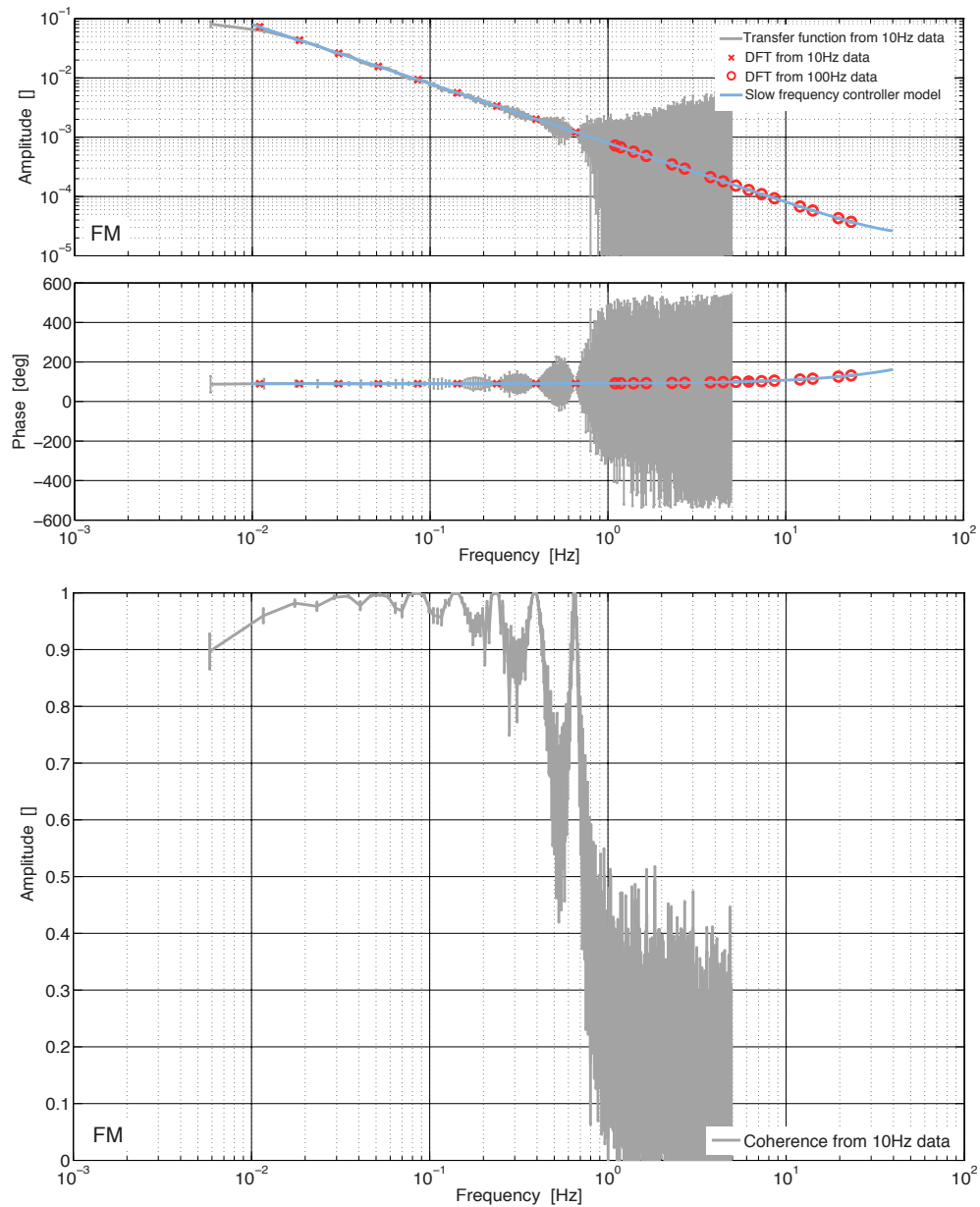
Figure 3.20: The results for the characterisation of the slow frequency loop controller from the EM test campaign investigation of the OLTF. The transfer function and coherence between the slow error and feedback signals using 1 Hz and 10 Hz data are shown in black and grey respectively. The DFT results are shown in red, with crosses representing the results from the 10 Hz data, and circles the results from the 100 Hz IDL data. A model based on the applied loop coefficients defined in the test campaign report is shown in green [32].

Figure 3.21: The results for the characterisation of the slow frequency loop controller from the FM test campaign investigation of the OLTF. The transfer function and coherence between the slow error and feedback signals using 10 Hz data are shown in grey. The DFT results are shown in red, with crosses representing the results from the 10 Hz data, and circles the results from the 100 Hz IDL data. A model based on the applied loop coefficients defined in the test campaign report is shown in blue [43].

150

test campaigns respectively. The y^{FF} channels are shown in Figures 8.6 and 8.10 for the EM and FM test campaigns. No 1 Hz data was available for Ψ_F, so the y^{FF} data at 1 Hz was not used in this investigation.

In a slight deviation from the general processing method, the Ψ_F timeseries is first converted to the frequency fluctuation before the interferometer, $\delta\nu$, by multiplication with the previously defined conversion coefficient, -125.64×10^6 Hz/rad. The analysis was then performed as described in the general method.

The transfer function of the frequency fluctuation and the fast feedback signal using the 10 Hz data was calculated. The DFT ratios for both the 10 Hz and 100 Hz data were also calculated. The results for the EM and FM test campaigns are shown in Figures 3.22 and 3.23. Also shown are the models for the slow actuator controller response, the fast actuator response, and the combined response. These models were based on the design values of the components, discussed in Box 2.3 and shown in Tables 3.7 and 3.8, and then fitted to the DFT results. The fast and slow actuator gains, G_F and G_S, and delays, τ_F and τ_S, were determined from the fit of the model, M, to the calculated results:

$$M(s, G_F, \tau_F, G_S, \tau_S) = A_F(s, G_F, \tau_F) + C_S(s)A_S(s, G_S, \tau_S) \quad (3.18)$$

where:

$$A_F(s, G, \tau) \;\; = \;\; G_F e^{-s\tau} \quad\quad\quad (3.19)$$

$$A_S(s, G, \tau) \;\; = \;\; \frac{G_S e^{-s\tau}}{s + 2} \quad\quad (3.20)$$

The results are shown in Table 3.9.

Open-loop transfer function and noise suppression function

The timeseries plots of the 10 Hz Ψ_F and ϵ^{FF} are shown in Appendix 8, Figures 8.6 and 8.8 for the EM campaign and 8.10 and 8.12 for the FM test campaign.

The transfer function of ϵ^{FF} and Ψ_F was calculated using the 10 Hz data, and the DFT results were determined using both the 10 Hz and
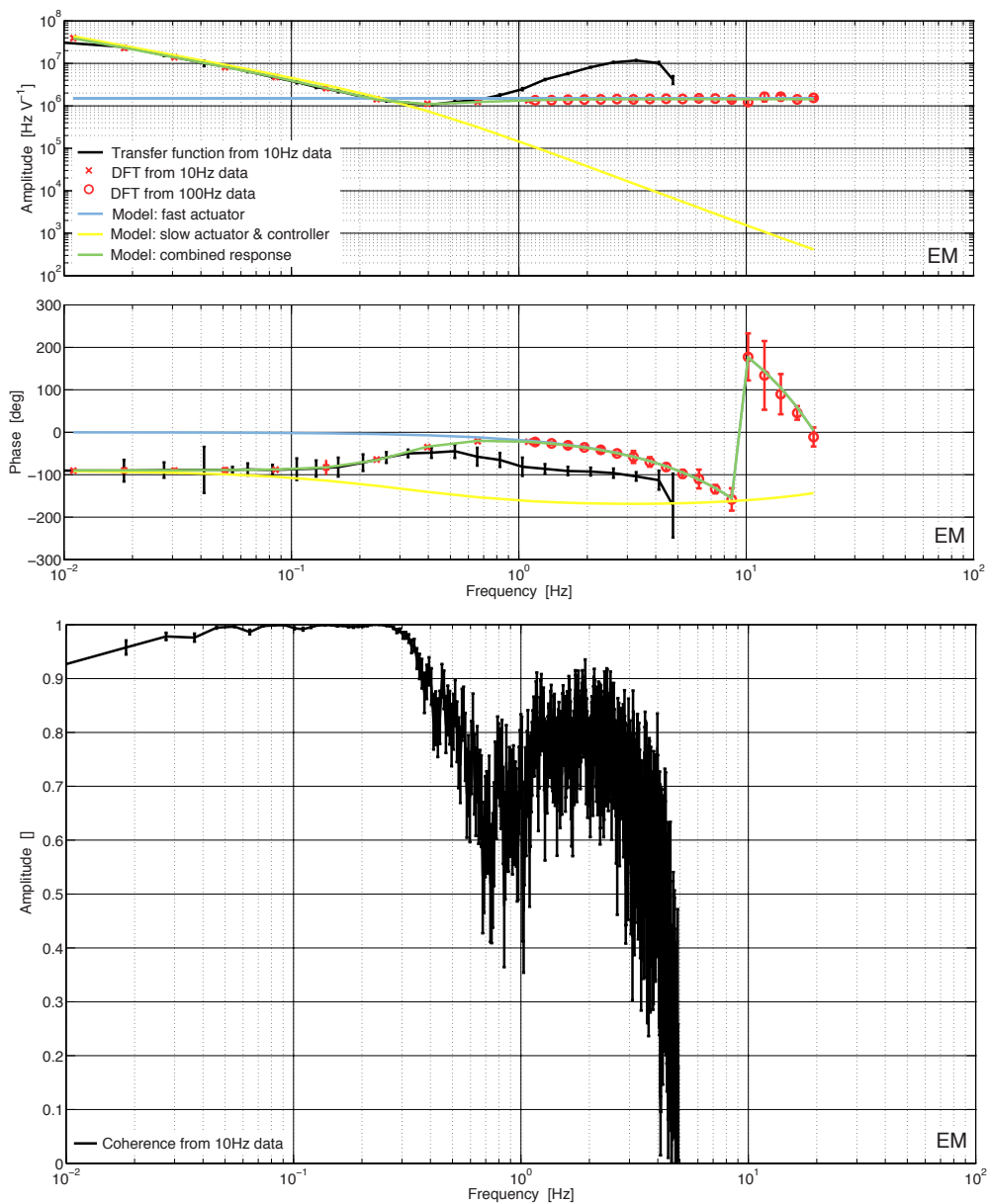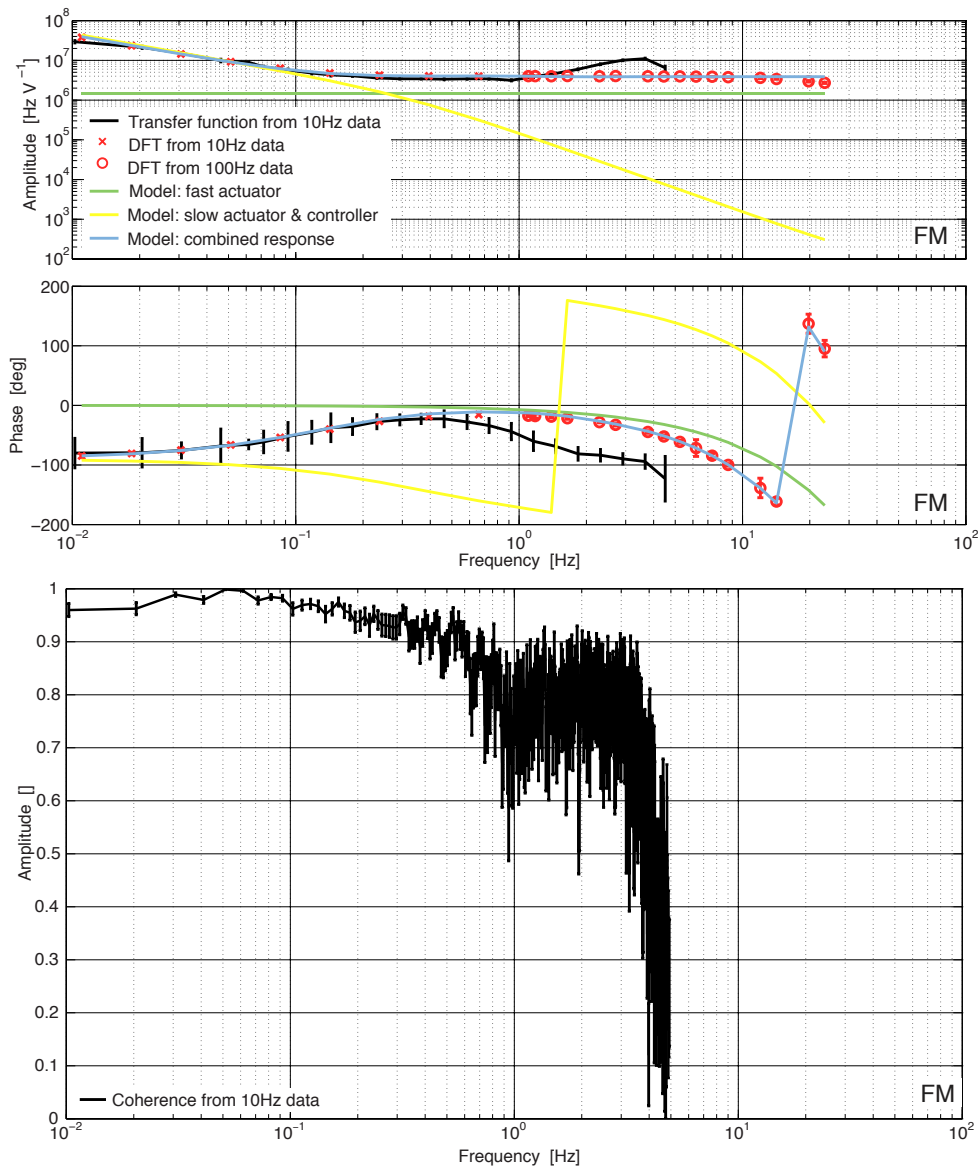
Figure 3.22: The response of the fast and slow frequency actuators, and the slow controller from the EM test campaign. The results from the transfer function method are shown, along with the results from the DFT method, with the 10 Hz result shown by red crosses, and the 100 Hz results by red circles. Also shown is the fitted model based on the loop design. The yellow line shows the component from the slow actuator and controller and the blue line shows the component from the fast actuator. The green line shows the combined response.

Figure 3.23: The response of the fast and slow frequency actuators, and the slow controller from the FM test campaign. The results from the transfer function method are shown, along with the results from the DFT method, with the 10 Hz result shown by red crosses, and the 100 Hz results by red circles. Also shown is the fitted model based on the loop design. The yellow line shows the component from the slow actuator and controller and the green line shows the component from the fast actuator. The blue line shows the combined response.

	Fast actuator, A_F		Slow actuator, A_S	
	Gain, G_F [Hz/V]	Delay, τ_F [s]	Gain, G_S [Hz/V]	Delay, τ_S [s]
EM	1.45×10^6	51.7×10^{-3}	5.39×10^8	0
FM	3.88×10^6	32.01×10^{-3}	5.42×10^8	0

Table 3.9: Results for the fast and slow frequency control loop actuator gains and delays, as measured using the results of the EM and FM test campaign OLTF investigations.

100 Hz data. The results for the EM and FM test campaigns are shown in Figures 3.24 and 3.25. A fit to a model, M, based on the design of the loop (see Box 2.3), and the values of the coefficients specified in Tables 3.8 and 3.7, is also shown. The model fit determines the fast and slow actuator gains, G_F and G_S, and delays, τ_F and τ_S:

$$M(s, G_F, \tau_F, G_S, \tau_S) = -X_F C_F(s) \left(A_F(s, G_F, \tau_F) + C_S(s) A_S(s, G_S, \tau_S) \right) \tag{3.21}$$

where:

$$X_F = \frac{-2\pi \times 0.38}{c} \tag{3.22}$$

$$A_F(s, G, \tau) = G_F e^{-s\tau} \tag{3.23}$$

$$A_S(s, G, \tau) = \frac{G_S e^{-s\tau}}{s + 2} \tag{3.24}$$

The calculated gain and stability characteristics of the frequency control loop are shown in Tables 3.10 and 3.11.

The equivalent noise suppression functions were also calculated from the model of the OLTF. The results for the EM and FM test campaigns are shown in Figures 3.26 and 3.27. The value of the suppression at 30 mHz is approximately -39 dB for the EM result, and -40 dB for the FM result.

Coupling of frequency noise via an applied modulation

Only the 10 Hz data was used in this investigation, as the x_{12} channel was not recorded at 100 Hz in either test campaign.
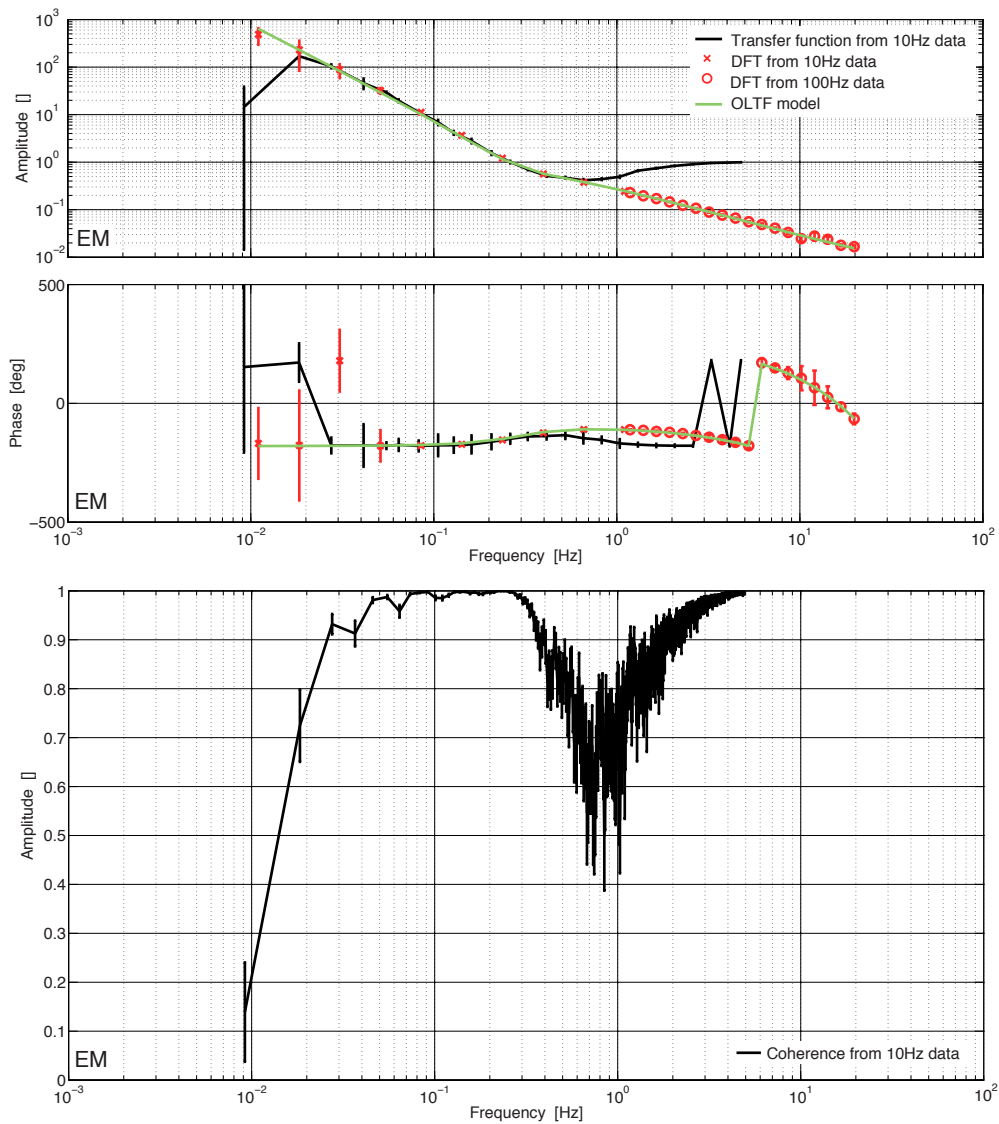
Figure 3.24: The open-loop transfer function, as calculated using the results of the EM test campaign OLTF investigation. The black trace shows the results from the transfer function of the 10 Hz data, the red crosses the DFT results for the 10 Hz data, and the red circles the DFT results from the 100 Hz data. The green line shows the model fitted to the DFT results.

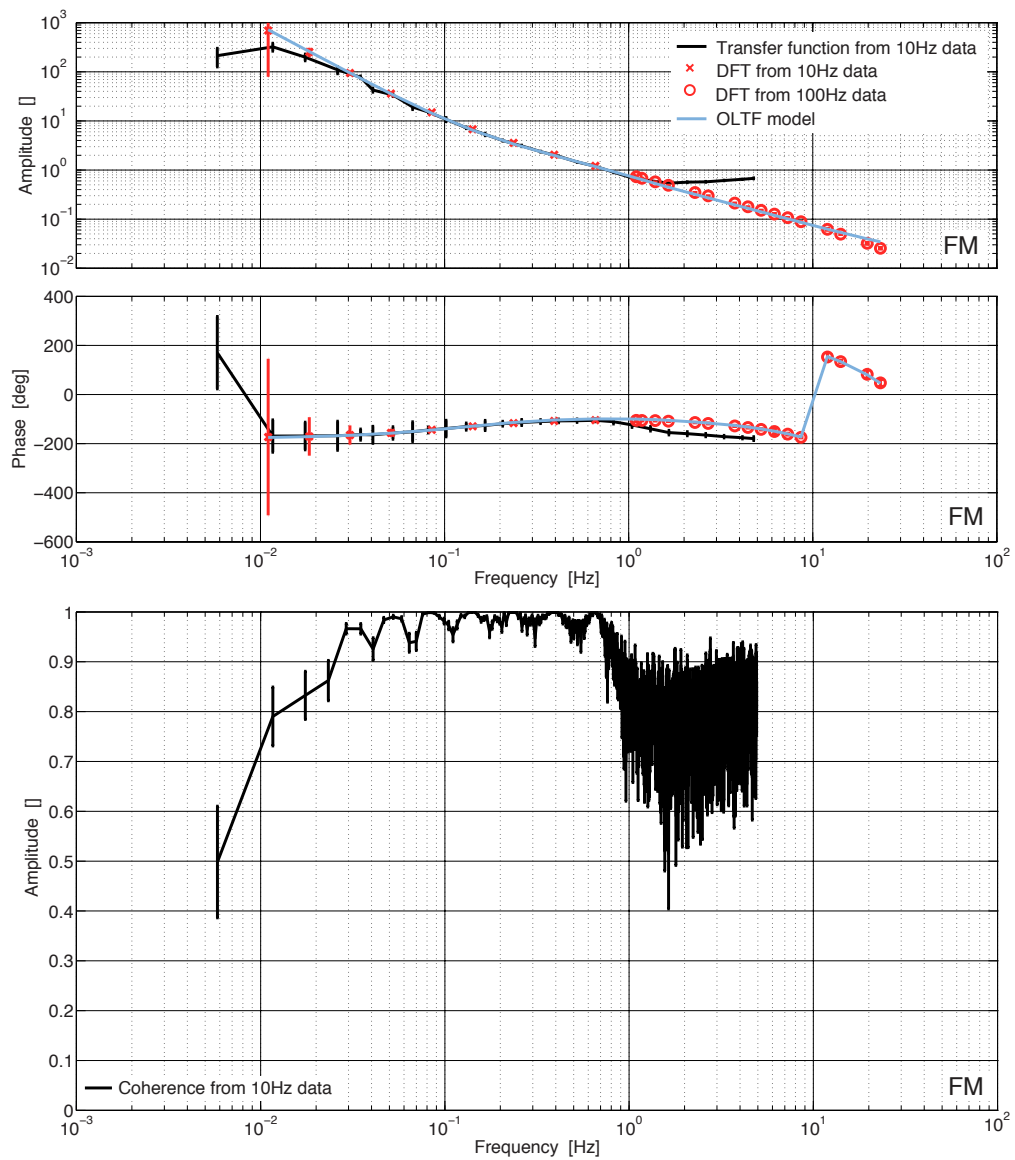# 3 Frequency noise characterisation

Figure 3.25: The open-loop transfer function, as calculated using the results of the FM test campaign OLTF investigation. The black trace shows the results from the transfer function of the 10 Hz data, the red crosses the DFT results for the 10 Hz data, and the red circles the DFT results from the 100 Hz data. The blue line shows the model fitted to the DFT results.

	Fast actuator, A_F		Slow actuator, A_S	
	Gain, G_F [Hz/V]	Delay, τ_F [s]	Gain, G_S [Hz/V]	Delay, τ_S [s]
EM	1.45×10^6	51.7×10^{-3}	5.39×10^8	0
FM	3.67×10^6	31.65×10^{-3}	5.46×10^8	0

Table 3.10: The fast and slow frequency control loop actuator gains and delays, as determined from the results of the EM and FM test campaign OLTF investigations.

	EM	FM
Unity gain frequency [Hz]	0.26	0.78
Gain at $30\,\mathrm{mHz}$ [dB]	38.67	39.92
Gain margin [dB]	0.46	0.78
Phase margin [deg]	34.2	74.5

Table 3.11: The gain and stability characteristics of the frequency control loop, as determined from the EM and FM test campaign fits to the OLTF.
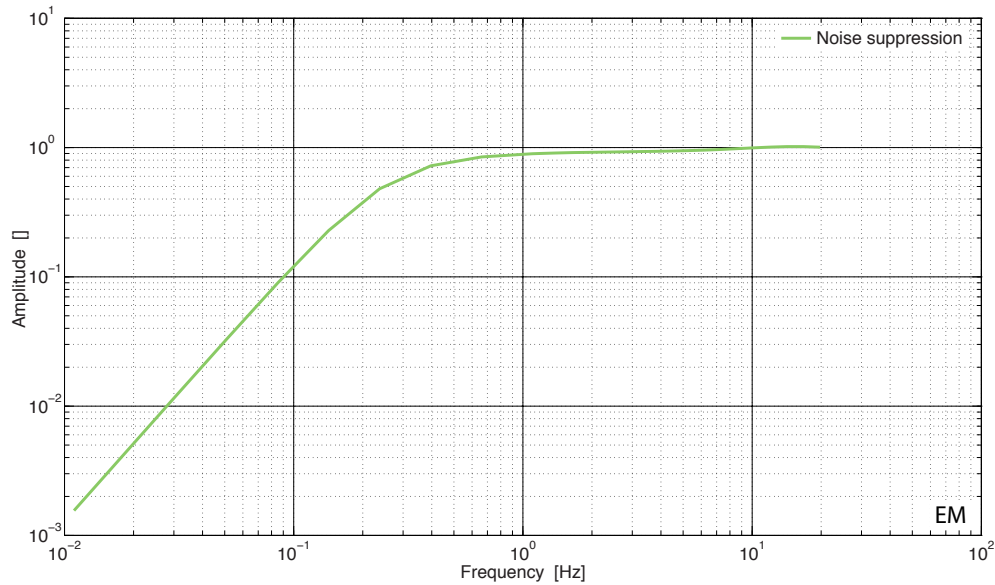
Figure 3.26: The noise suppression function for the frequency control loop determined from the modelled OLTF calculated, as fitted to the results of the EM test campaign.
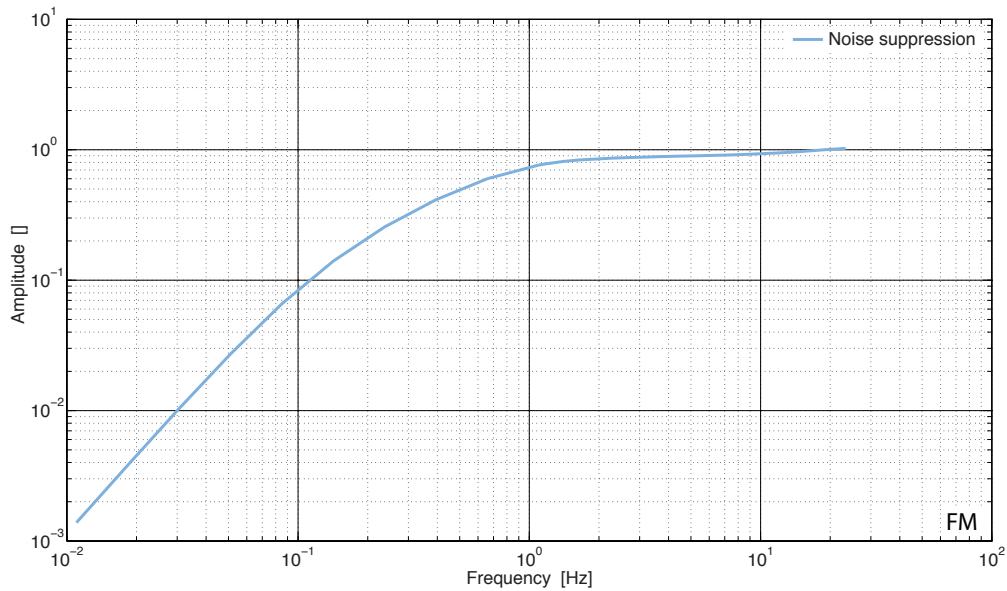
Figure 3.27: The noise suppression function for the frequency control loop determined from the modelled OLTF calculated, as fitted to the results of the FM test campaign.

The transfer functions and coherences of Ψ_F into x_{12} were calculated, as were the DFT ratios for the applied modulations. These are shown in Figures 3.28, and 3.29 for the EM and FM test campaigns respectively. Also shown for comparison are the equivalent transfer function and coherence results determined in the free-running frequency noise investigation, described in Section 3.1.

Note: In this analysis, the transfer functions were binned, such that the average of ten points per decade of the original transfer function was calculated. This smooths the result, and provides a better statistical error estimation.

At high frequencies, the transfer function from the EM investigation shows the same unexplained high noise that was found during the free-running frequency noise investigation. This is discussed in Box 3.2.

Two methods were used to determine the coupling coefficient, K, for frequency noise into differential displacement with units of m/rad:

1. Firstly, a frequency range with a flat transfer function was selected, where the coherence was also high. The average of the
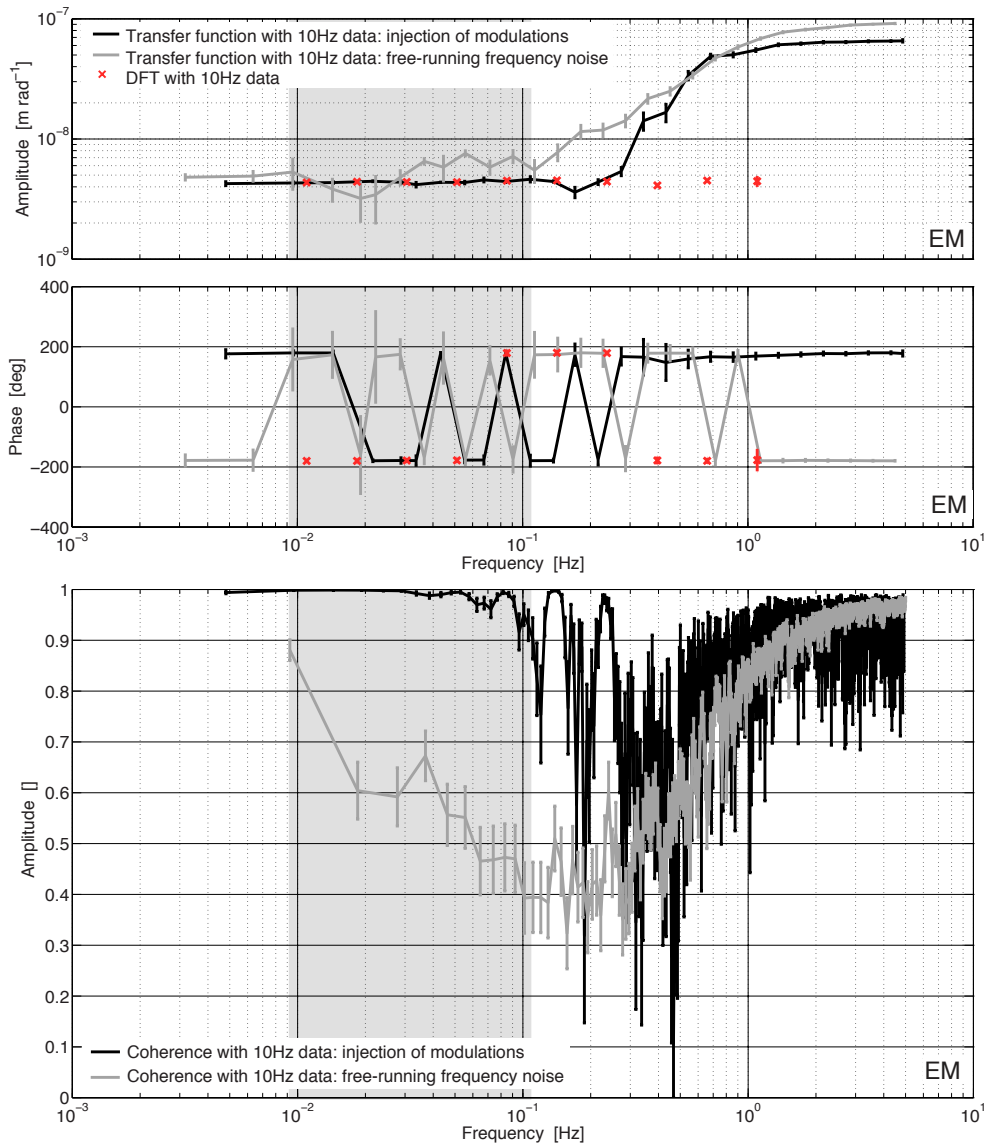
158

Figure 3.28: Plots of the transfer function and the coherence of Ψ_F and x_{12} for the EM test campaign investigation of the OLTF, used to determine the frequency noise coupling via an applied modulation. The grey shaded area represents the frequency region used to determine the coupling coefficient for frequency noise into differential displacement. Also shown is the equivalent transfer function determined in the free-running frequency investigation (see Section 3.1), in light grey. The transfer function is much flatter and the coherence higher with injected modulations. The results of calculating the coupling coefficient of frequency noise into the differential displacement via the DFT method are also shown in red. They are consistent with the coupling coefficient calculated from the transfer function.

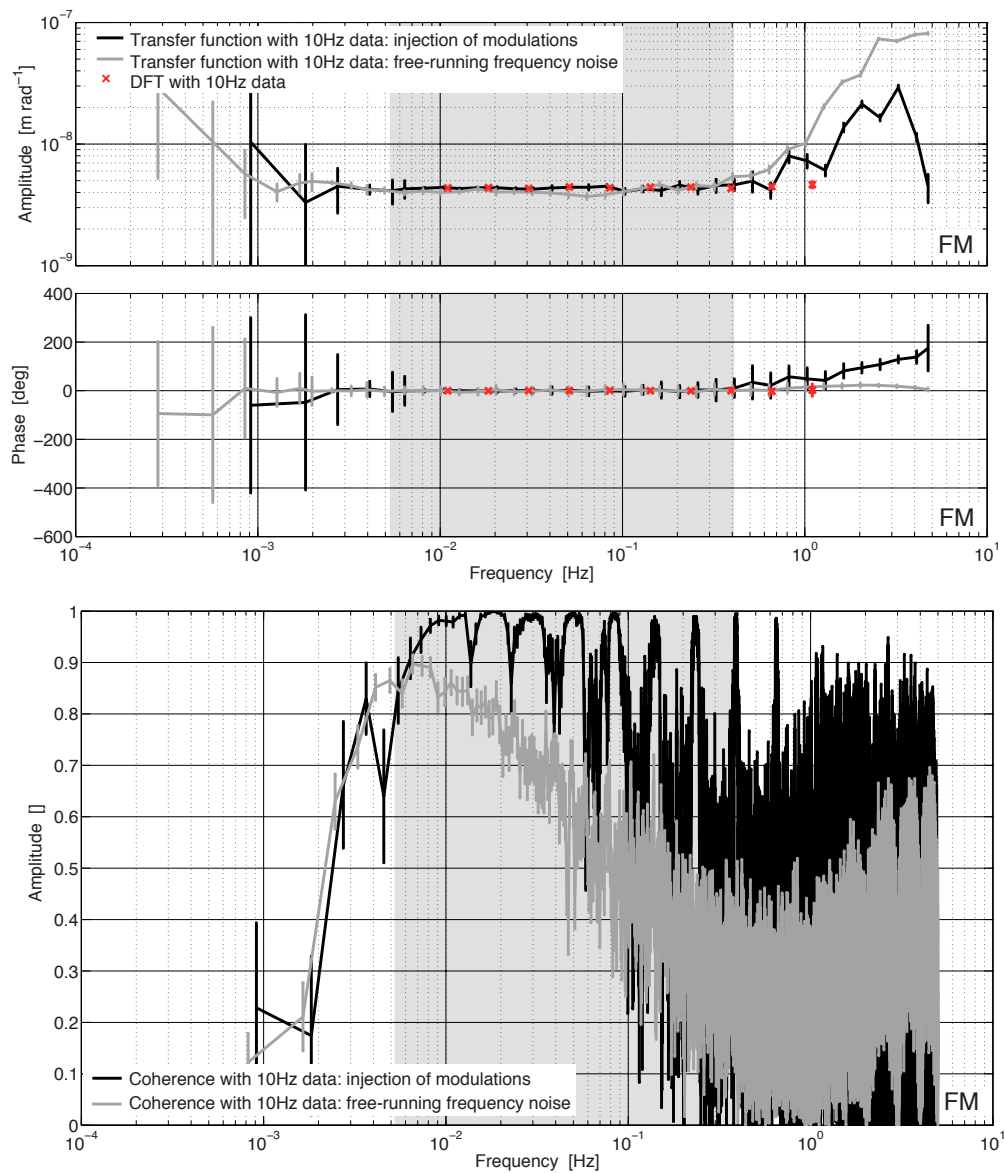# 3 Frequency noise characterisation

Figure 3.29: Plots of the transfer function and the coherence of Ψ_F and x_{12} for the FM test campaign investigation of the OLTF, used to determine the frequency noise coupling via an applied modulation. Also shown, in light grey, is the equivalent transfer function determined in the free-running frequency noise investigation (see Section 3.1). The transfer functions from each investigation are well matched, but the coherence is higher with the injected modulations. The grey shaded area represents the frequency region used to determine the coupling coefficient for frequency noise into differential displacement. The results of calculating the coupling coefficient of frequency noise into the differential displacement via the DFT method are also shown in red. They are consistent with the coupling coefficient calculated from the transfer function.

binned transfer function in this frequency range was calculated. This range is shown by the grey shaded area in the transfer function plots (Figures 3.28 and 3.29).

2. Secondly, the mean of the DFT ratios was calculated.

The results of both methods, for the EM and FM test campaigns, are shown in Table 3.12. The results for both methods, and in both the EM and FM campaigns, match within errors. This is expected, as the same optical bench was under test in both cases.

	Method	Coefficient [m/rad]	Error [m/rad]
EM	Transfer function	4.40×10^{-9}	5.90×10^{-11}
	DFT	4.40×10^{-9}	3.75×10^{-11}
FM	Transfer function	4.35×10^{-9}	1.58×10^{-10}
	DFT	4.41×10^{-9}	2.95×10^{-11}

Table 3.12: The calculated values of the coupling coefficient for frequency noise into the differential displacement measurement resulting from the EM and FM investigations where the laser frequency was modulated.

An estimate of the optical pathlength mismatch was then calculated from each of the coupling coefficient values, according to the method explained in Box 3.3. The results are presented in Table 3.13. Within errors, the results give the same pathlength mismatch in both methods, and in both test campaigns. The EM values are slightly higher, and the FM slightly lower, than the estimates calculated with the free-running frequency noise results. However, the values calculated for both campaigns with the injected modulation correspond within errors. This is as expected, as the same optical bench was used.

	Method	Pathlength mismatch [m]	Error [m]
EM	Transfer function	19.64×10^{-3}	2.63×10^{-4}
	DFT	19.64×10^{-3}	1.67×10^{-4}
FM	Transfer function	19.42×10^{-3}	7.05×10^{-4}
	DFT	19.69×10^{-3}	1.32×10^{-4}

Table 3.13: The calculated values of the upper limit of the optical pathlength mismatch between the reference and measurement beams in the x_{12} interferometer.

The DFT is performed on a timeseries segment which contains a modulation at a single frequency. From the analysis and the list of frequencies applied during the investigation, the calculated signal frequency in that segment has been determined. The DFT is performed at this frequency, and therefore if it is incorrect the results will be inaccurate.

Heterodyning describes the process of two signals, with frequency f and phase ϕ, being mixed. In this case, each quadrature is mixed separately:

$$\sin\theta\sin\varphi = \frac{1}{2}\cos(\theta-\varphi) - \frac{1}{2}\cos(\theta+\varphi) \qquad (3.25)$$

$$\sin\theta\cos\varphi = \frac{1}{2}\sin(\theta+\varphi) + \frac{1}{2}\sin(\theta-\varphi) \qquad (3.26)$$

where $\theta = (2\pi f_1 + \phi_1)$ and $\varphi = (2\pi f_2 + \phi_2)$.

In the analyses described in this thesis, $\sin\theta$ describes the sinusoid at the frequency calculated by the FFT, and $\sin\varphi$ is the sinusoid that was applied. When $f_1 = f_2$, the result from both quadratures will be a flat response with no fluctuating component. This demonstrates that the correct frequency has been determined. If the phase of the signals are also the same, then the DC value of the result will be zero.

Box 3.4: An explanation of why the heterodyne method is used to check whether the frequency at which a DFT was performed is the frequency of the originally applied modulation.

3.2.2 In-flight investigation

The control loop characterisation investigation is planned to be performed in science mode 1.2, with test mass one drag-free and test mass two controlled via electrostatic suspension[1]. The fast frequency control loop should be operating in the 'variable output y' state. The other control loops, including the slow control loop, should be in the 'nominal' operational state. A series of modulations at a range of frequencies should be applied, and all loop telemetry for the frequency control loop recorded at 10 Hz. The characteristics of the modulations that should be applied are given in Table 3.15. The selection of the applied frequency and duration are discussed in Box 3.6. An overview of the setup and telemetry required for the investigation is given in Table 3.14. The procedure for implementing the investigation in-flight is shown in Figure 3.30. This procedure includes the steps required for applying a modulation above 1 Hz with data recording at 100 Hz via the IDL, to allow for the case where the procedure is adapted to include modulations at higher frequencies than those specified in Table 3.15.

---

[1]The characterisation of the control loop could also be performed with the test masses fixed, during commissioning of the satellite for example. In this case it would not be possible to determine the coupling coefficient.

Investigation	Frequency control loop characterisation		
OMS state	TMs drag-free		
Loop states	SF	Nominal	
	FF	Variable output y	
	OPD	Nominal	
	SP	Nominal	
	FP	Nominal	
Telemetry required	128,3	x_{12}	LST10130
		Ψ_F	LST12406
	128,4	FF input modulation	LST17337
		FF error	LST17339
		FF feedback	LST17340
		SF error	LST17344
		SF feedback	LST17345
		OPD feedback	LST17350
		SP feedback	LST17357
	3,25	SF state	LST17364
		FF state	LST17361
		OPD state	LST17367
		FP state	LST17358
		SSC	SCT70388
Length	~ 3 hours		

Table 3.14: An overview of the key information relating to the frequency control loop characterisation investigation. For the telemetry names associated with each parameter refer to Appendix 7.

An overview of the procedure for the analysis of the in-flight investigation is given in Figure 3.30. The analysis, shown in Figure 3.31, can be split into several sub-analyses, each represented by a particular colour:

- General data preparation, represented by grey. This procedure is described in detail in Figure 3.32.

- Preparation of the data for the DFT analysis, shown in brown. The associated procedure is described in Figure 3.33.

- The fast controller characterisation is represented by blue, and the specific analysis procedure is shown in Figure 3.34.

	Shape	Frequency [Hz]	Duration [half periods]	Amplitude [rad]
1	sine	0.011	20	0.05
2	sine	0.0396	20	0.05
3	sine	0.0852	20	0.05
4	sine	0.1421	20	0.05
5	sine	0.237	20	0.05
6	sine	0.3953	20	0.05
7	sine	0.6594	20	0.05
8	sine	1.0	20	0.05

Table 3.15: The planned modulations that should be injected into the δx^{FF} input of the fast frequency control loop for the in-flight frequency control loop characterisation investigation.

- The slow controller characterisation is given in green, and shown in detail in Figure 3.35.

- The analysis of the fast and slow frequency actuator calibration is shown in yellow, and described in detail in Figure 3.2.2.

- The analysis to determine the OLTF and noise suppression function is shown in red, and the procedure for the analysis is given in Figure 3.37.

- The calculation of the coupling coefficient for frequency noise coupling into differential displacement is represented by blue, and the analysis procedure is given in Figure 3.38.

- The calculation of the upper limit on the mismatch between the measurement and reference beams in the X12 interferometer is represented in green and shown in figure 3.39.

3.3 Closed-loop frequency noise

The closed-loop frequency noise investigation is not an investigation in itself. Rather, it is a particular sub-analysis which can be applied to the data collected during an LPF science run. During such an
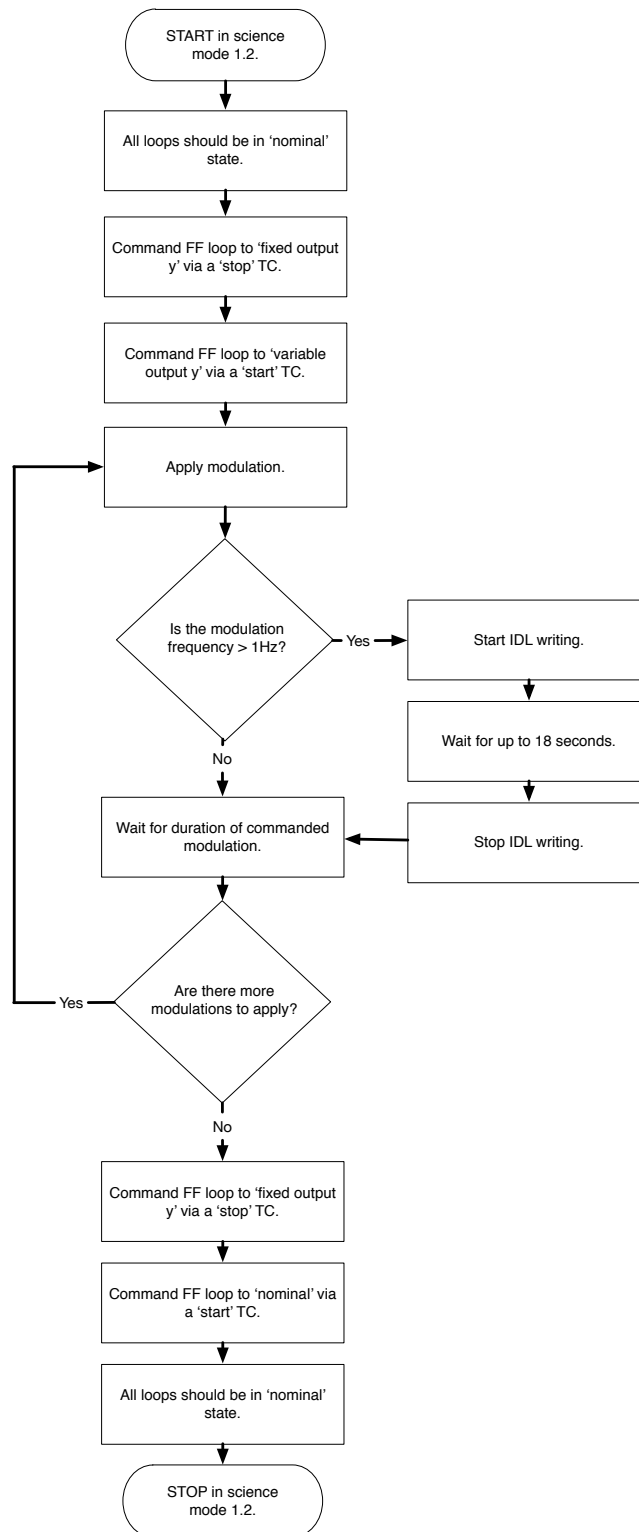
Figure 3.30: The procedure for performing the in-flight investigation to characterise the frequency control loops.

For each loop characterisation investigation several modulation frequencies have been selected. The next step is the definition of the peak-to-peak amplitude and the duration of the modulation. The fractional error on the measured signal at a particular frequency, $Y(f)$, must be less than 1%, such that:

$$\frac{\sigma(f)}{Y(f)} \leq 0.01, \tag{3.27}$$

where $\sigma(f)$ is the absolute error of a signal with noise spectrum $S_{xx}(f)$ and duration T, as defined by:

$$\sigma(f) = \sqrt{\left(\frac{2S_{xx}(f)}{T}\right)}. \tag{3.28}$$

The value of $Y(f)$ depends upon the amplitude of the injected signal, A, and the OLG at the frequency of the modulation:

$$Y(f) = A \times \text{OLG}(f). \tag{3.29}$$

The amplitude that can be applied is limited by the range of the actuator. Any signal larger than a pre-defined limit is clipped to prevent saturation of the actuator. Therefore, for each control loop the input amplitude is defined as half of the maximum range of the actuator. In order to meet the 1% requirement on the fractional error of the signal, it is necessary to calculate T. The value of $S_{xx}(f)$ is found from the spectrum of the closed-loop noise.

Box 3.5: Selection of the length of the applied modulation for the loop characterisation investigations.

3 Frequency noise characterisation

Selection of applied modulations for the frequency control loop characterisation

Eight modulation frequencies, shown in Table 3.15, were chosen based on the frequencies applied in the FM test campaign [43]. These frequencies were selected because they do not require the IDL, it is assumed that the selection of such frequencies relates to some specific characteristics of the system. They also cover a good range of the OLTF, as shown in the top plot below, and are not harmonics of each other.
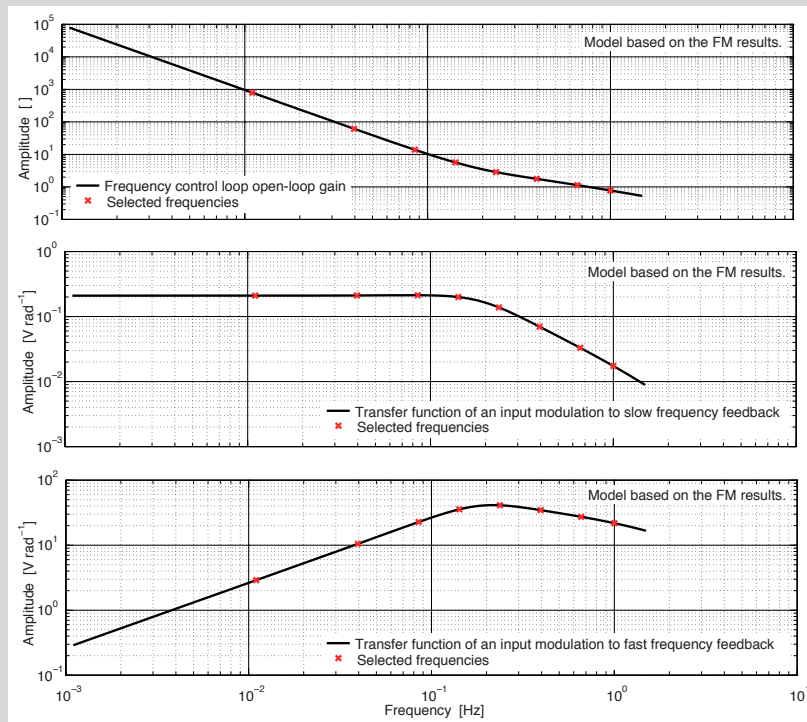
The amplitude of the modulations was also kept the same as for the FM test campaign, 0.05 rad, as the feedback signals at both the fast and slow actuators are well within their operational ranges. The range of the fast actuator is ±12.4 V and the range of the slow actuator is ±5 V. The transfer functions from an input modulation to a feedback signal to each actuator are shown above, to provide for the scenario where the modulations characteristics need to be adapted.

The calculated duration required for each modulation, according to the method in Box 3.5, was short, therefore a reasonable number of half periods that could be implemented to give a suitable investigation length were selected.

Box 3.6: The selection of the applied frequencies and modulations to be used in the in-flight investigation to characterise the frequency control loops.
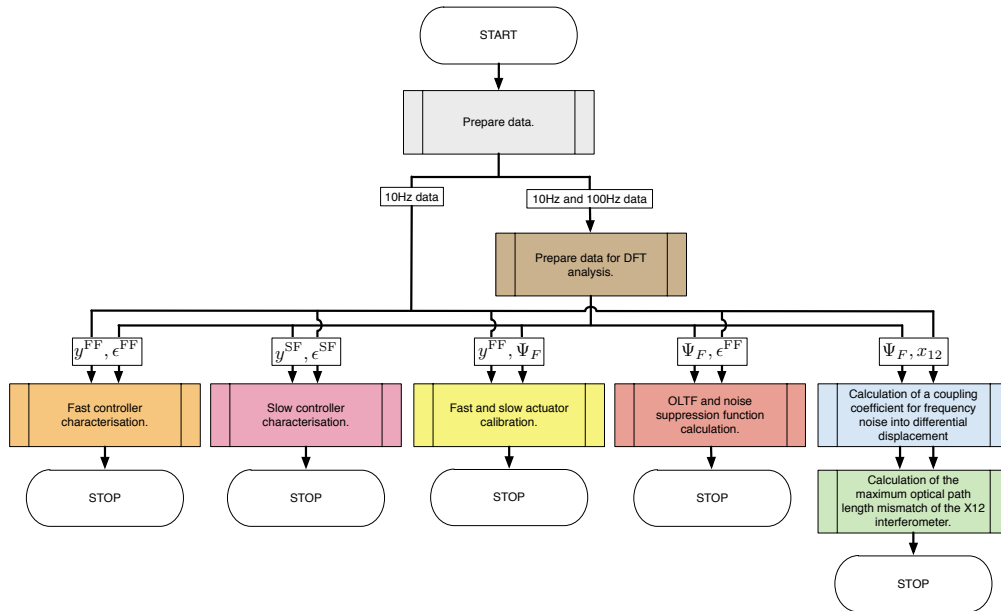
168

Figure 3.31: An overview of the in-flight analysis of the frequency control loop characterisation investigation. Each sub-analysis is explained in more detail in a separate diagram, with the same colour as the associated block shown here.

investigation, the satellite is operating in science mode 1.2, with test mass one drag-free, and test mass two electrostatically suspended. The aim is to maintain the drag-free condition of test mass one such that the measured differential displacement is as low as possible, this being the overall goal of the mission. To achieve this, the three OMS control loops would all be operating in their nominal, closed-loop, states. Therefore, the analysis of the data can be used to provide confirmation that the frequency control loop is operating to suppress the frequency noise as expected and required.

In this section, the analysis of the results of performance measurements from the EM, FM, and OSTT test campaigns are presented, focusing only on the frequency noise. These performance measurements are the ground-based equivalent of the in-flight science mode investigations, albeit without drag-free or suspended test masses. The analysis procedures applicable for the analysis of the in-flight investigations are also presented. For these investigations, no in-flight procedure for performing the measurement is given, as this is already well defined.

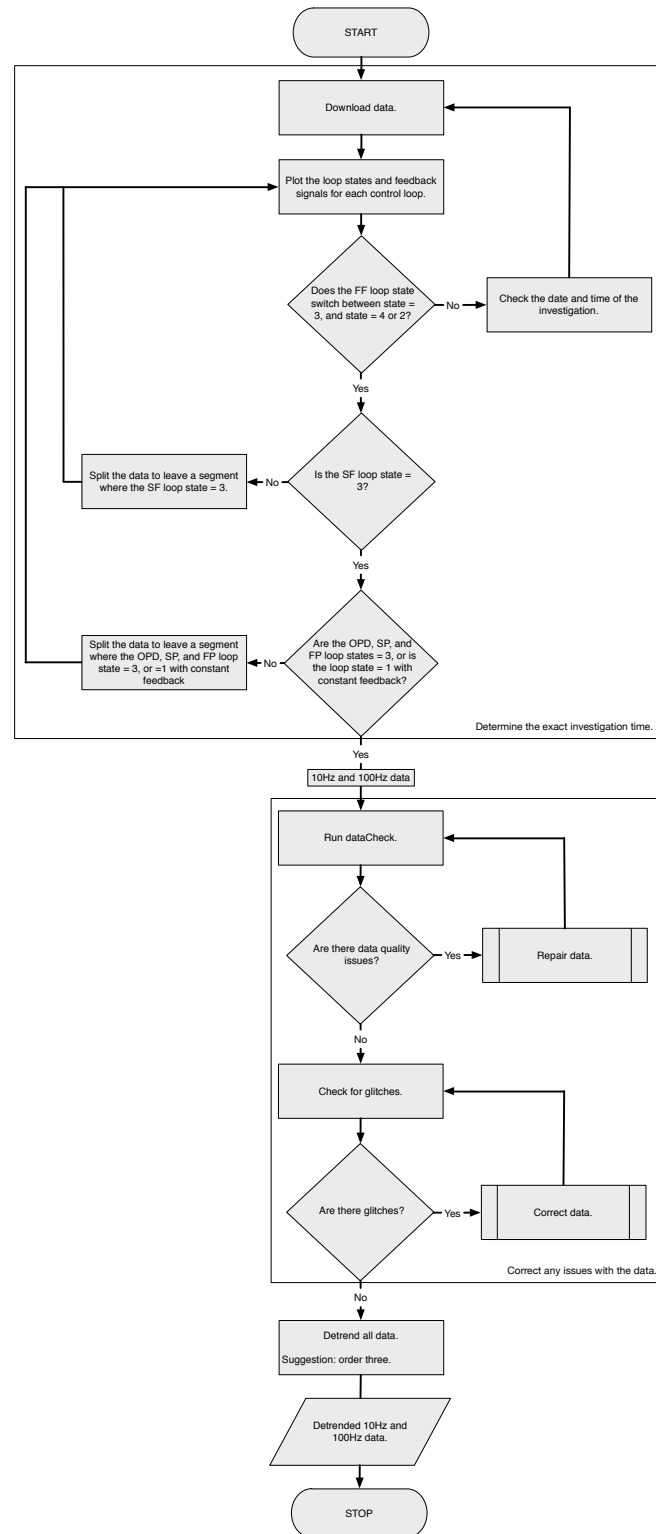**Figure 3.32:** The procedure for general data preparation for the in-flight frequency control loop characterisation investigation.

START

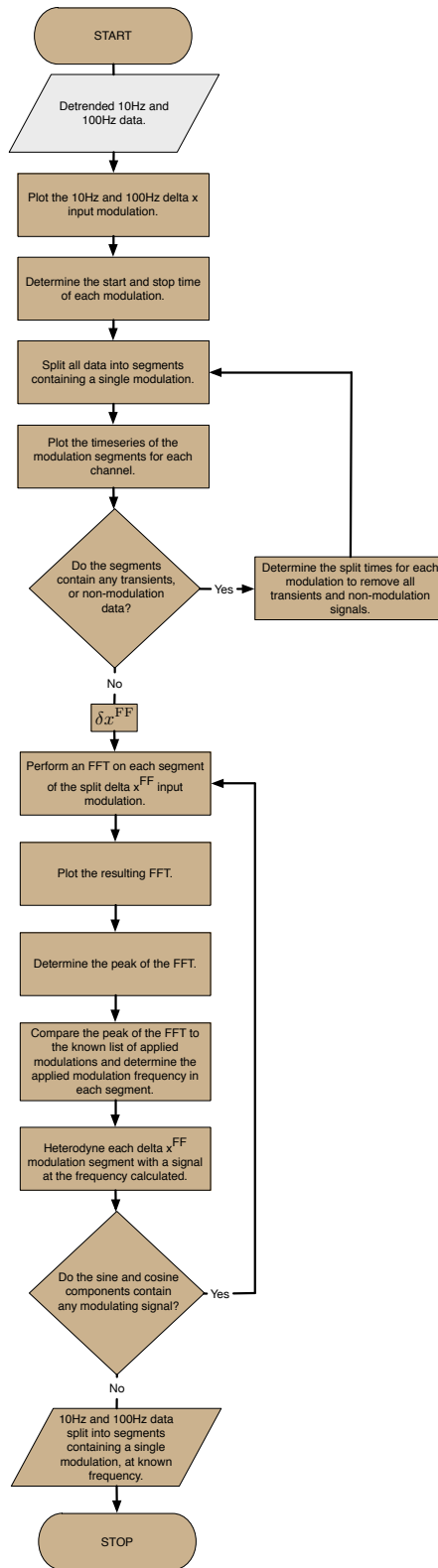Detrended 10Hz and 100Hz data.

Plot the 10Hz and 100Hz delta x input modulation.

Determine the start and stop time of each modulation.

Split all data into segments containing a single modulation.

Plot the timeseries of the modulation segments for each channel.

Do the segments contain any transients, or non-modulation data?

Determine the split times for each modulation to remove all transients and non-modulation signals.

Yes

No

δx^{FF}

Perform an FFT on each segment of the split delta x^{FF} input modulation.

Plot the resulting FFT.

Determine the peak of the FFT.

Compare the peak of the FFT to the known list of applied modulations and determine the applied modulation frequency in each segment.

Heterodyne each delta x^{FF} modulation segment with a signal at the frequency calculated.

Do the sine and cosine components contain any modulating signal?

Yes

No

10Hz and 100Hz data split into segments containing a single modulation, at known frequency.

STOP

Figure 3.33: The procedure for the preparation of the data for the DFT analysis, a sub-analysis of the in-flight frequency control loop characterisation investigation.

Chapter 3

3 Frequency noise characterisation

START

DFT method

Transfer function method

Detrended 10Hz data.

10Hz and 100Hz data split into segments containing a single modulation, at known frequency.

$y^{\mathrm{FF}}, \epsilon^{\mathrm{FF}}$

$y^{\mathrm{FF}}, \epsilon^{\mathrm{FF}}$

Calculate the transfer function of y^{FF} into e^{FF}.

Suggestion: 20 averages.
Windowing function.

Perform a DFT on each modulation segment of the y^{FF} and e^{FF} channels, at the frequency of the applied modulation.

Suggestion: 60 averages.
Windowing function.

Calculate the coherence of y^{FF} into e^{FF}.

Suggestion: 20 averages.

Calculate the ratio of the DFT results for the each applied modulation, f:

$$\mathrm{C}_{\mathrm{F}}^{f} = \frac{y^{\mathrm{FF}}}{\epsilon^{\mathrm{FF}}}$$

Transfer function and coherence of the fast controller response.

Join the results from all applied modulations.

$$\mathrm{C}_{\mathrm{F}}$$

DFT result for the fast controller response.

Create a model of the fast controller based on the expected digital controller coefficients.

Plot the transfer function results, the DFT result, and the model.

Does the model correspond to the calculated transfer function and DFT results?

No

Fit the model to the DFT results.

Yes

Actual a and b loop coefficients applied in the investigation.

STOP

STOP

Figure 3.34: The procedure for the analysis of the fast frequency controller response, a sub-analysis of the in-flight frequency control loop characterisation investigation.

172

Figure 3.35: The procedure for the analysis of the slow frequency controller response, a sub-analysis of the in-flight frequency control loop characterisation investigation.

3 Frequency noise characterisation
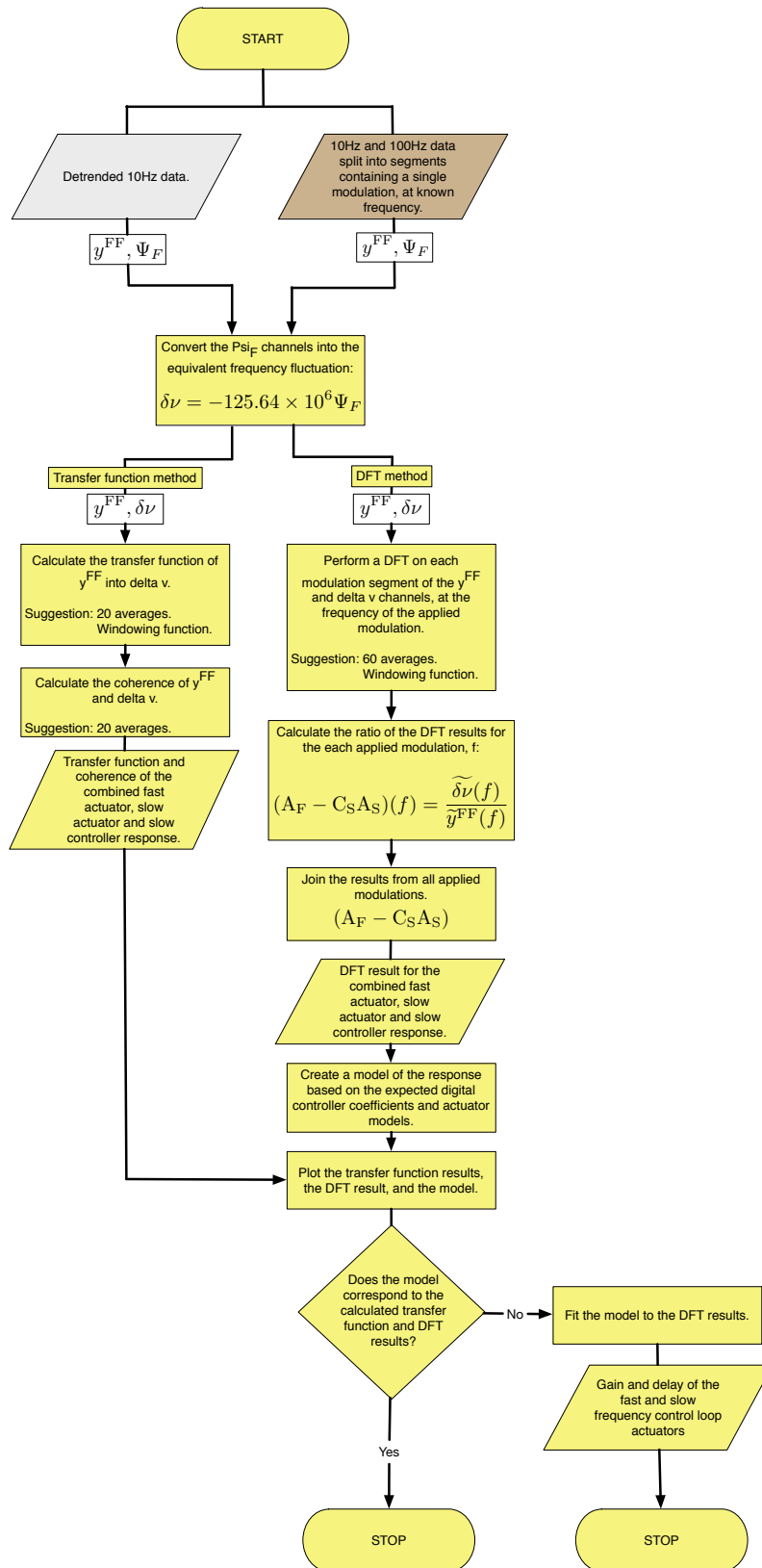
Figure 3.36: The procedure for the analysis of the combined fast and slow frequency actuator and slow controller response, a sub-analysis of the in-flight frequency control loop characterisation investigation.
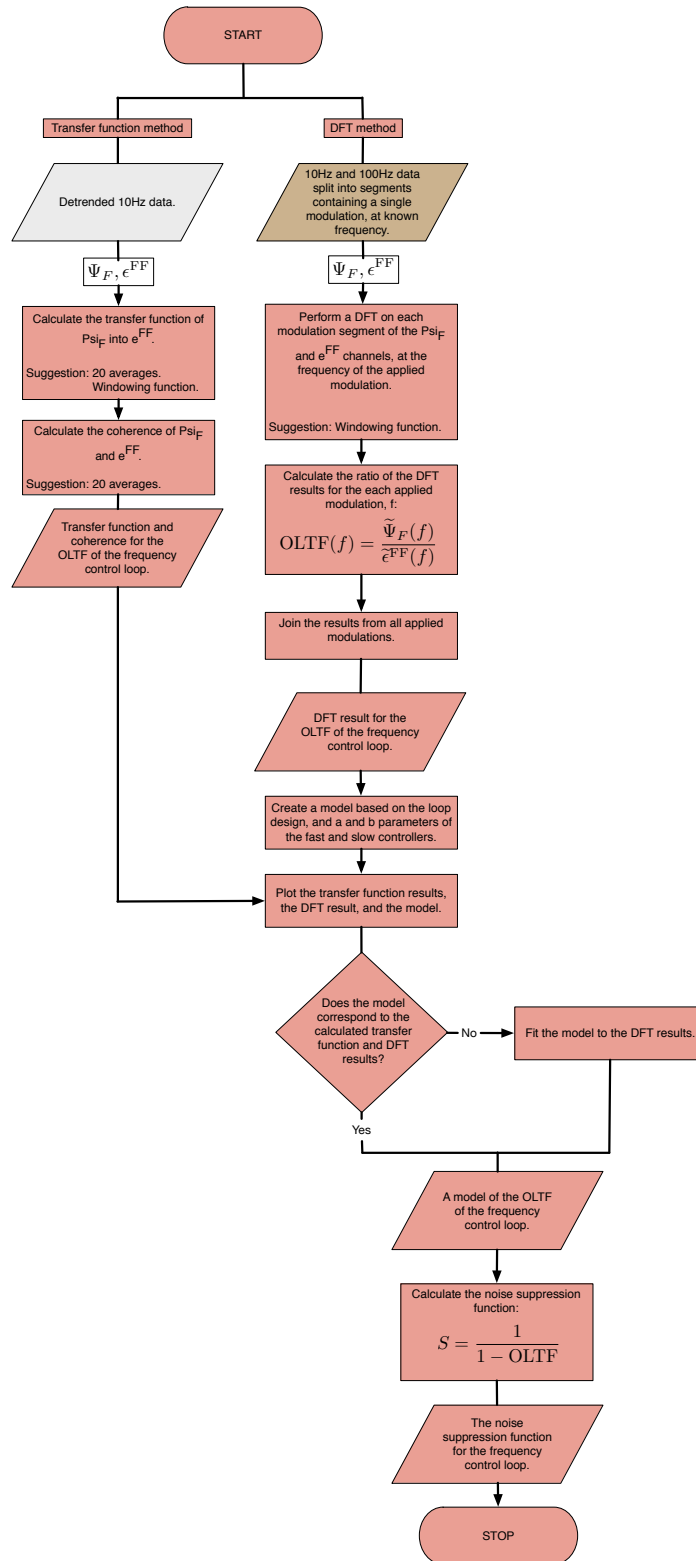
Figure 3.37: The procedure for the analysis of the fast and slow frequency control loop open-loop transfer function, a sub-analysis of the in-flight frequency control loop characterisation investigation.

3 Frequency noise characterisation
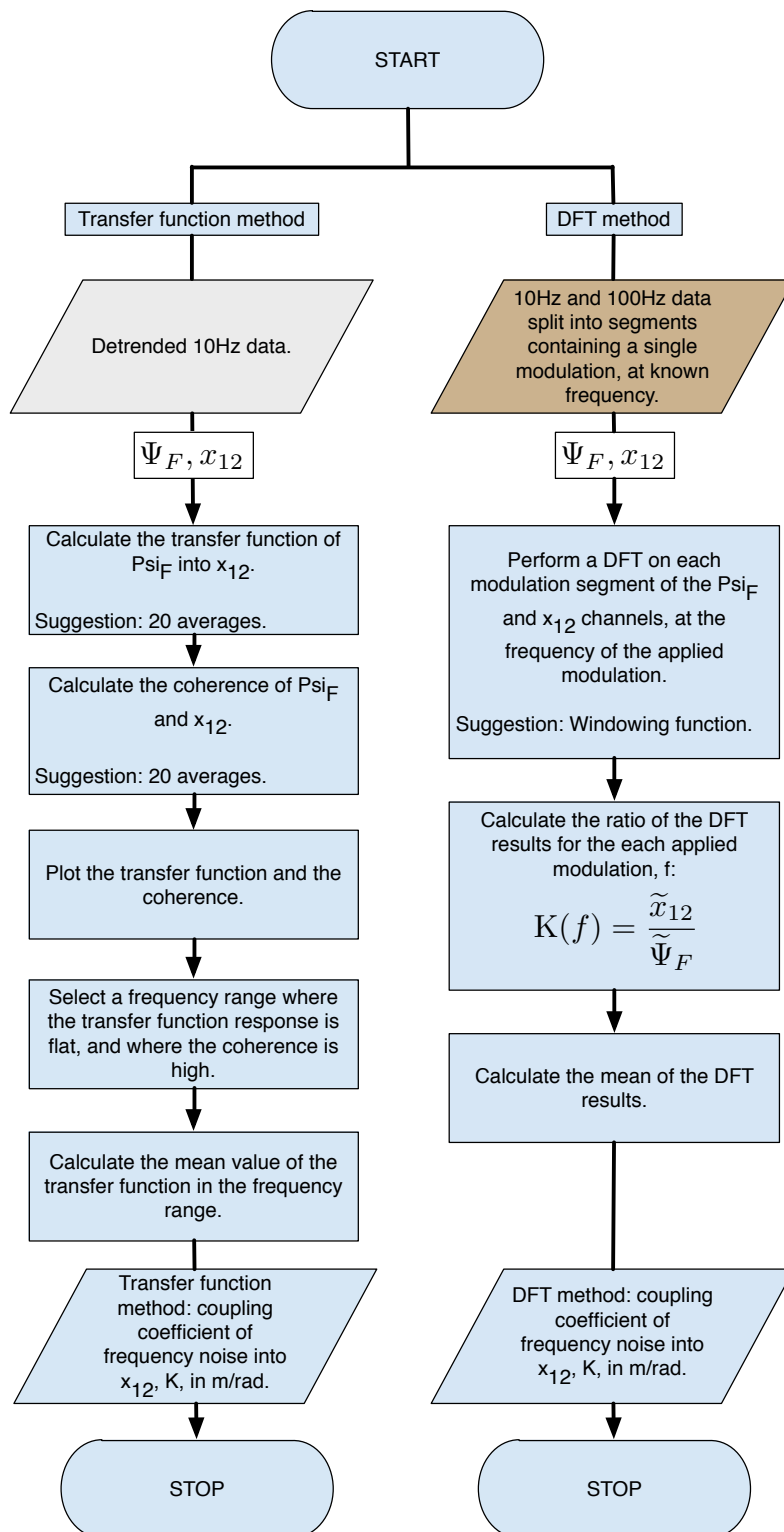
Figure 3.38: The procedure for the calculation of the coupling coefficient for frequency noise into differential test mass displacement, a sub-analysis of the in-flight frequency control loop characterisation investigation.
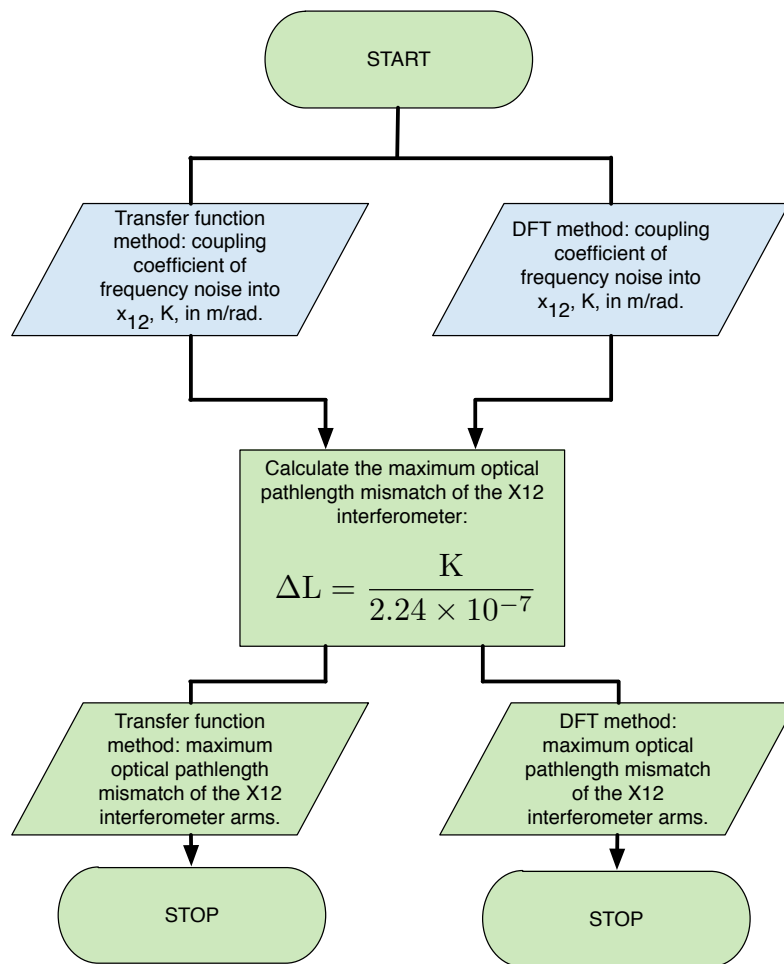
Figure 3.39: The procedure for the calculation of the upper limit of the X12 interferometer pathlength mismatch, a sub-analysis of the in-flight frequency control loop characterisation investigation.

3.3.1 Test campaign results

The closed loop frequency noise can be determined from both noise characterisation measurements where the frequency control loop was closed and other loops were open, or from performance measurements where all loops were closed. In each test campaign, a number of performance measurements were made. In the EM and FM test campaigns the setup was debugged in order to achieve the best possible measurement of the differential test mass displacement. In the OSTT test campaign measurements were made at two temperature levels. In the analyses presented here only the results demonstrating the best performance, i.e., the lowest measurement of residual test mass displacement, are given.

The information relating to the dates and times of the investigations, along with some specific details of the analyses can be found in Appendix 8, Section 8.3. The telemetry used in the analyses is shown in Table 3.16. The equivalent parameter names used in the LTPDA repositories can be found in Appendix 7. Initially all data was processed according to the steps under 'Overview of the analysis'. Following this, two sub-analyses were performed. The first determined the spectrum of the closed-loop frequency noise, and the second made a projection of the closed-loop frequency noise onto the differential test mass displacement measurement. The analysis procedures are described under the associated headings.

Overview of the analysis

1. The data, as specified in Table 3.16, was downloaded according to the times of the investigations given in the test campaign reports [32] [43] [44].

2. The loop states were checked to determine the times when all loops were operating under nominal conditions (state three).

3. The Ψ_F and x_{12} data was split based on the times determined.

4. The data was checked for data quality issues and glitches and repaired accordingly, as described in Appendix 9.

Parameter	Description	Frequency [Hz]	ID
S^{FF}	Fast freq. loop state	1 Hz	LST17361
S^{SF}	Slow freq. loop state	1 Hz	LST17364
S^{OPD}	OPD loop state	1 Hz	LST17367
S^{SP}	Slow power loop state	1 Hz	LST17358
y^{FF}	Fast freq. loop feedback	1 Hz	LST17340
		10 Hz	
y^{SF}	Slow freq. loop feedback	1 Hz	LST17345
		10 Hz	
y^{OPD}	OPD loop feedback	1 Hz	LST17350
		10 Hz	
y^{SP}	Slow power loop feedback	1 Hz	LST17357
		10 Hz	
Ψ_F	Freq. ifo. output	10 Hz	LST12406
x_{12}	X12 ifo. output	10 Hz	LST10130
SSC	Source sequence counter	10 Hz	SCT70388

Table 3.16: The telemetry parameters used in the analysis of the EM, FM, and OSTT test campaign performance investigations, for the analysis of the frequency noise contributions.

Chapter 3

Closed-loop frequency noise

1. The Ψ_F timeseries data was converted from radians to an equivalent frequency in Hz using the following relationship:

$$\Psi_F^{\mathrm{Hz}} = \frac{c}{2\pi \times 0.38} \Psi_F^{\mathrm{rad}} \tag{3.30}$$

2. The amplitude spectral density of the result was calculated. This was plotted along with the result from the free-running frequency noise investigation in the equivalent test campaign. The results for the EM and FM test campaigns are shown in Figures 3.40 and 3.41. The result from the hot phase OSTT measurement is shown in Figure 3.42, and the result from the cold phase is shown in Figure 3.43.

   Note: The amplitude spectral density was calculated using the default Hanning windowing function with 50 % overlap, 16 averages, and detrending of order one.

3. As an additional check that the loop was functioning as expected, the free-running frequency noise was multiplied by the noise suppression function (see Box 2.3). The noise suppression functions were determined from the model of the OLTF calculated in the control loop characterisation investigation, as shown in Figures 3.26 and 3.27. The results are shown in Figures 3.44, 3.45, 3.46, and 3.47.

   Note: As no loop characterisation investigation was performed during the OSTT test campaign, the model calculated from the results of the FM test campaign was used.

The spectra of the closed-loop frequency noise show that in all cases, the suppression achieved brought the noise level well below the requirement. The mismatch in the frequency noise level at high frequencies in the EM results may be an indication that there were different noise levels during each of the measurements, as they were performed at different times.

The plots with the expected closed-loop value of the frequency noise based on the calculated noise suppression function and free-running
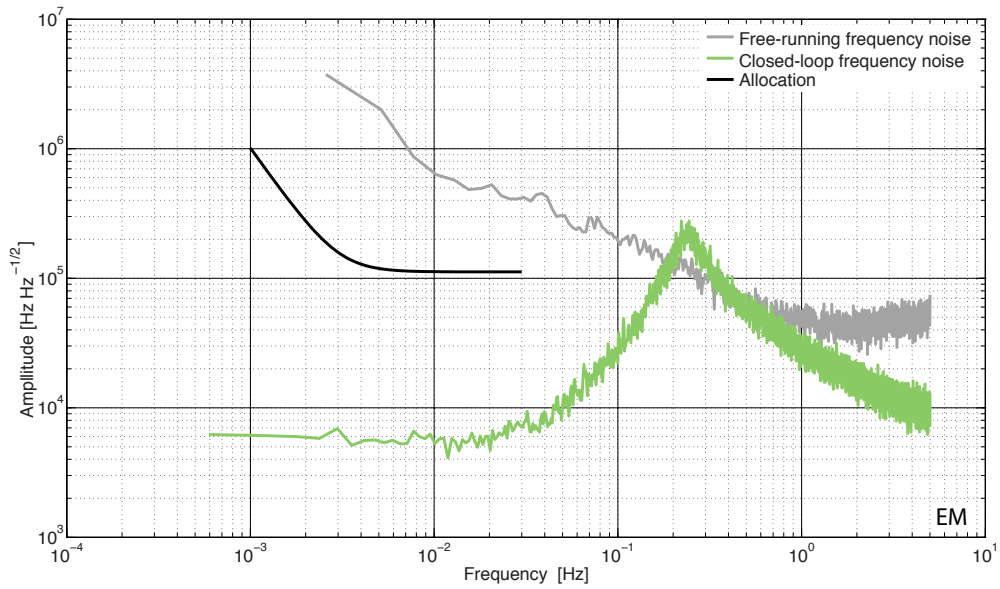
Figure 3.40: The closed-loop frequency noise, as measured during the EM test campaign. The free-running frequency noise from the EM campaign is shown in grey for comparison.
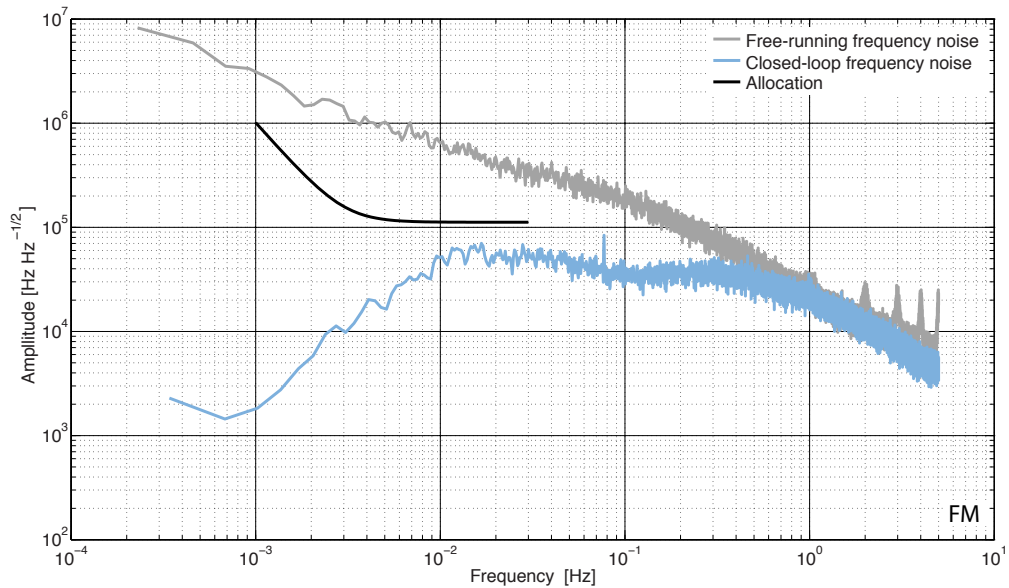
Figure 3.41: The closed-loop frequency noise, as measured during the FM test campaign. The free-running frequency noise from the FM campaign is shown in grey for comparison.

181
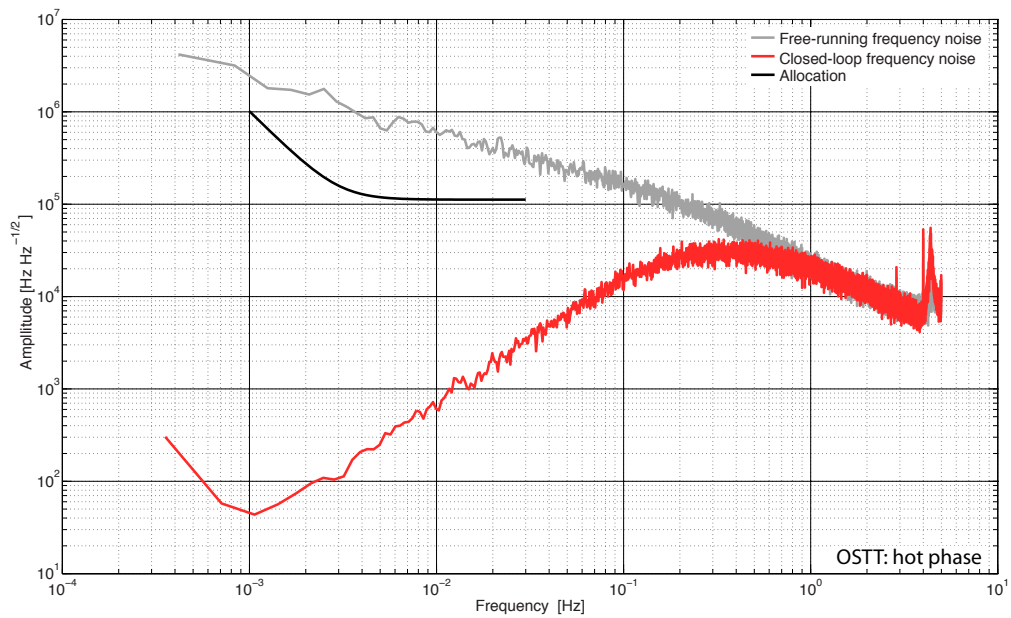
Figure 3.42: The closed-loop frequency noise, as measured during a hot performance measurement in the OSTT test campaign. The free-running frequency noise from the OSTT campaign is shown in grey for comparison.
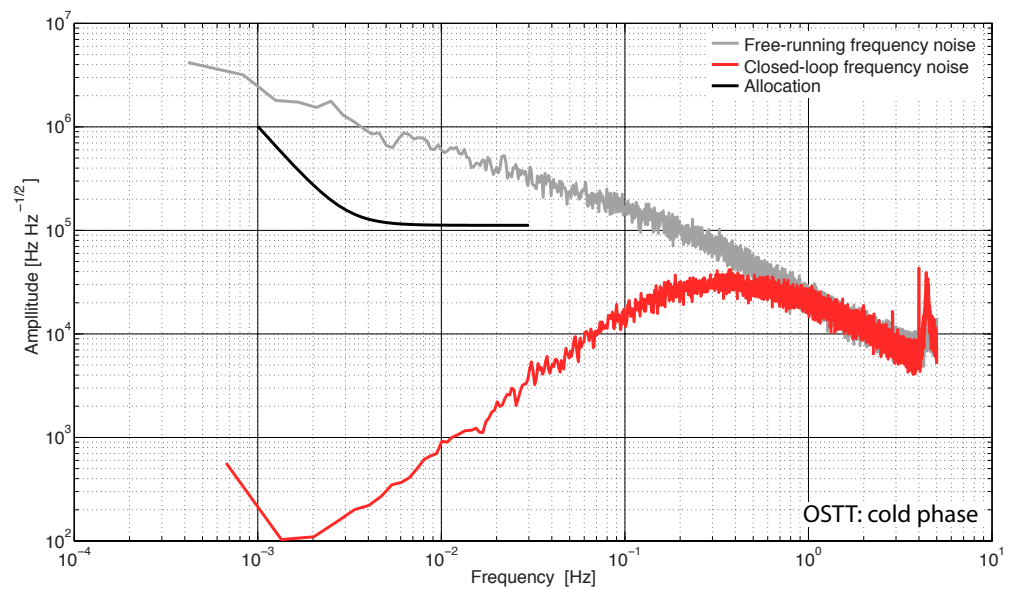
Figure 3.43: The closed-loop frequency noise, as measured during a cold performance measurement in the OSTT test campaign. The free-running frequency noise from the OSTT campaign is shown in grey for comparison.

noise do not all show the expected result. The EM result shows excess noise at low frequencies, and the FM result shows excess noise up to approximately 0.1 Hz. This could be due to a different noise level during the closed-loop measurement, or it could be that the loop may have a slightly different response when it is operating under closed conditions. The OSTT result matches the expected results, even though the exact control loop characteristics were not known, and were based on the FM noise suppression function.

The value of the closed-loop frequency noise at 30 mHz is shown in Table 3.17, along with the equivalent value of the free-running frequency noise and the gain of the OLTF.

	Free-running $[\mathrm{Hz}/\sqrt{\mathrm{Hz}}]$	OLG [dB]	Closed-loop $[\mathrm{Hz}/\sqrt{\mathrm{Hz}}]$
EM	4.20×10^5	38.67	6.93×10^3
FM	4.05×10^5	39.92	5.58×10^4
OSTT hot	3.21×10^5	NA	4.5×10^3
OSTT cold	3.21×10^5	NA	1.78×10^4

Table 3.17: The value of the closed-loop frequency noise at 30 mHz, as measured in the performance measurements of the EM, FM, and OSTT test campaigns. Also given are the values of the open-loop gain and free-running frequency noise at the same frequency.

Frequency noise component of the differential test mass displacement

1. The Ψ_F data was multiplied by the coupling coefficient for frequency noise into the differential test mass displacement, K, as determined from the frequency control loop characterisation test campaign analyses (see note below). The values of the coefficients used are given in Table 3.18.

   Note: The coupling coefficients were determined by two methods during the control loop characterisation analyses, the mean value was used in this analysis. As no control loop characterisation investigation was performed during the OSTT test campaign, the mean of the coefficients calculated during the free-running frequency noise investigations was used.
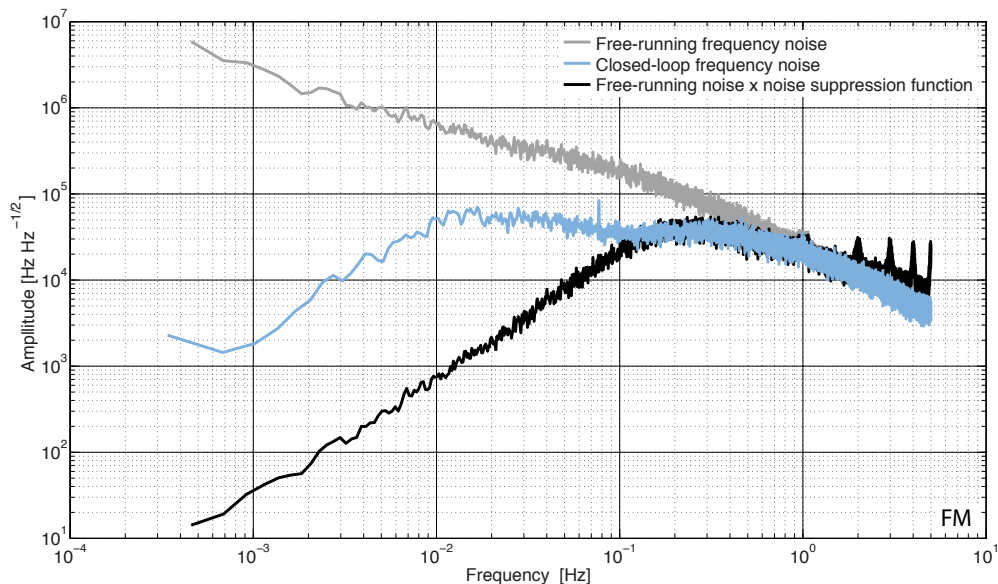
3 Frequency noise characterisation
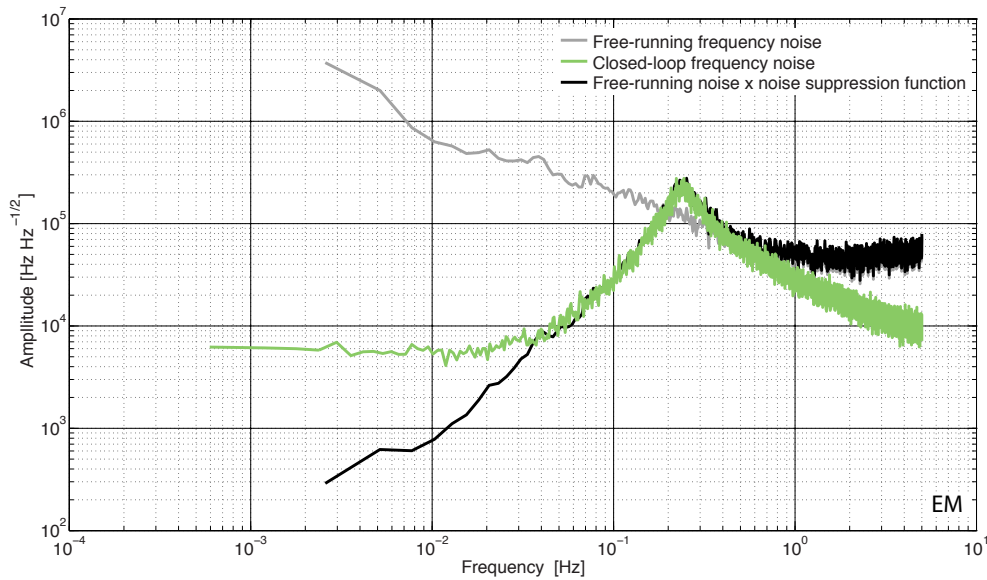
Figure 3.44: The free-running frequency noise from the EM test campaign, shown in grey, was multiplied by the calculated frequency control loop noise suppression function. The result of this is shown in black along with the measured value of the closed-loop frequency noise in green. The excess noise at low frequencies may be a result of differing noise levels between the two measurements, as they were performed at different times.
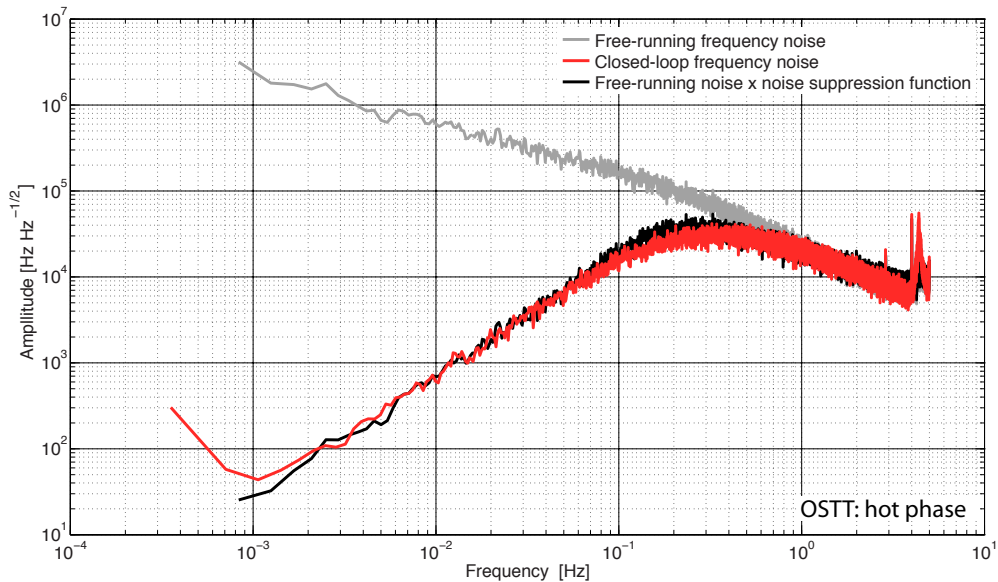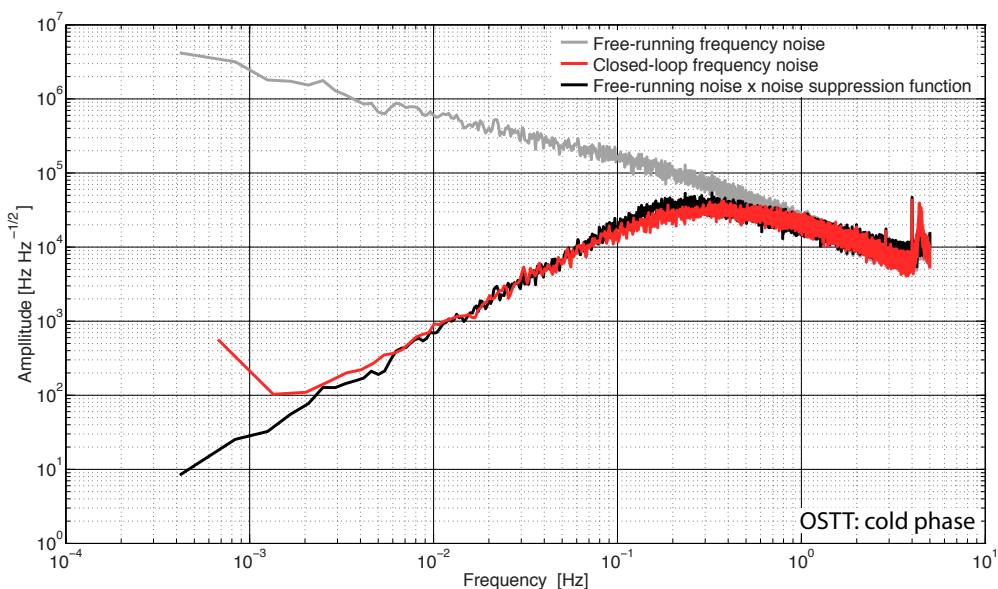

Figure 3.45: The free-running frequency noise from the FM test campaign, shown in grey, was multiplied by the calculated frequency control loop noise suppression function. The result of this is shown in black along with the measured value of the closed-loop frequency noise in blue. The excess noise at low frequencies may be a result of differing noise levels between the two measurements, as they were performed at different times.

Figure 3.46: The free-running frequency noise from the hot phase of the OSTT test campaign, shown in grey, was multiplied by the calculated frequency control loop noise suppression function from the FM test campaign, as no loop characterisation investigations were performed during the OSTT test campaign. The result of this is shown in black along with the measured value of the closed-loop frequency noise in red.

Figure 3.47: The free-running frequency noise from the cold phase of the OSTT test campaign, shown in grey, was multiplied by the calculated frequency control loop noise suppression function from the FM test campaign, as no loop characterisation investigations were performed during the OSTT test campaign. The result of this is shown in black along with the measured value of the closed-loop frequency noise in red.

	Coupling coefficient [m/rad]
EM	4.40×10^{-9}
FM	4.38×10^{-9}
OSTT	2.85×10^{-11}

Table 3.18: Values of the coupling coefficient for frequency noise into differential test mass displacement used in the analysis of the closed-loop frequency measurements.

2. The amplitude spectral density of the result was plotted along with the amplitude spectral density of the x_{12} channel. This gave the projection of the closed-loop frequency noise onto the differential test mass displacement. These results for the EM and FM test campaigns are shown in Figures 3.48 and 3.49. The results from the hot and cold phases of the OSTT test campaign are shown in Figures 3.50 and 3.51. For comparison, the equivalent results from the free-running frequency noise investigation are also shown.

   Note: The amplitude spectral densities were calculated using the default Hanning windowing function with 50 % overlap, 16 averages, and detrending of order one.
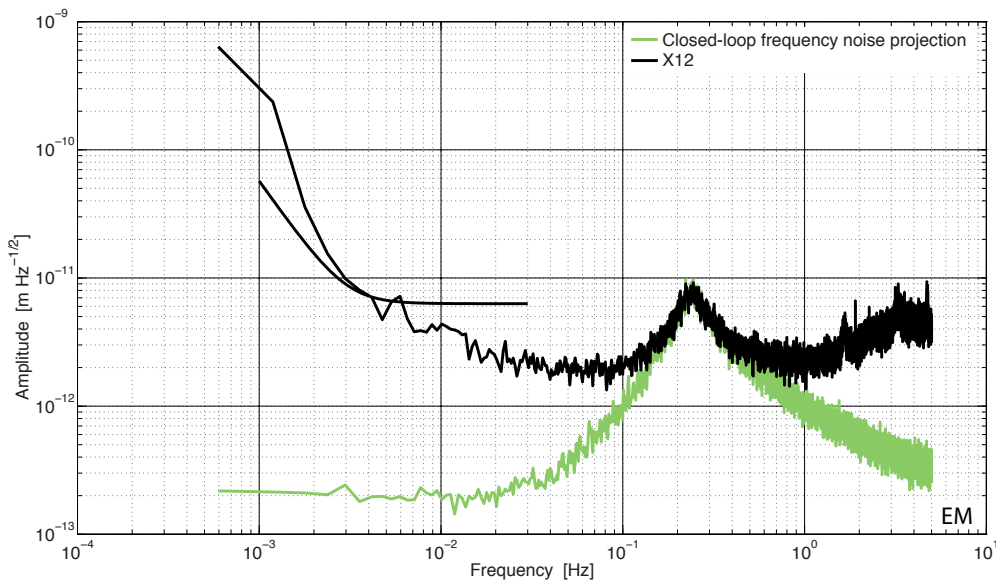
Figure 3.48: The projection of the closed-loop frequency noise onto the differential test mass displacement during an EM performance measurement.
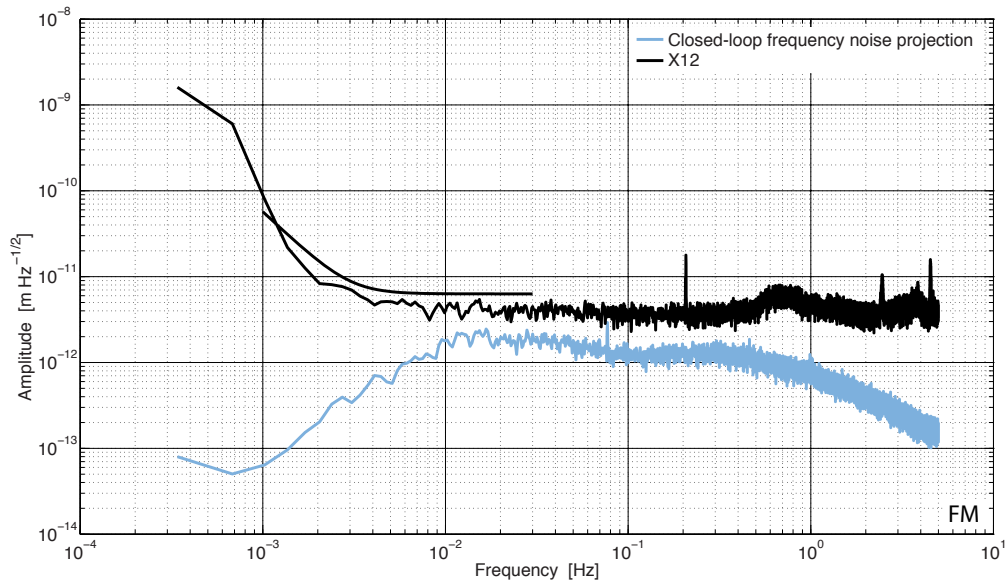
Figure 3.49: The projection of the closed-loop frequency noise onto the differential test mass displacement during an FM performance measurement.
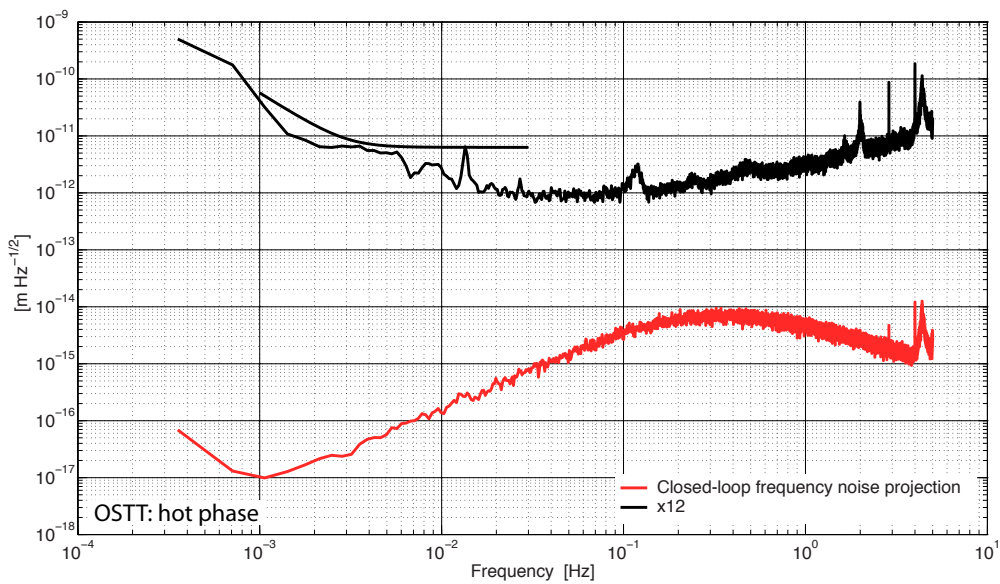
Figure 3.50: The projection of the closed-loop frequency noise onto the differential test mass displacement during a hot phase OSTT performance measurement.

Chapter 3
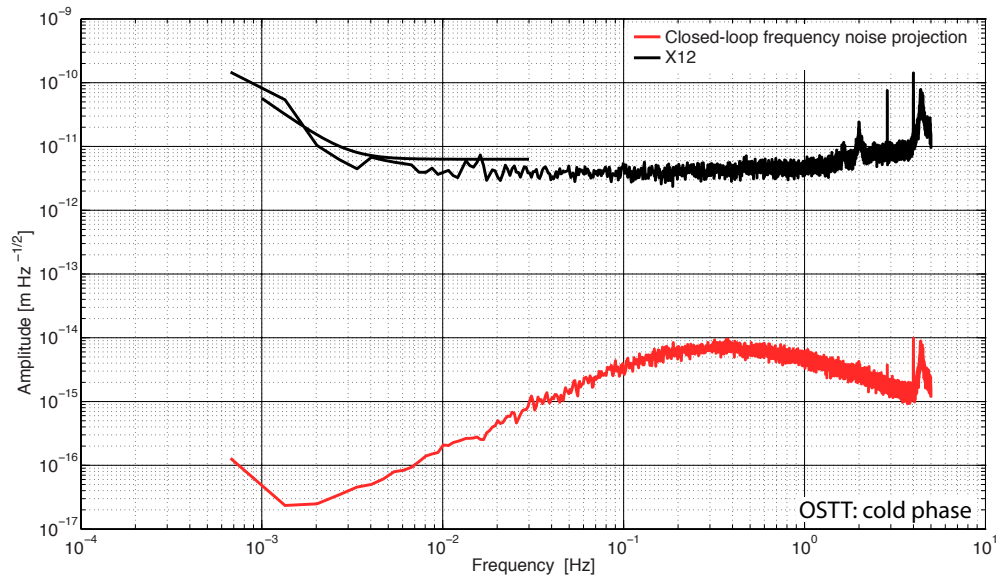
Figure 3.51: The projection of the closed-loop frequency noise onto the differential test mass displacement during a cold phase OSTT performance measurement.

Apart from a peak in the EM spectrum, the frequency noise projections onto the differential test mass displacement measurements demonstrate that the frequency noise is not the limiting noise source.

3.3.2 In-flight investigation

As previously mentioned, the specific procedure for an in-flight performance measurement is not described here, as it is already a well defined investigation. An overview of the suggested analysis procedure for the in-flight investigation is given in Figure 3.52. The sub-analyses for the data preparation, determination of the closed-loop frequency noise spectrum, and the projection of the frequency noise component onto the differential test mass displacement are given in Figures 3.53, 3.54a, and 3.54b.
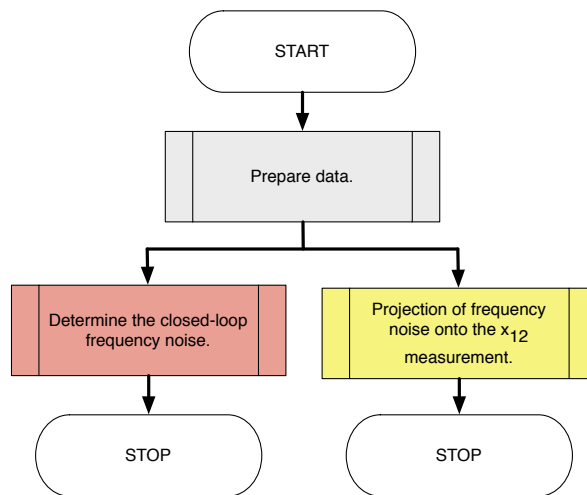
Figure 3.52: Overview of the in-flight frequency noise performance analysis.
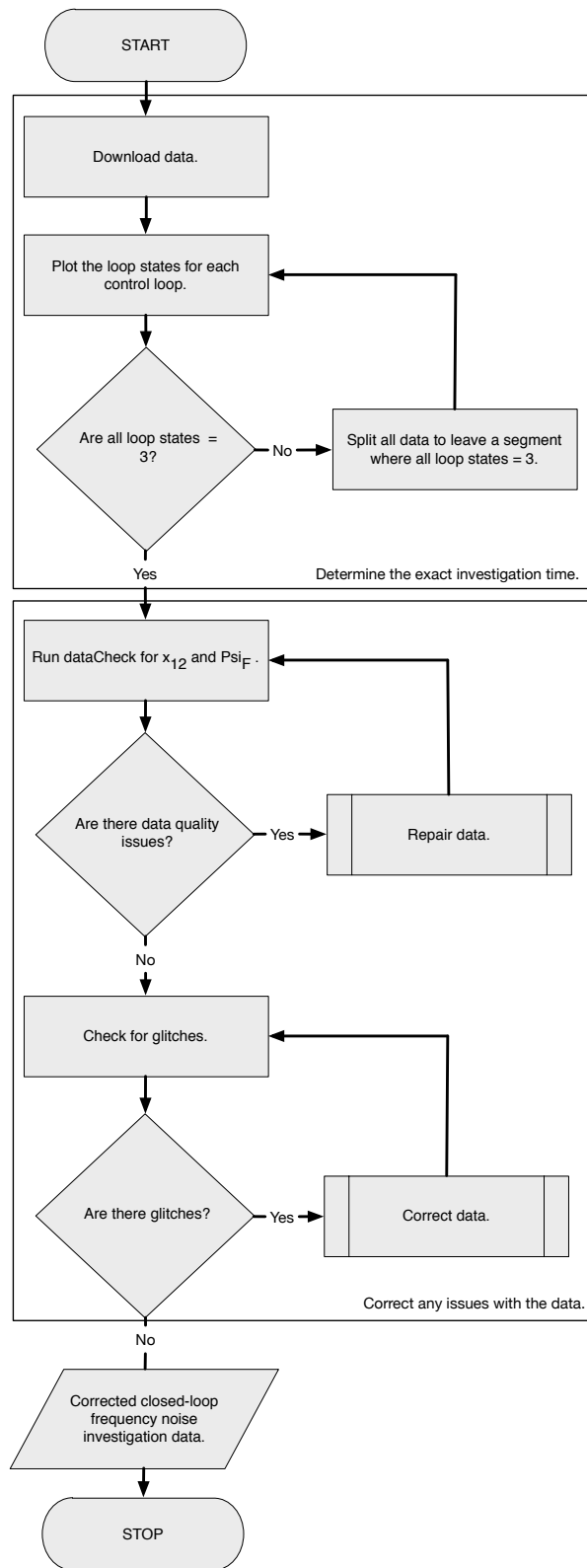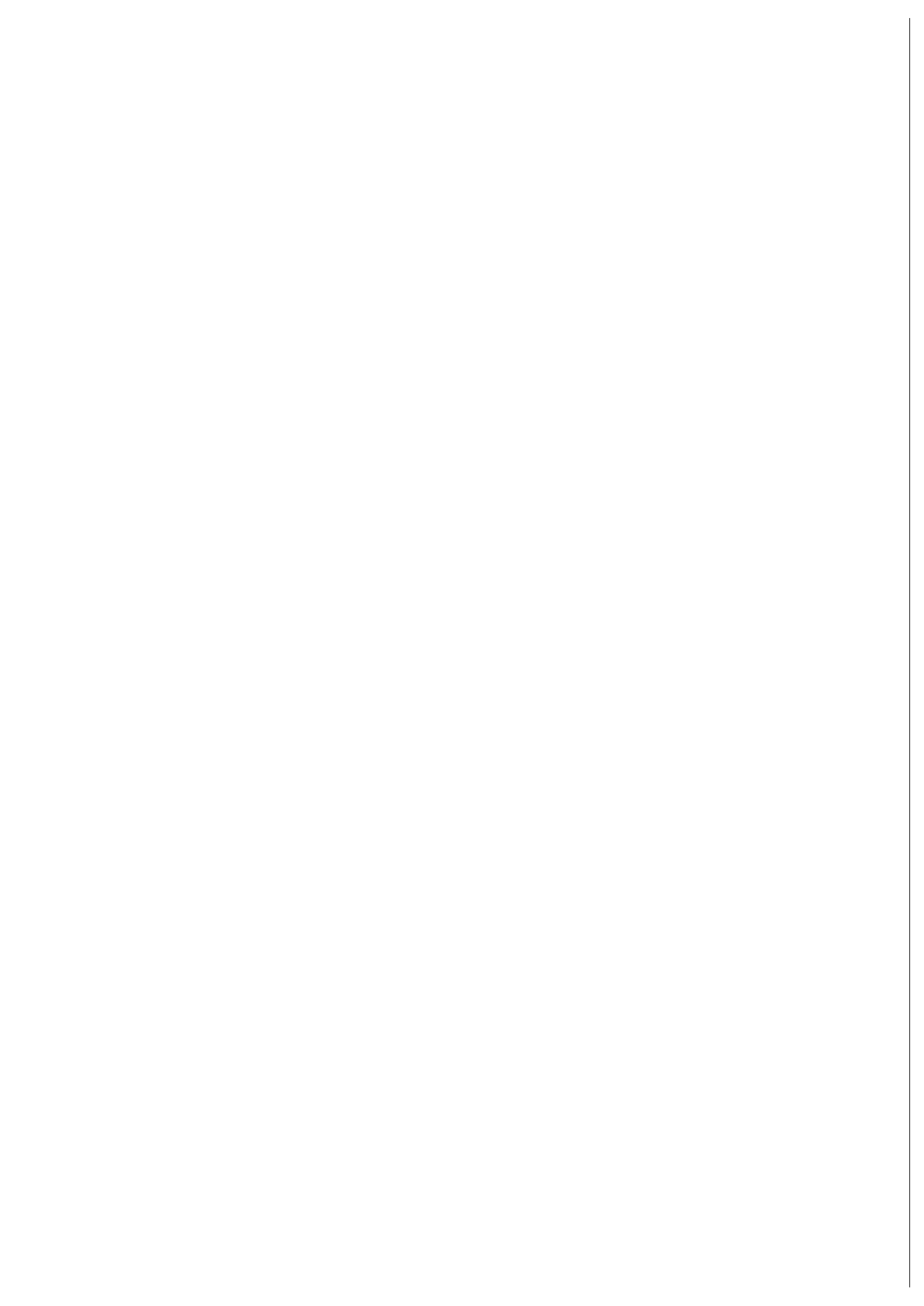
Figure 3.53: Data preparation sub-analysis procedure for the closed-loop frequency noise investigation.
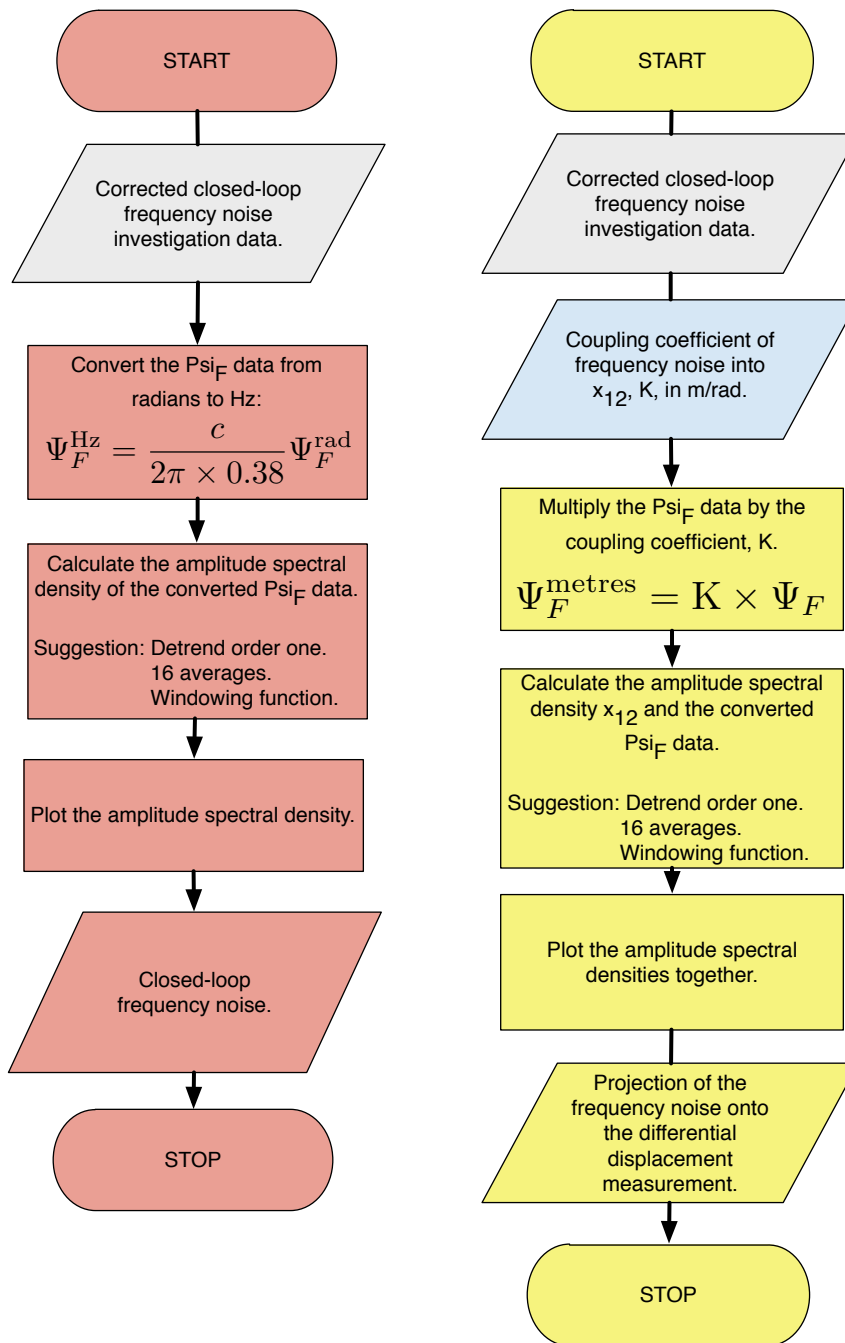
(a) Closed-loop frequency noise spectra sub-analysis.

(b) Closed-loop frequency noise projection sub-analysis.

Figure 3.54

191

4. Optical pathlength difference noise characterisation

Contents

The aims of this set of investigations are to measure the OPD noise, determine the coupling into the measurement of the differential test mass displacement, and characterise the control loop. The investigations can be split into the following:

- Measurement of free-running OPD noise:

    - Calculation of the free-running OPD noise spectrum;

- Determination of a broadband coupling coefficient for OPD noise into differential test mass displacement.

- Characterisation of the OPD control loop:

  - Controller characterisation;

  - Actuator calibration;

  - Calculation of the OLTF and noise suppression function;

  - Calculation of a coupling coefficient via applied modulations.

- Calculation of the OPD noise component of a closed-loop measurement.

The motivation for the investigations and related analyses are given in the following sections. The results of the equivalent investigations performed during the EM, FM, and OSTT test campaigns are also presented. Suggested procedures for performing and analysing the data in-flight are also given.

4.1 Free-running OPD noise

This investigation is necessary in order to determine the level of the free-running OPD noise. An additional output from the investigation is a coupling coefficient for OPD noise into the differential test mass displacement measurement.

Free-running optical pathlength difference noise

The primary aim of the free-running OPD noise investigation is the measurement of the OPD noise without any control loop suppression. This is necessary to:

- characterise the OPD noise;

- determine the gain required by the OPD control loop;

- provide a reference for comparison with the closed-loop noise measurement.

The OPD noise level depends upon the fluctuating optical pathlength mismatch between the measurement and reference beams in the interferometers, in addition to the coupling of electrical sidebands at the heterodyne frequency from the RF signals that drive the AOMs. The origin of this noise is discussed in detail in Section 2.2.2.

The OPD noise is measured by the reference interferometer output, Ψ_R, and the spectrum of the output is the measurement of the OPD noise level.

$$\widetilde{\mathrm{OPD}} \longrightarrow \boxed{\begin{array}{c} \text{Reference} \\ \text{interferometer} \end{array}} \longrightarrow \Psi_R$$
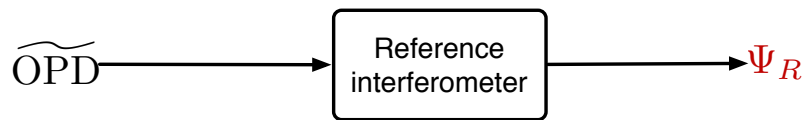
The level of the free-running noise, along with the allocation for the suppressed value of $\widetilde{\Psi}_R$ can be used to determine the amount of gain required by the OPD control loop. This is discussed in Box 4.1.

The results from the FM and OSTT test campaigns provide the best estimates of the free-running OPD noise that can be expected in-flight, as they were performed with setups that are most representative of the flight configuration.

195

4 Optical pathlength difference noise characterisation

The allocation for the OPD noise, measured by Ψ_R, is:

$$\delta\widetilde{\Psi}_R \leq 1.6 \times 10^{-3} \sqrt{1 + \left(\frac{f}{3\,\mathrm{mHz}}\right)^{-4}} \frac{\mathrm{rad}}{\sqrt{\mathrm{Hz}}} \qquad (4.1)$$

in the measurement bandwidth of $1\,\mathrm{mHz} \leq f \leq 30\,\mathrm{mHz}$, as discussed in Section 2.2.2.

In order to meet this requirement, the free-running OPD noise, Ψ_R^{fr}, must be suppressed by the OPD control loop. The amount of gain required to achieve this level of suppression is defined by:

$$\mathrm{OLG}(f) \geq 20 \log\left(\frac{\widetilde{\Psi}_R^{\mathrm{fr}}}{\widetilde{\Psi}_R}\right) \mathrm{dB} \qquad (4.2)$$

The value of Ψ_R^{fr} is the result of the free-running OPD noise investigation.

Box 4.1: Calculating the amount of OPD loop gain required to suppress the measured OPD noise determined in the free-running OPD noise investigation [32].

Broadband coupling of optical pathlength difference noise

A large part of the OPD noise, due to the common-mode pathlength fluctuations in the interferometers, is removed by the subtraction of the reference interferometer measurement from the output, as discussed in Section 2.2.2. The remaining noise is due to imperfect subtraction, and the coupling of electrical sidebands from the RF signals that drive the AOMs. This noise is non-linear, but the requirement is that it must contribute less than $2 \times 10^{-12}\mathrm{m}/\sqrt{\mathrm{Hz}}$ at $30\,\mathrm{mHz}$ to the differential test mass displacement measurement. The higher OPD noise level with the OPD control loop free-running can be used to determine a coupling coefficient, M, for the OPD noise into the x_{12} channel.
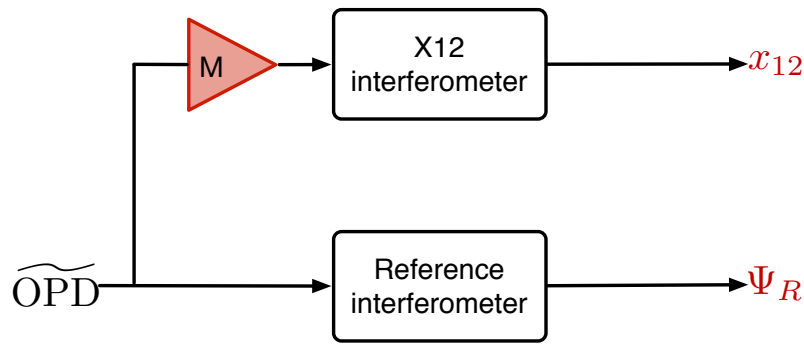
Figure 4.1: A simplified block diagram showing the coupling of OPD noise, $\widetilde{\text{OPD}}$, into the measurement of the differential test mass displacement via a coupling coefficient, M.

The broadband coupling coefficient, in units of m/rad, can be calculated from the transfer function of the Ψ_R and x_{12} channels. The coefficient can be used to project the OPD noise component onto a measurement of the differential test mass displacement.

4.1.1 Test campaign results

Free-running OPD noise measurements were performed in the EM, FM, and the OSTT test campaigns. The information for each measurement and the corresponding analysis can be found in Appendix 8, Tables 8.8, 8.9, and 8.10 for the EM, FM, and OSTT campaigns respectively. Initially, all of the timeseries data was analysed in the same manner, as described under 'Overview of the analysis'. The analysis of the free-running OPD noise, and the calculation of the broadband coupling coefficient are then described under the associated headings.

Overview of the analysis

The telemetry used in this analysis can be found in Table 4.1. The names of the parameters in each of the LTPDA databases can be found in Appendix 7. The initial processing of the data was performed as follows:

1. The data, defined in Table 4.1, was downloaded according to the

4 Optical pathlength difference noise characterisation

Parameter	Description	Frequency [Hz]	ID
S^{FF}	Fast frequency loop state	1 Hz	LST17361
S^{SF}	Slow frequency loop state	1 Hz	LST17364
S^{OPD}	OPD loop state	1 Hz	LST17367
S^{SP}	Slow power loop state	1 Hz	LST17358
y^{FF}	Fast frequency feedback	1 Hz	LST17340
		10 Hz	
y^{SF}	Slow frequency feedback	1 Hz	LST17345
		10 Hz	
y^{OPD}	OPD feedback	1 Hz	LST17350
		10 Hz	
y^{SP}	Slow power feedback	1 Hz	LST17357
		10 Hz	
Ψ_R	Ref. ifo. output	10 Hz	LST12407
x_{12}	X12 ifo. output	10 Hz	LST10130

Table 4.1: The telemetry parameters used in the analyses of the EM, FM and OSTT test campaign free-running OPD noise investigations.

dates and times defined in the associated test campaign reports [32] [43] [46].

2. The data was split to leave a segment where the OPD control loop was open (state = 1, feedback = 0), and the other control loops were in a stable operating state for the duration of the measurement.

3. The main channels, Ψ_R and x_{12}, were checked to identify any data quality issues, and repaired accordingly. More details about data quality issues and their repair can be found in Appendix 9.

   Note: Due to glitches in the timeseries, the data in both the EM and OSTT test campaigns was split, reducing the length of data for analysis. The result was that any low frequency effects, in both the free-running and coupling coefficient analyses, were not observable.

4. The Ψ_R and x_{12} channels were detrended with order three to remove any DC offset in addition to any linear, quadratic, and

cubic effects.

Free-running optical pathlength difference noise

The pre-processed Ψ_R channel was then used to determine the free-running OPD noise as follows:

1. The amplitude spectral density of Ψ_R was calculated using 16 averages. The results from the EM, FM, and OSTT test campaigns are shown in Figure 4.2.
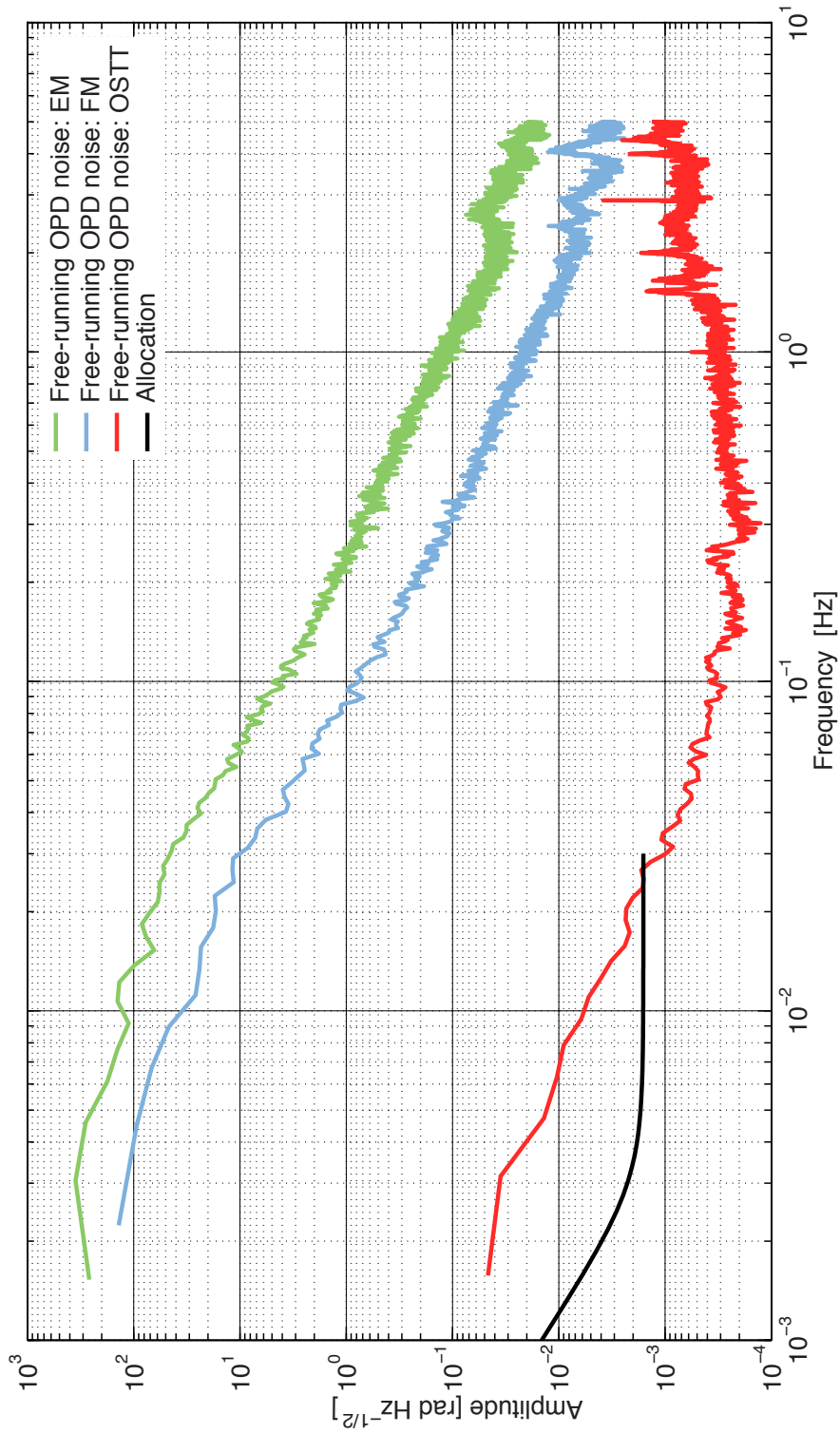
Figure 4.2: Spectra of the free-running OPD noise as measured in the EM (green), FM (blue), and OSTT (red) test campaigns.

The magnitude of the OPD noise decreases with each test campaign, and the most representative results, from the OSTT test campaign, show a dramatic reduction in the noise level. This is likely to be because the setup under test was more stable, being entirely isolated within the satellite body and a vacuum tank for the duration of the measurement. The OSTT result can be considered to be the best estimate of the noise level that can be expected in-flight. The level of the OPD noise at 30 mHz, along with the control loop gain required for the noise to be suppressed to the required 1.6×10^{-3} rad/$\sqrt{\text{Hz}}$ level, are given in Table 4.2. The OSTT value is less than the requirement at 30 mHz, but increases at lower frequencies and therefore suppression is still required.

	OPD noise [rad/$\sqrt{\text{Hz}}$]	Suppression required	Gain [dB]
EM	40	27.6×10^{-3}	88.8
FM	10	5.27×10^{-3} s	74.4
OSTT	1×10^{-3}	NA	NA

Table 4.2: Approximate values of the free-running OPD noise at 30 mHz, with the suppression and minimum gain required for the frequency control loop to suppress the noise to the allocated level. The OSTT value is less than the requirement at 30 mHz, so no values for the suppression are given here, although the noise level at lower frequencies is above the requirement and requires suppression.

Broadband coupling of optical pathlength difference noise

The pre-processed x_{12} and Ψ_R channels were used to determine the coupling coefficient, M, for OPD noise into differential displacement noise as follows:

1. The transfer function of Ψ_R into x_{12} was calculated.

   Note: The transfer function was calculated using 20 averages, and a Hanning windowing function with a 50 % overlap.

2. The transfer function was binned, and the results for the EM, FM, and OSTT test campaigns are shown in Figures 4.3, 4.4, and 4.5 respectively.

4 Optical pathlength difference noise characterisation

3. The coherence of Ψ_R and x_{12} was calculated. The results are shown alongside the respective transfer function plots.

   Note: Calculated with 20 averages.

4. Ideally, a frequency range would have been selected where the transfer function was relatively flat, and the coherence was high. However, the EM and FM transfer functions do not show a very flat response and the coherence is less than 0.5 indicating a low coupling of OPD noise into the x_{12} output. Therefore, a frequency range nearest to the measurement bandwidth of $1\,\mathrm{mHz} \leq f \leq 30\,\mathrm{mHz}$ was used. From the OSTT result the low frequency region, corresponding to the measurement bandwidth, showed high coherence, and was selected. The selected region is highlighted in grey on the respective transfer function plots.

5. A coupling coefficient was calculated by determining the mean value of the transfer function in the selected frequency region. This determined an upper-limit estimate of the coupling coefficient. The results are shown in Table 4.3.

Campaign	Coefficient [m/rad]	Error [m/rad]
EM	3.66×10^{-13}	3.16×10^{-13}
FM	3.00×10^{-12}	2.05×10^{-12}
OSTT	4.44×10^{-9}	1.45×10^{-10}

Table 4.3: The calculated values of the coupling coefficient for free-running OPD noise into the differential displacement measurement.

For both the EM and FM test campaigns the coupling of the OPD noise into the x_{12} channel was determined to be very low, equivalent to zero, when considering the relative size of the errors. The coupling coefficient from the OSTT results was higher. Considering the low coherence of the channels, and the difficulty in selecting a region of the transfer function, these coefficients cannot be considered as anything more than upper limits on the coupling of OPD noise into differential test mass displacement.
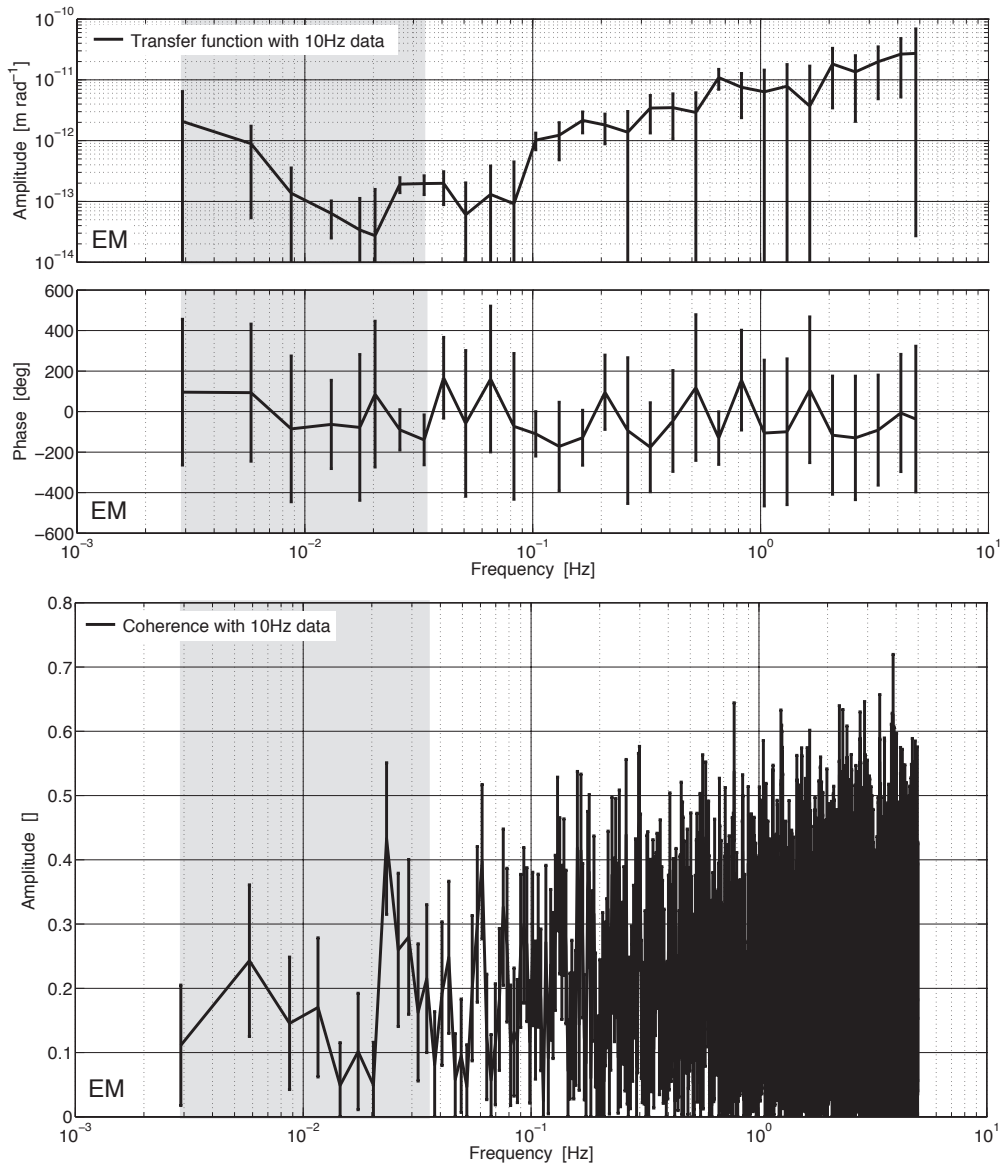
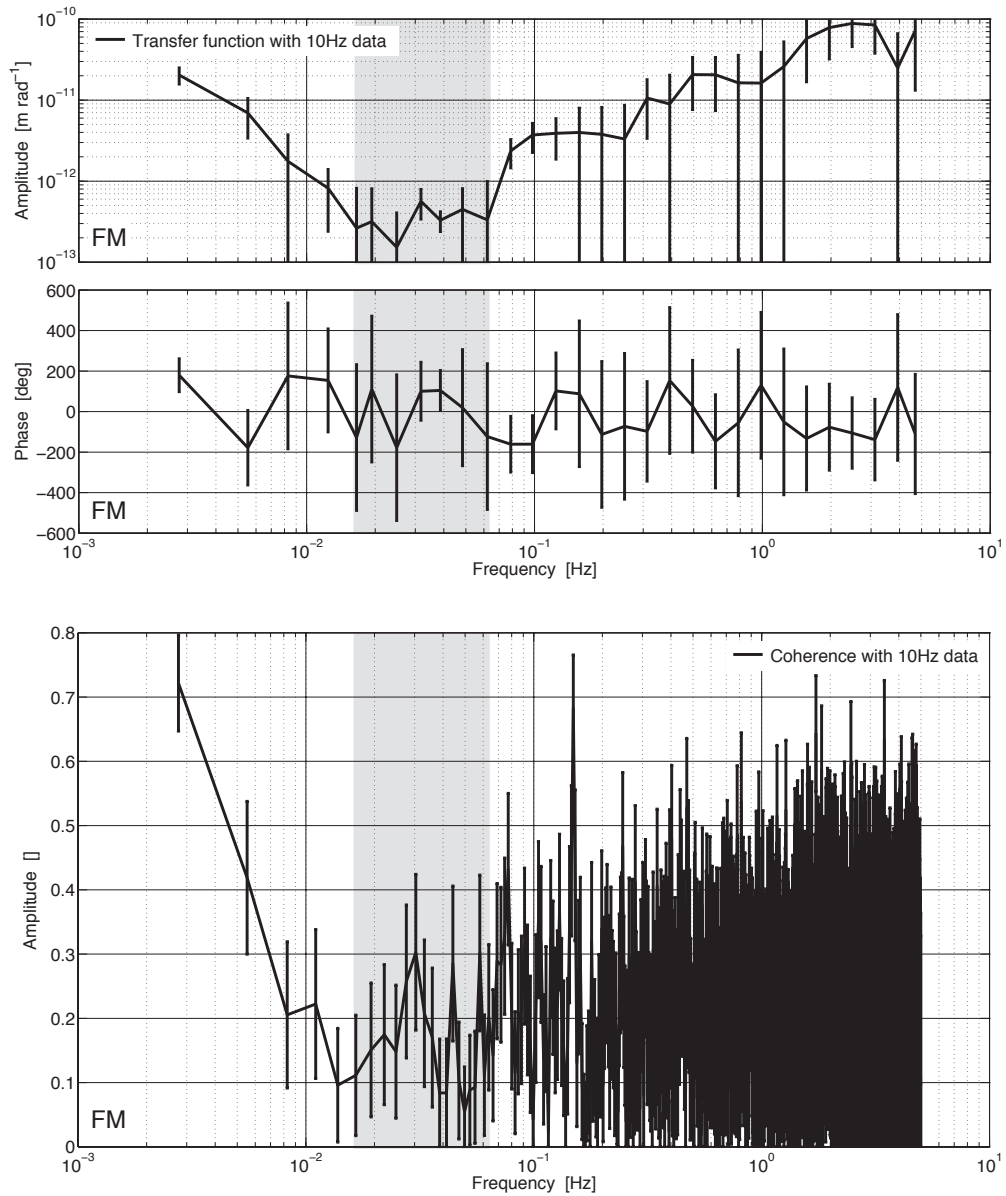**Figure 4.3:** Plots of the transfer function and coherence of Ψ_R and x_{12} for the EM test campaign investigation of the free-running OPD noise. The grey shaded area represents the frequency region used to determine the coupling coefficient for OPD noise into differential displacement.
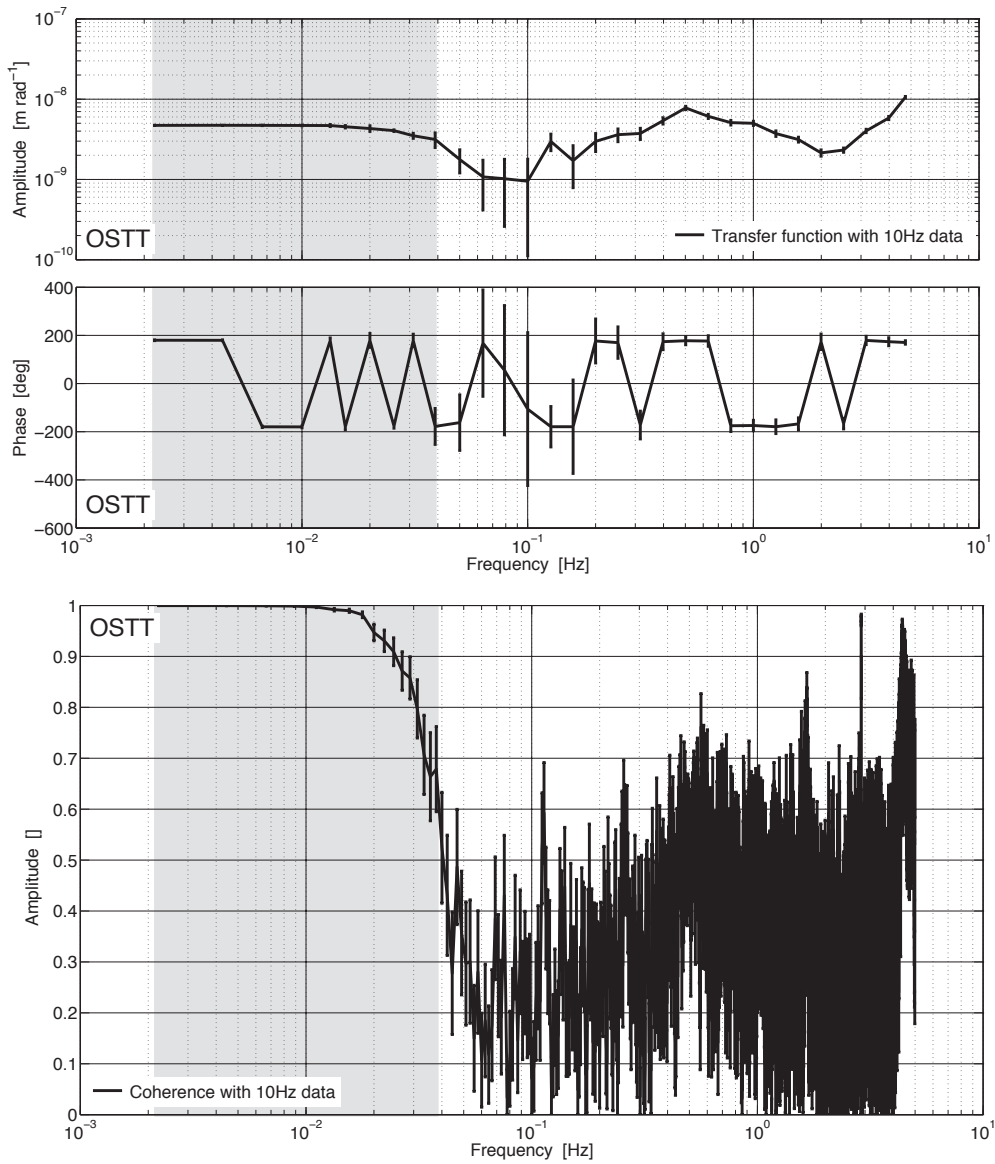
Chapter 4

Figure 4.4: Plots of the transfer function and coherence of Ψ_R and x_{12} for the FM test campaign investigation of the free-running OPD noise. The grey shaded area represents the frequency region used to determine the coupling coefficient for OPD noise into differential displacement.

Figure 4.5: Plots of the transfer function and coherence of Ψ_R and x_{12} for the OSTT test campaign investigation of the free-running OPD noise. The grey shaded area represents the frequency region used to determine the coupling coefficient for OPD noise into differential displacement.

4 Optical pathlength difference noise characterisation

OPD noise component of the differential test mass displacement

The coupling coefficient was used to determine the OPD noise component of the differential test mass displacement:

1. The Ψ_R data was multiplied by the calculated coupling coefficient. The amplitude spectral density of the result and the amplitude spectral density of x_{12} were plotted together to show the projection of the OPD noise onto the differential displacement measurement. The results are shown in Figure 4.6.

   Note: Due to the large errors on the EM and FM coupling coefficients, only the OSTT result was used.

The results shows that at low frequencies, where the coupling coefficient was calculated, the projection of the OPD noise does not accurately reflect the differential displacement results. This implies that there is potentially another noise source influencing both the Ψ_R and x_{12} channels. This is similar to the effect observed in the frequency noise characterisation investigations discussed in Box 3.2.
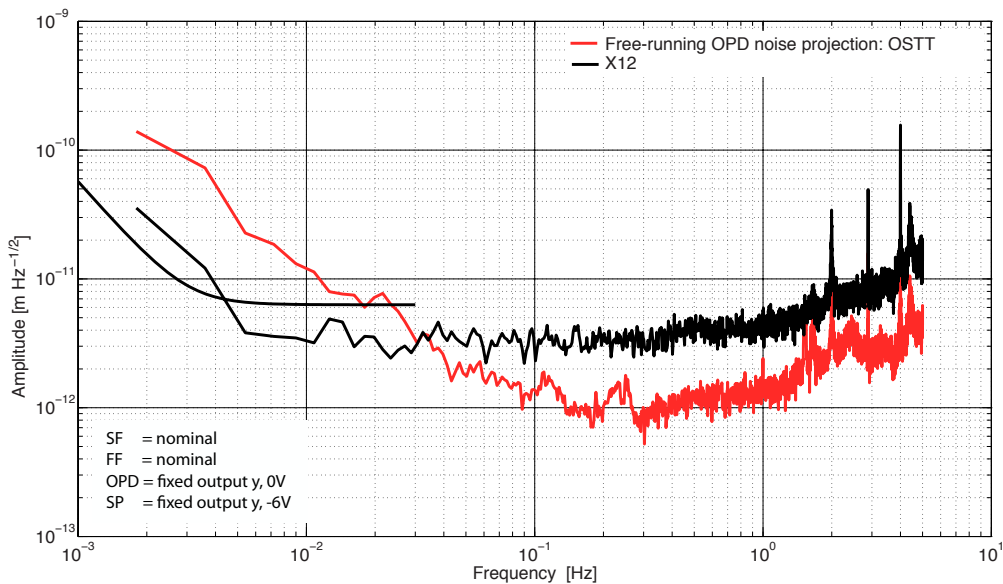

Figure 4.6: A plot of the free-running OPD noise in the OSTT test campaign projected onto the x_{12} measurement, plotted with the allocation for the OMS measurement noise in the measurement bandwidth.

The x_{12} spectrum from the OSTT results shows that the overall noise level is very low, as the requirement for the noise of the differential displacement is almost achieved even with free-running OPD noise.

4.1.2 In-flight investigation

The in-flight free-running OPD noise investigation requires the test masses to be controlled via DFACS science mode 1.2. In this mode, test mass one is maintained in drag-free conditions, and test mass two is suspended using the capacitive actuators. The requirements for the setup of the investigation, and the telemetry required, are shown in Table 4.4. The OPD loop should be operating in the 'fixed feedback y' state with zero feedback, with the other loops operating under nominal conditions. The measurement is run for 10 hours, this duration was selected to ensure that a segment of at least 10000 s would be suitable for use in the analysis, i.e., without glitches. The procedure for implementing the in-flight investigation is given in Figure 4.7.

An overview of the suggested in-flight analysis is given in Figure 4.8. The analysis is split into several sub-analyses, each represented by a particular colour:

- the data preparation, represented by gray, is shown in Figure 4.9;

- the free-running OPD spectrum segment of the analysis, represented by red, is detailed in Figure 4.10a;

- the procedure for calculating the coupling coefficient for OPD noise into differential test mass displacement, represented in blue, is shown in Figure 4.10b;

- the procedure for projecting the OPD noise component onto the differential test mass displacement, represented by yellow, is shown in Figure 4.11.

Chapter 4

Investigation	Free-running OPD noise		
OMS state	TMs drag-free		
Loop states	SF	Fixed output y	
	FF	Fixed output y	
	OPD	Nominal	
	SP	Nominal	
	FP	Nominal	
Telemetry required	128,3	x_{12}	LST10130
		Ψ_R	LST12407
	128,4	SF feedback	LST17345
		FF feedback	LST17340
		OPD feedback	LST17350
		SP feedback	LST17357
	3,25	SF state	LST17364
		FF state	LST17361
		OPD state	LST17367
		FP state	LST17358
		SSC	SCT70388
Length	10 hours		

Table 4.4: An overview of the key information relating to the experiment for measuring the free-running OPD noise. For the telemetry names associated with each parameter refer to Appendix 7.
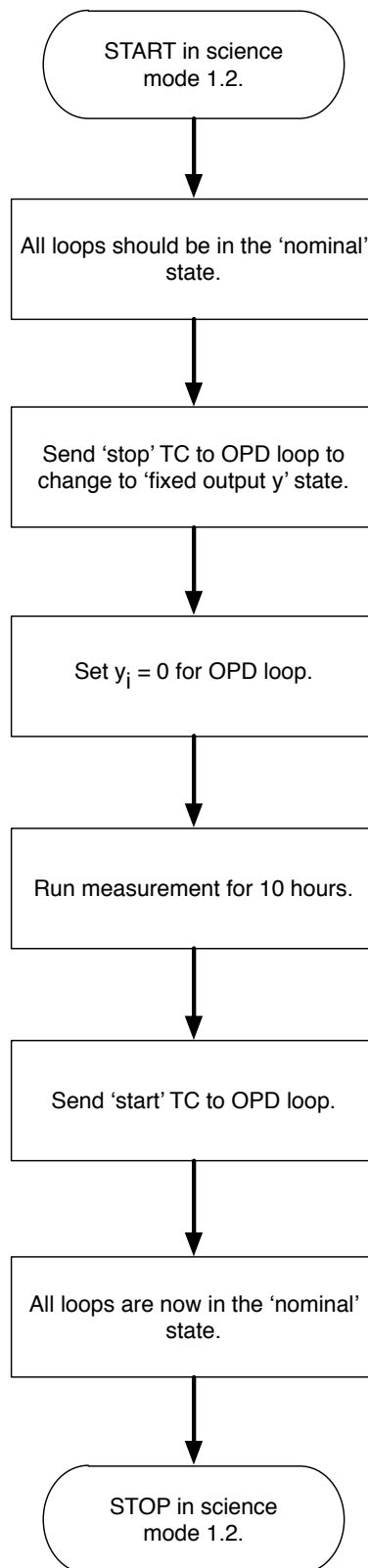
START in science
mode 1.2.

All loops should be in the 'nominal'
state.

Send 'stop' TC to OPD loop to
change to 'fixed output y' state.

Set $y_i = 0$ for OPD loop.

Run measurement for 10 hours.

Send 'start' TC to OPD loop.

All loops are now in the 'nominal'
state.

STOP in science
mode 1.2.

Chapter 4

Figure 4.7: A flowchart showing the in-flight procedure for measuring the free-running OPD noise.
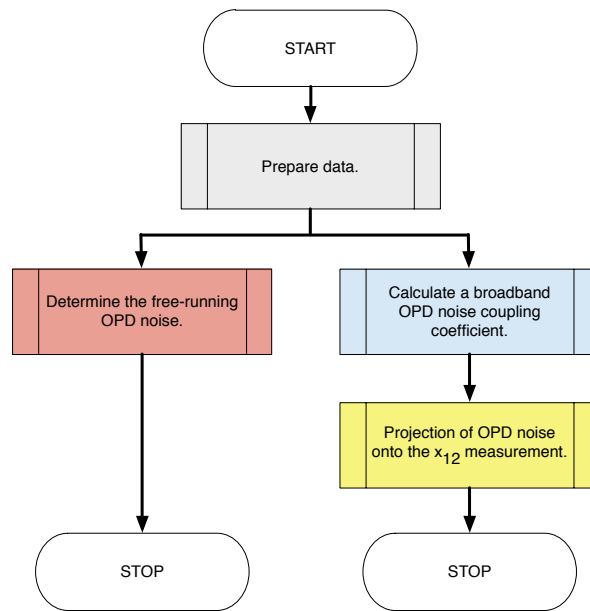
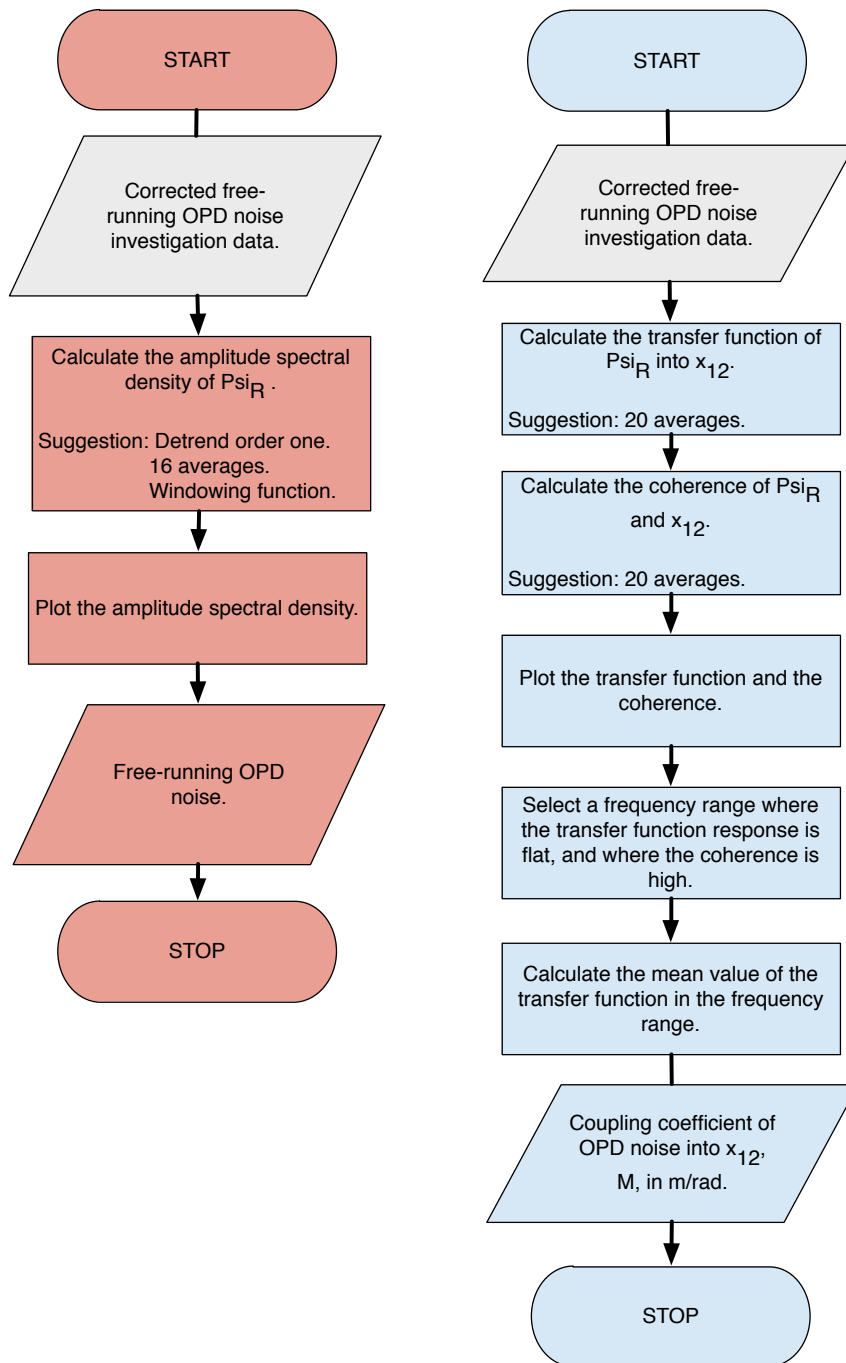**Figure 4.8:** A flowchart showing the overview of the suggested in-flight free-running OPD noise analysis.
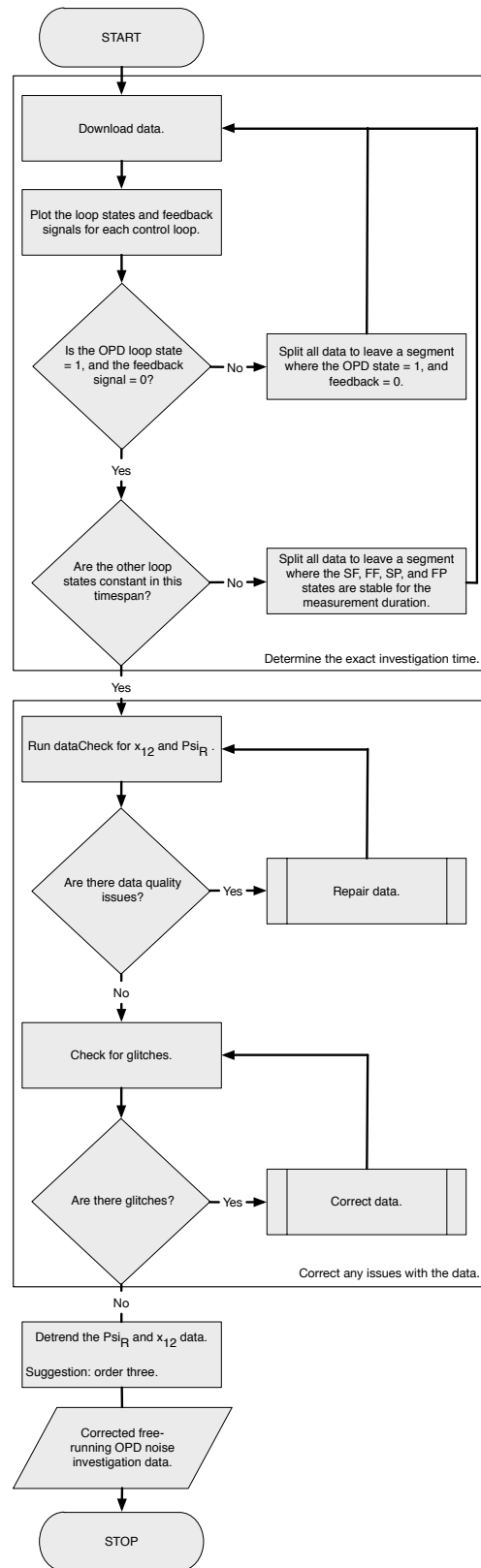
Figure 4.9: A flowchart showing the data preparation step of the suggested in-flight free-running OPD noise analysis.

(a) A flowchart showing the determination of the spectrum step of the suggested in-flight free-running OPD noise analysis.

(b) A flowchart showing the procedure for calculating a coupling coefficient for OPD noise into differential test mass displacement step of the suggested in-flight free-running OPD noise analysis.
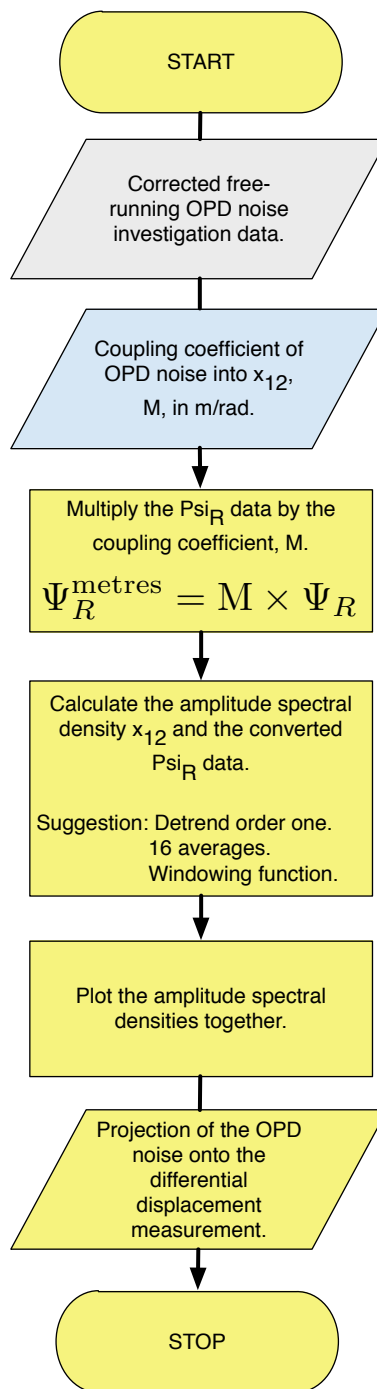
Figure 4.10

Figure 4.11: The procedure for projecting an OPD noise measurement onto the differential test mass displacement.

4.2 Control loop characterisation

The in-flight characterisation of the OPD control loop is necessary in order to:

- to ensure the loop is functioning as expected;

- to determine whether the response of the OPD loop needs to be changed via the redefinition of the a and b coefficients of the controller.

This investigation requires known modulation signals at a range of frequencies to be input into the OPD control loop via the δx^{OPD} input. Using the available control loop telemetry parameters, the results of the investigation can be analysed to determine the response of the individual loop components, and the loop as a whole. The individual analyses are:

- controller characterisation;

- actuator calibration;

- determination of the OLTF and noise suppression function;

and additionally:

- calculation of a coupling coefficient for OPD noise into differential test mass displacement.

Each of these sub-analyses is based upon the transfer function of combinations of the available loop parameters, as detailed in the following sections. As for the characterisation of the frequency control loop, two methods can be used to determine the results. The first method involves directly calculating the transfer function between the appropriate timeseries parameters. The second method involves splitting the timeseries parameters into segments, each containing a modulation at a single frequency. A DFT of each segment can be calculated at the frequency of the applied modulation. The ratio of the DFTs from the required parameters should produce the same result as the transfer function method.

214

The motivation for each sub-analysis is presented under the associated heading below. The results of the OPD control loop OLTF investigations performed during the EM and FM ground-based test campaigns are then discussed. Finally, a procedure for performing the investigation in-flight is presented, along with a suggested method for the analysis of the data.

Controller characterisation

The response of the OPD loop controller is the result of the digital control law described in Section 2.3, with some coefficients, a and b. These coefficients are predefined and uploaded into the SDP. If necessary, they can be changed in-flight via telecommand. These parameters are the only part of the loop that can be changed during in-flight operation to alter the overall loop behaviour.
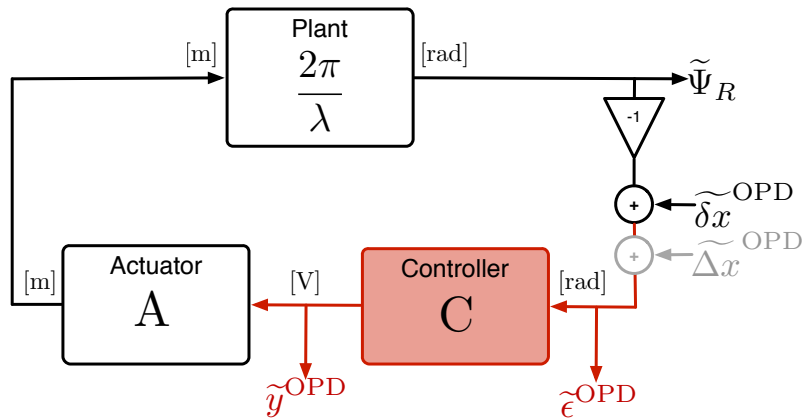

Figure 4.12: A simplified block diagram of the OPD control loop with the components and signals required for the characterisation of the controller highlighted in red. Each loop component is represented by the associated Laplace transform.

The response of the controller is determined by the relationship between the output and input of the controller. These parameters, the OPD feedback signal, y^{OPD}, and the OPD error signal, ϵ^{OPD}, are available on-ground via the telemetry. The steady-state response of the controller is therefore defined according to:

$$C(f) = \frac{\widetilde{y}^{\mathrm{OPD}}}{\widetilde{\epsilon}^{\mathrm{OPD}}} \; .$$

(4.3)

where the tilde represents the FT of the signal.

The result can be compared to a model based on the expected a and b coefficients that have been implemented in the DMU, as described in Box 2.4. If the model does not match the result, then the model can be fitted to the result to determine the actual a and b values that were applied.

Actuator calibration

The OPD loop actuators are two PZTs that act in a push-pull configuration to adjust the relative length of the reference and measurement beams in the LMU. The gain of the actuators needs to be determined in order to ensure that they are functioning as required. This is particularly important for the OPD control loop in order to identify if both actuators are functioning correctly. In the case where one actuator is not functioning, the full feedback can be applied via the other actuator. If the calculated gain of the actuators is not as high as required, then the loop will not suppress the OPD noise to the required level. In this scenario, the a and b coefficients of the controller need to be redefined to compensate.
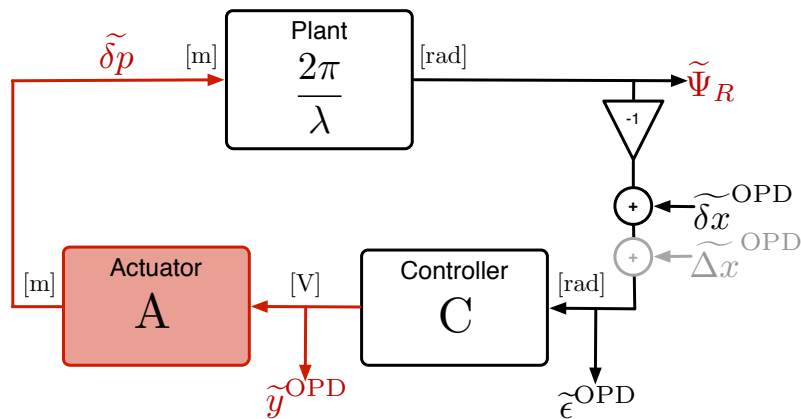

Figure 4.13: A simplified block diagram of the OPD control loop, with the components and signals required for the calibration of the actuator highlighted in red. Each loop component is represented by the associated Laplace transform.

The output from the actuator, referred to here as the applied pathlength change, δp, is not an available loop output. However, it can be

calculated from the output of the reference interferometer, Ψ_R:

$$\delta p = \frac{\lambda}{2\pi} \Psi_R \tag{4.4}$$

where $\lambda = 1064 \times 10^{-9}$m. This can be rewritten to define a constant for the conversion of Ψ_R, in radians, to δp, in metres:

$$\frac{\delta p}{\Psi_R} = 1.69 \times 10^{-7} \frac{\text{m}}{\text{rad}} \tag{4.5}$$

The steady-state response of the actuator is defined by:

$$\text{A}(f) = \frac{\widetilde{\delta p}}{\widetilde{y}^{\text{OPD}}} \tag{4.6}$$

where the tilde represents the FT of the signal.

The amplitude of the resulting Bode plot defines the gain of the actuator. To enable a more accurate determination of the gain, a model based on the design parameters of the actuator can be made, and fitted to the results. The phase of the Bode plot will also determine any delay introduced in the actuator.

Open-loop transfer function and noise suppression function

The calculation of the OLTF is necessary in order to:

- Ensure that the gain of the loop is sufficient to accurately suppress the OPD noise to meet the specified allocation. The allocation for the OPD noise is 1.6×10^{-3} rad/$\sqrt{\text{Hz}}$ at $30\,\text{mHz}$ (see Section 2.2.2). The gain required depends upon the free-running OPD noise as measured in the investigation described in Section 4.1.

- Determine whether the loop is stable, i.e., whether the phase and gain margin of the loop are sufficiently large.

4 Optical pathlength difference noise characterisation

If the OLTF of the loop does not meet the requirements for the gain and/or stability then it would be necessary to redefine the digital control law coefficients of the controller.
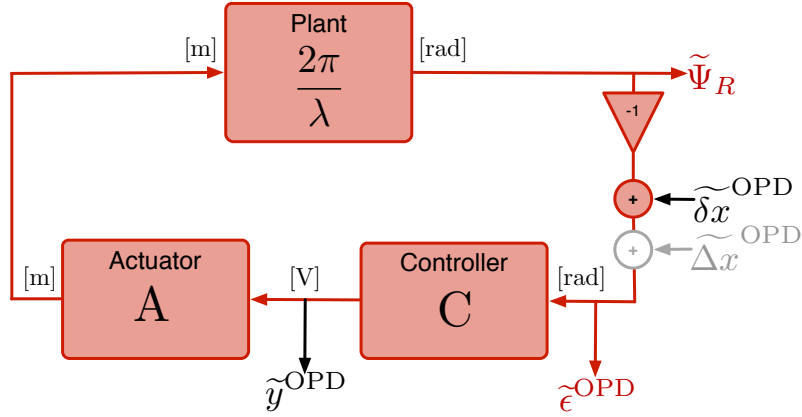

Figure 4.14: A simplified block diagram of the OPD control loop, with the components and signals required for the calculation of the OLTF highlighted in red. Each loop component is represented by the associated Laplace transform.

The steady-state OLTF is defined according to:

$$\text{OLTF}(f) \quad = \quad \text{C}(f) \times \text{A}(f) \times \text{X}_R(f) \tag{4.7}$$

$$= \quad \frac{\widetilde{\Psi}_R}{\widetilde{\epsilon}^{\text{OPD}}} \tag{4.8}$$

where $\text{X}_R(f)$ represents the plant response, defined in the diagram by $2\pi/\lambda$, and the tilde represents the FT of the signal.

A Bode plot of the OLTF will allow the key characteristics of the control loop to be determined:

- **Loop gain**: The amplitude of the OLTF Bode plot determines the gain of the control loop.

- **Phase and gain margin**: The phase difference between the phase at the unity gain frequency and $-180°$ defines the phase margin. The gain margin is the difference in amplitude between unity and the frequency at which the phase reaches $-180°$.

- The loop delay can be determined from the phase of the Bode plot.

A model of the OLTF loop response can be made based on the original design of the control loop, as described in Box 2.4. By fitting the model to the calculated OLTF, the actual values of the loop components can be calculated.

Additionally, the noise suppression function, S, can be calculated as an additional measure of the noise suppression achieved by the control loop:

$$S = \frac{1}{1 + \text{OLTF}} \tag{4.9}$$

The amplitude of the Bode plot of S defines the amount of noise suppression achieved at a particular frequency.

Coupling of optical pathlength noise via an applied modulation

Any residual pathlength mismatches in the reference and measurement beams of the interferometer, as well as sideband noise as a result of the coupling of the RF signals driving the AOM, will result in OPD noise. This noise will couple into the measurement of the differential test mass displacement via the X12 interferometer (see Section 2.2.2).
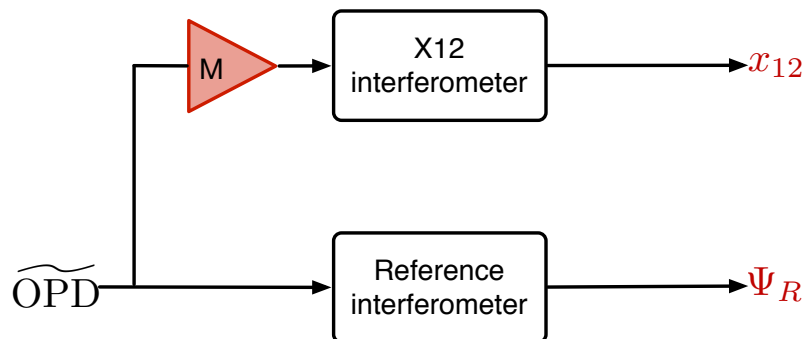

Figure 4.15: A simplified block diagram showing the coupling of OPD noise, $\widetilde{\text{OPD}}$, into the measurement of the differential test mass displacement via the coupling coefficient M.

4 Optical pathlength difference noise characterisation

Using the same method described in Section 4.1, the coupling coefficient, M, with units of m/rad, can be calculated according to:

$$\mathrm{M} = \frac{\widetilde{x}_{12}}{\widetilde{\Psi}_R} \qquad (4.10)$$

where the tilde denotes the FT of the signal.

This value should be more accurate than the calculated broadband coupling coefficient, as the applied modulations induce a much larger applied pathlength change in the interferometers, which should produce larger signals in the x_{12} channel.

4.2.1 Test campaign results

During the EM and FM test campaigns, characterisation of the OPD actuator was performed via the injection of a triangular waveform [32] [43]. As this investigation is not representative of the planned in-flight investigation, the results have not been analysed in this document. No specific investigation was performed to determine the response of the controller in any of the test campaigns. However, sinusoidal modulations at a range of frequencies were injected into the δx^{OPD} input as part of the OLTF investigations during the EM and FM test campaigns. No equivalent investigation was performed during the OSTT test campaign. It is possible to use the results of the OLTF investigation to determine the response of both the controller and the actuator, as well as to calculate the OLTF and a coupling coefficient for OPD noise into differential test mass displacement.

The following sections describe the analysis of the EM and FM test campaign OPD OLTF investigations. Initially, all data was processed in the same way. Subsequently, the previously mentioned transfer function and DFT methods were used to determine the results for each sub-analysis.

The data pre-processing and an overview of the transfer function and DFT analyses are given under 'Overview of the analysis'. The specific details and results of each sub-analysis are then described under the associated heading.

Overview of the analysis

The telemetry parameters used in the following analyses are given in Table 4.5. The equivalent parameter names used in the LTPDA repositories are given in Appendix 7.

Parameter	Description	Frequency [Hz]	ID
S^{FF}	Fast frequency loop state	1 Hz	LST17361
S^{SF}	Slow frequency loop state	1 Hz	LST17364
S^{OPD}	OPD loop state	1 Hz	LST17367
S^{SP}	Slow power loop state	1 Hz	LST17358
y^{FF}	Fast freq. loop feedback	1 Hz	LST17340
		10 Hz	
y^{SF}	Slow freq. loop feedback	1 Hz	LST17345
		10 Hz	
y^{OPD}	OPD loop feedback	1 Hz	LST17350
		10 Hz	
		100 Hz	LST18350
y^{SP}	Slow power loop feedback	1 Hz	LST17357
		10 Hz	
δx^{OPD}	OPD loop input modulations	10 Hz	LST17348
		100 Hz	LST18348
ϵ^{OPD}	OPD loop error	1 Hz	LST17349
		10 Hz	
		100 Hz	LST18349
Ψ_R	Ref. ifo. output	10 Hz	LST12407
		100 Hz	LST15643
x_{12}	X12 ifo. output	10 Hz	LST10130

Table 4.5: The telemetry parameters used in the analyses of the EM and FM test campaign free-running frequency noise investigations.

The analyses of the EM and FM OLTF investigation were performed as follows:

1. The data, as defined in Table 4.5, was downloaded according to the investigation dates and times defined in the EM and FM test campaign reports [32] [43]. The related information can be found in Appendix 8, Tables 8.11 and 8.13.

2. The loop state and feedback signals were checked, and the data split, to ensure they were in the following condition:

   - OPD: switching between 'nominal' and 'testing offset Δx' or 'variable output y' (state 3 and states 4 or 2).

   - Other loops: either 'nominal' or 'fixed output y' with a constant feedback signal, and remaining in this condition for the duration of the investigation.

3. Each channel, with the exception of the loop state and feedback signals, was detrended with order three. This removed any DC offsets, in addition to any linear, quadratic, or cubic drifts.This was performed to reduce spectral leakage from large, low-frequency components below the band of interest.

   Note: The Ψ_R timeseries used in the actuator calibration sub-analysis was processed to determine the equivalent pathlength fluctuation, δp, before detrending. This step is described in more detail under the associated heading.

At this point in the analysis two methods for determining the required outputs were applied:

- **Transfer function method**: Only 10 Hz data was used to determine the transfer function. Not all 1 Hz data was available, and the 100 Hz data contained gaps between the applied modulations.

  1. The 10 Hz data contained gaps where input modulations above 1 Hz were applied, for recording by the IDL. The timeseries data was split to remove timespans where there were large gaps. The information regarding the split times can be found in Appendix 8, Tables 8.11 and 8.13 for the EM and FM analyses respectively.

  2. The data was checked for data quality issues and repaired accordingly.

  3. The transfer function of the required channels was calculated using 20 averages and the Hanning windowing function with 50 % overlap. This transfer function was then

binned to smooth the data, and provide a better statistical estimate of the error. The results are given under each sub-analysis heading.

4. The coherence of the required channels was also calculated, using 20 averages, to show the frequency regions where the transfer functions are most representative.

- **The DFT method**: Both the 10 Hz and 100 Hz data was used in the analysis of the results via the DFT method.

    1. Limited information regarding the start and end time of each applied modulation was available in the test campaign reports. It was therefore necessary to manually determine the times at which each modulation was applied. The times were determined from the 10 Hz and 100 Hz δx^{OPD} timeseries, which showed the applied modulation signal.

    2. All channels were split according to the start and stop times, such that the timeseries data now exists as segments, each containing a modulation signal at one frequency.

    3. For all channels, the modulation segments were plotted and visually inspected. The segments were checked to ensure that they contained no transients at the beginning and end of the modulation, and to ensure that only modulation signals were within the segment. The shortest split times were selected for which these conditions were met, and all channels were split according to these new times.

    4. An FFT was performed on the segments of the δx^{OPD} input modulation signal to determine the modulation frequency contained within each segment. These frequencies were used as a reference for selecting the actual applied frequency from the list in the campaign test report [32] [43].

    5. To check that the selected frequency was correct, the timeseries segments of the δx^{OPD} channels were heterodyned at that frequency. This is described in Box 3.4.

    6. A DFT was performed on all of the channel segments at

223

the calculated frequencies.

7. The ratio of the DFTs of the channels required in each analysis were calculated, as described under the following headings.

Note: Additional steps were required for the analysis of the coupling of OPD noise into differential displacement noise. These steps are detailed under the associated heading below.

Controller characterisation

Both the transfer function and DFT methods were used to determine the controller response from the EM and FM test campaign results. A model, based on the controller coefficients defined in the test reports, was also made. The associated plots are shown in Figures 4.16 and 4.17. The same controller coefficients were used for both campaigns, and are given in Table 4.6. The models matched the DFT and transfer function results, and therefore no fit was required.

	EM/FM
a0	2.004×10^{-2}
a1	-1.996×10^{-2}
a2	-2.004×10^{-2}
a3	1.9961×10^{-2}
b0	1.0
b1	3.0
b2	-3.0
b3	1.0

Table 4.6: The digital control law coefficients for the EM and FM controller response models, used in the analysis of the OPD OLTF investigation.

Actuator calibration

In a deviation from the general processing method, the Ψ_R channel was converted to an equivalent applied pathlength fluctuation, δp. This gave the pathlength change applied by the OPD actuators,
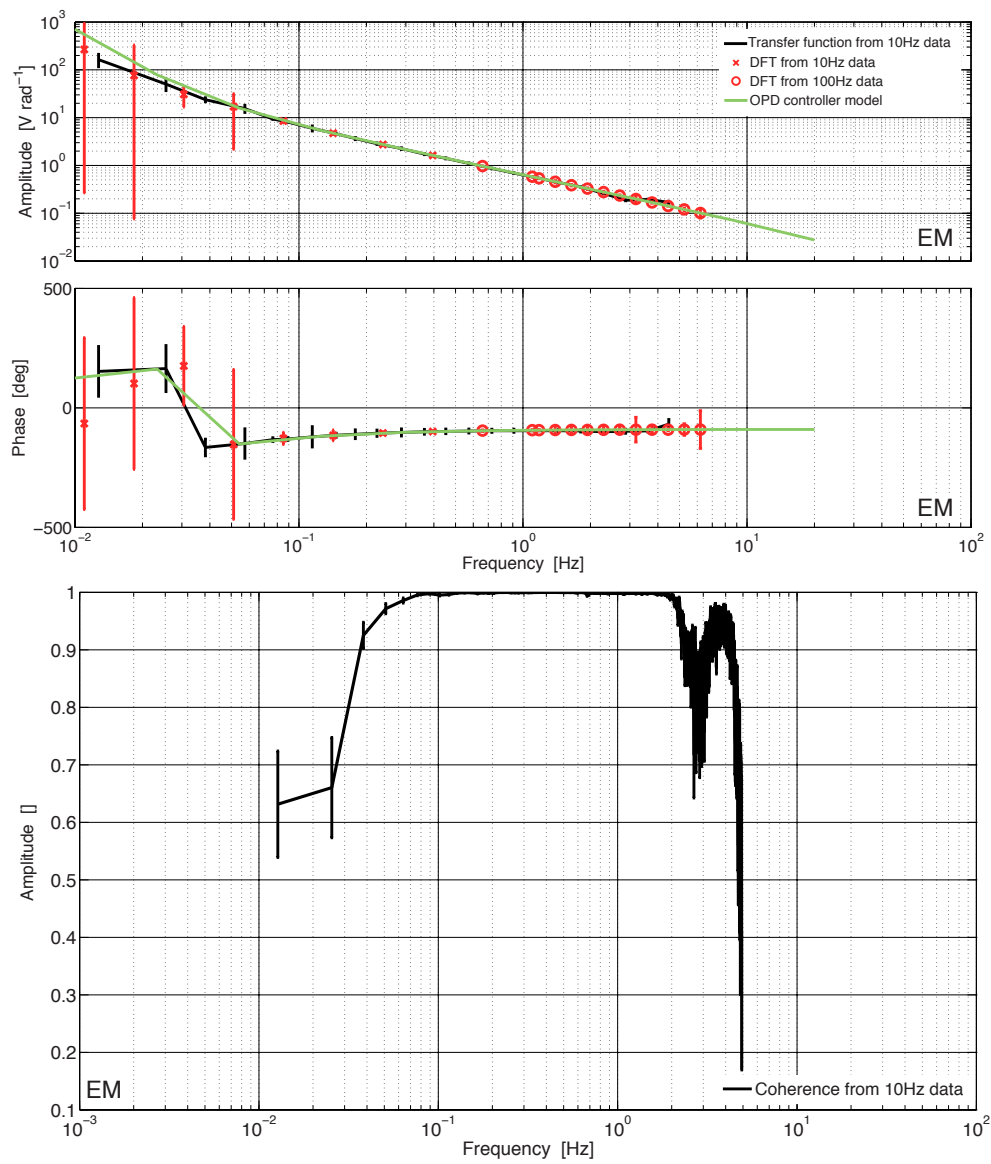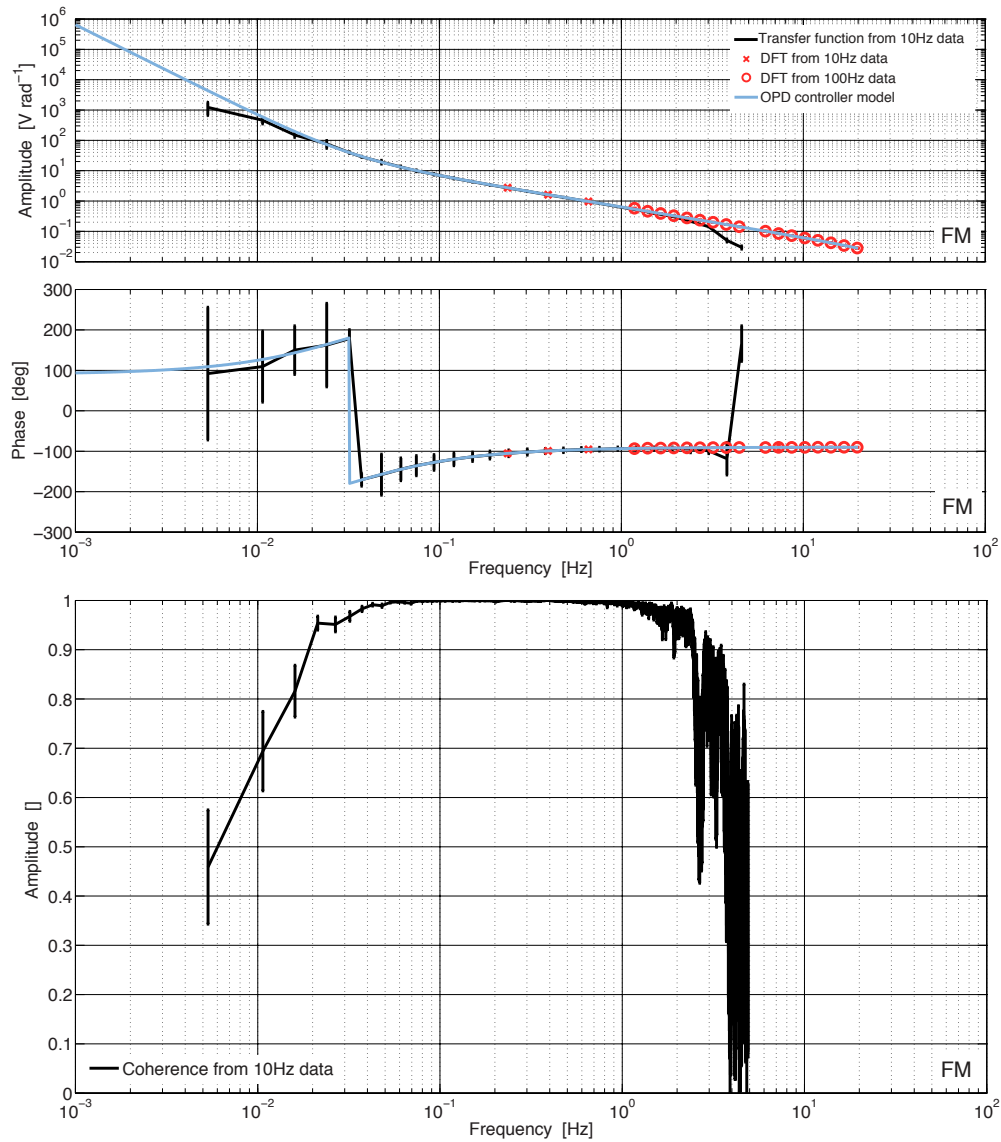
Figure 4.16: The response of the OPD controller, as calculated using the OLTF investigation in the EM test campaign. The transfer function is shown in black, with the results from the DFT method in red. The calculated model, based on the loop design, is shown in green.

Figure 4.17: The response of the OPD controller, as calculated using the OLTF investigation in the FM test campaign. The transfer function is shown in black, with the results from the DFT method in red. The calculated model, based on the loop design, is shown in blue.

and was calculated with the previously defined conversion coefficient, 1.69×10^{-7} m/rad.

The transfer function of δp and the feedback signal, y^{OPD}, were calculated, as were the equivalent DFT results. A model, M, based on the design of the actuator (see Box 2.4) was also determined, and fitted to the results to determine the gain, G, and delay, τ:

$$M(s, G, \tau) \quad = \quad \frac{Ge^{-s\tau}}{s + 60\pi} \tag{4.11}$$

The associated plots for the EM and FM analyses are shown in Figures 4.18 and 4.19. The values of the actuator gain calculated from the model fit are shown in Table 4.7. In order to fit the model, an extra pole at 30 Hz was added to the model described in Box 2.4, this is shown in Equation 4.11.

	Gain, G [m/V]	Delay, τ [s]
EM	0.9×10^{-6}	45×10^{-3}
FM	4.3×10^{-7}	18×10^{-3}

Table 4.7: Results for the OPD actuator gain and delay, as measured using the EM and FM OLTF investigations.

Open-loop transfer function and noise suppression

The calculated OLTF plots, from both the transfer function and DFT methods are shown in Figures 4.20 and 4.21, for the EM and FM test campaigns respectively. Also shown is a model, M, fitted to the DFT results, based on the original loop design described in Box 2.3:

$$M(a, G, \tau) = X_R C(s) A(s, G, \tau) \tag{4.12}$$

where:

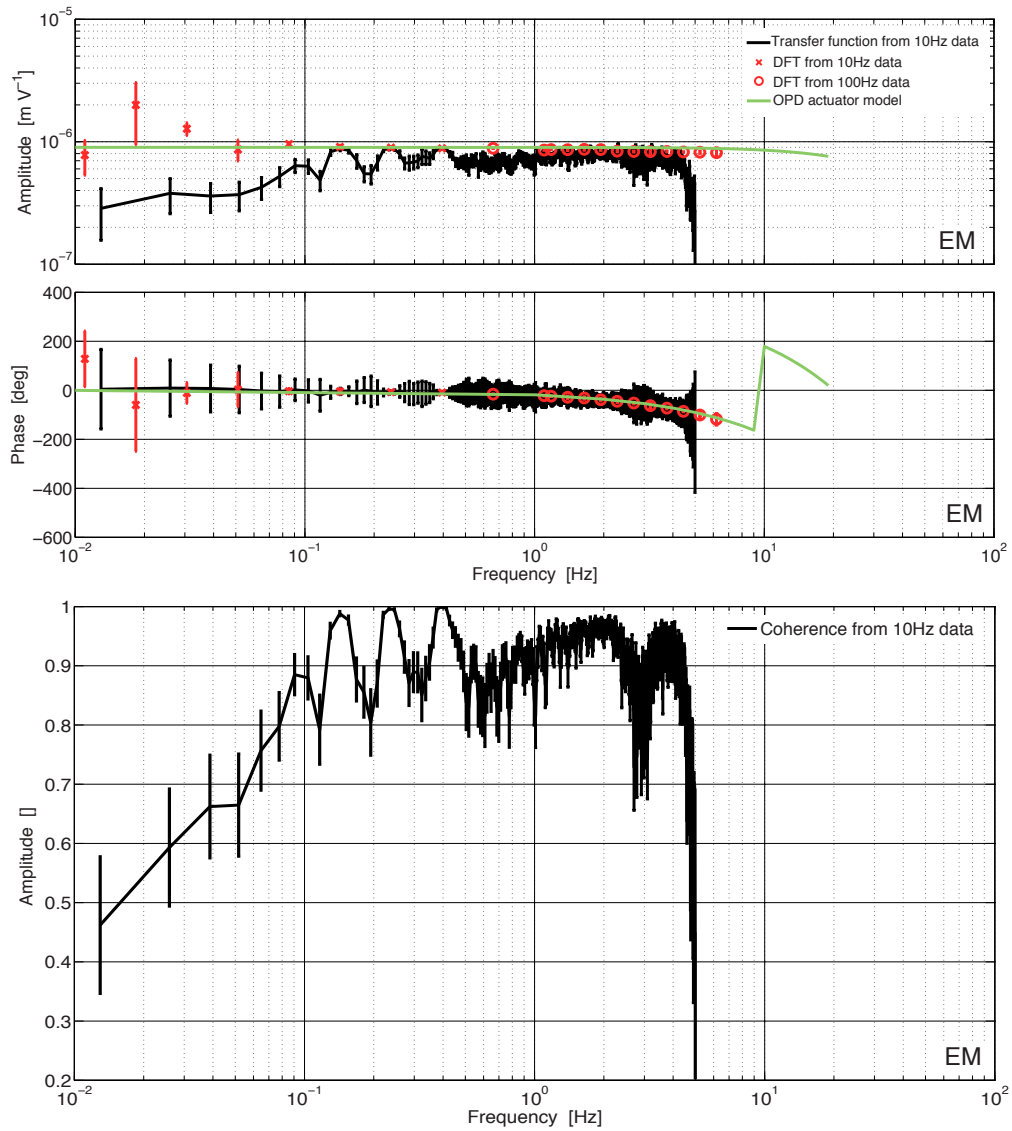# 4 Optical pathlength difference noise characterisation

Figure 4.18: The response of the OPD control loop actuator in the EM test campaign, as calculated using the transfer function method (black trace), the DFT method (red trace), and a model fitted to the results (green trace).
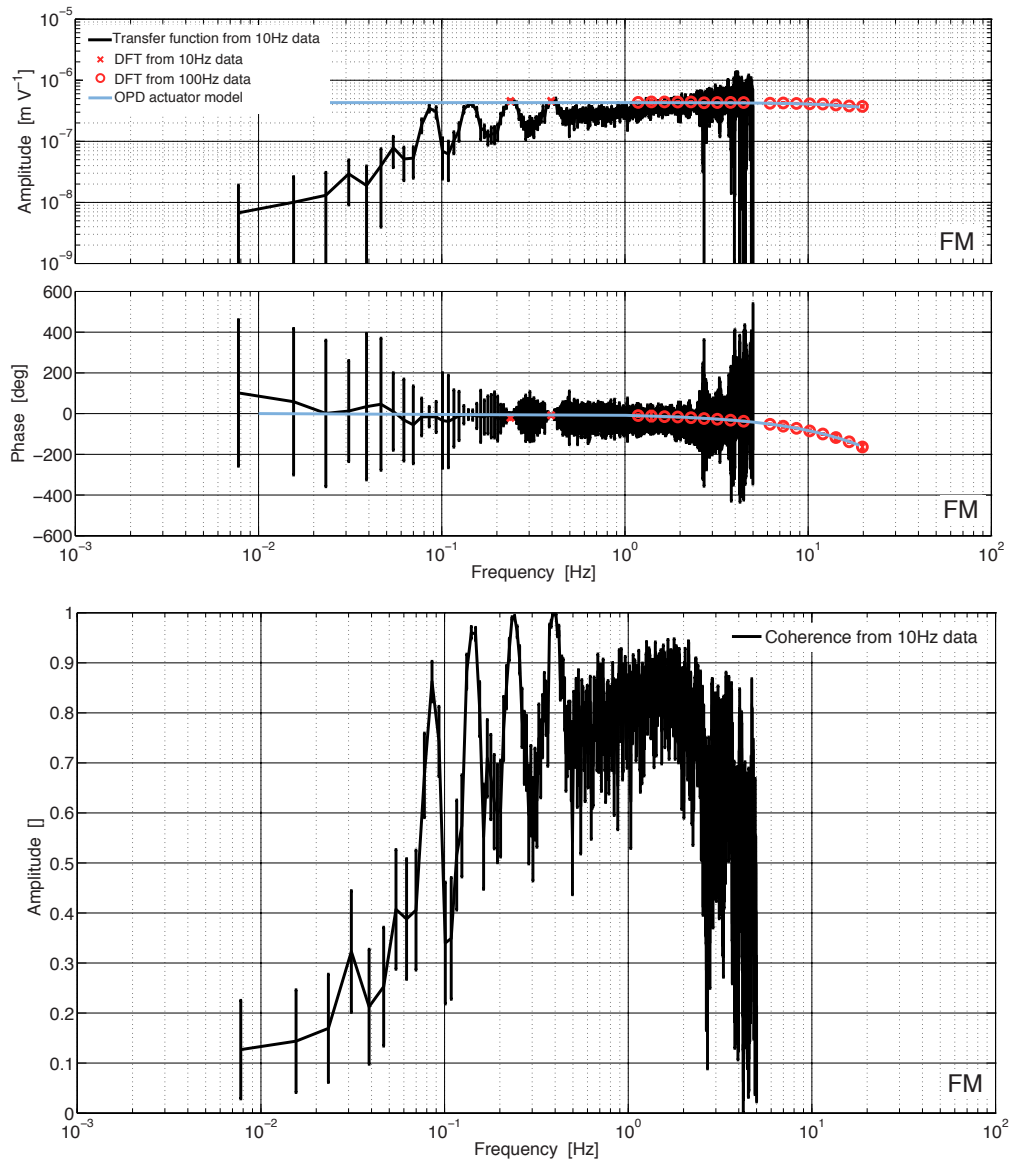
Figure 4.19: The response of the OPD control loop actuator in the FM test campaign, as calculated using the transfer function method (black trace), the DFT method (red trace), and a model fitted to the results (blue trace).

$$X_R \;=\; \frac{2\pi}{1064 \times 10^{-9}} \tag{4.13}$$

$$A(s, G, \tau) \;=\; \frac{Ge^{-s\tau}}{s + 60\pi} \tag{4.14}$$

The loop gain, G, and delay, τ, as determined from the fit to the DFT results, are given in Table 4.8. The loop characteristics are shown in Table 4.9.

	Gain, G [m/V]	Delay, τ [s]
EM	7.12×10^{-7}	48.46×10^{-3}
FM	4.40×10^{-7}	18.22×10^{-3}

Table 4.8: Results for the OPD actuator gain and delay, as determined from the results of the EM and FM test campaign OLTF investigations.

	EM	FM
Unity gain frequency [Hz]	2.65	1.65
Gain margin [dB]	4.56	1.31
Phase margin [deg]	34.1	74.0

Table 4.9: The gain and stability characteristics determined from the EM and FM test campaign fits to the OLTF.

The noise suppression models were calculated from the model of the OLTF, and are shown in Figures 4.22 and 4.23. The noise suppression at 30 mHz is -45.15 dB for the EM test campaign, and -30.55 dB for the FM campaign.

Coupling of optical pathlength noise via an applied modulation

The transfer functions and coherences of the x_{12} and the Ψ_R channels were calculated, as were the DFT ratios of the modulation segments. The results for the EM and FM test campaigns are shown in Figures 4.24 and 4.25. Only 10 Hz data was used in this analysis, as the x_{12} channel was not recorded at 100 Hz.
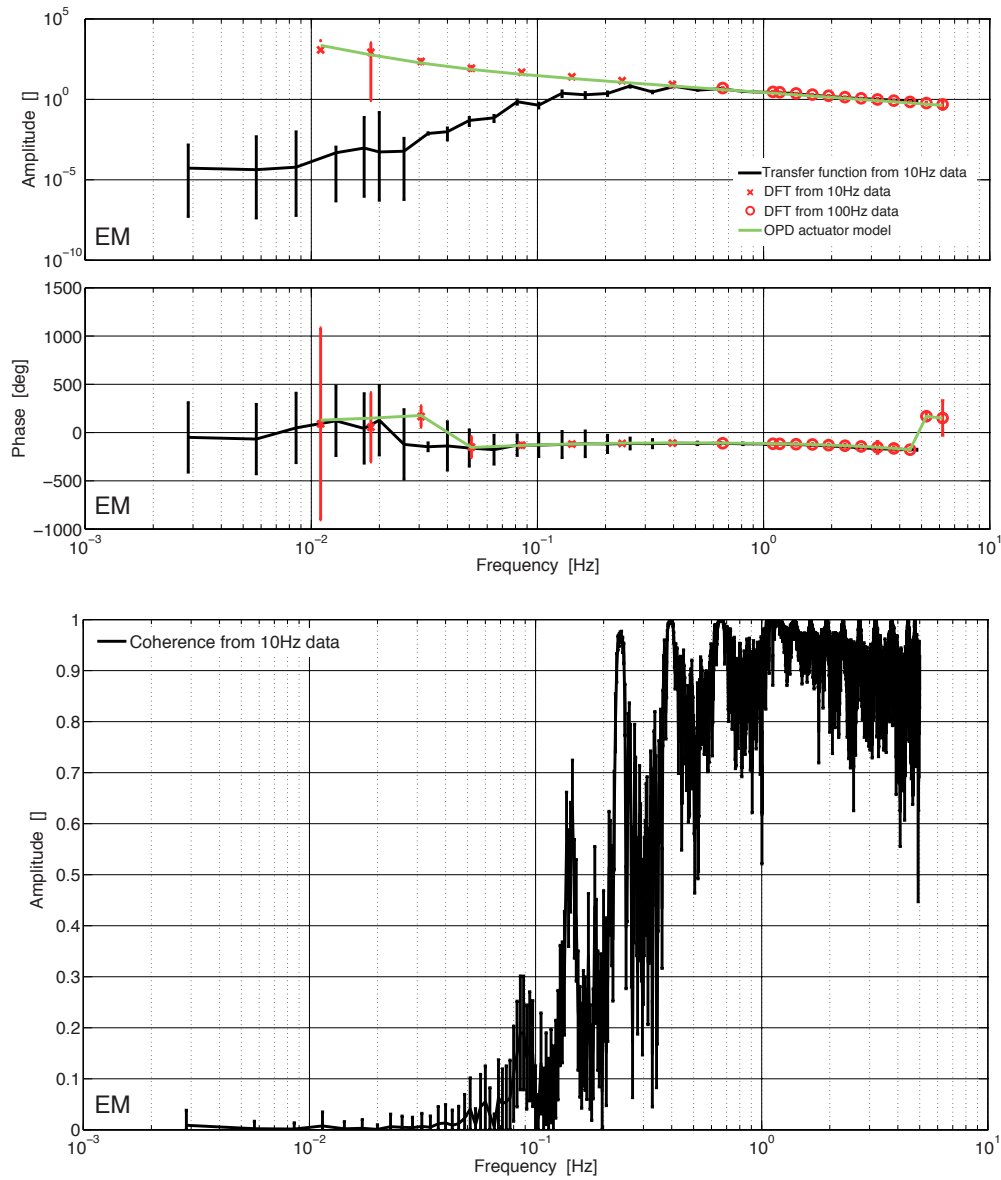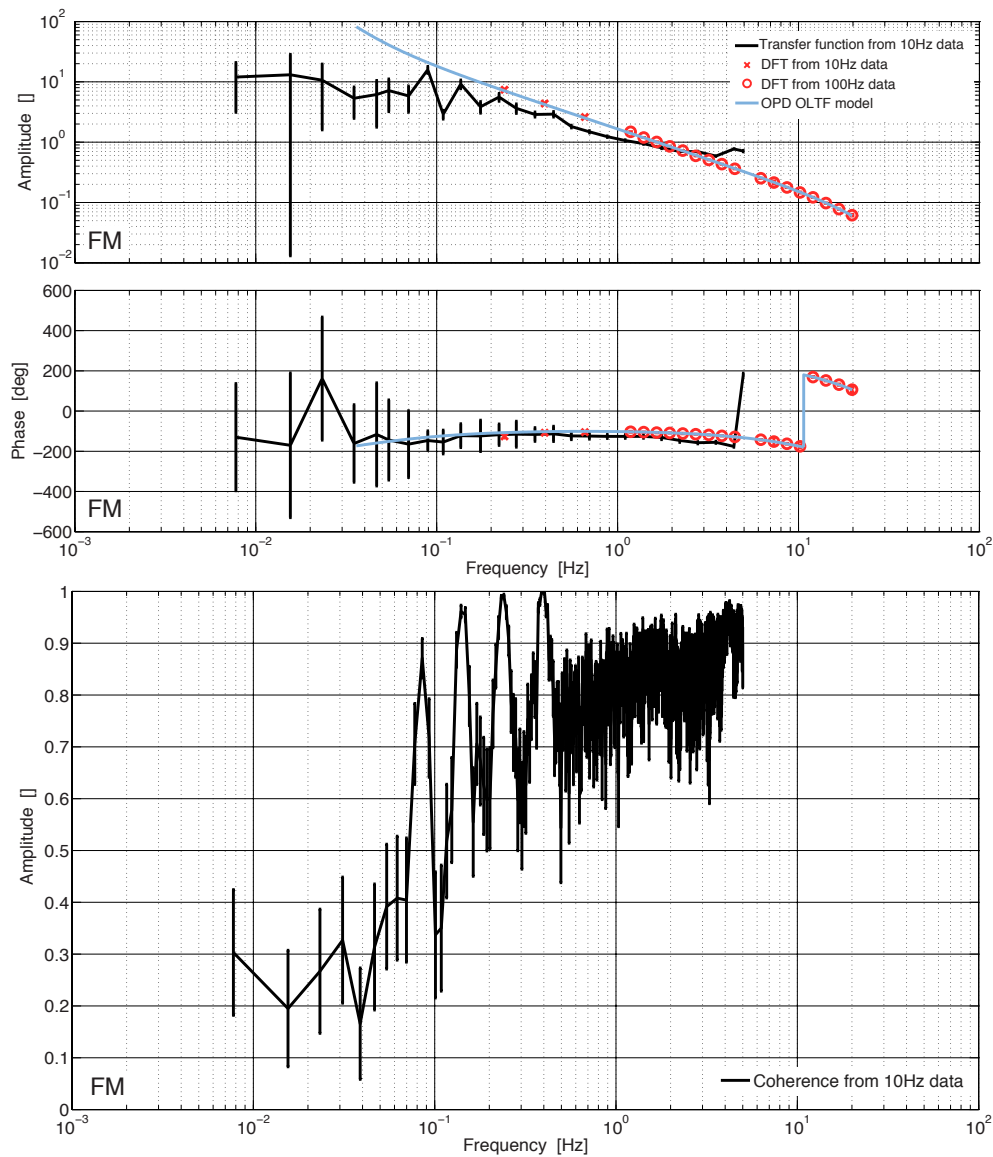
Figure 4.20: The OLTF results from the EM test campaign investigation. The transfer function results are shown in black, along with the coherence. The results from the DFT method using the 10 Hz and 100 Hz data is shown in red, and the fitted model is shown in green.

Chapter 4

231

Figure 4.21: The OLTF results from the FM test campaign investigation. The transfer function results are shown in black, along with the coherence. The results from the DFT method using the 10 Hz and 100 Hz data is shown in red, and the fitted model is shown in blue.
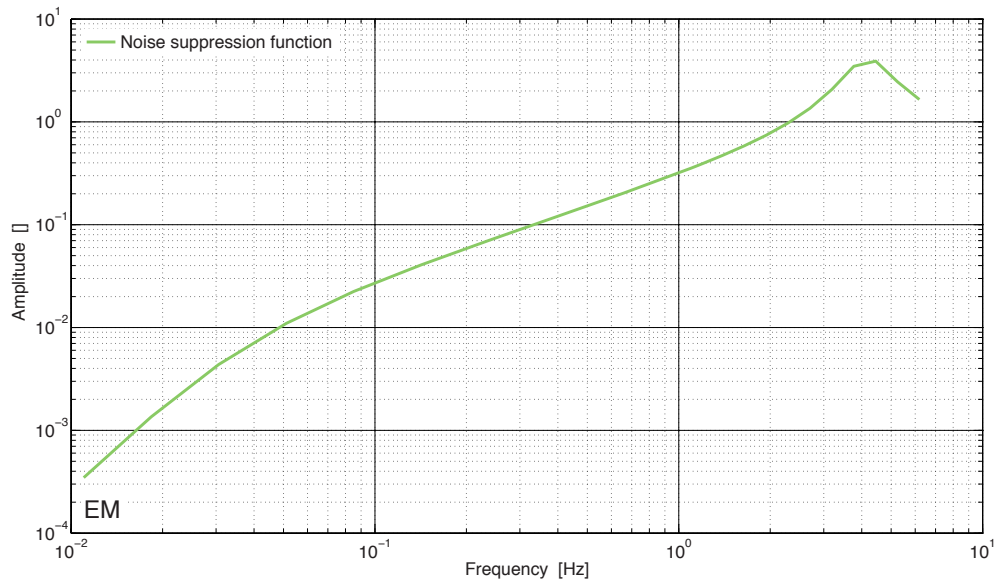
Figure 4.22: The model of the OPD control loop noise suppression function from the EM test campaign. This was calculated using the model fitted to the measured OLTF.
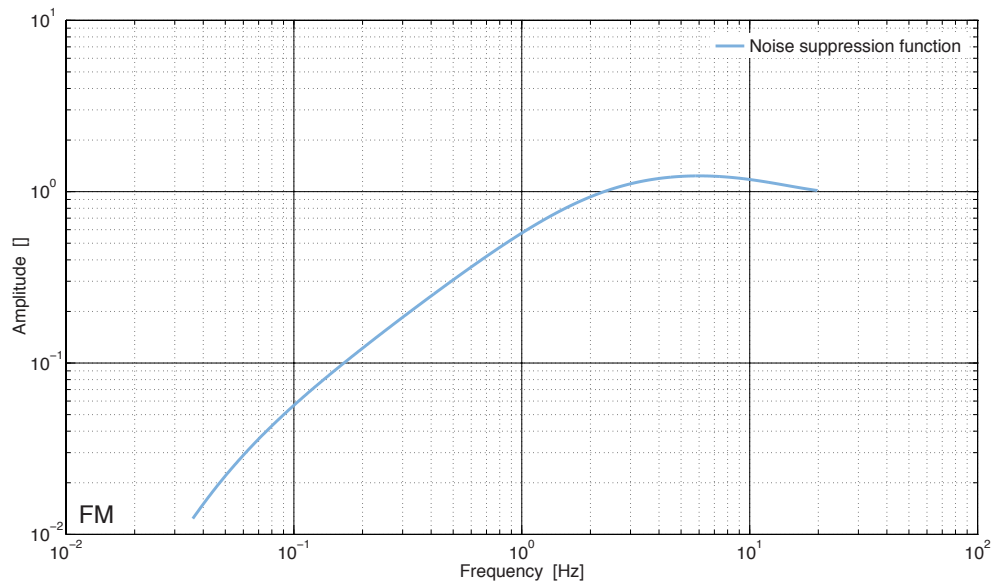

Figure 4.23: The model of the OPD control loop noise suppression function from the FM test campaign. This was calculated using the model fitted to the measured OLTF.

Figure 4.24: The transfer function, coherence, and DFT results to determine the coupling between the OPD noise measured by the Ψ_R channel, and the differential test mass displacement, x_{12}. These results are determined from the analysis of the EM test campaign OLTF investigation. The equivalent results from the free-running OPD noise investigations are shown in grey for comparison. The shaded areas of the plots shown the frequency region used to determine the coupling coefficient.
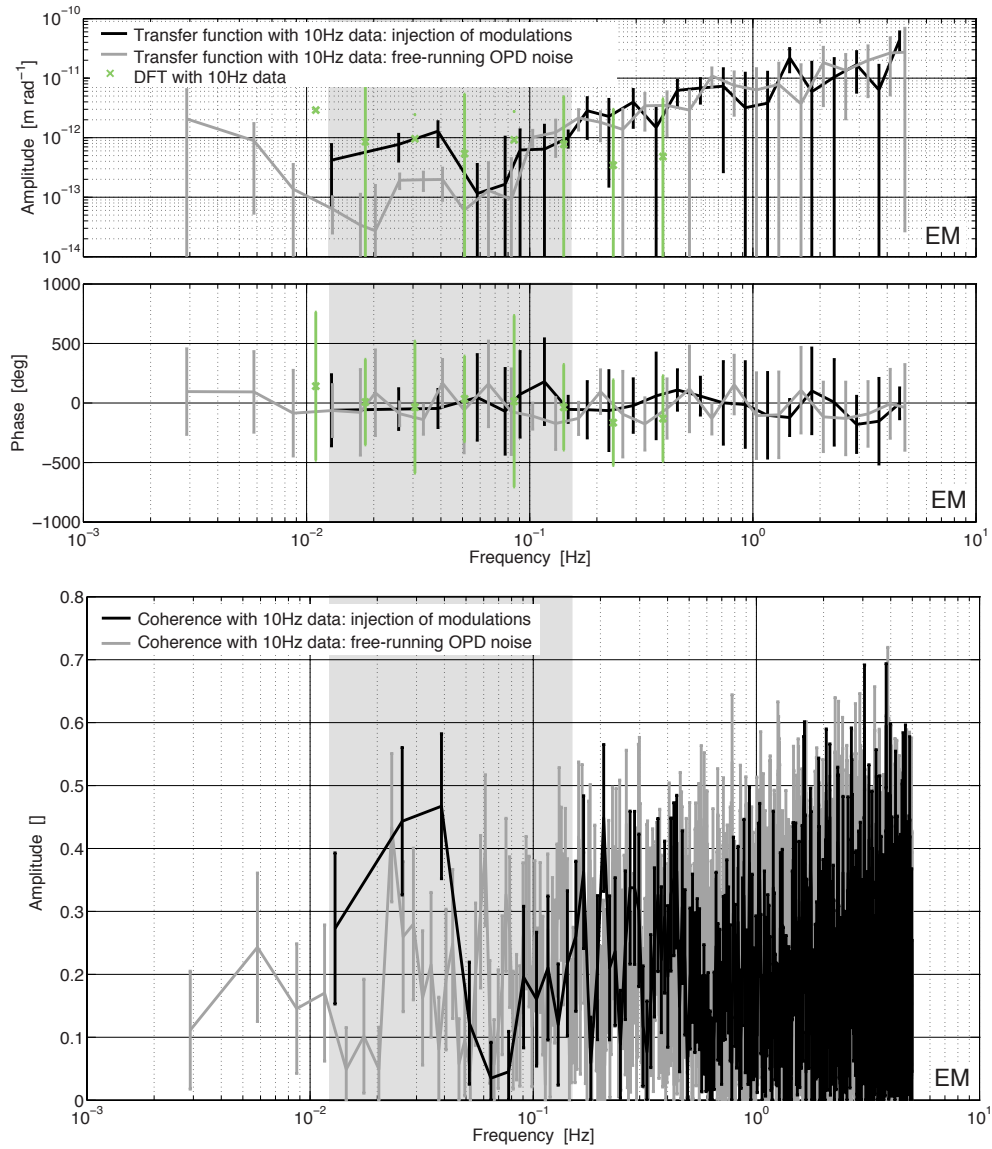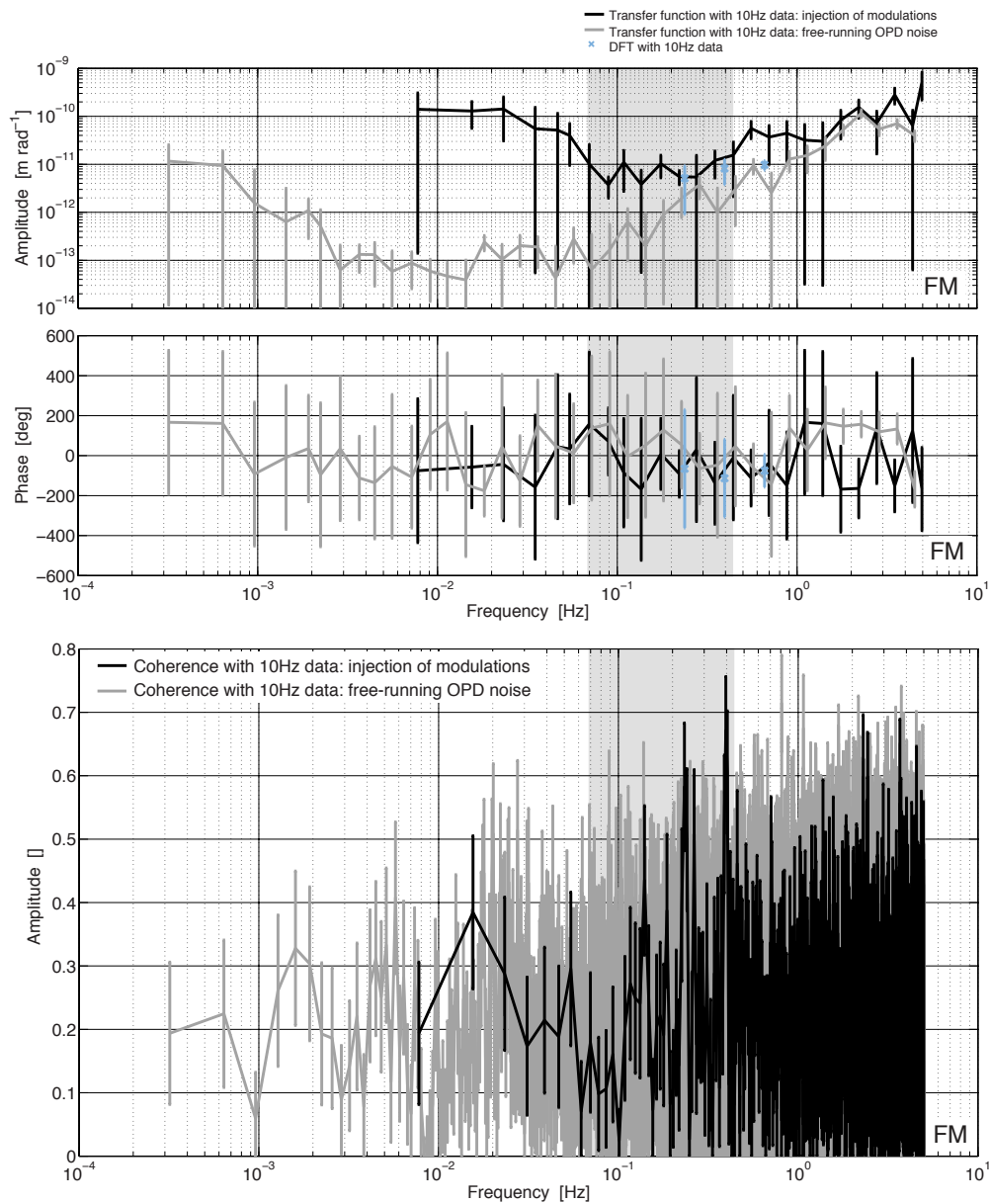
Figure 4.25: The transfer function, coherence, and DFT results to determine the coupling between the OPD noise measured by the Ψ_R channel, and the differential test mass displacement, x_{12}. These results are determined from the analysis of the FM test campaign OLTF investigation. The equivalent results from the free-running OPD noise investigations are shown in grey for comparison. The shaded areas of the plots shown the frequency region used to determine the coupling coefficient.

Chapter 4

4 Optical pathlength difference noise characterisation

Two methods were used to determine the coupling coefficient, M, for the OPD noise into the differential test mass displacement:

1. Ideally, a frequency range would have been selected where the transfer function response was relatively flat, and the coherence was high. However, as for the calculation of a broadband coupling coefficient from a free-running OPD noise investigation (see Section 4.1), this was not possible. Both the EM and FM transfer functions are not very flat, and the coherence was low. To calculate a coupling coefficient, a somewhat flat region of the transfer function was selected, around the frequency region of the DFT results (see below). The mean value of the transfer function in the determined frequency range was calculated to give a value of M. The frequency range selected for each calculation are shown on the transfer function plots in Figures 4.24 and 4.25.

2. The mean of the DFT results was also calculated to give a value of M.

The results of both methods, for the EM and FM test campaigns, are shown in Table 4.10.

	Method	Coefficient [m/rad]	Error [m/rad]
EM	Transfer function	2.88×10^{-13}	3.02×10^{-13}
	DFT	9.74×10^{-13}	2.88×10^{-13}
FM	Transfer function	3.50×10^{-12}	3.28×10^{-12}
	DFT	7.67×10^{-12}	1.36×10^{-12}

Table 4.10: The calculated values of the coupling coefficient for OPD noise into the differential displacement measurement with the injection of modulations.

The coupling coefficients calculated using the two methods do not correspond within errors for both the EM and FM test campaigns. The errors on all of the calculated coefficient values are very large, in some cases larger than the calculated coefficient. This indicates that the coupling of OPD noise into differential test mass displacement can be considered to be zero. This reinforces the result determined from the free-running OPD noise investigation (see Section 4.1). However, despite the predicted low coupling, the coupling coefficient should still

be determined in-flight.

4.2.2 In-flight investigation

The in-flight OPD control loop characterisation investigation is analogous to the frequency control loop characterisation investigation described in Section 3.1. The investigation is planned to be performed in science mode 1.2, with test mass one drag-free, and test mass two controlled via electrostatic suspension[1]. The OPD control loop should be operating in the 'variable output y' state, to allow a series of modulations to be applied via the δx^{OPD} input. The other control loops should be in the 'nominal' state. The required telemetry, which should be recorded at 10 Hz, is defined along with the loop setup in Table 4.11. The characteristics of the modulations to be applied are given in Table 4.12. The selection of the modulation frequency and duration are discussed in Box 4.2. The procedure for implementing the investigation in-flight is shown in Figure 4.26. This procedure includes the steps required for applying a modulation above 1 Hz with data recording at 100 Hz via the IDL, to allow for the case where the procedure is adapted to include modulations at higher frequencies than those specified here.

An overview of the suggested analysis procedure for the flight data is shown in Figure 4.27. The analysis consists of several sub-analyses, each represented by a diagram in a particular colour:

- the preparation of the data, shown in grey, is described in Figure 4.28;

- the procedure for characterising the OPD controller, shown in orange, is shown in Figure 4.29;

- the procedure for the calibration of the OPD actuators is shown in yellow in Figure 4.30.

- The procedure for determining the OPD loop OLTF and noise suppression function is shown in red in Figure 4.31;

---

[1]The characterisation of the control loop could also be performed with the test masses fixed, during commissioning of the satellite for example. In this case it would not be possible to determine the coupling coefficient.

- the procedure for calculating the coupling coefficient for OPD noise into differential test mass displacement is shown in blue in Figure 4.32.

Investigation	OPD control loop characterisation		
OMS state	TMs drag-free		
Loop states	SF	Nominal	
	FF	Nominal	
	OPD	Variable output y	
	SP	Nominal	
	FP	Nominal	
Telemetry required	128,3	x_{12}	LST10130
		Ψ_R	LST12407
	128,4	OPD input modulation	LST17348
		OPD error	LST17349
		OPD feedback	LST17350
		FF feedback	LST17340
		SF feedback	LST17345
		SP feedback	LST17357
	3,25	SF state	LST17364
		FF state	LST17361
		OPD state	LST17367
		FP state	LST17358
		SSC	SCT70388
Length	$\sim$3 hours		

Table 4.11: An overview of the key information relating to the OPD control loop characterisation investigation. For the telemetry names associated with each parameter refer to Appendix 7.
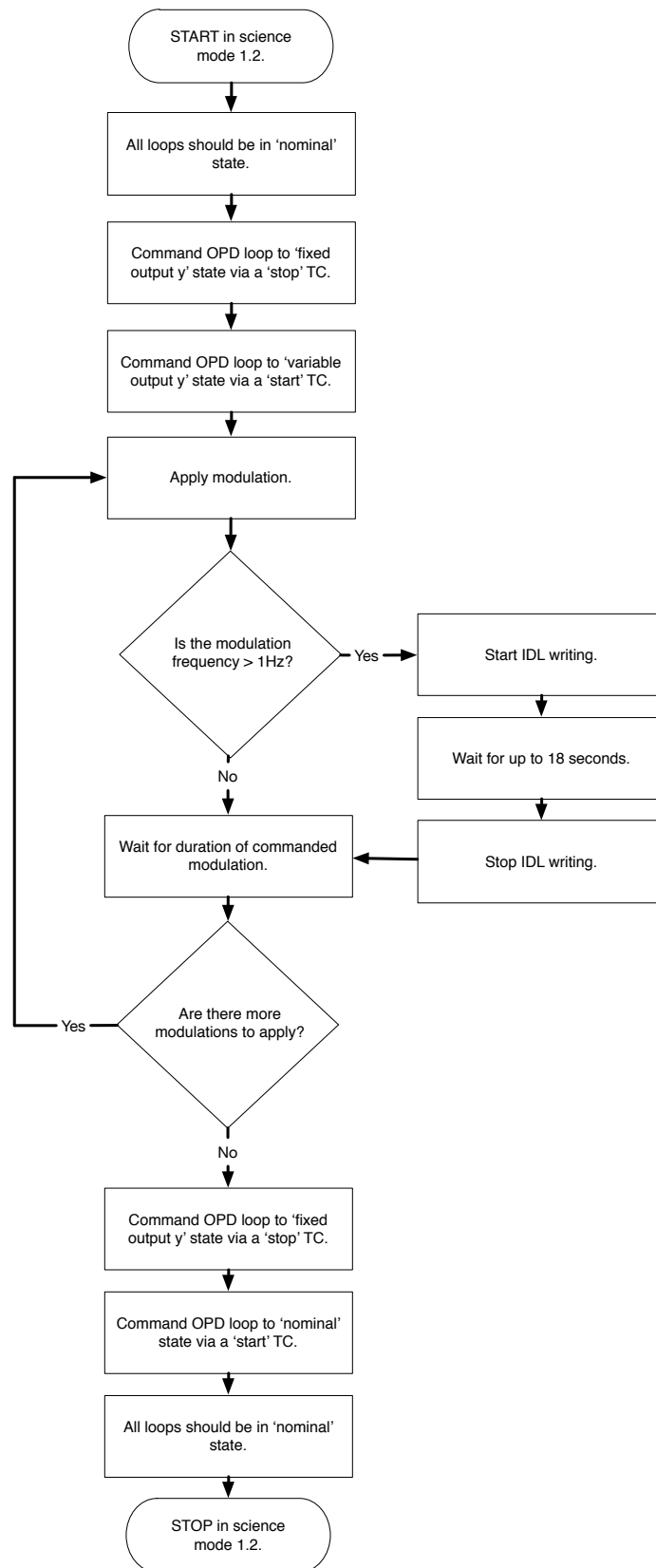
Figure 4.26: The procedure for implementing the OPD control loop characterisation investigation in-flight. The procedure for recording an input modulation with a frequency above 1 Hz using the IDL has also been given.

	Shape	Frequency [Hz]	Duration [half periods]	Amplitude [rad]
1	sine	0.011	20	1
2	sine	0.0396	20	1
3	sine	0.0852	20	1
4	sine	0.1421	20	1
5	sine	0.237	20	1
6	sine	0.3953	20	1
7	sine	0.6594	20	1
8	sine	1.0	20	1

Table 4.12: The planned modulations that should be injected into the δx^{OPD} input of the OPD control loop for the in-flight OPD control loop characterisation investigation.

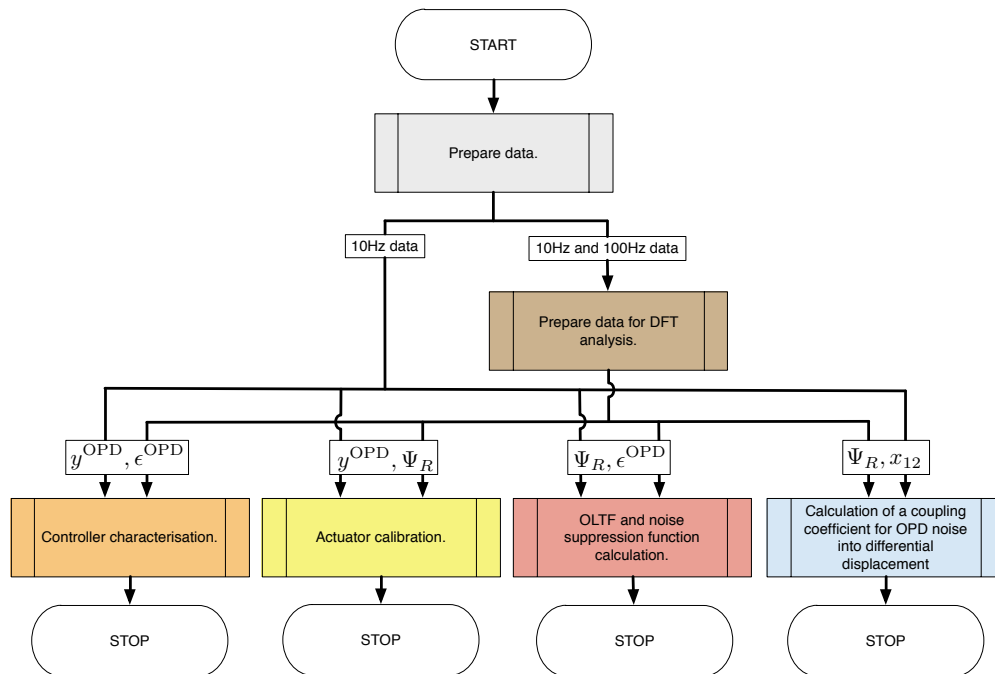**Figure 4.27:** An overview of the suggested procedure for the analysis of the OPD control loop characterisation investigation.
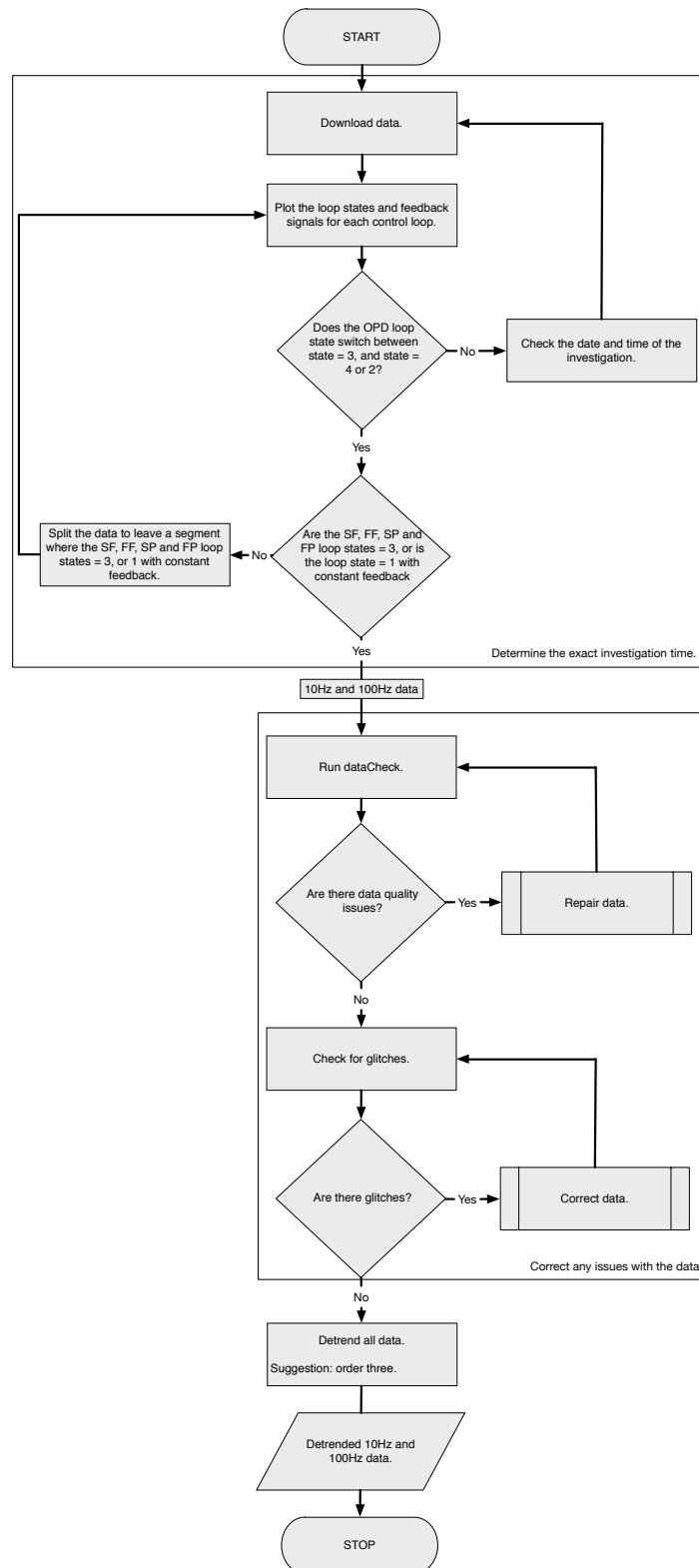
Figure 4.28: The data preparation sub-analysis of the OPD control loop characterisation investigation.
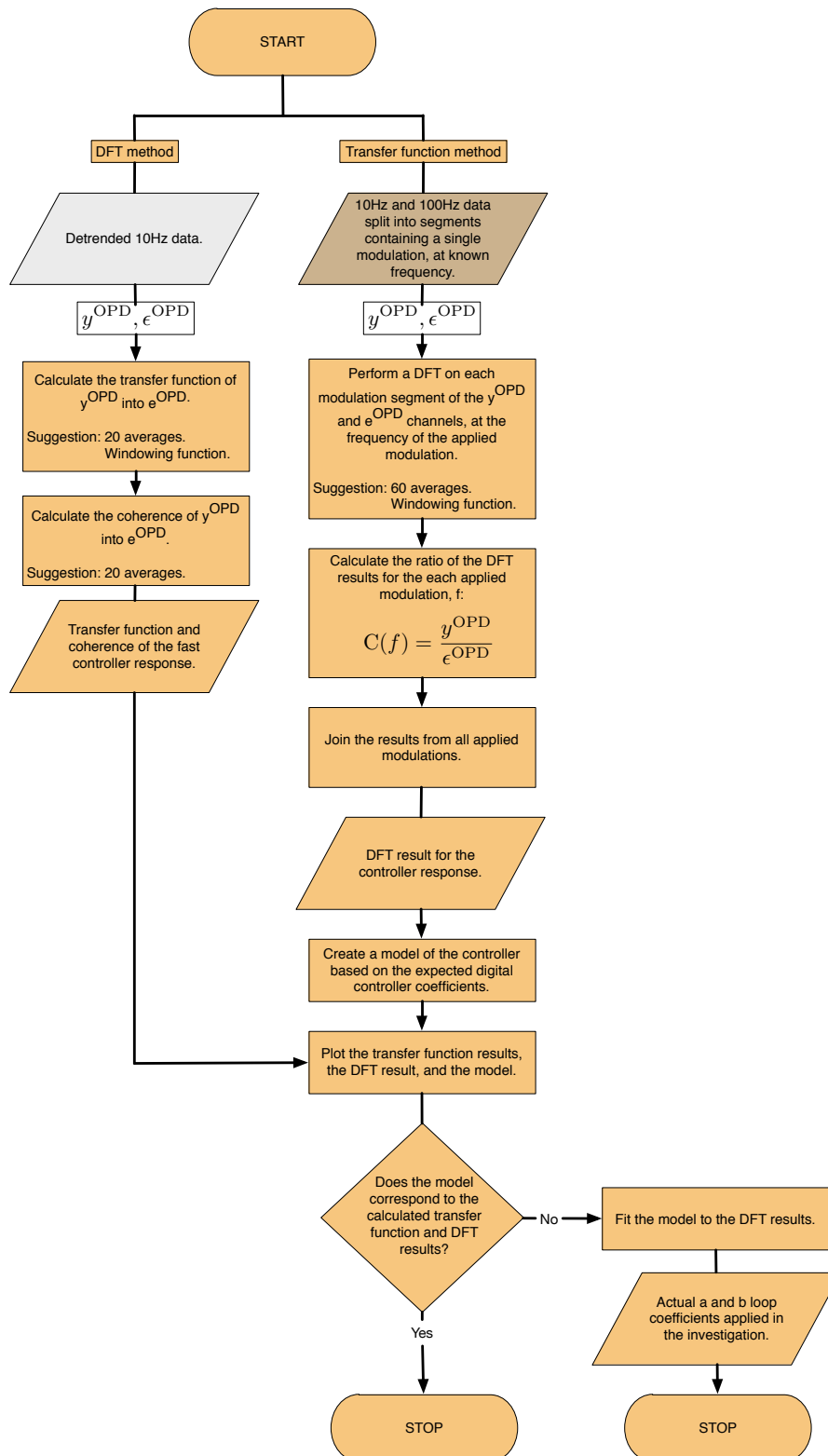
4 Optical pathlength difference noise characterisation

Figure 4.29: The controller characterisation sub-analysis of the OPD control loop characterisation investigation.
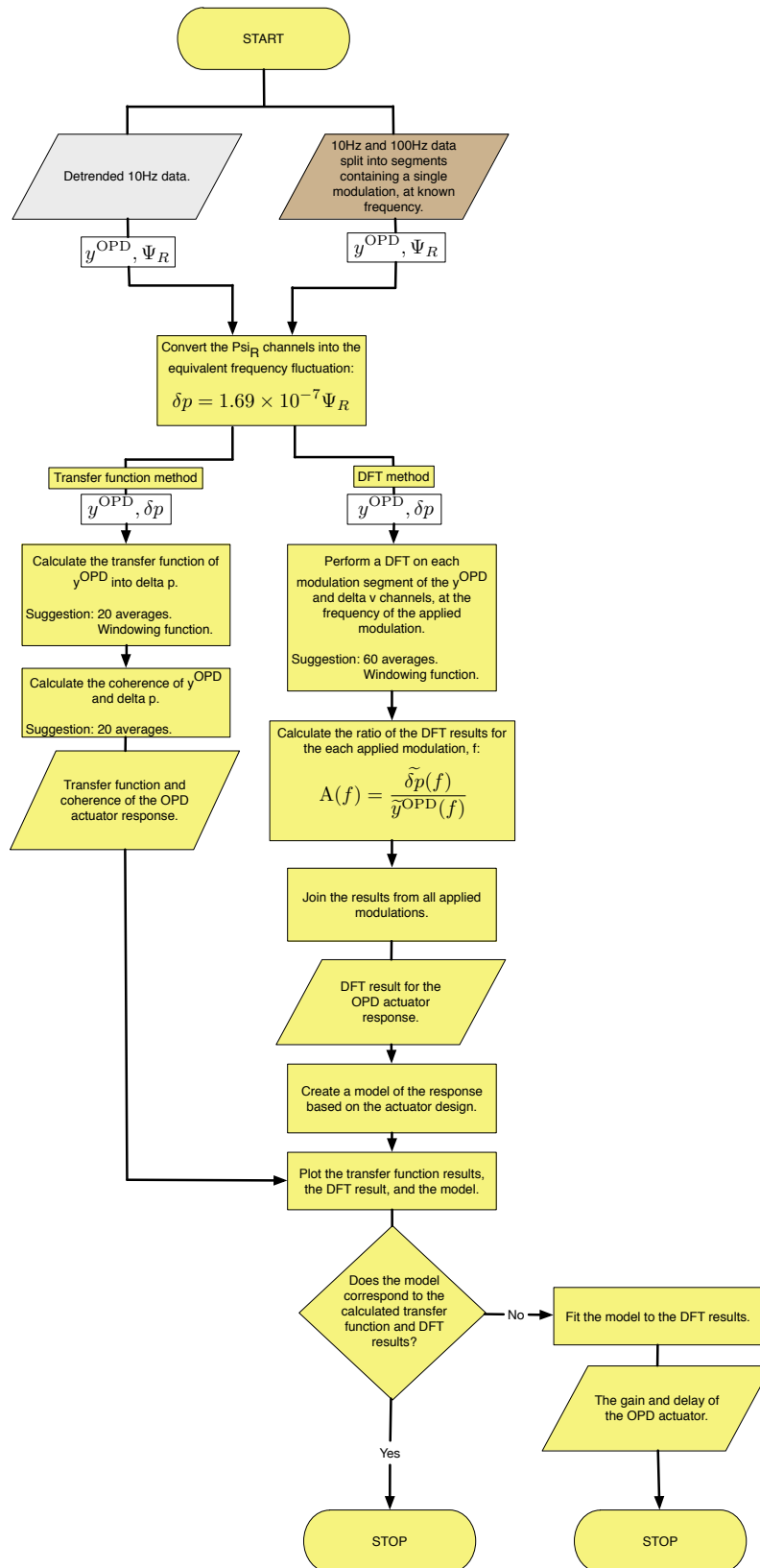
Figure 4.30: The actuator calibration sub-analysis of the OPD control loop characterisation investigation.
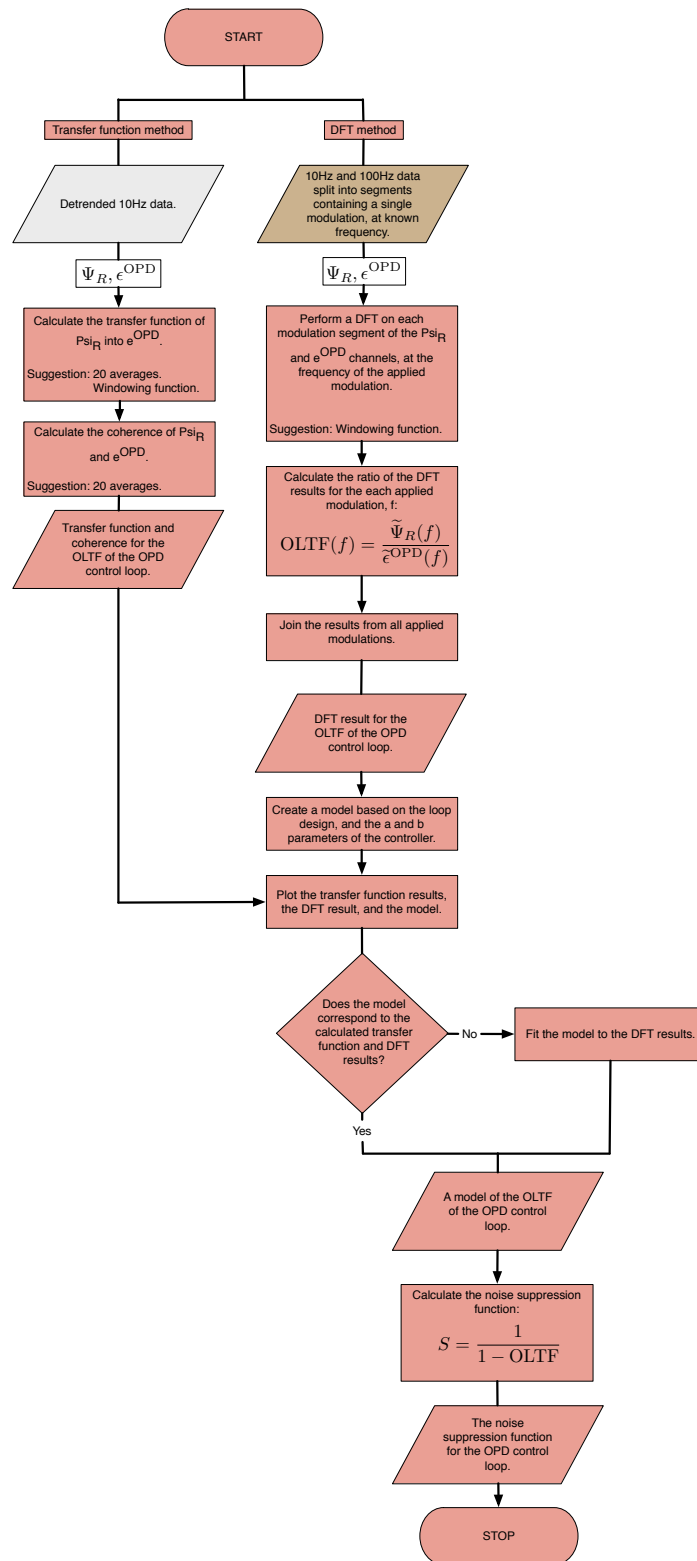
4 Optical pathlength difference noise characterisation

Figure 4.31: The OLTF and noise suppression function sub-analysis of the OPD control loop characterisation investigation.
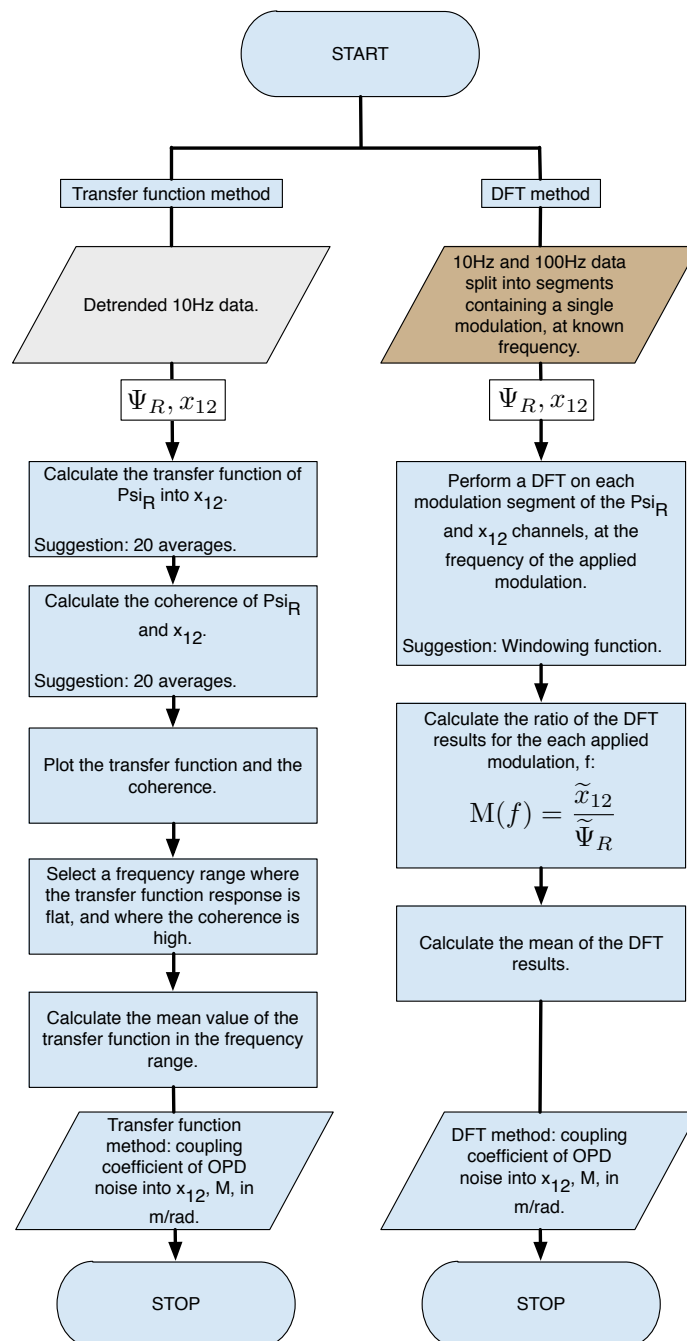
Figure 4.32: The calculation of an OPD noise to differential displacement coupling coefficient sub-analysis of the OPD control loop characterisation investigation.

Selection of applied modulations for the OPD control loop characterisation

In the same way as for the frequency control loop characterisation eight modulation frequencies, shown in Table 4.12, were chosen based on the frequencies applied in the FM test campaign [43]. These frequencies were selected because they do not require the IDL, it is assumed that the selection of such frequencies relates to some specific characteristics of the system. They also cover a good range of the OLTF, as shown in the top plot below, and are not harmonics of each other.
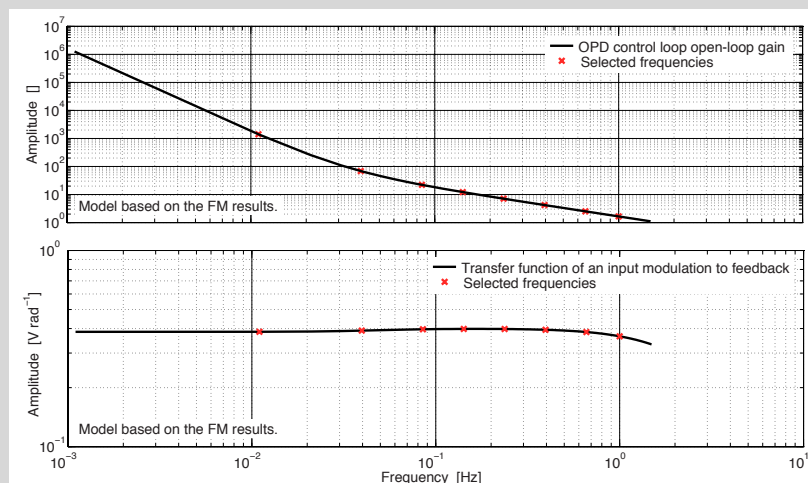
The amplitude of the modulations was also kept the same as for the FM test campaign, 1 rad, as the feedback signals at the actuator are well within the actuator range of $\pm 60.5\,\text{V}$ [43].

The transfer function from an input modulation to a feedback signal to the actuator are shown above, to provide for the scenario where the modulations characteristics need to be adapted. The calculated duration required for each modulation, according to the method in Box 3.5, was short, therefore a reasonable number of half periods that could be implemented to give a suitable investigation length were selected, this is based on the number used in the FM campaign.

Box 4.2: The selection of the modulations to be applied in the in-flight investigation to characterise the OPD control loop.

4.3 Closed-loop OPD noise

The determination of the closed-loop OPD noise is necessary in order to ensure that the measurement of the differential test mass displacement is not limited by OPD noise. This investigation would also identify if the loop was operating as expected.

The closed-loop OPD noise investigation is not an independent investigation, but rather a particular analysis of the data collected during a LPF science run. During a science run, the satellite is operating in science mode 1.2, such that test mass one is drag-free and test mass two is electrostatically suspended. The aim is to minimise the residual test mass displacement, and, as such, the OMS control loops should be operating under nominal conditions. The analysis of the Ψ_R and x_{12} channels can be used to determine the closed-loop OPD noise.

In this section, the performance measurements from the EM, FM, and OSTT test campaigns are analysed, focusing only on the OPD noise. These measurements are equivalent to an in-flight performance measurement, but without drag-free test masses. The suggested analysis procedure for the in-flight measurement is also presented. No procedure for performing such an investigation is given, as it is already a well defined part of the EMP.

4.3.1 Test campaign results

A number of performance measurements were made during the EM, FM, and OSTT test campaigns. For the OSTT test campaign, performance measurements were made under both hot and cold thermal conditions. In this section, only the measurements demonstrating the lowest achieved residual test mass displacement are presented. The same measurements were also analysed for the closed-loop frequency noise component, as described in Section 3.3.

The information relating to the date and times of the investigations analysed can be found in Appendix 8, Section 8.3. The telemetry parameters used in the analyses are given in Table 4.13, and the equivalent parameter names used in the LTPDA repositories can be found in Appendix 7.

4 Optical pathlength difference noise characterisation

Parameter	Description	Frequency [Hz]	ID
S^{FF}	Fast freq. loop state	1 Hz	LST17361
S^{SF}	Slow freq. loop state	1 Hz	LST17364
S^{OPD}	OPD loop state	1 Hz	LST17367
S^{SP}	Slow power loop state	1 Hz	LST17358
y^{FF}	Fast freq. loop feedback	1 Hz	LST17340
		10 Hz	
y^{SF}	Slow freq. loop feedback	1 Hz	LST17345
		10 Hz	
y^{OPD}	OPD loop feedback	1 Hz	LST17350
		10 Hz	
y^{SP}	Slow power loop feedback	1 Hz	LST17357
		10 Hz	
Ψ_R	Ref. ifo. output	10 Hz	LST12407
x_{12}	X12 ifo. output	10 Hz	LST10130
SSC	Source sequence counter	10 Hz	SCT70388

Table 4.13: The telemetry parameters used in the analysis of the EM, FM, and OSTT test campaign performance investigations for the analysis of the OPD noise contributions.

Initially all of the data was processed in the same way, as described under the 'Overview of the analysis' subheading. The determination of the closed-loop OPD noise is described under the 'Closed-loop OPD noise' subsection.

Overview of the analysis

1. The data specified in Table 4.13 was downloaded according to the times specified in the test campaign reports [32] [43] [44].

2. The loop state and feedback signals for each of the loops were checked to determine the start and end times for a segment where all of the loops were operating under nominal conditions (state = 3).

3. The Ψ_R and x_{12} channels were split according to these times.

4. The data was checked for data quality and glitches and repaired accordingly, as described in Appendix 9.

Closed-loop OPD noise

In the same way as described in the free-running OPD noise investigation, the OPD noise is determined by calculating the amplitude spectral density of the reference interferometer output, Ψ_R. The results for the EM, FM, OSTT hot phase, and OSTT cold phase are shown in Figures 4.33, 4.34, 4.35, and 4.36.

The results for the EM and FM test campaigns are not below the requirement, but even so, the OPD noise was not the limiting noise, and the differential test mass displacement was below the requirement. The differential test mass displacement spectra can be seen in Section 3.3.1.

In order to demonstrate the function of the control loop the free-running OPD noise measurement determined in Section 4.1 was multiplied by the modelled noise suppression function, calculated in Section 4.2. The results are shown in Figures 4.37 to 4.40. If the control loop was implemented with the same parameters as determined in

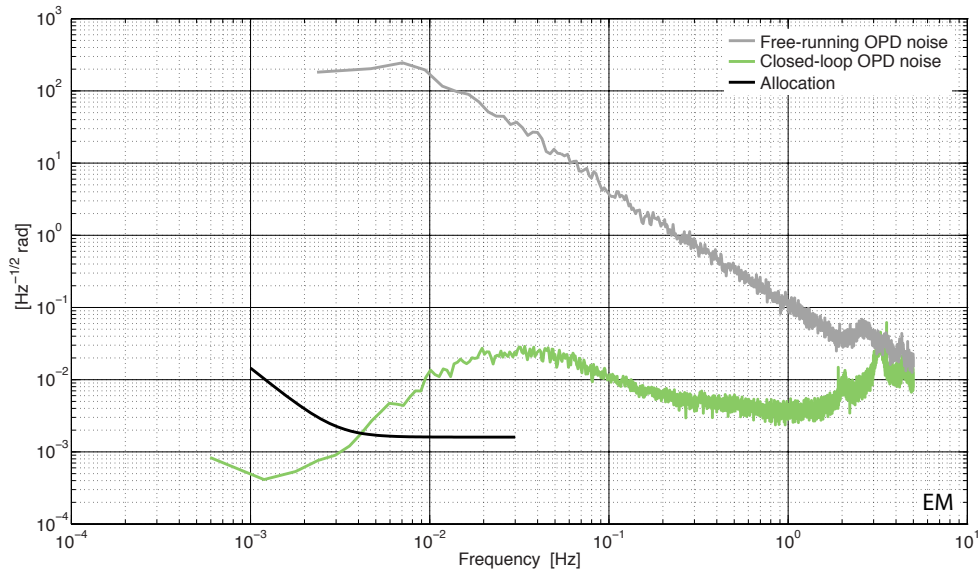# 4 Optical pathlength difference noise characterisation

Figure 4.33: The closed-loop OPD noise, shown in green, as calculated from the EM test campaign result. Also shown is the result from the free-running investigation.
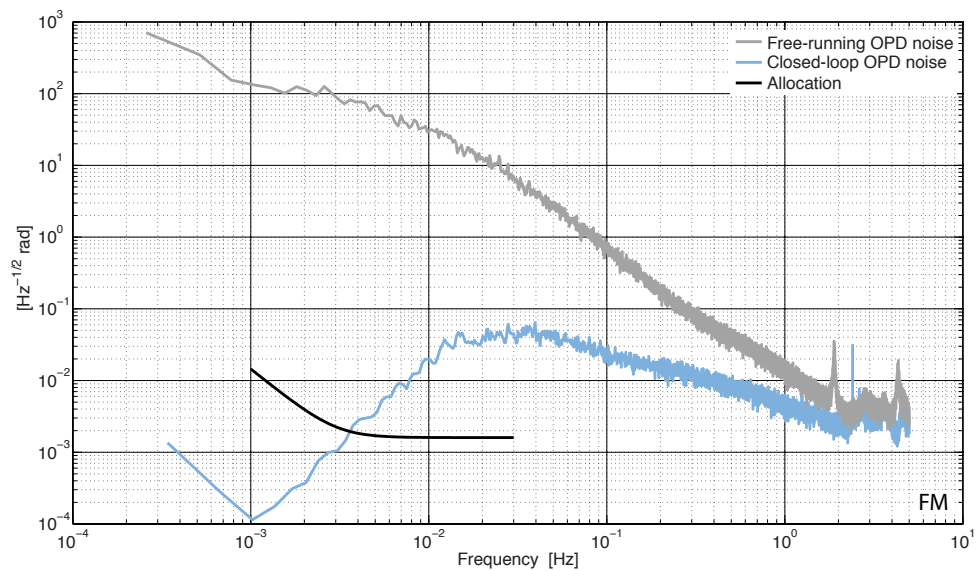

Figure 4.34: The closed-loop OPD noise, shown in blue, as calculated from the FM test campaign result. Also shown is the result from the free-running investigation.

Figure 4.35: The closed-loop OPD noise, shown in red, as calculated from the OSTT test campaign result, where the satellite was in the hot phase. Also shown is the result from the free-running investigation.
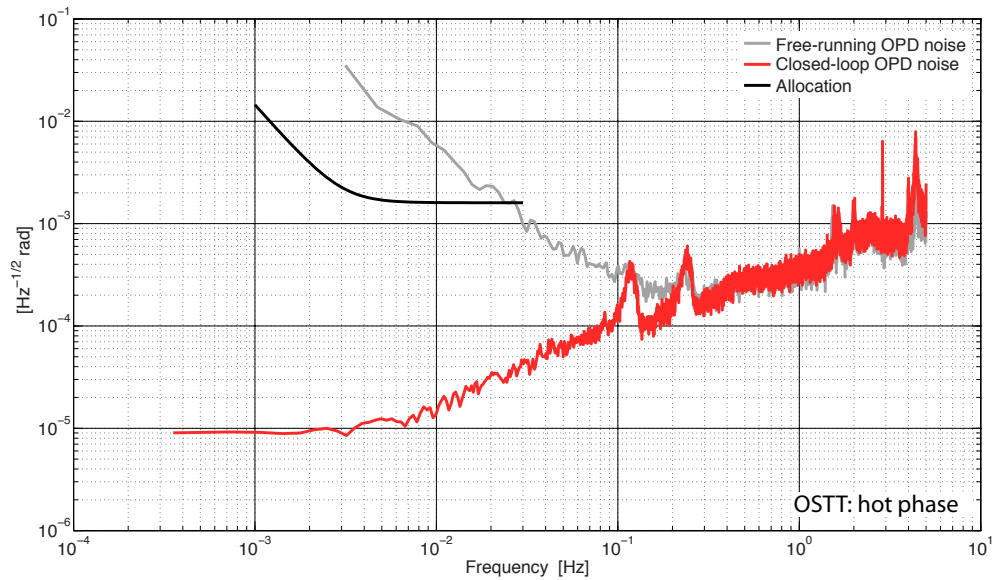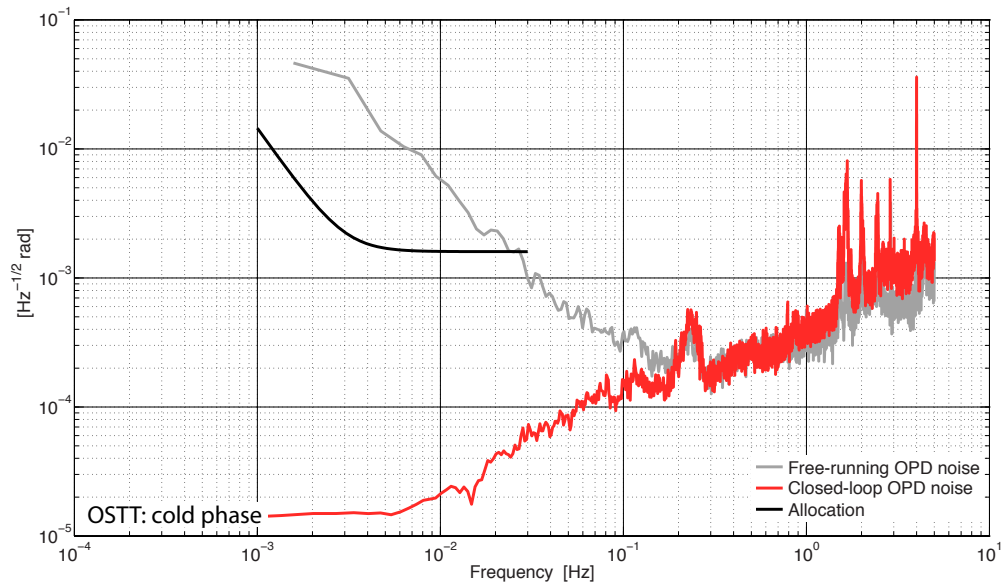

Figure 4.36: The closed-loop OPD noise, shown in red, as calculated from the OSTT test campaign result, where the satellite was in the cold phase. Also shown is the result from the free-running investigation.

Chapter 4

251

the control loop characterisation investigation, and the free-running frequency noise had the same characteristics as previously measured, then the result of the multiplication should correspond to the measured closed-loop noise. As no loop characterisation measurement was performed during the OSTT campaign, the FM model was used.

The results for the EM campaign and the hot and cold phases of the OSTT campaign do not correspond. As for the frequency noise results, this implies that either the noise level differed between the measurement times, or the control loop has a different response when operating under completely closed-loop conditions. The noise suppression function of the EM control loop showed a large servo bump, which may have caused the loop to be unstable. The FM results match as expected.

The coupling coefficients for OPD noise into differential test mass displacement, calculated in Sections 4.1 and 4.2, demonstrated that the coupling could be considered to be zero. Therefore, no projection of the OPD noise onto the differential test mass displacement were made, as any results would not provide any accurate information.

Figure 4.37: A plot of the free-running OPD noise multiplied by the noise suppression function for the EM test campaign, plotted along with the measured closed-loop noise.
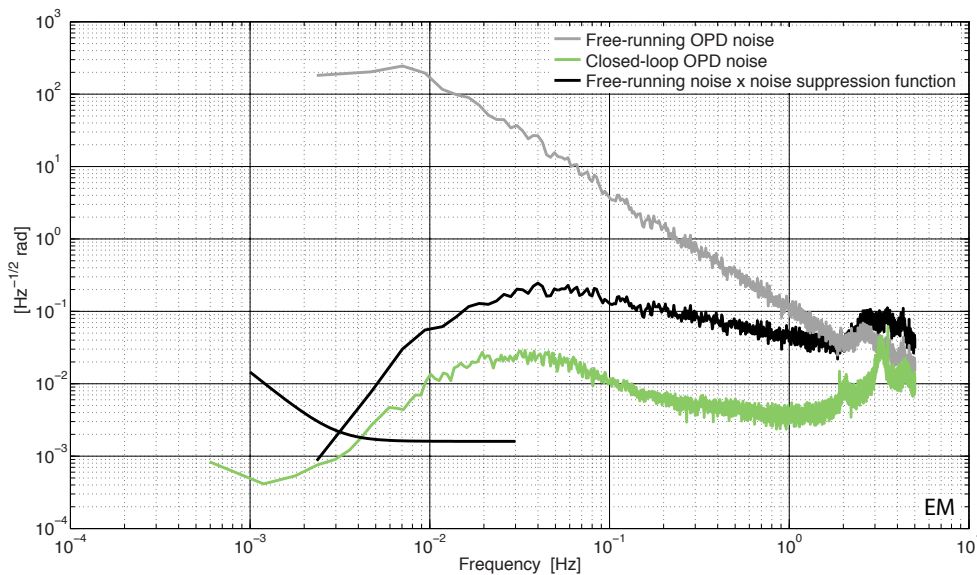
Figure 4.38: A plot of the free-running OPD noise multiplied by the noise suppression function for the FM test campaign, plotted along with the measured closed-loop noise.
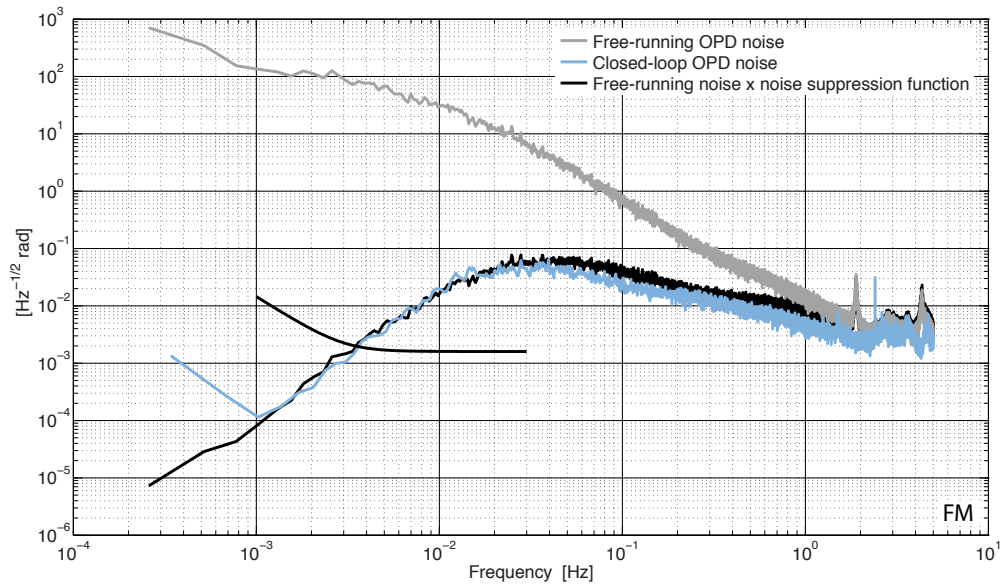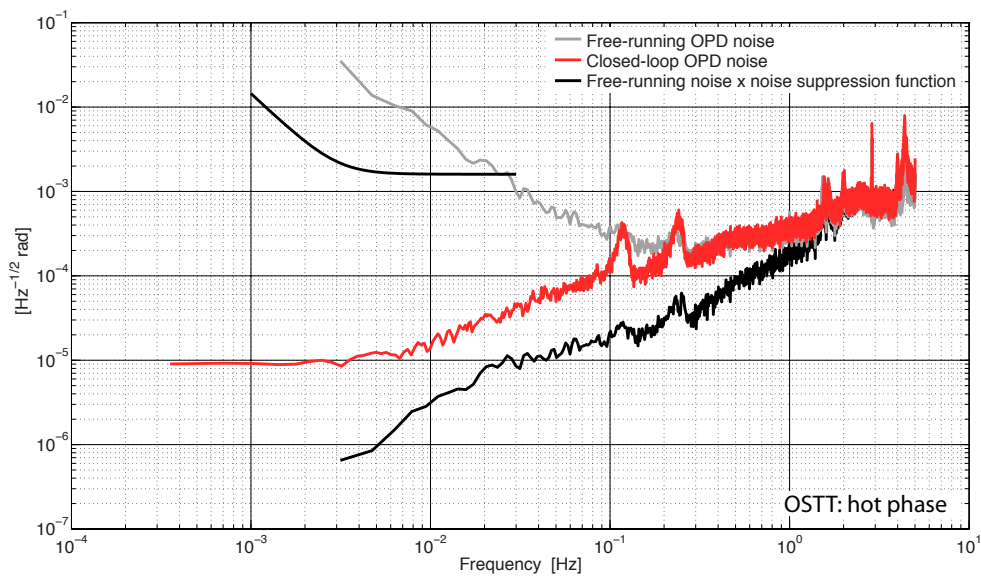

Figure 4.39: A plot of the free-running OPD noise multiplied by the noise suppression function for the OSTT test campaign during the hot phase, plotted along with the measured closed-loop noise.
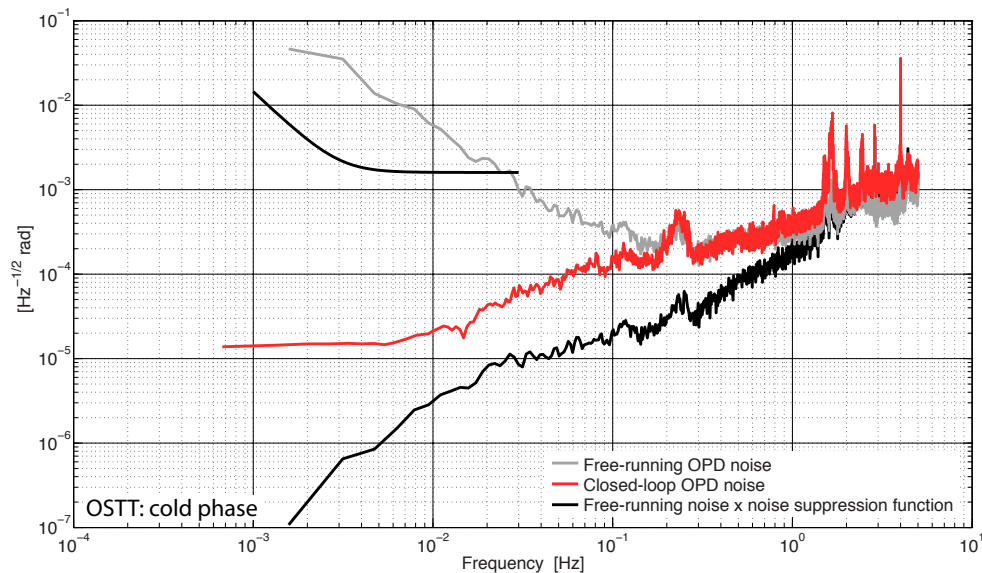
Figure 4.40: A plot of the free-running OPD noise multiplied by the noise suppression function for the OSTT test campaign during the cold phase, plotted along with the measured closed-loop noise.

4.3.2 In-flight investigation

The in-flight investigations from which the closed-loop OPD noise can be determined are well defined, and therefore not presented here. An overview of the suggested procedure for the analysis of the in-flight investigation is given in Figure 4.41. The data preparation procedure is shown in Figure 4.42. The sub-analysis procedure for the calculation of the closed-loop OPD noise spectrum is given in Figure 4.43a, and the procedure for projecting the OPD noise component onto the differential test mass displacement measurement is shown in Figure 4.43b.
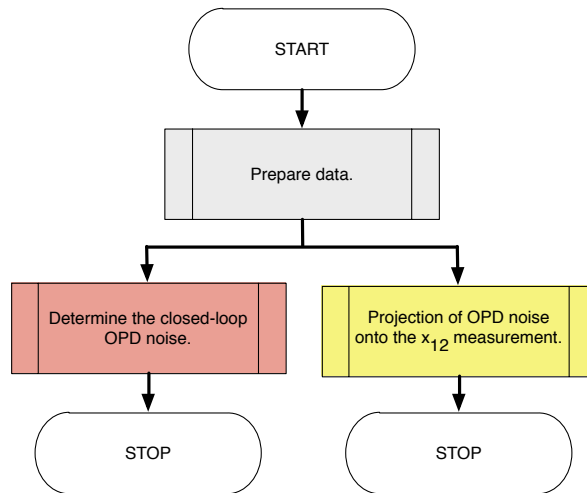
Figure 4.41: An overview of the closed-loop OPD noise sub-analyses for the in-flight data analysis. This analysis requires data from a performance measurement. The sub-analyses are each described in separate figures.

Chapter 4

255
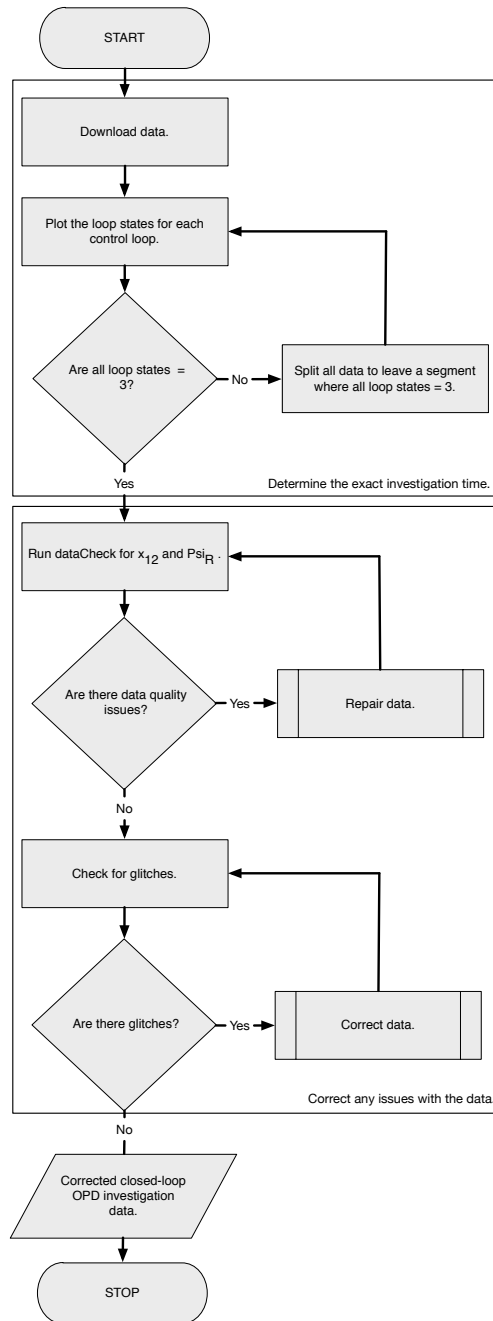
Figure 4.42: A procedure for the data preparation step of the in-flight closed-loop OPD noise analysis.
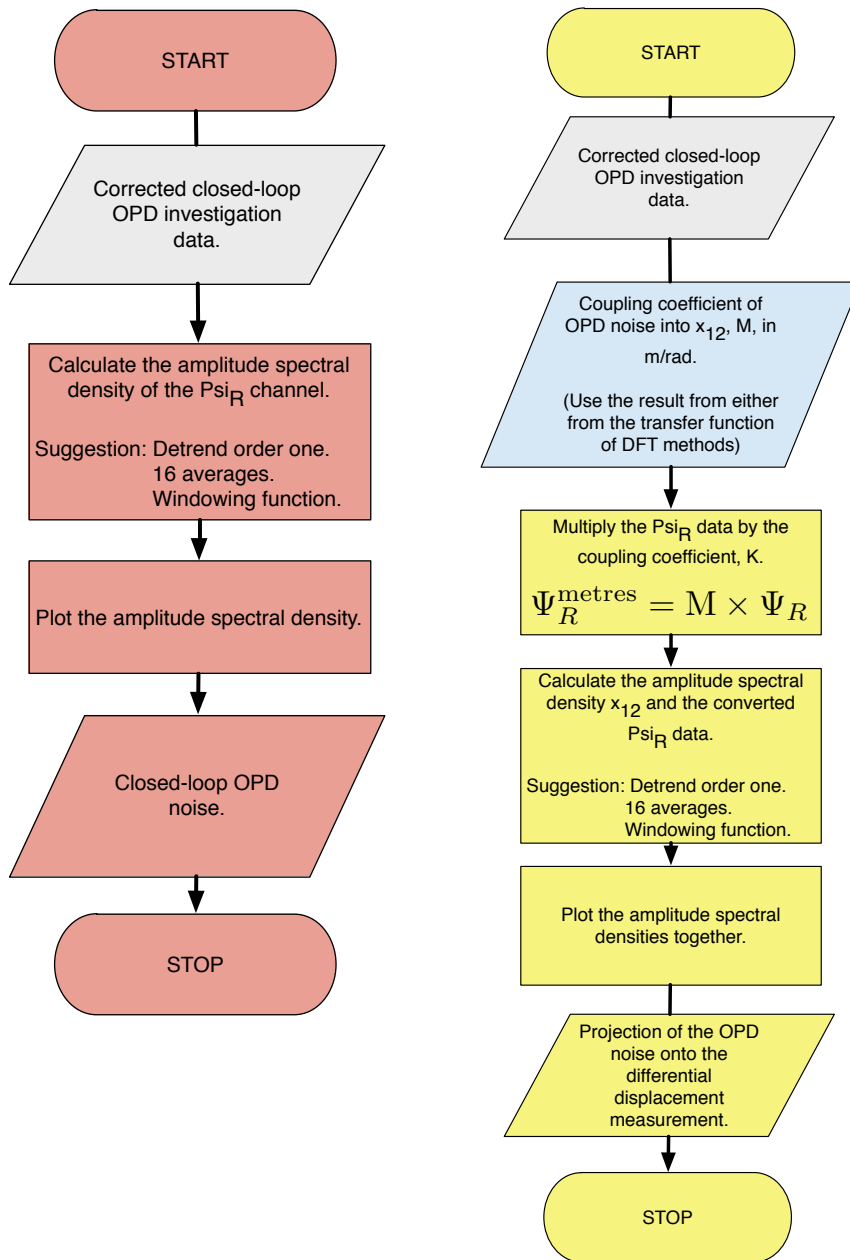
(a) The suggested analysis procedure for calculating the spectrum of the closed-loop OPD noise from an in-flight performance investigation.

(b) The suggested analysis procedure for projecting the OPD noise component onto the measured differential test mass displacement.

Figure 4.43

5 Amplitude noise characterisation

Contents

The following sections describe investigations to characterise the contribution of amplitude noise to the measurement of the differential test mass displacement. In contrast to the chapters describing the frequency and optical pathlength difference noise, only the results of the OSTT test campaign have been analysed and presented here. This is because the subsystems used in the OSTT test campaign were most representative of the in-flight setup. This impacts the amplitude control loop more than the frequency and OPD control loops, as different photodiodes were used.

5 Amplitude noise characterisation

5.1 Estimation of the beam power on the optical bench

For the amplitude noise investigations it is necessary to determine the beam power incident on each of the test masses. This section describes methods by which this can be achieved. While the methods described here are specifically to determine the power at the test masses, similar procedures can be followed to estimate the power at any point on the optical bench.

The following channels contain information relating to the beam powers, and are downloaded with the main science data in the 128,3 packet:

- Σ_R: The normalised processed sum of the power on the reference interferometer quadrants;

- Σ_1: The normalised processed sum of the power on the X1 interferometer quadrants.

The housekeeping 3,25 packet contains data with a 1 Hz sampling rate:

- Power monitor one: The signal from the beam one (measurement beam) single element photodiode;

- Power monitor two: The signal from the beam two (reference beam) single element photodiode.

Additionally, the following channels can be selectively downloaded with the configurable 128,4 packet:

- Σ_F: The processed sum of the power on the frequency interferometer quadrants;

- Σ_{12}: The processed sum of the power on the X12 interferometer quadrants.

In order to use these channels to determine the beam power at any point on the optical bench, it is first necessary to convert the telemetry output into the equivalent power before the photodiode. The conver-

sion of the Σ_i quadrant photodiode outputs is described in Box 5.1, and the conversion of the single element photodiode power monitor channels is described in Box 5.2.

From the conversions, an estimate of the power is known in front of the single-element and the quadrant photodiodes. The powers calculated from the Σ_i telemetry are higher resolution than the power monitor power values, as the ADC is more accurate and the measurement noise is lower. The two power monitor parameters provide an estimate of the DC level, but the 1 Hz data gives a poor measurement of any high frequency fluctuations. To demonstrate this, the amplitude spectral densities of the powers calculated at the amplitude photodiodes, PDA1 and PDA2, and the quadrant photodiodes, PDR and PD1, along with the coherence of the PDA1 and PD1 channels, are shown in Figure 5.1. At low frequencies, the results from the amplitude photodiodes and the quadrant photodiodes correspond, and there is high coherence. These results are taken from the OSTT test campaign free-running amplitude noise investigation, discussed in Section 5.2.

The path of each beam on the optical bench is known, as are estimates of the reflectivities, ρ, and transmissivities, τ, of the optical components, given in Table 5.1. More accurate values can be found in [61]. There are two possible methods for calculating the power at each test mass (and at any position on the optical bench):

Component		Front face		Back face	
Type	Label	ρ	τ	ρ	τ
Beamsplitter	BS1-2/4-10	0.49	0.49	0.005	0.995
	BS11	0.08	0.82	0	1.00
	BS16	0.08	0.82	0.005	0.995
Mirror	M1/5-6/8/10-12/14-15	0.997	0.003	-	-
Window	WIN1, WIN2	0.005	0.995	0.005	0.995
Test mass*	TM1, TM2	1.00	0	-	-

Table 5.1: Estimates of the coefficients of reflection, ρ, and transmission, τ, for each of the components on the LPF optical bench. *The test mass is assumed to be perfectly reflective. For more accurate values, see [61].

1. Using the calculated power in front of the X1 interferometer quadrant photodiodes, P^{X1}, and tracing the beam backwards using the values for the coefficients on that particular path[1].

5 Amplitude noise characterisation
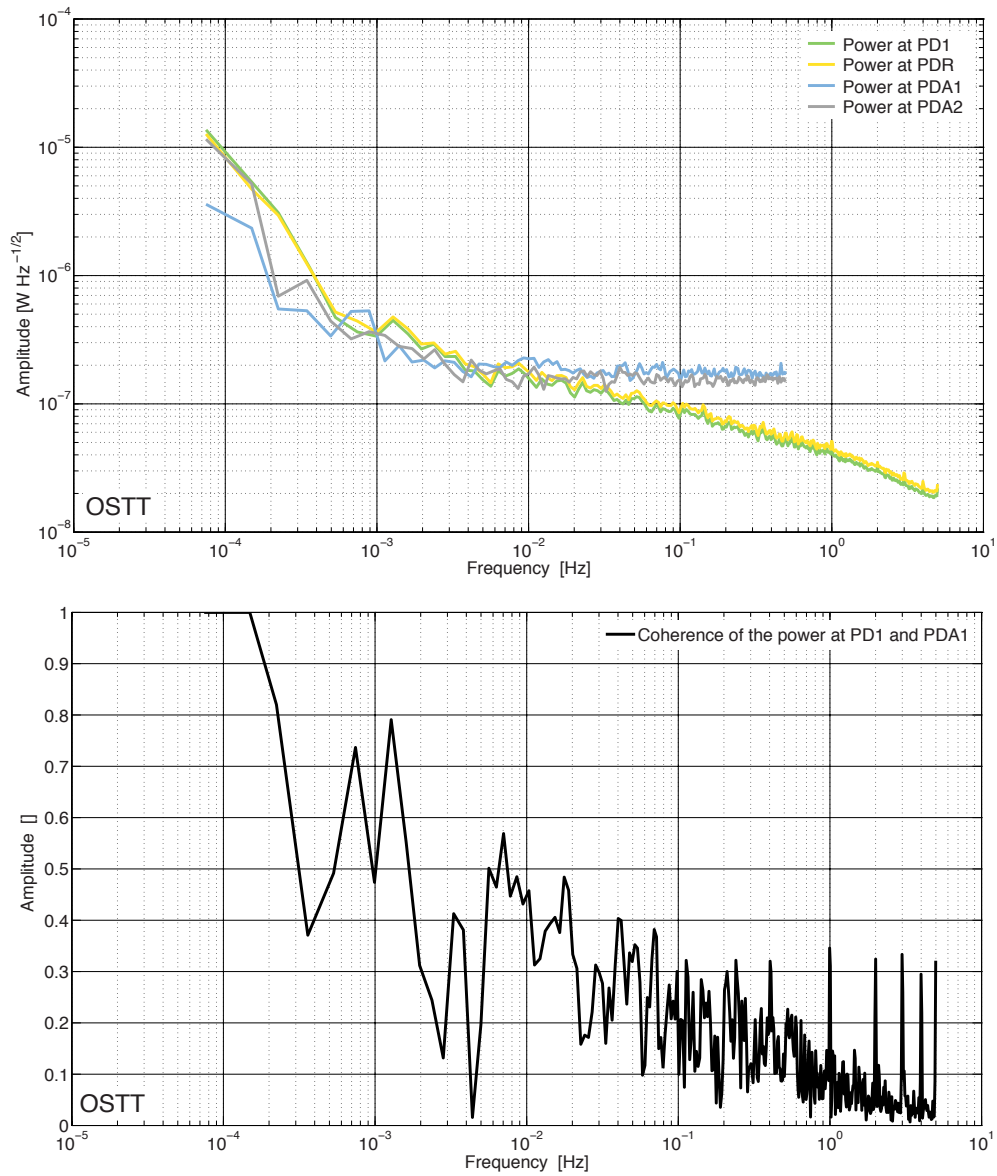
Figure 5.1: The amplitude spectral densities of the power calculated at PDA1 (blue), PDA2 (grey), PD1 (green), and PDR (yellow), along with the coherence of the PDA1 and PD1 powers (black). The results are taken from the free-running amplitude noise investigation in the OSTT test campaign. The amplitude spectral densities were calculated with 16 averages, and the coherence using 'lcohere' with detrending of order one and 12 averages [60].
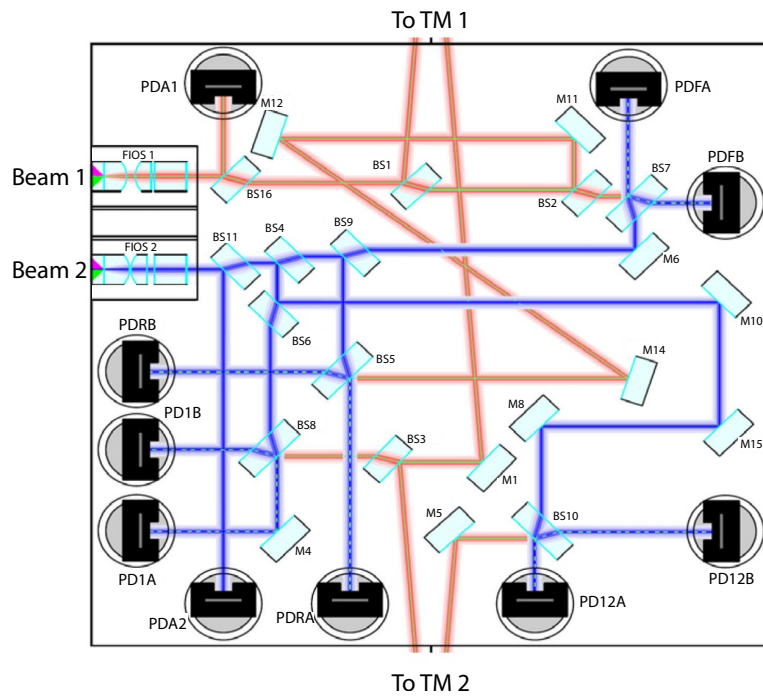
Figure 5.2: A diagram of the optical bench showing the fibre-injectors, the labelled mirrors and beamsplitters, and the photodiodes.

However, the Σ_i output during a measurement using two beams, i.e., any interferometric measurement, is the sum of the reference and measurement beams. The fraction of the power in each of the two beams, N_1 and N_2, needs to be estimated. There are several methods which can be used to make this estimation:

- The converted power in front of the single-element photo-diodes, along with the reflectivity of beamsplitters BS11 and BS16, can be used to determine the power, P_1 and P_2, of the measurement and reference beam after each FIOS:

$$P_1 = \frac{P_{\mathrm{PDA1}}}{\rho_{\mathrm{BS16}}} \tag{5.1}$$

$$P_2 = \frac{P_{\mathrm{PDA2}}}{\rho_{\mathrm{BS11}}} \tag{5.2}$$

---

[1]A disadvantage of tracing the calculated power at a quadrant photodiode back to the test mass is that the value must be split to give a power contribution from both the measurement and reference beams. This process assumes that the power fluctuations are the same in each beam.

- A short investigation could be performed during which one beam is switched off, and the output from the Σ_i telemetry recorded. This would then be repeated with the other beam switched off. The power in each beam, P_1 and P_2, could then be determined by converting the Σ_1 parameter in each case, according to the method described in Box 5.1. The procedure for implementing such an investigation in-flight is given in Section 5.1.1. Ideally, this investigation would be periodically repeated during the mission, to determine if the relative beam powers are changing, and if so, how.

- Both the Σ_R and Σ_1 telemetry parameters are always available via the 128,3 packet. These parameters should both contain the same proportion of power from the reference and measurement beams, so it should be possible to calculate the power in each beam mathematically. This method is described in Box 5.3.

For each of the above cases the fraction of the power in each beam is calculated according to:

$$N_1 = \text{mean}\left(\frac{P_1}{P_1 + P_2}\right) \tag{5.3}$$

$$N_2 = \text{mean}\left(\frac{P_2}{P_1 + P_2}\right) \tag{5.4}$$

The power in each of the two beams in front of the X1 QPD, P_1^{X1} and P_2^{X1}, can then be calculated:

$$P_1^{\text{X1}} = P^{\text{X1}} \times N_1 \tag{5.5}$$

$$P_2^{\text{X1}} = P^{\text{X1}} \times N_2 \tag{5.6}$$

where P^{X1} is the power in front of an X1 interferometer quadrant photodiode, calculated according to the method described in Box 5.1. The beam one value can be traced backwards through the appropriate optical components to determine the power at test mass one, P_{TM1}, according to:

$$P_{\text{TM1}} \quad = \quad \frac{P_1^{\text{X1}}}{C_{\text{TM1}\rightarrow\text{PD1}}} \tag{5.7}$$

where $C_{\text{TM1}\rightarrow\text{PD1}}$ is the coefficient determined by multiplying the applicable coefficients of reflection and transmission of the optical components between the X1 photodiode and test mass one, as given in Table 5.1. The calculated value of this coefficient, taken by averaging the coefficients for the nominal and redundant beampaths, is shown in Table 5.2.

Coefficient	Value
$C_{\text{TM1}\rightarrow\text{PD1}}$	23.49×10^{-2}
$C_{\text{TM1}\rightarrow\text{TM2}}$	47.88×10^{-2}

Table 5.2: The coefficient for tracing beam one from test mass one to PD1, and the coefficient for tracing beam one from test mass one to test mass two.

In order to determine the power at test mass two, the power calculated at test mass one, P_{TM1}, must be propagated forward:

$$P_{\text{TM2}} = P_{\text{TM1}} \times C_{\text{TM1}\rightarrow\text{TM2}} \tag{5.8}$$

where $C_{\text{TM1}\rightarrow\text{TM2}}$ is a coefficient determined by multiplying the appropriate coefficients of reflection and transmission of the optical components between test mass one and test mass two. The value of this coefficient, calculated using the coefficients given in Table 5.1, is given in Table 5.2.

Ideally, more than one of these methods should be implemented to ensure the consistency of the result.

2. The converted values from the power monitors can be traced forward:

$$P_{\text{TM1}} \quad = \quad P_{\text{PDA1}} \times C_{\text{PDA1}\rightarrow\text{TM1}} \tag{5.9}$$
$$P_{\text{TM2}} \quad = \quad P_{\text{PDA1}} \times C_{\text{PDA1}\rightarrow\text{TM2}} \tag{5.10}$$

Chapter 5

where P_{PDA1} is the power in front of the beam one SEPD, calculated as described in Box 5.2. The coefficients $C_{\mathrm{PDA1}\to\mathrm{TM1}}$ and $C_{\mathrm{PDA1}\to\mathrm{TM2}}$, are calculated by multiplying the appropriate coefficients of reflection and transmission along the associated beampath and are shown in Table 5.3.

Coefficient	Value
$C_{\mathrm{PDA1}\to\mathrm{TM1}}$	5.5787
$C_{\mathrm{PDA1}\to\mathrm{TM2}}$	2.6713

Table 5.3: The coefficient for tracing beam one from PDA1 to TM1, and the coefficient for tracing beam one from PDA1 to TM2.

This would not require a separate investigation to determine the relative powers of each beam, but the accuracy of the result would be lower than using the converted Σ_i parameters.

As an example of the two methods, the equivalent power at PDA1 and the beam one component at PD1 propagated to test mass one are shown in Figure 5.3. These results are taken from the free-running amplitude noise investigation presented in Section 5.2.
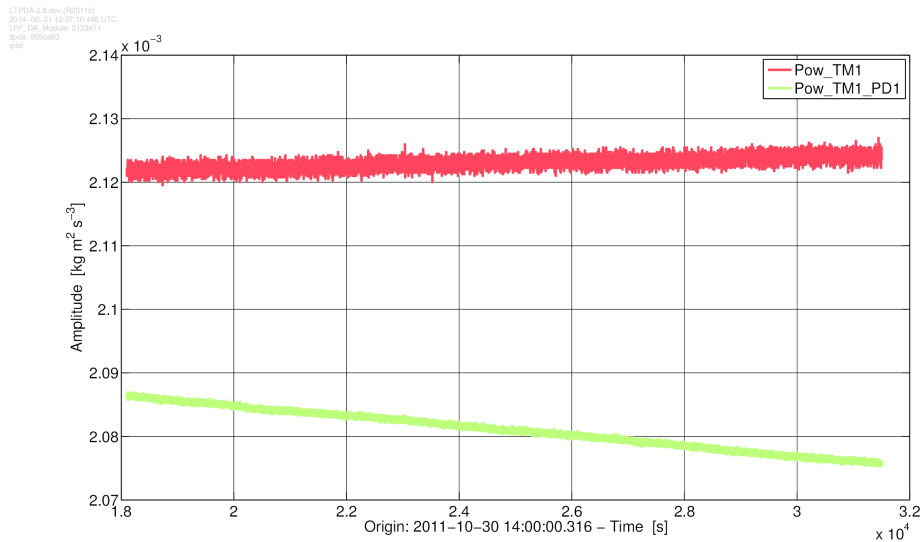
Figure 5.3: The equivalent power at test mass one calculated from the propagation of the calculated power at PDA1 (red) and from the calculated beam one component of the power at PD1 (green). These results are taken from the free-running amplitude noise investigation presented in Section 5.2

LTPDA methods

Several LTPDA methods have been implemented to facilitate such analyses:

- To convert the power monitor channels from PDA1 and PDA2 into an equivalent power, as described in Box 5.2, the 'calibrateOMSSingleElementPower' method was implemented.

- The 'calibrateOMSQuadPower' method converts the Σ_i channel into an equivalent power at the photodiode, using the method described in Box 5.1.

- The 'propagateOMSPower' method was implemented to propagate the power at the PD1 photodiode to test mass one, and from test mass one to test mass two, as well as from PDA1 to the two test masses. This method uses the coefficients determined by multiplying the reflectivities and transmissivities of the optical components in each beam path, as described above.

- The PDA1 and PDA2 photodiodes can be propagated forward to each photodiode, the mean value determined, and the result visually displayed on a diagram of the optical bench, using the 'displayOMSBeamPowers' method, implemented by M. Hewitson. An example of the output is shown in Figure 5.4. This can be used during any in-flight investigation where the power monitor signals are available to monitor the power on the optical bench.

5.1.1 In-flight investigation

The in-flight investigation to determine the fraction of the power in each beam is the only in-flight investigation required to determine the beam power on the optical bench. A suggested procedure for performing this investigation is detailed in Figure 5.5. The setup and telemetry required for this investigation is given in Table 5.4. In order to provide estimates of the spectral density of the fluctuations down to $1\,\mathrm{mHz}$, each measurement should have a duration of at least $10000\,\mathrm{s}$ [56]. The analysis should be performed as described above, with the
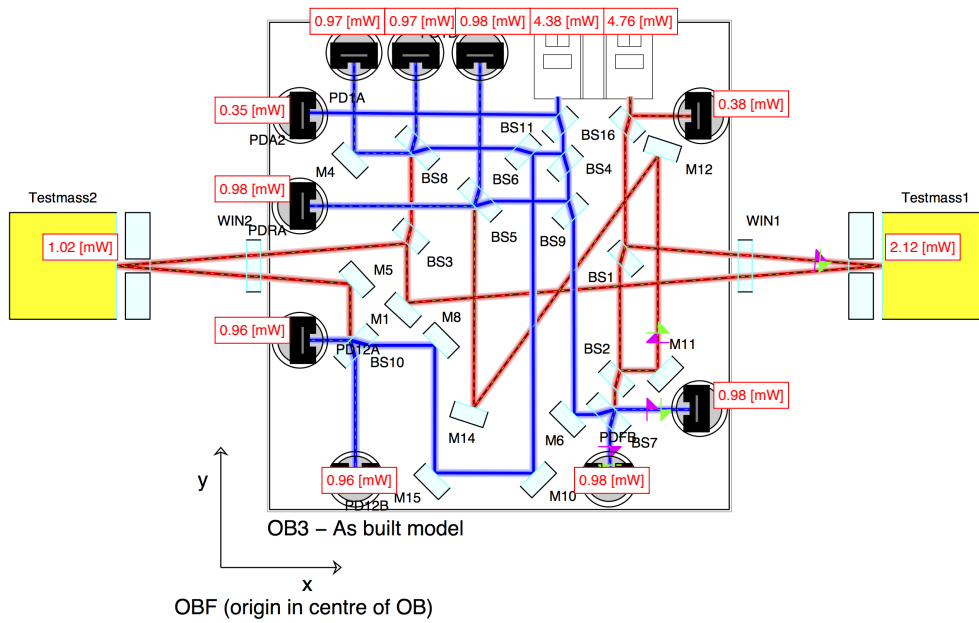
Figure 5.4: An example of the output from the 'displayOMSBeamPowers' method which shows the powers at the fibre injectors, the test masses, and at each photodiode, determined by propagating the power at PDA1 and PDA2.

initial data preparation step described in Figure 5.6.

Investigation	Determine power on the optical bench		
Telemetry required	128,3	Σ_1	LST12408
		Σ_R	LST12409
	3,25	Fast power mon. one	LLT10052
		Fast power mon. two	LLT10053
		SSC	SCT70388
Length	~ 6 hours		

Table 5.4: An overview of the key information relating to the method for determining the power on the test masses. For the telemetry names associated with each parameter refer to Appendix 7.

```
                    ┌─────────────────────┐
                    │  START in acc. mode. │
                    └─────────────────────┘
                              │
                              ▼
                    ┌─────────────────────┐
                    │  Turn off beam two.  │
                    └─────────────────────┘
                              │
                              ▼
                    ┌─────────────────────┐
                    │    Wait 10000s.      │
                    └─────────────────────┘
                              │
                              ▼
                    ┌─────────────────────┐
                    │   Turn on beam two.  │
                    └─────────────────────┘
                              │
                              ▼
                    ┌─────────────────────┐
                    │  Turn off beam one.  │
                    └─────────────────────┘
                              │
                              ▼
                    ┌─────────────────────┐
                    │    Wait 10000s.      │
                    └─────────────────────┘
                              │
                              ▼
                    ┌─────────────────────┐
                    │   Turn on beam one.  │
                    └─────────────────────┘
                              │
                              ▼
                    ┌─────────────────────┐
                    │   STOP in acc. mode. │
                    └─────────────────────┘
```

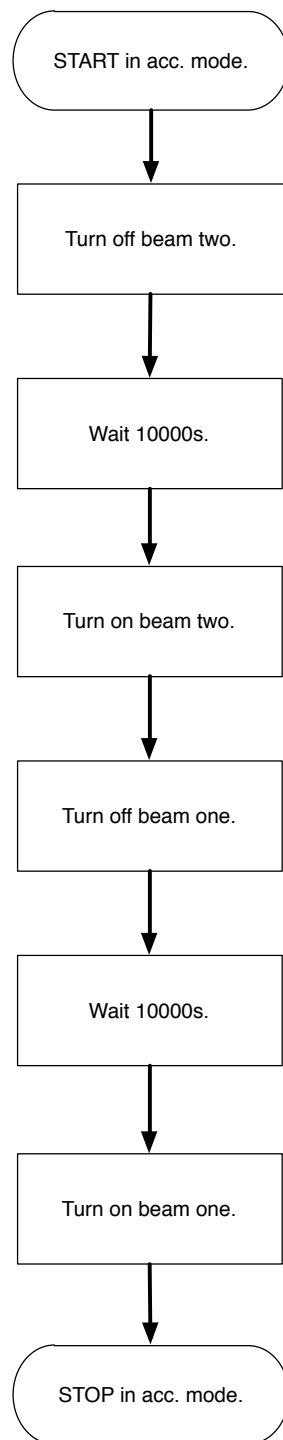**Figure 5.5:** The suggested method for determining the relative power in each of the reference and measurement beams in-flight.
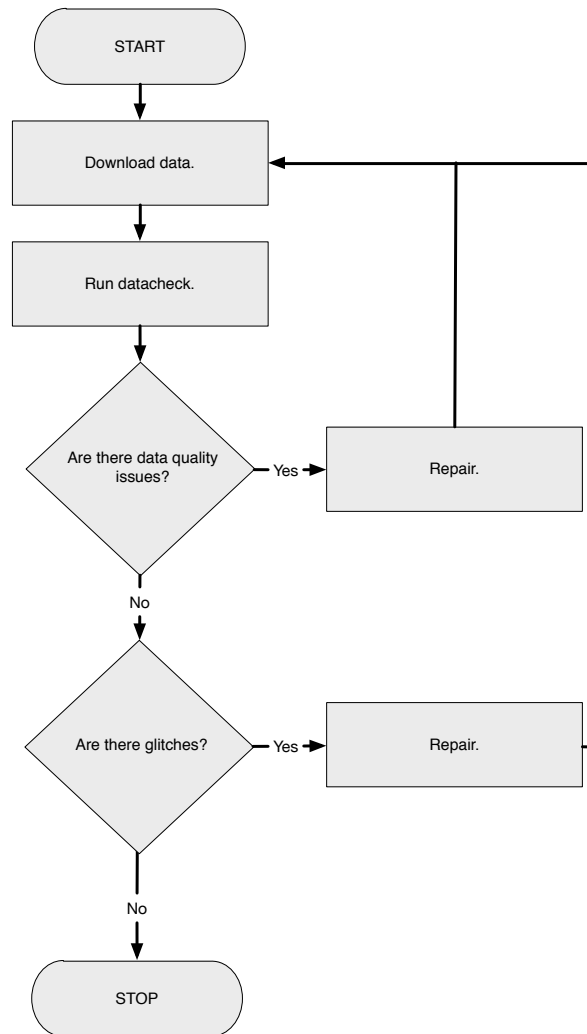
Chapter 5

Figure 5.6: The data preparation method for analysing the relative power in each of the reference and measurement beams in-flight.

Conversion of Σ_i to an equivalent power

Under nominal operation the Σ_i parameter represents the average total power that is incident on the nominal and redundant photodiodes in a particular interferometer, i. The data has been processed through the phasemeter and the DMU, as described in Section 1.4, so the units of the output are not in Watts, but are dimensionless values, normalised to the range of the analogue-to-digital convertor in the phasemeter. In order to convert the Σ_i value the following procedure is necessary:

- Convert the normalised value to a voltage:

$$V_i = \Sigma_i \times X^{\mathrm{ADC}} \tag{5.11}$$

  where X^{ADC} is the ADC range. The range of the ADC is 2.5 V.

- Convert the voltage to the current input into the TIA, I_i:

$$I_i = \frac{V_i}{R} \tag{5.12}$$

  where R is the resistance of the trans-impedance amplifier, here taken to be $3320\,\Omega$.

- The current can be converted to an equivalent power, P^i, according to:

$$P^i = \frac{h\nu}{\eta q} I_i \tag{5.13}$$

  where h = Planck's constant, ν is the frequency of the light, η is the photodiode efficiency ≈ 0.8, and q is the charge of an electron.

Box 5.1: Calculation of the power in front of a quadrant photodiode from the Σ_i telemetry parameters.

> **Conversion of the power monitor output into an equivalent power**
>
> The output from the two laser power monitors is a current, I_i, in units of μA, where i =PDA1 or PDA2, for the power in front of PDA1 and PDA2 respectively. This is converted into an equivalent power incident on the photodiode according to:
>
> $$P_i = \frac{h\nu}{\eta q} I_i \qquad (5.14)$$
>
> where h = Planck's constant, ν is the frequency of the light, η is the photodiode efficiency ≈ 0.8, and q is the charge of an electron.

Box 5.2: Calculation of the power in front of a single element photodiode from beam monitor telemetry parameters.

Calculation of the relative beam power with Σ_1 and Σ_R

Both Σ_1 and Σ_R contain components from both the measurement and reference beams (beams 1 and 2 respectively). The power in each beam depends upon the optical path travelled, defined by the coefficients of transmission and reflection of each optical component in that path. The equivalent power, P^{X1} and P^R, calculated from Σ_1 and Σ_R, as described in Box 5.1, can be defined as follows:

$$P^R = C_1^{\text{ref}} P_1 + C_2^{\text{ref}} P_2 \tag{5.15}$$

$$P^{X1} = C_1^{X1} P_1 + C_2^{X1} P_2 \tag{5.16}$$

where P_1 and P_2 are the beam powers at FIOS1 and FIOS2 respectively (see Equations 5.1 and 5.2), and C is the path dependent coefficient. The coefficient subscript shows which beam is being considered, and the superscript defines the interferometer. For example, C_1^{ref}, is the coefficient for propagating beam 1 in the reference interferometer. Each coefficient can be calculated by multiplying together the coefficients of reflection or transmission of the optical components in the beam path. The beam paths are shown in Figure 1.11, and the coefficients of reflection and transmission in Table 5.1. The calculated coefficients are shown in the table below. It should be noted that these coefficients are the average of the coefficients for the nominal and redundant beam paths.

Coefficient	Value
C_1^{ref}	10.65×10^{-2}
C_2^{ref}	10.74×10^{-2}
C_1^{X1}	10.48×10^{-2}
C_2^{X1}	10.73×10^{-2}

By rearranging Equations 5.15 and 5.16, the beam power at each FIOS can be calculated:

$$P_1 = \frac{P_R - \frac{C_2^{\text{ref}}}{C_2^{X1}} P^{X1}}{C_1^{\text{ref}} - \frac{C_2^{\text{ref}}}{C_2^{X1}} C_1^{X1}} \tag{5.17}$$

273

$$P_2 = \frac{P_R - \frac{C_1^{\text{ref}}}{C_1^{\text{X1}}} P^{\text{X1}}}{C_2^{\text{ref}} - \frac{C_1^{\text{ref}}}{C_1^{\text{X1}}} C_2^{\text{X1}}} \tag{5.18}$$

A similar procedure can be applied when using the values of the power determined from the Σ_{12} and Σ_F parameters.

Note: This method requires the coefficients of reflection and transmission to be well known. Even small changes in the calculated coefficients result in large discrepancies in the calculated powers.

Box 5.3: Calculating the relative beam proportion of the beam power in the measurement and reference beams using the Σ_R and Σ_1 telemetry parameters.

5.2 Free-running amplitude noise

The aim of this investigation is to determine the amplitude noise characteristics when both the fast and slow control loops are open. The investigation yields several results:

- estimation of the free-running RIN;

- contribution of power noise to the differential test mass displacement:

    - coupling of noise at the heterodyne frequency;

    - contribution from the radiation pressure noise.

Free-running relative intensity noise

The RIN describes the ratio of the power fluctuations and the mean power. This can be calculated from the Σ_i telemetry. Initially the Σ_i parameter must be converted to an equivalent power, P^i, using the method described in Box 5.1. The relative intensity noise is then:

$$\text{RIN} \quad = \quad \frac{P^i}{\text{mean}(P^i)} \tag{5.19}$$

$$\tag{5.20}$$

The amplitude spectral density of this value is the measurement of the amplitude noise. This can be compared to the result of the closed-loop amplitude noise investigation to determine whether the control loop is operating as required.

Coupling of noise at the heterodyne frequency

The power that reaches the X12 quadrant photodiodes is processed by the phasemeter and the DMU to determine the differential test mass displacement measurement, x_{12}, as described in Section 1.4. Amplitude noise at frequencies around the heterodyne frequency, f_{het}, will couple directly into the measurement.

A broadband coupling coefficient, with units of m/ Hz, can be calculated from the transfer function of the x_{12} data and the power received at the quadrant photodiodes, P_i. This power is determined from the Σ_i channels, according to the method described in Box 5.1. Although the Σ_{12} channel is not downloaded unless requested, the power in front of the photodiodes in each interferometer are derived from the same beams, so any of the Σ_i channels can be used to determine the coupling.

A projection of the f_{het} amplitude noise onto the measured differential test mass displacement could then be determined by multiplying the power at the photodiode, P_i, by the coupling coefficient. The amplitude spectral density of the result, plotted with the amplitude spectral density of x_{12}, gives the projection.

Contribution of the radiation pressure noise

In order to calculate the contribution of the radiation pressure noise to the differential test mass displacement it is first necessary to calculate

the power at each of the test masses, P_{TM1} and P_{TM2}. This is achieved using the methods described in Section 5.1. The amplitude spectral density of the power at each test mass, $\widetilde{P}_{\text{TM1}}$ and $\widetilde{P}_{\text{TM2}}$ can be used to determine the displacement induced at each test mass according to:

$$\widetilde{x}_{\text{TM1}}^{\text{low freq. RIN}} \quad = \quad \frac{\widetilde{P}_{\text{TM1}}}{2cm\pi^2 f^2} \tag{5.21}$$

$$\widetilde{x}_{\text{TM2}}^{\text{low freq. RIN}} \quad = \quad \frac{\widetilde{P}_{\text{TM1}}}{2cm\pi^2 f^2} \tag{5.22}$$

where f is the Fourier frequency, and m $= 1.96\,\text{kg}$, the mass of the test mass [56]. The total contribution of the radiation pressure noise to the differential test mass displacement, $\widetilde{x}_{12}^{\text{low freq. RIN}}$, is therefore:

$$\widetilde{x}_{12}^{\text{low freq. RIN}} = \widetilde{x}_{\text{TM1}}^{\text{low freq. RIN}} + \widetilde{x}_{\text{TM2}}^{\text{low freq. RIN}} \tag{5.23}$$

5.2.1 Test campaign results

In the OSTT test campaign, an investigation with the fast amplitude control loop free-running was only performed during the hot phase. This section presents the results of that investigation, which provides the best estimate of the free-running amplitude noise that can be expected in-flight. Initially, the data was processed as described under 'Overview of the analysis'. The free-running RIN, the coupling of noise at the heterodyne frequency, and the contribution of the radiation pressure noise were then analysed as described under the associated heading. Specific information relating to the investigation can be found in Appendix 8, Table 8.19.

Overview of the analysis

1. The data, specified in Table 5.5, was downloaded according to the times specified in the test campaign report [44].

2. The data was split based on the loop states and feedback to leave a segment where the fast (and slow) amplitude control

Parameter	Description	Frequency [Hz]	ID
S^{FF}	Fast frequency loop state	1 Hz	LST17361
S^{SF}	Slow frequency loop state	1 Hz	LST17364
S^{OPD}	OPD loop state	1 Hz	LST17367
S^{FP}	Fast power loop state	1 Hz	LLT10031
S^{SP}	Slow power loop state	1 Hz	LST17358
y^{FF}	Fast frequency feedback	1 Hz	LST17340
		10 Hz	
y^{SF}	Slow frequency feedback	1 Hz	LST17345
		10 Hz	
y^{OPD}	OPD feedback	1 Hz	LST17350
		10 Hz	
y^{SP}	Slow power feedback	1 Hz	LST17357
		10 Hz	
F^1	Beam one fast power feedback	1 Hz	LLT10048
F^2	Beam two fast power feedback	1 Hz	LLT10049
$\mathrm{Mon}_1^{\mathrm{FP}}$	Beam one power monitor (PDA1)	1 Hz	LLT10052
$\mathrm{Mon}_2^{\mathrm{FP}}$	Beam two power monitor (PDA2)	1 Hz	LLT10053
Σ_1	Power at PD1	10 Hz	LST12408
Σ_R	Power at PDR	10 Hz	LST12409
x_{12}	X12 ifo. output	10 Hz	LST10130

Table 5.5: The telemetry parameters used in the analyses of the OSTT test campaign free-running amplitude noise investigations.

Chapter 5

loops were open (state = 1), and the other loop states were in a stable condition for the duration of the measurement.

3. The data was checked for data quality issues and glitches and repaired accordingly, as detailed in Appendix 9.

4. The power monitor channels from PDA1 and PDA2 were converted to the equivalent power, as described in Box 5.2. Similarly, the Σ_1 and Σ_R channels were converted to the equivalent power, as described in Box 5.1.

5. The amplitude spectral densities of the calculated powers, detrended with order three, were determined, and the result is shown in Figure 5.1. Also shown is the coherence between the PDA1 and PD1 channels. The spectra show the difference in the measurement of the amplitude fluctuations by the PDA photodiodes compared to the quadrant photodiodes, which were previously discussed in Section 5.1.

   Note: The amplitude spectral densities were calculated with 16 averages, and detrending of order one. The coherence was calculate using 'lcohere' and 12 averages. The order three detrending removes any DC offset, and linear, quadratic, and cubic drifts.

6. It is expected that the Σ_1 and Σ_R channels should exhibit almost identical characteristics. In order to check this, the coherence of the two channels was calculated, using the 'lcohere' method and 12 averages. The result, given in Figure 5.7, shows that the channels are coherent.

7. The calculated powers at PDA1 and PDA2 were propagated to the test masses and other photodiodes using the 'displayOMS-BeamPowers' method described in Section 5.1. The output diagram of the optical bench with the associated power levels are shown in Figure 5.8.

   The ratios of the power at the photodiodes from each FIOS are within a few percent of the those determined when the optical bench was characterised by Institute for Gravitational Research, (IGR) [22]. It is possible that the differences may be accounted for if more accurate values for the coefficients of transmissivity and reflectivity are used, for example, those in [61].
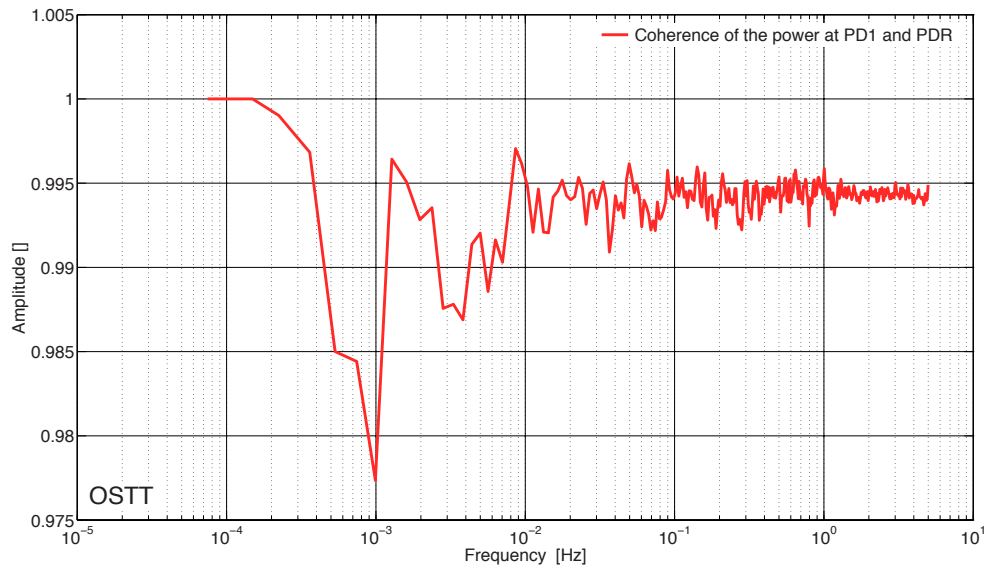
Figure 5.7: The coherence of the power at PD1 and PDR, converted from the Σ_1 and Σ_R parameters during a free-running amplitude control loop investigation in the hot phase of the OSTT test campaign.
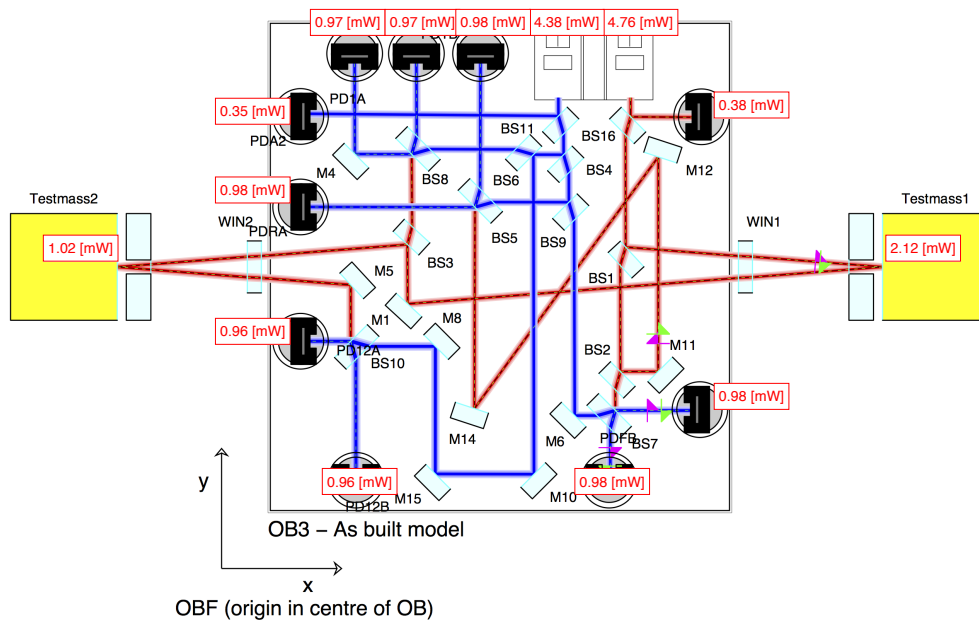

Figure 5.8: The power on the optical bench during the hot phase of the OSTT test campaign free-running amplitude noise investigation. The powers were calculated using the 'displayOMSBeamPowers' method, and are propagated forward from the power at the PDA1 and PDA2 photodiodes.

279

5 Amplitude noise characterisation

Free-running relative intensity noise

The relative intensity noise was calculated as follows:

1. The RIN was calculated from the power at PD1 according to:

$$\text{RIN} = \frac{P^{\text{X1}}}{\text{mean}(P^{\text{X1}})} \tag{5.24}$$

2. The amplitude spectral density of the RIN was calculated, the result, along with the allocation are shown in Figure 5.9.
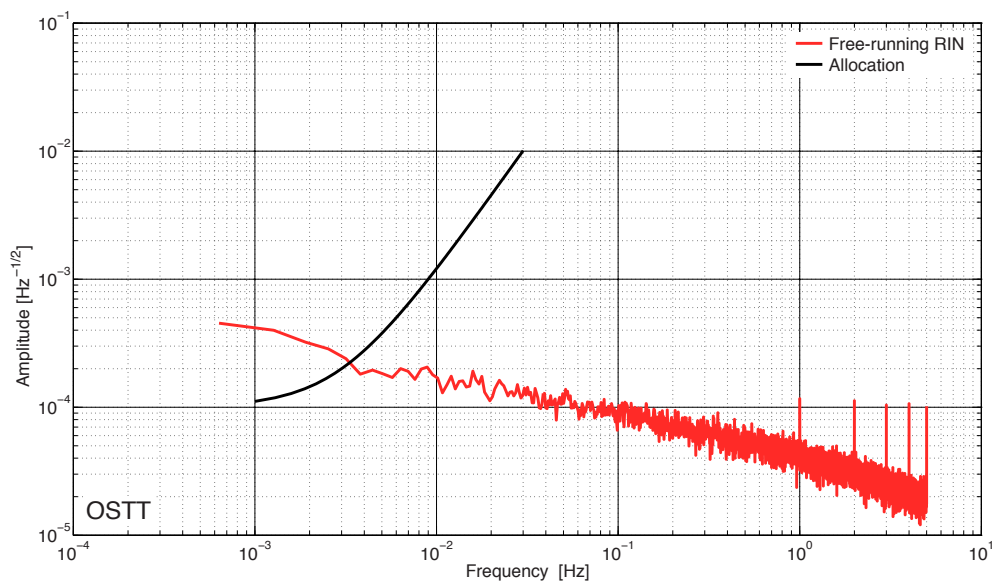

Figure 5.9: The amplitude spectral density of the free-running relative intensity noise, determined from the OSTT test campaign free-running amplitude noise investigation. Also shown is the allocation for the relative intensity noise in black.

> **Note**: The amplitude spectral density was calculated with 16 averages, and detrending of order one.

Coupling of noise at the heterodyne frequency

The coupling of the noise at the heterodyne frequency was determined as follows:

1. The data was detrended with order three to remove any DC offset, and linear, quadratic and cubic drifts.

2. The transfer function and coherence of the power at PD1 into the x_{12} channel was calculated. The results are shown in Figure 5.10.

   Note: The transfer function was calculated with 20 averages, using a Hanning windowing function with a default 50 % overlap. The coherence was calculated with 12 averages and detrending of order one.

The coherence between the two channels is low, and there are large errors on the calculated transfer function. These results indicate that there is a very low degree of coupling from amplitude noise at the heterodyne frequency into the differential test mass displacement. It is therefore not possible to determine a valid coupling coefficient from this data, and therefore no projection of this noise onto the measured differential test mass displacement was made.

Contribution of the radiation pressure noise

1. The fraction of the power in the beam one was determined from the powers calculated at PDA1 and PDA2:

$$N_1 = \text{mean}\left(\frac{P_1}{(P_1 + P_2)}\right) \tag{5.25}$$

$$= 0.52 \tag{5.26}$$

2. The power at PD1 was split into this fraction.

3. The resulting power was propagated to TM1 using the 'propagateOMSPower' method described in Section 5.1.

   Note: For interest, the beam from PDA1 was also propagated forward to TM1. The difference in the calculated power is approximately 2 %. This also highlighted the difference in the time dependance of the power, as any differences in the two beams
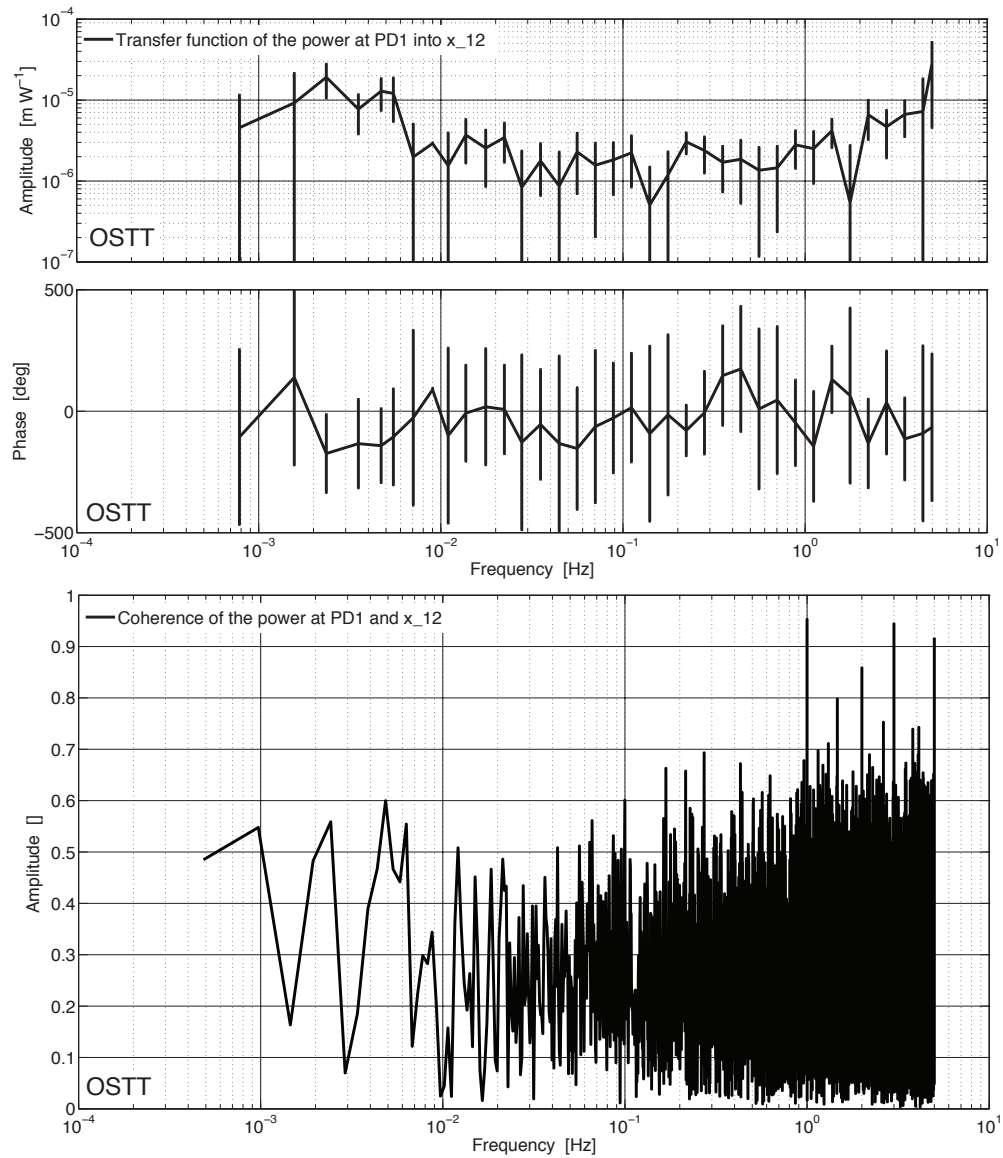
Figure 5.10: The transfer function and coherence of the power at PD1, calculated from the Σ_1 channel, with the differential test mass displacement measurement, x_{12}. This result is from the free-running amplitude noise investigation in the hot phase of the OSTT test campaign.

that interfere to produce the measured power at PD1 cannot be determined by this method.

4. The total force that would have impinged on both of the test masses, if they were drag-free, was then calculated according to:

$$F_{\text{total}} = \frac{3}{2}\frac{2P_{\text{TM1}}}{c},\tag{5.27}$$

where the 3/2 is assuming that the power at TM2 is half the power at TM1. The amplitude spectral density of the force is shown in Figure 5.11.

Figure 5.11: The amplitude spectral density of the force which would have resulted from radiation pressure noise during the OSTT test campaign free-running amplitude noise investigation.

Note: The amplitude spectral density was calculated with 16 averages and detrending of order one.

5. The equivalent displacement was determined according to:

$$\widetilde{x}_{12} = \frac{F_{\text{total}}}{4m\pi^2 f^2}\tag{5.28}$$
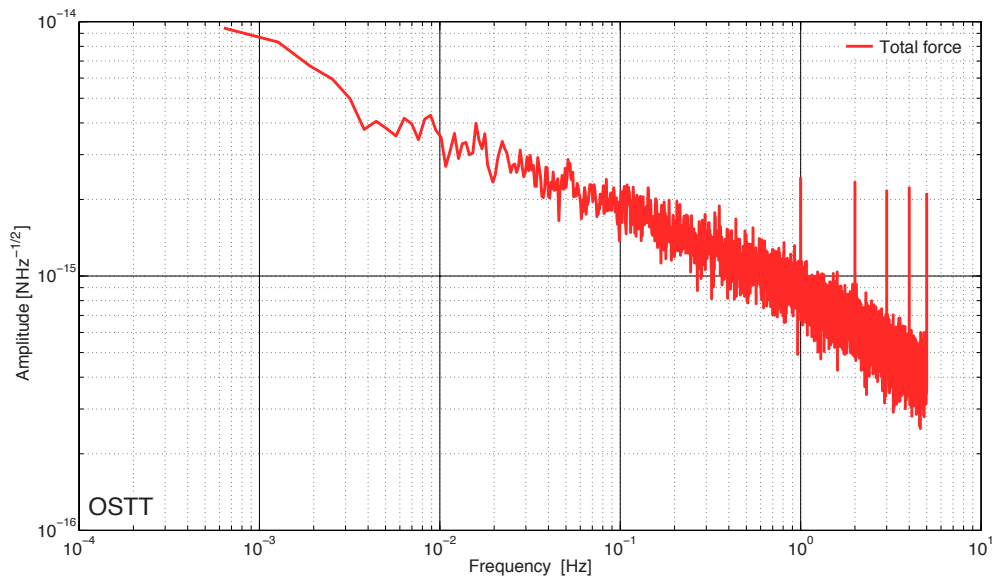
The result is shown in Figure 5.12.

283

Figure 5.12: The amplitude spectral density of the displacement which would have resulted from radiation pressure noise during the OSTT test campaign free-running amplitude noise investigation. The allocation for the displacement due to radiation pressure noise is shown in black.

The results are only valid when assuming a test mass that is not spring-coupled to the satellite. In reality, the spring-coupling below $1\,\mathrm{mHz}$ would produce a displacement of the form:

$$\widetilde{x}_{12}(f) = \frac{3P_{\mathrm{TM1}}(f)}{mc(\omega^2 - \omega_{\mathrm{stiff}}^2)} \tag{5.29}$$

where $P_{\mathrm{TM1}}(f)$ is the spectrum of the power at test mass one, $\omega = 2\pi f$ (where f is the Fourier frequency), and $\omega_{\mathrm{stiff}}^2$ is the stiffness (spring-coupling).

A plot of the amplitude spectral density of the x_{12} channel, alongside the estimated displacement due to the radiation pressure noise, is shown in Figure 5.13. It should be remembered that there were no drag-free test masses during the time at which the x_{12} measurement was made, and as such, the radiation pressure noise displacement shown is not a projection.
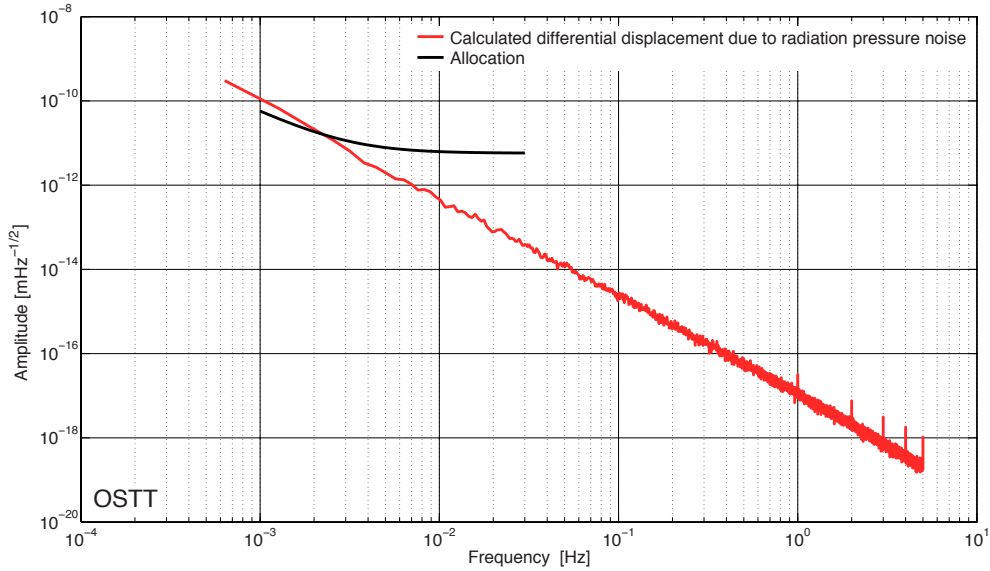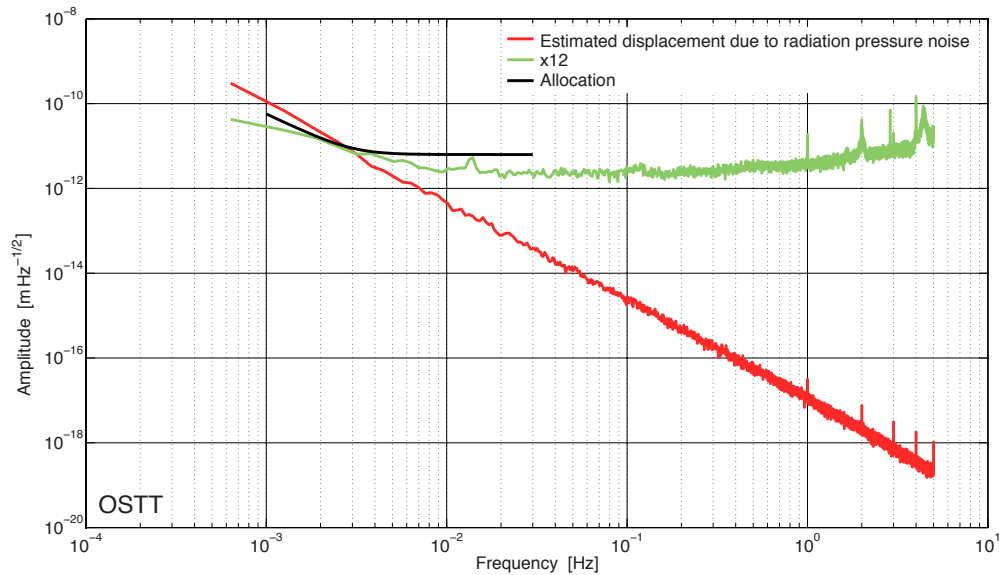
Figure 5.13: The amplitude spectral density of the displacement which would have resulted from radiation pressure noise during the OSTT test campaign free-running amplitude noise investigation is shown in red, alongside the measured differential test mass displacement, shown in green. It should be noted, that the radiation pressure noise did not influence the measurement of the differential test mass displacement shown here, as the test masses were not drag-free. The allocation for the displacement due to radiation pressure noise is shown in black.

Chapter 5

285

5.2.2 In-flight investigation

The setup required for the investigation is given in Table 5.6, along with the telemetry required for the analysis. The data should be prepared as detailed in Figure 5.6, and analysed according to the method shown in Figure 5.14.

Investigation	Free-running amplitude noise		
OMS state	TMs drag-free		
Loop states	SF	Nominal	
	FF	Nominal	
	OPD	Nominal	
	SP	Fixed output y, feedback $= 0\,\mathrm{V}$	
	FP	Open	
Telemetry required	128,3	x_{12}	LST10130
		Ψ_R	LST12407
		Σ_1	LST12408
		Σ_R	LST12409
	128,4	SF feedback	LST17345
		FF feedback	LST17340
		OPD feedback	LST17350
		SP feedback	LST17357
	3,25	SF state	LST17364
		FF state	LST17361
		OPD state	LST17367
		FP state	LST17358
		Fast power mon. one	LLT10052
		Fast power mon. two	LLT10053
		SSC	SCT70388
Length	10 hours		

Table 5.6: An overview of the key information relating to the investigation for measuring the free-running amplitude noise. For the telemetry names associated with each parameter refer to Appendix 7.
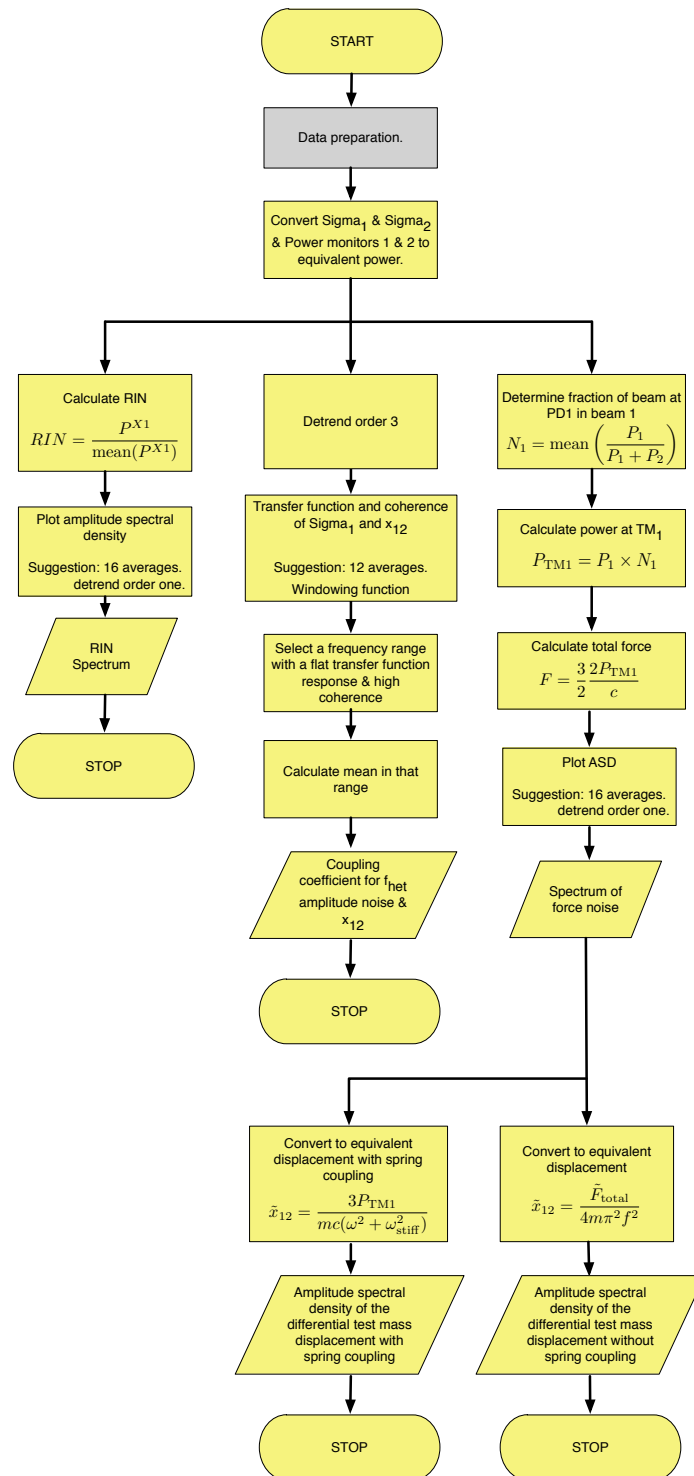
Figure 5.14: The analysis procedure for the in-flight free-running or closed loop amplitude noise investigations.

5.3 Closed-loop amplitude noise

The closed-loop amplitude noise investigation is not a stand-alone investigation, but is a sub-analysis of the results of an LPF science run. This is the same science run described for both the closed-loop frequency and OPD noise investigations, explained in Sections 3.3 and 4.3.

5.3.1 Test campaign results

In this section, the analysis of the results of an OSTT performance measurement, with focus on the amplitude control loop are presented. In this investigation all of the control loops operating under closed-loop conditions, with the exception of the slow amplitude control loop. The selected investigation was also analysed during the closed-loop frequency and OPD noise investigations, it was selected as it demonstrated the lowest measurement of the differential test mass displacement.

No in-flight investigation procedure is presented, as this is well defined in the experimental master plan. The analysis should be performed as for the free-running amplitude noise investigation.

The analysis of the closed-loop amplitude noise investigation is performed in the same manner as for the free-running amplitude noise investigation, presented in Section 5.2. The telemetry used in the analysis is shown in Table 5.7. The equivalent names used in the LTPDA repository can be found in Appendix 7.

The information relating to the date and times of the investigation can be found in Appendix 8, Table 8.20[1]. The initial analysis preparation of the data is described under 'Overview of the analysis'. The sub-analyses, to determine the closed-loop RIN and the estimation of the radiation pressure noise that would be present during such an investigation in-flight, were performed following exactly the same procedure as in the free-running investigation. For specific details of these sub-analyses, Section 5.2 should be consulted.

---

[1]Unlike the same measurement for the frequency and OPD closed-loop noise, the amplitude noise investigation analysis information is presented separately. This

Parameter	Description	Frequency [Hz]	ID
S^{FF}	Fast frequency loop state	1 Hz	LST17361
S^{SF}	Slow frequency loop state	1 Hz	LST17364
S^{OPD}	OPD loop state	1 Hz	LST17367
S^{FP}	Fast power loop state	1 Hz	LLT10031
S^{SP}	Slow power loop state	1 Hz	LST17358
y^{FF}	Fast frequency feedback	1 Hz	LST17340
		10 Hz	
y^{SF}	Slow frequency feedback	1 Hz	LST17345
		10 Hz	
y^{OPD}	OPD feedback	1 Hz	LST17350
		10 Hz	
y^{SP}	Slow power feedback	1 Hz	LST17357
		10 Hz	
F^1	Beam one fast power feedback	1 Hz	LLT10048
F^2	Beam two fast power feedback	1 Hz	LLT10049
$\mathrm{Mon}_1^{\mathrm{FP}}$	Beam one power monitor (PDA1)	1 Hz	LLT10052
$\mathrm{Mon}_2^{\mathrm{FP}}$	Beam two power monitor (PDA2)	1 Hz	LLT10053
Σ_1	Power at PD1	10 Hz	LST12408
Σ_R	Power at PDR	10 Hz	LST12409
x_{12}	X12 ifo. output	10 Hz	LST10130

Table 5.7: The telemetry parameters used in the analysis of the OSTT test campaign free-running amplitude noise investigations.

Chapter 5

5 Amplitude noise characterisation

Overview of the analysis

1. The data, specified in Table 5.7, was downloaded according to the times specified in the test campaign report [44].

2. The data was split based on the loop states and feedback to leave a segment where the fast amplitude control loop was closed (state = 1), and the other loop states in a stable condition for the duration of the measurement. In this investigation, all of the control loops, with the exception of the slow amplitude control loop, were in the nominal state.

3. The data was checked for data quality issues and glitches and repaired accordingly, as detailed in Appendix 9.

4. The power monitor channels from PDA1 and PDA2 were converted into an equivalent power in front of the photodiodes, PDA1 and PDA2, as described in Box 5.2. Similarly, Σ_1 and Σ_R channels were converted into an equivalent power in front of PD1 and PDR, as described in Box 5.1.

5. For comparison with the free-running amplitude noise investigation, the amplitude spectral densities of the PDA1, PDA2, PD1 and PDR powers were calculated, in addition to the coherence of the PDA1 and PD1 channels. The results are shown in Figure 5.15, along with the results from the free-running investigation.

   Note: The amplitude spectral densities were calculated with 16 averages, and detrending of order one. The coherence was calculate using 'lcohere' and 12 averages. The order three detrending removes any DC offset, and linear, quadratic, and cubic drifts.

   As for the free-running analysis, the coherence of the PDA1 and PD1 channels is low, apart from at low frequencies. Again, the sensing noise (including digitisation noise) and low resolution of the single-element photodiodes limits their use for measuring the amplitude noise fluctuations. This explains the difference in the amplitude spectral densities of the single-element photodiodes and quadrant photodiodes shown in Figure 5.15.

---

is because the split times required to remove any glitches are different in this investigation, as the data comes from a different packet.
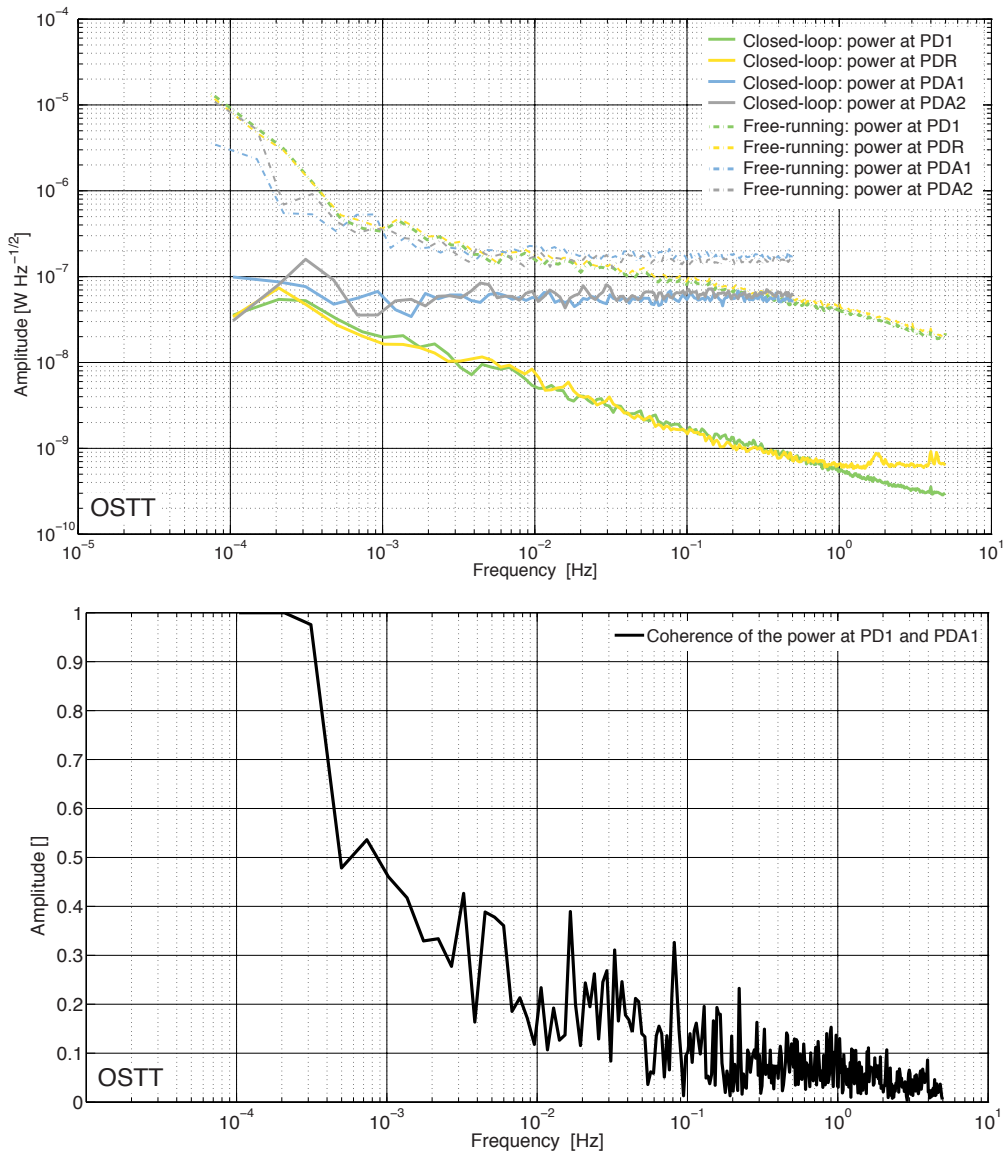
Figure 5.15: The amplitude spectral densities of the power calculated at PDA1 (blue), PDA2 (gray), PD1 (green), and PDR (yellow), along with the coherence of the PDA1 and PD1 powers (black). The results with solid lines are taken from the closed-loop amplitude noise investigation, and the dashed lines from the free-running amplitude noise investigation, both in the OSTT test campaign. The difference between the results from the single-element photodiodes and the quadrant photodiodes is the low resolution and sensing noise that is inherent in the readout of the single-element photodiode signals.

291

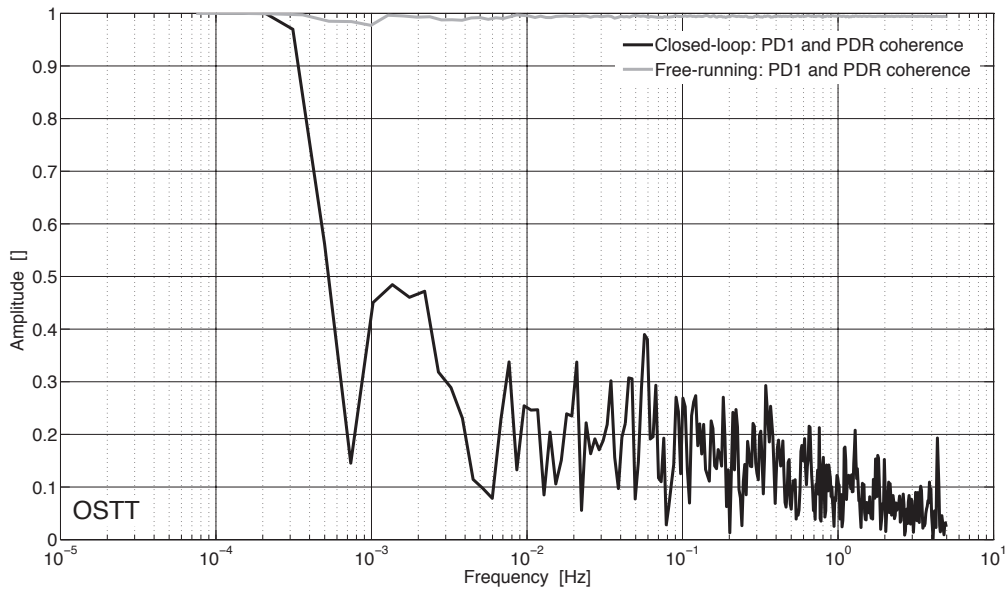6. The coherence of the Σ_1 and Σ_R channels were checked, the result is shown in Figure 5.16.

Figure 5.16: The coherence of the powers at PD1 and PDR as measured during the closed-loop amplitude measurement in the OSTT test campaign.

Note: The coherence was calculated using the 'lcohere' method and 12 averages.

The coherence of the channels is low, indicating that the coherent noise in the beams which was shown in the free-running amplitude noise investigation is well suppressed.

7. The calculated powers at PDA1 and PDA2 were propagated to the test masses and other photodiodes using the 'displayOMS-BeamPowers' method described in Section 5.1. The output diagram of the optical bench with the associated power levels are shown in Figure 5.17.

Closed-loop relative intensity noise

The closed-loop relative intensity noise, calculated according to the method described in Section 5.2, is shown in Figure 5.18. The result determined in the free-running amplitude measurement is also shown for comparison. The results show that the RIN has been suppressed
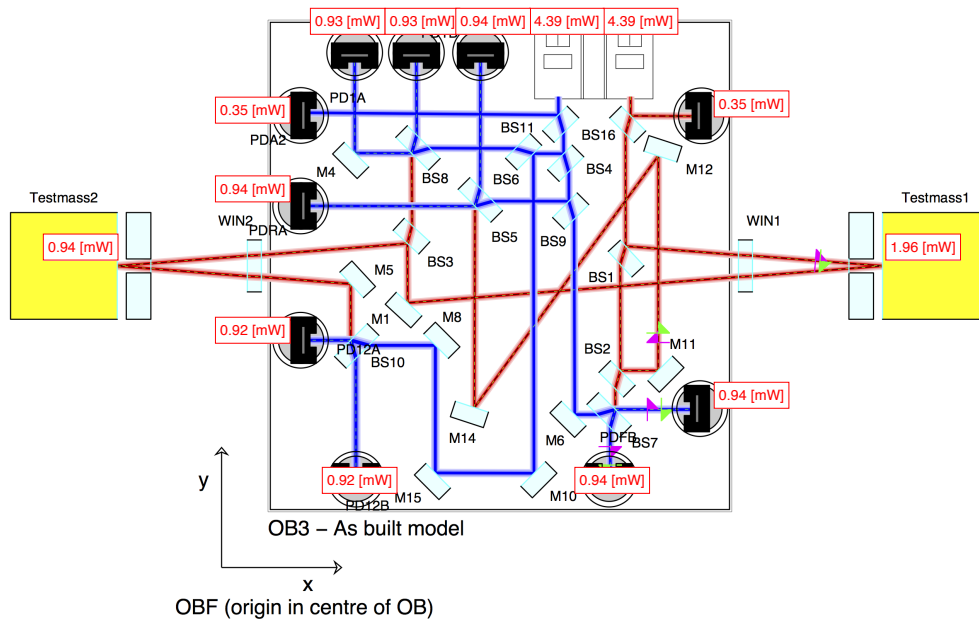
Figure 5.17: The power on the optical bench during the OSTT test campaign closed-loop amplitude noise investigation. The powers were calculated using the 'displayOMSBeamPowers' method, and are propagated forward from the power at the PDA1 and PDA2 photodiodes.

to below the requirement, by a factor of ~ 55, across all frequencies.

Contribution of the radiation pressure noise

The power at TM1 from the power of beam one at PD1 (50 % of the total power) propagated to TM1 was determined, and compared to the equivalent power propagated forward from PD1A. The difference in the measured DC power level is $\sim 1\%$. The total force noise, from the power incident on both TM1 and TM2, calculated using the power in beam one at PD1, is shown in Figure 5.19. The equivalent differential test mass displacement that would be induced by this force, if the test masses were free-floating, and not taking into account any spring coupling, are shown in figure 5.20. For comparison, the amplitude spectral density of the x_{12} channel during this measurement is shown with the predicted displacement from radiation pressure noise in Figure 5.21. The radiation pressure noise may have caused the differential test mass displacement measurement to go above the requirement, but only at low frequencies.
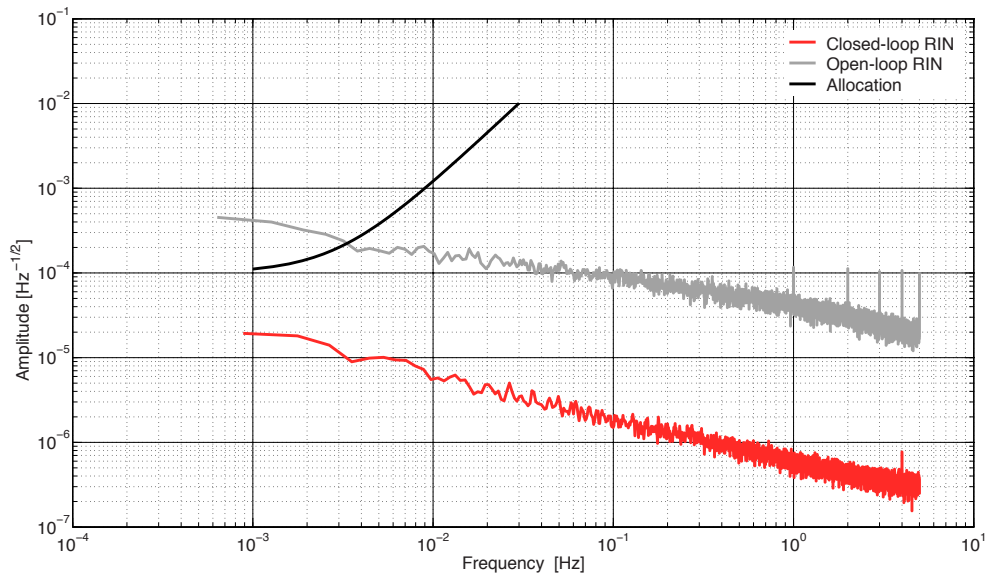
Figure 5.18: A comparison of the amplitude spectral density of the RIN during a closed-loop amplitude loop measurement (red), and an open-loop amplitude measurement (grey), along with the allocation (black).

Figure 5.19: The force noise due to the power incident on both test masses during a closed-loop amplitude control loop investigation. The power was propagated from the fraction of the power in beam one at PD1. The result from the free-running amplitude noise measurement is also shown in grey as a reference.

294

Figure 5.20: The estimated displacement noise that would have contributed to the differential test mass displacement measurement if the test masses were drag free. This result was determined from the OSTT test campaign investigation. The free-running estimate is also shown in grey.
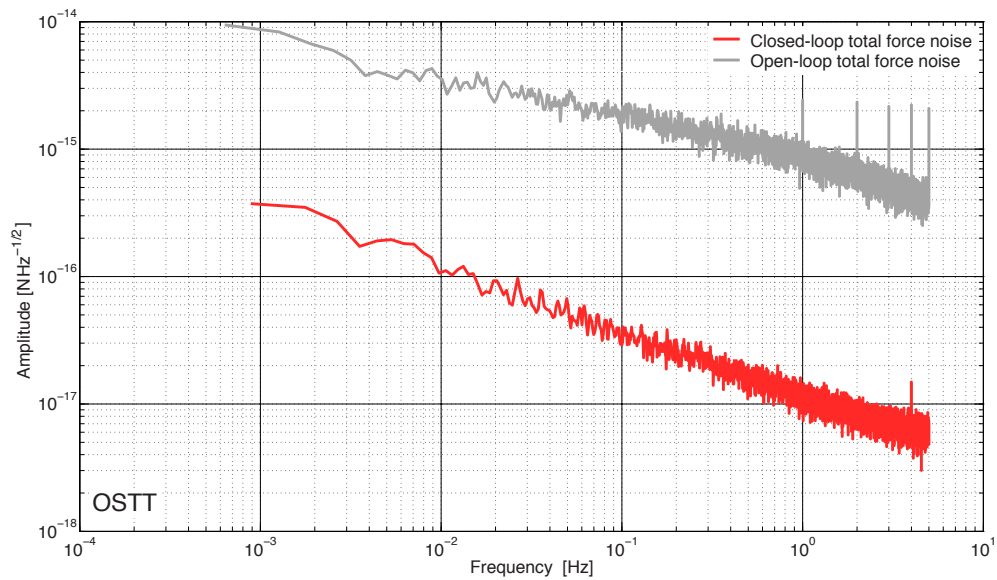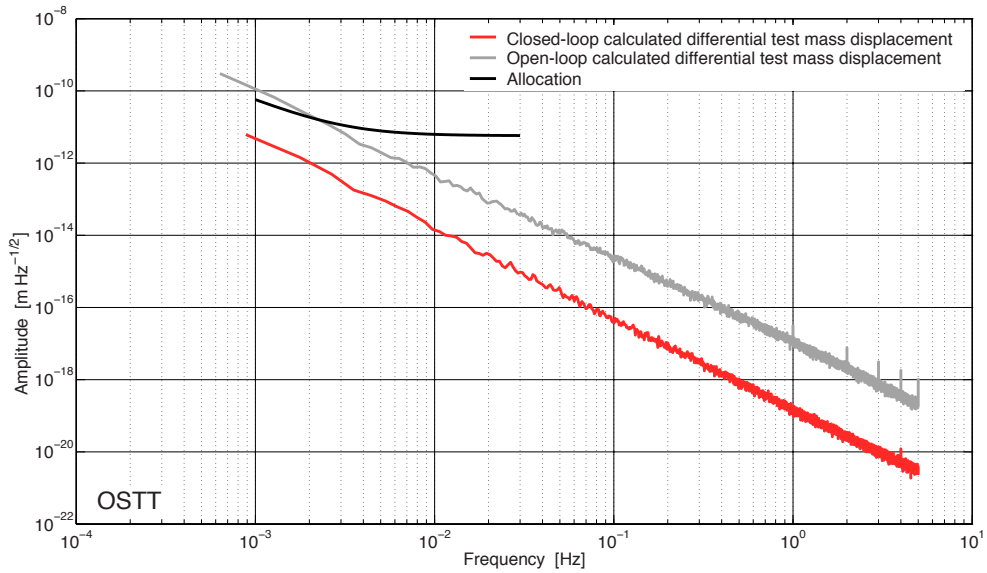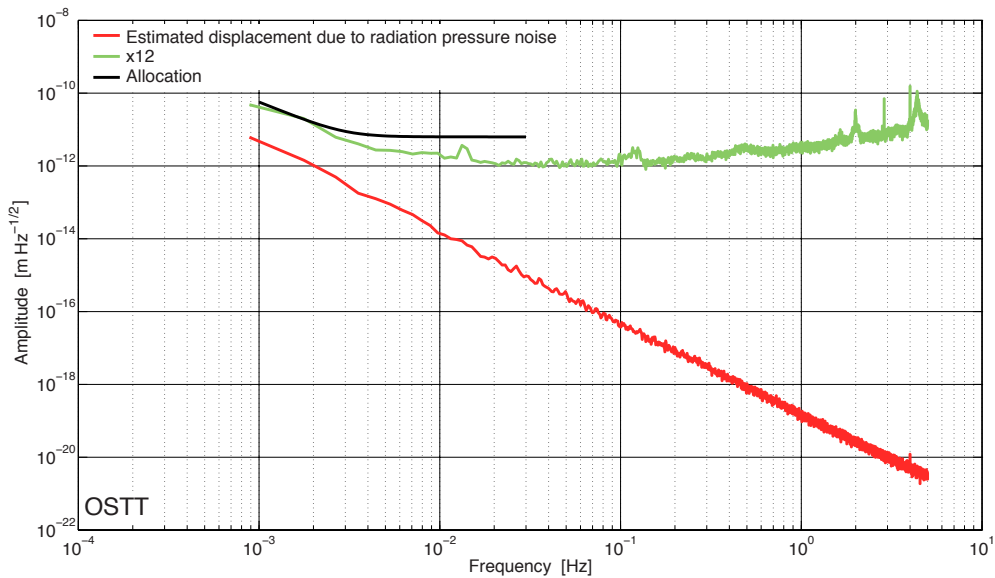

Figure 5.21: The estimated displacement noise that would have contributed to the differential test mass displacement measurement if the test masses were drag free. This result was determined from the OSTT test campaign investigation. The amplitude spectral density of the measured differential test mass displacement during the investigation is also plotted.

295

5.4 Contribution of the radiation pressure noise to the differential test mass displacement

The radiation pressure noise contribution to the OMS differential test mass displacement noise is described in detail in Section 2.2.3. The radiation pressure noise can be determined in two ways. Firstly, by estimating the power fluctuations at the test mass using the available telemetry during a free-running or closed-loop noise measurement, as described in Section 5.2. Secondly, by a specific investigation whereby the laser power is modulated to induce a modulating force at the test mass. This section describes this investigation, and is an extension of the method described in [56].

The magnitude of the radiation pressure noise depends upon the fluctuating power incident on the test mass. In a free-running or closed-loop amplitude noise investigation the coupling of the radiation pressure noise into the differential displacement measurement is difficult to determine. This is because the magnitude of the induced displacement is low relative to other sources of displacement noise. In order to more accurately determine the coupling the laser power can be modulated by injecting a modulation signal, of $\sim 10\,\mathrm{mHz}$ with an amplitude of $\sim 100\mu\mathrm{W}$[1] for example, into the δx^{SP} slow power control loop input. This induces a larger force noise on the test mass, and therefore results in a larger signal in the x_{12} differential test mass displacement measurement.

The investigation procedure and analysis are described in [56], but the procedures for converting the Σ_i channels into equivalent powers should be taken into account. The procedure for performing the inital measurement of the amplitude fluctuations in each beam is as described in Section 5.1, but with the appropriate fast power loop operating. The force noise can be calculated in the same way as described in Section 5.2, but taking into account the noise suppression function of the loops (see Box 2.5).

---

[1]This is the power required at the test mass, this needs to be converted to an equivalent value at the δx^{SP} input.

6 Conclusions and outlook

Contents

6.1 Summary of proposed investigations

A number of investigations and analyses have been proposed in this document. They enable the frequency, OPD, and amplitude noise contributions to the differential test mass displacement measurement, under both free-running and closed-loop conditions, to be determined. In addition, they allow the characterisation of other optical metrology systems characteristics, including the response of the control loops, to be evaluated in-flight.

Ideally, all of these experiments would be performed at some stage of the mission. However, the limited mission duration imposes restrictions of the number of investigations that can be performed. The overall goal is the measurement of the residual acceleration of the drag-free test mass, which means that the science runs are prioritised.

6 Conclusions and outlook

As such, the investigations presented have been categorised to define conditions in which they could, or should, be performed. In some cases only specific parts of an investigation are required. These categories are:

- **Routine monitoring**: These investigations should be performed regularly to monitor key system characteristics. They include investigations that can be performed as part of the weekly station keeping when the satellite is not operating in science mode, as well as analysis of data that is available as part of the standard 128,3 or housekeeping packets.

- **Diagnostics**: These investigations should be performed in the case that an unexpected result is observed, e.g., if the measured differential displacement is higher than expected, in order to determine the cause and mitigate appropriately.

- **Noise contributions**: These investigations allow the noise level of the frequency, OPD, and amplitude to be determined via dedicated experiments. Additionally, the coupling of the noise into the differential test mass displacement can be calculated.

6.1.1 Routine monitoring

There are two types of routine monitoring considered here:

1. **Evaluation of OMS characteristics using parameters available during science runs**:

   - The power on the optical bench can be estimated whenever there are power monitor or Σ_i parameters available, as shown in Section 5.1. This would allow unexpected behaviour of the laser power to be identified.

   - The combination of the available power monitors and Σ_i channels allow the power at various points on the optical bench to be compared with some degree of accuracy. This would allow the identification of an issue with a particular set of photodiodes. For example, if the power monitors indicated that a certain power should be incident at PD1,

but the value measured by PD1 was very different.

- Similar to the previous point, the combination of the powers known from several Σ_i parameters may allow some analytical evaluation of the degradation of the optical surfaces. This may allow changes in the reflectivity of the test mass to be inferred.

2. **Investigations that could be performed without drag-free test masses during weekly station keeping**:

   - The free-running frequency and OPD noise investigations could be performed if a long enough timespan was available.

   - The frequency and OPD loop characterisation investigations could be performed, but without the ability to determine a coupling coefficient for the noise into the differential test mass displacement.

   - The relative power, and power fluctuations, in each of the beams could be evaluated, using the procedure defined in Section 5.1.

6.1.2 Diagnostics

If the noise levels in the x_{12} channel are higher than the requirement then the noise source needs to be identified and, where possible, the noise suppressed. Considering the case where unexpected noise levels has been observed, the following procedure for the identification and mitigation procedure is suggested:

1. Perform a free-running investigation with the frequency, OPD, and amplitude control loops open. Determine the free-running frequency noise, OPD noise, an estimate of the radiation pressure noise, and the coupling of the amplitude noise at f_{het}. These analyses are described in Sections 3.1, 4.1, and 5.2.

2. These results can be compared to the results expected from the ground-based test campaigns.

Chapter 6

3. If a particular noise level is significantly higher than measured or estimated on ground, then a control loop characterisation investigation, with the test masses drag free, should be performed. The coupling of the noise into the x_{12} channel should also be determined.

4. For the frequency and OPD loops: If the calculated open-loop gain of the control loop is not sufficient to suppress the noise to the required level, then the a and b coefficients of the digital control law should be redefined. In the case of the OPD loop, the actuator response should be checked to ensure that they are both operating as expected. If one is not, then the full feedback signal should be reassigned to the other actuator.

5. If it is not clear which noise source is causing the problem, then loop characterisation investigations should be performed for both the frequency and OPD control loops, and a noise coupling with injected modulations should be performed for the radiation pressure noise coupling.

6.1.3 Noise contributions

Frequency noise

- **Free-running frequency noise[1], 10 hours**: This investigation is described in Section 3.1.

  - If the test masses are fixed then only the free-running frequency noise can be determined.

  - If the test masses are drag-free (science mode 1.2), then a low accuracy estimate of the coupling between frequency noise and differential test mass displacement can be determined.

- **Coupling into x_{12}, ~2 hours**: As described in Section 3.2. This would require the test masses to be drag-free (science mode 1.2).

Note: A rough estimate of a coupling coefficient could also be determined from the free-running frequency noise investigation, although the result would be significantly less accurate.

Optical pathlength difference noise

- **Free-running OPD noise[1], 10 hours**: As described in Section 4.1.

    - If the test masses are fixed then only the optical pathlength noise can be determined.

    - If the test masses are drag-free then a low accuracy estimate of a coupling coefficient for OPD noise into differential test mass displacement could be determined.

- **Coupling into x_{12}, $\sim$2 hours**: As described in Section 4.2. This investigation requires drag-free test masses.

    Note: A rough estimate of a coupling coefficient could also be determined from the free-running OPD noise investigation, although the result would be significantly less accurate.

Amplitude noise

- **Free-running amplitude noise[1], 10 hours**: As described in Section 5.2.

    - If the test masses are fixed then only the free-running RIN can be calculated. The contribution due to the radiation pressure noise could be estimated, as the power on the photodiodes is available whenever the interferometers are operating.

    - If the test masses are drag-free then the coupling of the amplitude noise at the heterodyne frequency into the differential test mass displacement could be estimated.

Chapter 6

- **Coupling of radiation pressure noise, ~3 hours**: As described in Section 5.4.
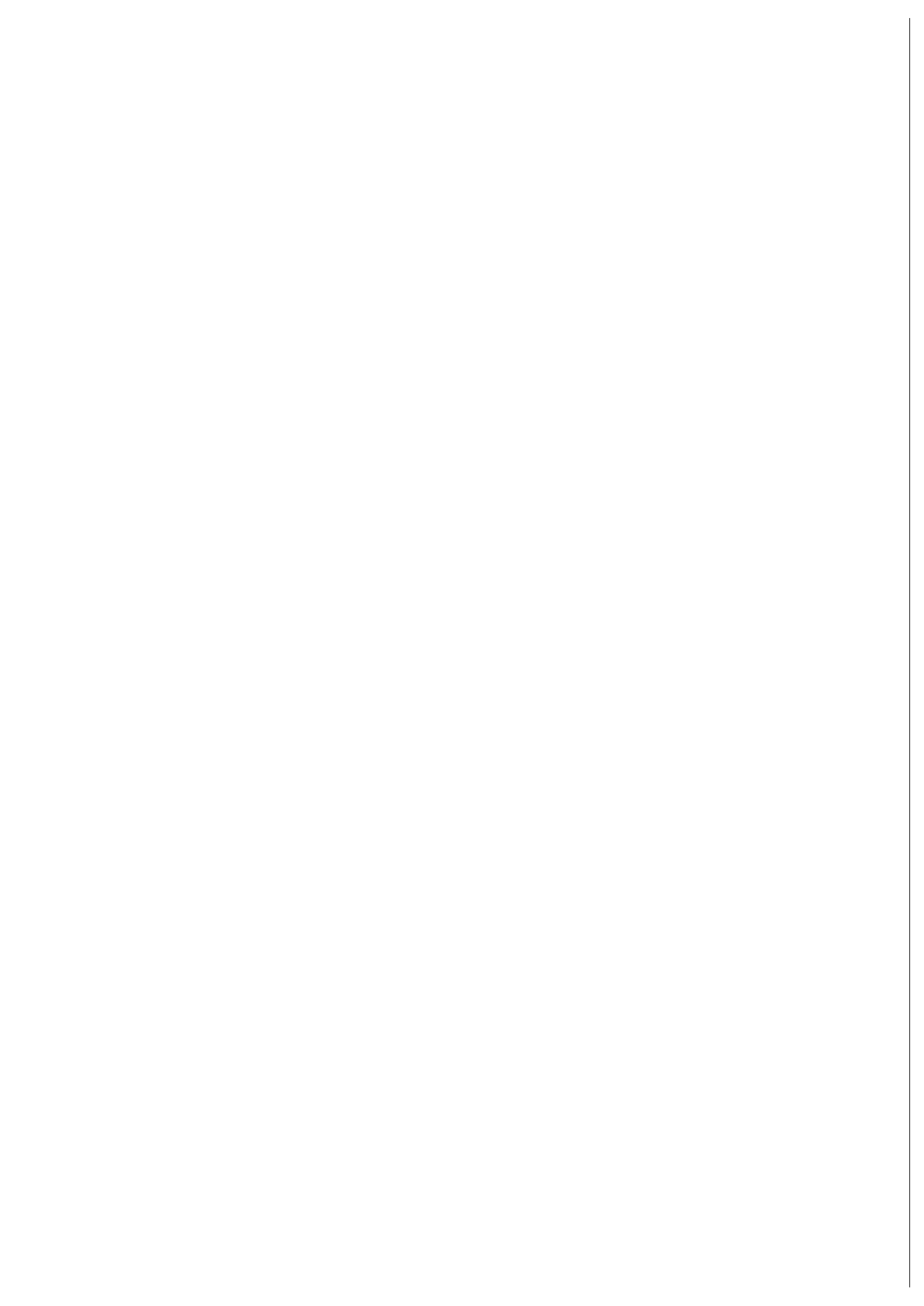
6.2 Outlook

The analysis of the investigations performed on the flight hardware during the ground-based test campaigns provides the best available estimate of the noise levels that can be expected in-flight. To summarise:

- The magnitude of the free-running frequency noise of the laser determined from the OSTT test campaign did not meet the allocated noise level, however, the coupling into the differential test mass displacement was negligible. As such, the measurement of the differential test mass displacement was not limited by frequency even without suppression. Where the frequency noise was suppressed, the expected noise behaviour based on the expected loop response (based on the FM loop) was shown. The suppressed noise was significantly below the required noise level, and was far from limiting the differential test mass displacement measurement.

- The free-running OPD noise determined from the OSTT results was very close to meeting the required level. The coupling of OPD noise into differential test mass displacement was zero, and the differential test mass displacement measurement almost met the required level without OPD suppression. The closed-loop measurement showed that the OPD could be brought below the required level, and was far from limiting the differential test mass displacement measurement.

- The amplitude noise investigations from the OSTT test campaign demonstrated that there was effectively no coupling of noise at the heterodyne frequency, even with the amplitude noise free-running. The estimated contribution of the free-running radiation pressure noise may be significant during flight according

---

[1]The free-running frequency, OPD, and amplitude noise investigations could be performed concurrently.

to the OSTT data. With stabilisation, the estimated contribution would be below the allocation, and not limiting.

These results demonstrate that the levels of the frequency, OPD, and amplitude noise are low, and can be suitably suppressed, and as such are not expected to be limiting noise sources in-flight, unless the in-flight noise is higher than expected. The result is that the measurement of the required differential test mass displacement is expected to be achievable in-flight, but it is not clear what noise sources limit the measurement.

Chapter 6

7 Appendix: Parameter naming conventions

This appendix contains the telemetry names used in the test campaign repositories and in-flight. Where spaces are left, the name was not found.

7 Appendix: Parameter naming conventions

Main interferometer outputs				
Thesis	Units	Freq. [Hz]	Campaign	Name
x_{12}	[m]	10	EM	DMU_X12_FILT
			FM	DMU_X12_FILT
			OSTT	DMU_X12_FILT
			Flight	DMU_X12_FILT LST10130
x_1	[m]	10	EM	DMU_X1_FILT
			FM	DMU_X1_FILT
			OSTT	DMU_X1_FILT
			Flight	DMU_X1_FILT LST10119
Ψ_F	[rad]	10	EM	DMU_PSI_F_FILT
			FM	DMU_PSI_F_FILT
			OSTT	DMU_PSI_F_FILT
			Flight	DMU_PSI_F_FILT LST12406
Ψ_R	[rad]	10	EM	DMU_PSI_R_FILT
			FM	DMU_PSI_R_FILT
			OSTT	DMU_PSI_R_FILT
			Flight	DMU_PSI_R_FILT LST12407

Table 7.1: Labelling conventions for the main interferometer outputs.

Main interferometer outputs: 100 Hz				
Thesis	Units	Freq. [Hz]	Campaign	Name
x_{12}	[m]	100	EM	
			FM	
			OSTT	
			Flight	LONG_PHASE_12 LST15644
x_1	[m]	100	EM	
			FM	
			OSTT	
			Flight	LONG_PHASE_1 LST15643
Ψ_F	[rad]	100	EM	
			FM	
			OSTT	
			Flight	LONG_PHASE_F32 LST18645
Ψ_R	[rad]	100	EM	
			FM	
			OSTT	
			Flight	LONG_PHASE_R32 LST18646

Table 7.2: Naming convention for the main interferometer output channels from the IDL.

Appendix

7 Appendix: Parameter naming conventions

DWS test mass angles				
Thesis	Units	Freq. [Hz]	Campaign	Name
ϕ_1	[rad]	10	EM	DMU_DWS_PHI_1_FILT
			FM	DMU_DWS_PHI_1_FILT
			OSTT	DMU_DWS_PHI_1_FILT
			Flight	DMU_DWS_PHI_1_FILT LST10135
η_1	[rad]	10	EM	DMU_DWS_ETA_1_FILT
			FM	DMU_DWS_ETA_1_FILT
			OSTT	DMU_DWS_ETA_1_FILT
			Flight	DMU_DWS_ETA_1_FILT LST10136
ϕ_2	[rad]	10	EM	DMU_DWS_PHI_2_FILT
			FM	DMU_DWS_PHI_2_FILT
			OSTT	DMU_DWS_PHI_2_FILT
			Flight	DMU_DWS_PHI_2_FILT LST10137
η_2	[rad]	10	EM	DMU_DWS_ETA_2_FILT
			FM	DMU_DWS_ETA_2_FILT
			OSTT	DMU_DWS_ETA_2_FILT
			Flight	DMU_DWS_ETA_2_FILT LST10138

Table 7.3: Labelling conventions for the DWS test mass angular outputs.

Fast frequency loop parameters: 10 Hz				
Thesis	Units	Freq. [Hz]	Campaign	Name
S	[]	1	EM	FAST_LOOP_STATE
			FM	FAST_FreqLoopSTATE_1HZ
			OSTT	FAST_FreqLoopSTATE_1HZ
			Flight	FAST_FreqLoopSTATE_1HZ LST17361
δx	[rad]	10	EM	FAST_LOOP_VAR_SETPOINT
			FM	FAST_LOOP_VAR_SETPOINT
			OSTT	
			Flight	FAST_FreqLoopVarSetpnt LST17338
Δx	[rad]	10	EM	
			FM	
			OSTT	
			Flight	FAST_FreqLoopOFFSET LST17337
ϵ	[rad]	10	EM	FAST_LOOP_CTRL_ERROR
			FM	FAST_LOOP_CTRL_ERROR
			OSTT	FAST_FreqLoopCtrlErr
			Flight	FAST_FreqLoopCTRL_ERR LST17339
y	[V]	10	EM	FAST_LOOP_CTRL_OUT
			FM	FAST_LOOP_CTRL_OUT
			OSTT	FAST_FreqLoopCtrlOUT
			Flight	FAST_FreqLoopCTRL_OUT LST17340

Table 7.4: Naming convention for the 10 Hz fast frequency control loop parameters.

7 Appendix: Parameter naming conventions

Fast frequency loop parameters: 100 Hz				
Thesis	Units	Freq. [Hz]	Campaign	Name
δx	[rad]	100	EM	
			FM	
			OSTT	FAST_LOOP_VAR_SETPOINT32
			Flight	FAST_FreqLoopVarSetpnt32 LST18338
Δx	[rad]	100	EM	
			FM	
			OSTT	
			Flight	FAST_FreqLoopOFFSET32 LST18337
ϵ	[rad]	100	EM	
			FM	
			OSTT	
			Flight	FAST_FreqLoopCTRL_ERR32 LST18339
y	[V]	100	EM	
			FM	
			OSTT	
			Flight	FAST_FreqLoopCTRL_OUT32 LST18340

Table 7.5: Fast frequency control loop IDL parameters.

Slow frequency loop parameters: 10 Hz				
Thesis	Units	Freq. [Hz]	Campaign	Name
S^{SF}	[]	1	EM	SLOW_LOOP_STATE
			FM	SLOW_FreqLoopSTATE_1HZ
			OSTT	SLOW_FreqLoopSTATE_1HZ
			Flight	SLOW_FreqLoopSTATE_1HZ LST17364
δx	[V]	10	EM	SLOW_LOOP_VAR_SETPOINT
			FM	SLOW_LOOP_VAR_SETPOINT
			OSTT	Can't find.
			Flight	SlowFreqLoopVAR_SETPOINT LST17343
Δx	[V]	10	EM	
			FM	
			OSTT	
			Flight	SlowFreqLoopOFFSET LST17342
ϵ	[V]	10	EM	SLOW_LOOP_CTRL_ERROR
			FM	SLOW_LOOP_CTRL_ERROR
			OSTT	SLOW_FreqLoopCtrlErr
			Flight	SlowFreqLoopCTRL_ERROR LST17344
y	[V]	10	EM	SLOW_LOOP_CTRLL_OUTPUT
			FM	SLOW_LOOP_CTRL_OUTPUT
			OSTT	SLOW_FreqLoopCtrlOUT
			Flight	SlowFreqLoopCTRL_OUTPUT LST17345

Table 7.6: Naming convention for the 10 Hz slow frequency control loop parameters.

Appendix

311

7 Appendix: Parameter naming conventions

Slow frequency loop parameters: 100 Hz				
Thesis	Units	Freq. [Hz]	Campaign	Name
δx	[V]	100	EM	
			FM	
			OSTT	
			Flight	SlowFreqLoopVAR_SETPNT32 LST18343
Δx	[V]	100	EM	
			FM	
			OSTT	
			Flight	SlowFreqLoopOFFSET32 LST18342
ϵ	[V]	100	EM	
			FM	
			OSTT	
			Flight	SlowFreqLoopCTRL_ERROR32 LST18344
y	[V]	100	EM	
			FM	
			OSTT	
			Flight	SlowFreqLoopCTRL_OUT32 LST18345

Table 7.7: Naming convention for the slow frequency control loop IDL parameters.

OPD loop parameters: 10 Hz				
Thesis	Units	Freq. [Hz]	Campaign	Name
S	[]	1	EM	OPD_LOOP_STATE_1HZ
			FM	OPD_LOOP_STATE_1HZ
			OSTT	OPD_LOOP_STATE_1HZ
			Flight	OPD_LOOP_STATE_1HZ LST17367
δx	[rad]	10	EM	OPD_LOOP_VAR_SETPOINT
			FM	OPD_LOOP_VAR_SETPOINT
			OSTT	
			Flight	OPD_LOOP_VAR_SETPOINT LST17348
Δx	[rad]	10	EM	
			FM	
			OSTT	
			Flight	OPD_LOOP_OFFSET LST17347
ϵ	[rad]	10	EM	OPD_LOOP_CONTROL_ERROR
			FM	OPD_LOOP_CONTROL_ERROR
			OSTT	OPD_LOOP_CONTROL_ERROR
			Flight	OPD_LOOP_CONTROL_ERROR LST17349
y	[V]	10	EM	OPD_LOOP_CTRL_OUTPUT
			FM	OPD_LOOP_CONTRL_OUTPUT
			OSTT	OPD_LOOP_CTRL_OUTPUT
			Flight	OPD_LOOP_CONTRL_OUTPUT LST17350

Table 7.8: Naming convention for the 10 Hz OPD control loop parameters.

Appendix

7 Appendix: Parameter naming conventions

OPD loop parameters: 100 Hz				
Thesis	Units	Freq. [Hz]	Campaign	Name
δx	[rad]	100	EM	
			FM	
			OSTT	
			Flight	OPD_LOOP_VAR_SETPOINT32 LST18348
Δx	[rad]	100	EM	
			FM	
			OSTT	
			Flight	OPD_LOOP_OFFSET32 LST18347
ϵ	[rad]	100	EM	
			FM	
			OSTT	
			Flight	OPD_LOOP_CONTROL_ERROR32 LST18349
y	[V]	100	EM	
			FM	
			OSTT	
			Flight	OPD_LOOP_CONTRL_OUTPUT32 LST18350

Table 7.9: Naming convention for the OPD control loop IDL parameters.

Slow power loop parameters: 10 Hz				
Thesis	Units	Freq. [Hz]	Campaign	Name
S	[]	1	EM	SLOW_PLOOP_STATE_1HZ
			FM	AMPL_CtrlLoop_STATE
			OSTT	
			Flight	AMPL_CtrlLoop_STATE LST17358
δx	[]	10	EM	
			FM	
			OSTT	
			Flight	AMPL_CtrlLoopVarSETPOINT LST17355
Δx	[]	10	EM	
			FM	
			OSTT	
			Flight	AMPL_CtrlLoop_OFFSET LST17354
ϵ	[V]	10	EM	SLOW_PLOOP_CTRL_ERR
			FM	AMPL_CtrlLoopCtrlERR
			OSTT	
			Flight	AMPL_CtrlLoopCTRL_ERR LST17356
y	[V]	10	EM	SLOW_PLOOP_CTRL_OUT
			FM	AMPL_CtrlLoopCtrlOUT_1HZ
			OSTT	
			Flight	AMPL_CtrlLoopCTRL_OUT LST17357

Table 7.10: Naming convention for the 10 Hz slow power control loop parameters. The units for δx and Δx are not specified in the mission database.

Appendix

315

7 Appendix: Parameter naming conventions

Fast power loop parameters				
Thesis	Units	Freq. [Hz]	Campaign	Name
s^{FP}	[]	1	EM	
			FM	
			OSTT	LM_SUM_DIFF_LOOP_STAT
			Flight	LLT10031
$\mathrm{Mon}_1^{\mathrm{FP}}$	$[\mu A]$	1	EM	
			FM	
			OSTT	LM_Pwr_MONITOR_1
			Flight	LLT10052
$\mathrm{Mon}_2^{\mathrm{FP}}$	$[\mu A]$	1	EM	
			FM	
			OSTT	LM_Pwr_MONITOR_2
			Flight	LLT10053
ϵ_1^{FP}	[V]	1	EM	
			FM	
			OSTT	LM_Pwr_STAB_Err1
			Flight	LLT10046
ϵ_2^{FP}	[V]	1	EM	
			FM	
			OSTT	LM_Pwr_STAB_Err2
			Flight	LLT10047
F^1	[V]	1	EM	
			FM	
			OSTT	LM_FEEDBACK_Sig_1
			Flight	LLT10048
F^2	[V]	1	EM	
			FM	
			OSTT	LM_FEEDBACK_Sig_2
			Flight	LLT10049

Table 7.11: Naming convention for the fast power control loop parameters.

Fast power loop parameters				
Thesis	Units	Freq. [Hz]	Campaign	Name
$RF\_Mon_1^{FP}$	[V]	1	EM	
			FM	
			OSTT	LM_RF_AMPLITUDE_1
			Flight	LLT10050
$RF\_Mon_2^{FP}$	[V]	1	EM	
			FM	
			OSTT	LM_RF_AMPLITUDE_2
			Flight	LLT10051

Table 7.12: Naming convention for the fast power control loop parameters, continued.

Σ_i: 10 Hz				
Thesis	Units	Freq. [Hz]	Campaign	Name
Σ_1	[]	10	EM	
			FM	
			OSTT	DMU_SIGMA_1_FILT
			Flight	LST12408
Σ_R	[]	10	EM	
			FM	
			OSTT	DMU_SIGMA_R_FILT
			Flight	LST12409

Table 7.13: Naming convention for the Σ_1 and Σ_R parameters. It should be noted that in the mission database these parameters have units of radians, it is believed that they are dimensionless.

Appendix

7 Appendix: Parameter naming conventions

Source sequence counter: 10 Hz				
Thesis	Units	Freq. [Hz]	Campaign	Name
SSC	[]	10	EM	SSC
			FM	SSC
			OSTT	SSC
			Flight	SC_SSC SCT70388

Table 7.14: Naming convention for the SSC parameters.

8 Appendix: Investigation information

Contents

This appendix contains information relating to the analyses of the EM, FM, and OSTT test campaign investigations presented in Chapters 3, 4, and 5. Also shown are the original and detrended timeseries plots of the telemetry parameters used in some analyses. These plots can be compared to the equivalent plots from the in-flight investigations, as a quick check that the behaviour of each parameter is as expected.

Appendix

8.1 Frequency noise characterisation

8.1.1 Free-running frequency noise

Investigation ref.	TC-OMS-L-PO-001	
Downloaded timespan	2009-12-07	00:01:00
	Times	23:59:00
Investigation information	SF: fixed output y, feedback = 0 V.	
	FF: fixed output y, feedback = 0 V.	
	OPD: fixed output y, feedback = 1.5 V.	
	SP: fixed output y, feedback = 0 V.	
Free-running frequency analysis notes	Split for SF/FF states/feedback: 21173 s to 33559 s.	
	Split for other states: 23711 s to end.	
	Data repaired: yes.	
	Split due to data repair: none.	
	A glitch was identified between 27206 s and 28290 s.	
	The data was split to give two glitch-free segments.	
	Segment one:	1st split for glitches: 23711 s to 27012 s.
	Segment two:	2nd split for glitches: 27981 s to 33559 s.
Free-running frequency coupling	Segment one:	Freqs. used for coupling coeff.: 0.036589 Hz to 0.11295 Hz.
	Segment two:	Freqs. used for coupling coeff.: 0.011295 Hz to 0.084714 Hz.

Table 8.1: Measurement details for the EM free-running frequency noise analyses [32].

Appendix
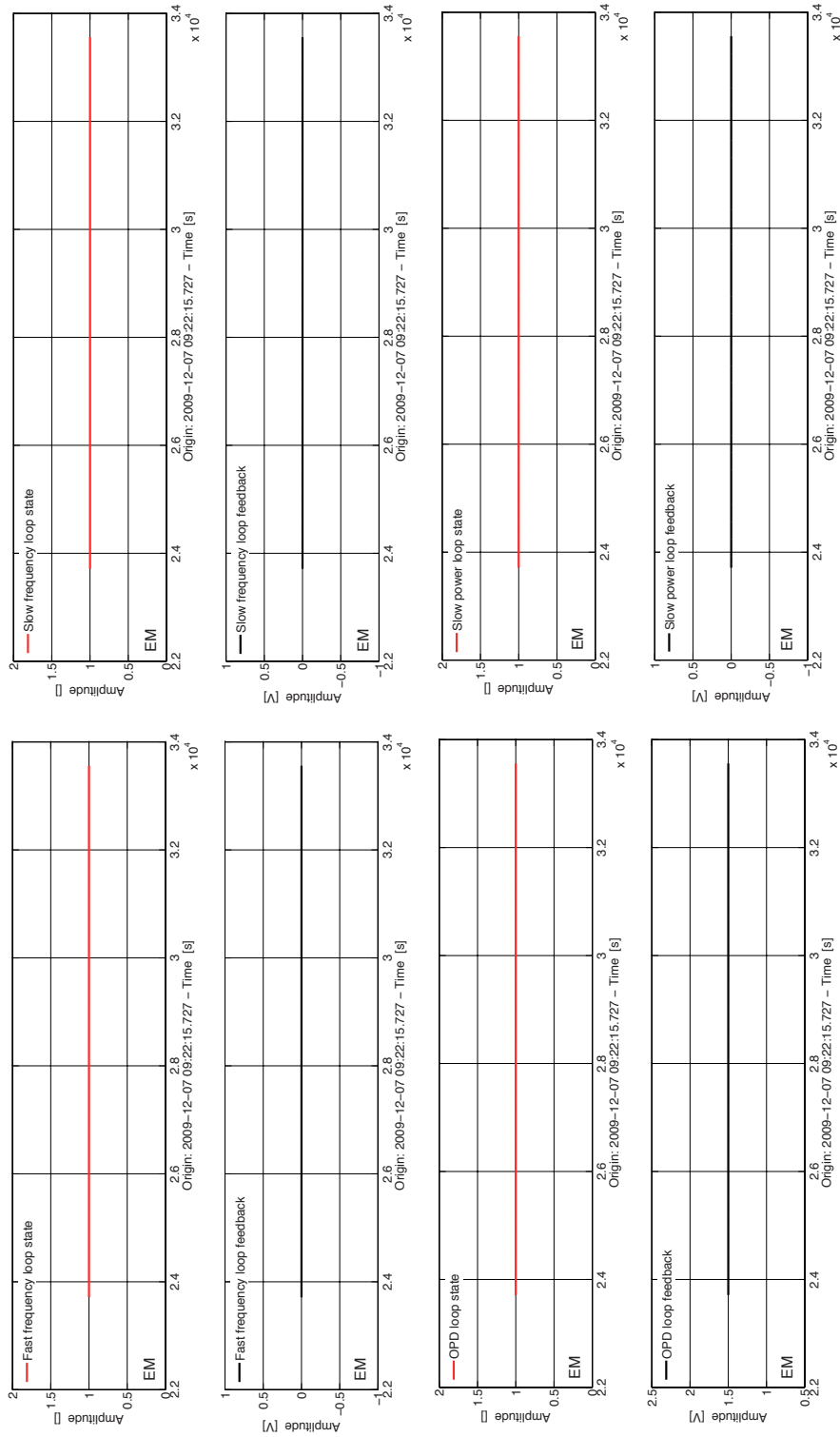
Figure 8.1: An example of the loops state and feedback signals during a free-running frequency noise measurement. These results are from the analysis of the EM free-running frequency noise investigation.
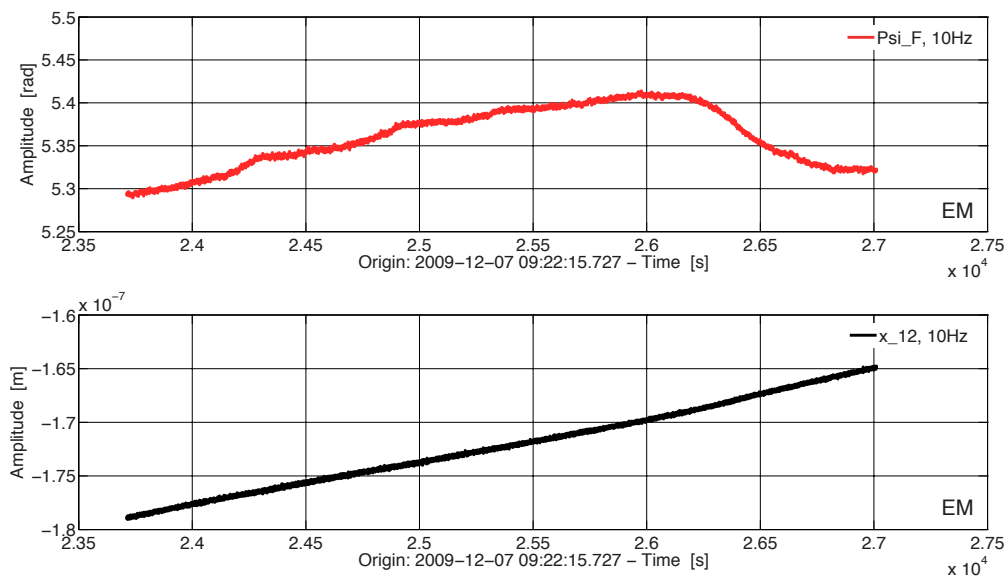
Figure 8.2: The original and detrended timeseries of the Ψ_F and x_{12} data used in the analysis of the EM free-running frequency noise investigation. The EM campaign data was analysed in two segments, due to a glitch in the middle of the investigation. The above plots show the timeseries from the first segment.

Investigation ref.	TC-OMS-L-PO-001, Run 2	
Downloaded timespan	2010-08-31	Times	21:00:00
	2010-09-01		08:00:00
Investigation info.	SF: fixed output y, feedback = 2.6 V. FF: fixed output y, feedback = 0 V. OPD: fixed output y, feedback = -3.5 V. SP: variable output y, feedback = 0 V. FP: open	
Free-running freq. info.	Split for SF/FF states/feedback: 3362 s to 40476 s. Split for other states: None. Data quality issues: Gaps. Duplicate samples. Backward jumps in main channels. No backward jumps in SSC. Data repaired: Yes. Split due to data repair: None. Split for glitches: None.	
Free-running freq. coupling info.	Freqs. used for coupling coeff.: 0.0090136 Hz to 0.11615 Hz.	

Table 8.2: Measurement details for the FM free-running frequency noise analyses [43].
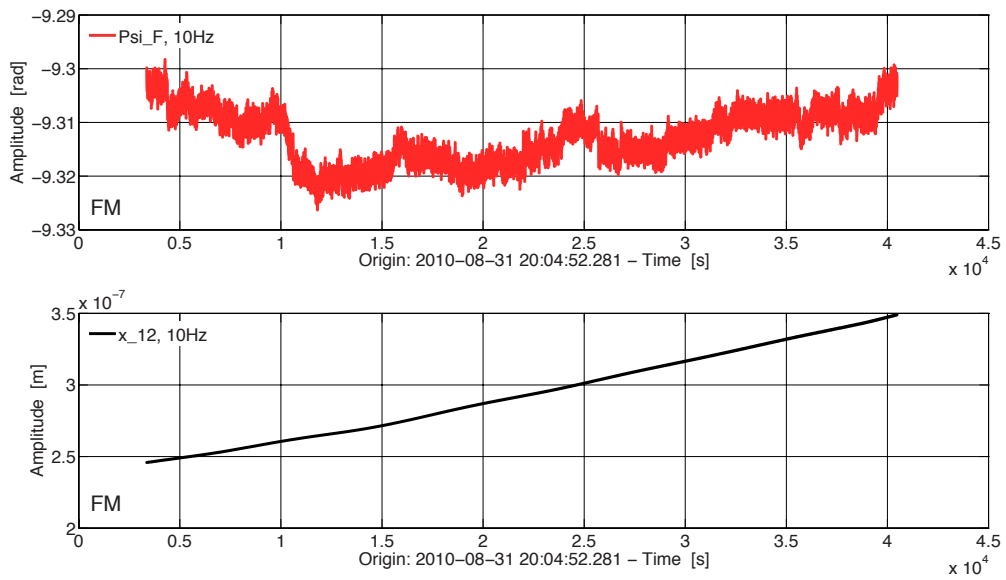
Figure 8.3: The timeseries' of the original and detrended Ψ_F and x_{12} data used in the analysis of the FM free-running frequency noise investigation.

OSTT free-running noise measurements, Run 3		
Downloaded timespan	2011-10-29	Times
		01:13:00
		11:25:00
Investigation info.	SF: fixed output y, feedback = 0 V.	
	FF: fixed output y, feedback = 0 V.	
	OPD: nominal, feedback = varying (loop closed).	
	SP: fixed output y, feedback = -6 V.	
	FP closed	
Free-running freq. info.	Split for SF/FF states/feedback: None.	
	Split for other states: none.	
	Data quality issues: Gaps.	
	Backward jumps in main channels.	
	Same backward jumps in SSC.	
	Data repaired: Yes.	
	Split due to data repair: None.	
	Split for glitches: 16408 s to 36794 s.	
Free-running freq. coupling info.	Freqs. used for coupling coeff.: 0.0090136 Hz to 0.11615 Hz.	

Table 8.3: Measurement details for the OSTT free-running frequency analyses [44].
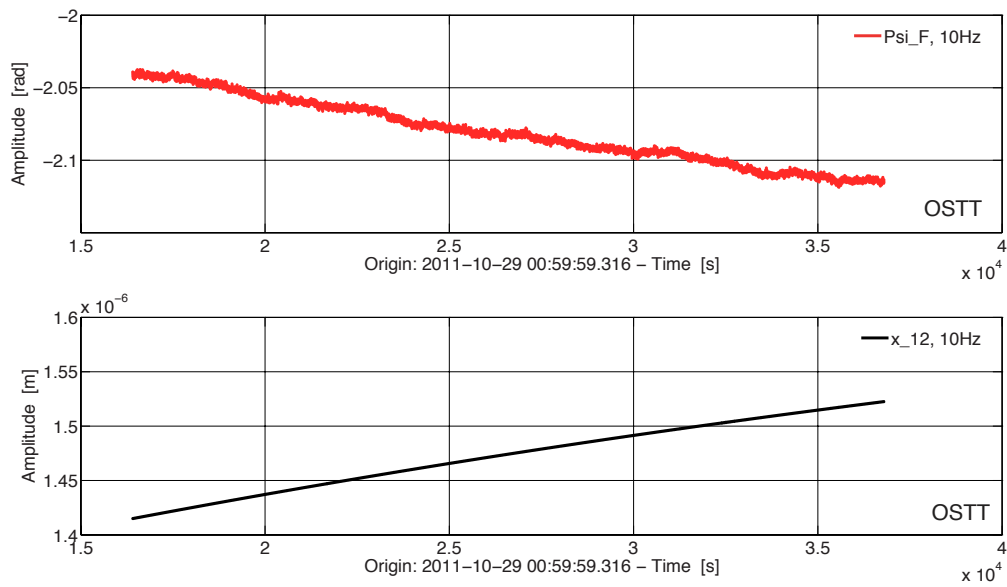
Figure 8.4: The timeseries of the split and repaired Ψ_F and x_{12} data used in the analysis of the OSTT free-running frequency noise investigation.

8.1.2 Control loop characterisation

Appendix

Investigation ref.	TC-OMS-L-SF-003/TC-OMS-FF-003		
Downloaded timespan	2009-12-02	Times	10:06:00
			11:41:00
Investigation info.	SF: nominal, feedback = varying (loop closed).		
	FF: nominal/testing offset Δx, feedback = varying.		
	OPD: nominal, feedback = varying (loop closed).		
	SP: fixed output y, feedback = 0 V.		
	FP closed		
Transfer function method	1 Hz data	Split: 5247.45 to end.	
	10 Hz data	Split: 5070.80 to end.	

Table 8.4: Measurement details for the EM fast and slow frequency control loop OLTF investigation [32].
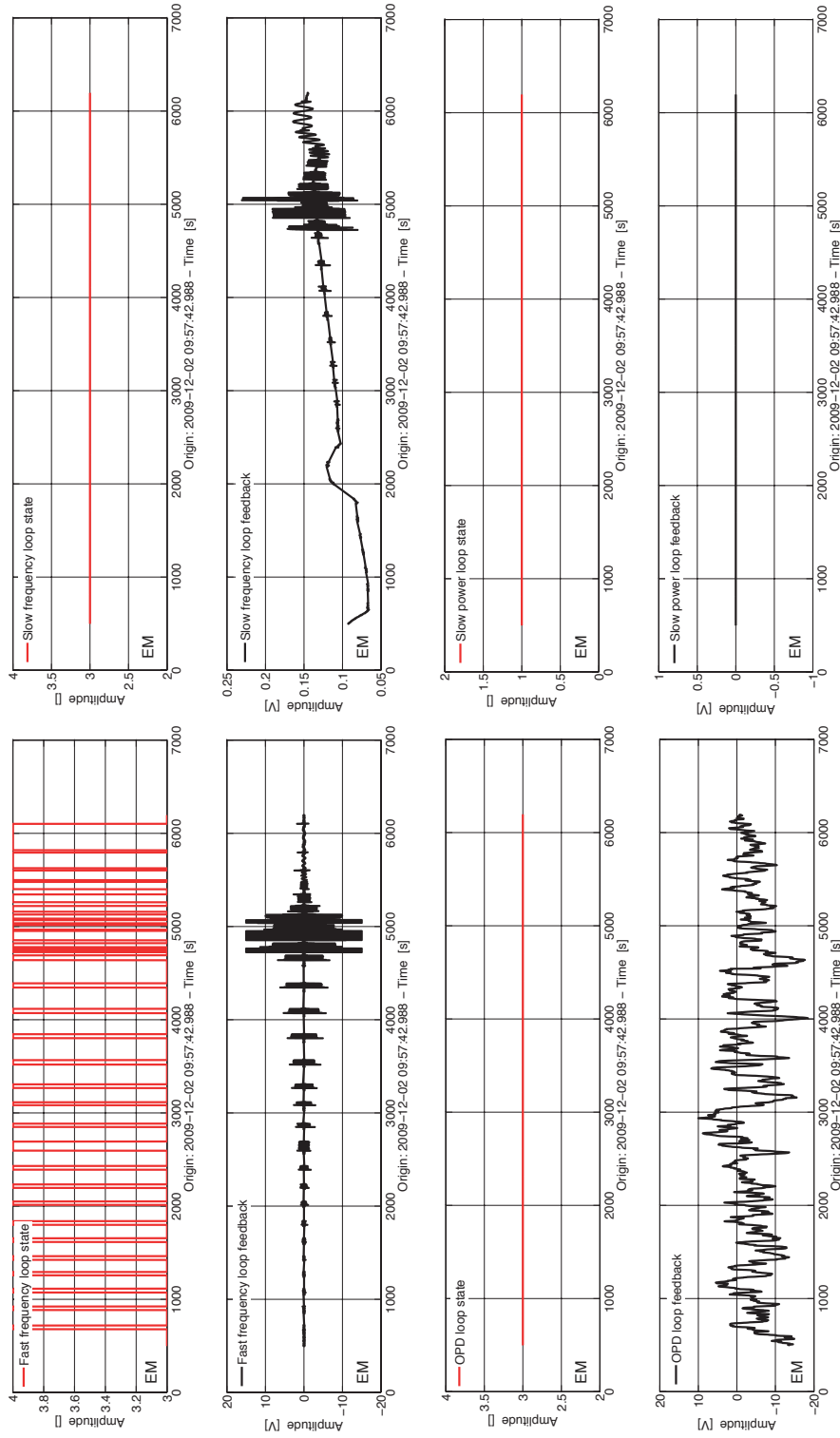
Figure 8.5: Plots showing the loops states and feedback signals, at 1 Hz, for the control loop characterisation investigation in the EM test campaign.

Appendix

329

8 Appendix: Investigation information

	Segment	Start time [s]	End time [s]	Frequency [Hz]
10 Hz data	1	4637.90	4690.00	1.1
	4	4778.60	4819.80	0.6594
	6	4965.79	5016.80	0.3963
	8	5093.00	5128.00	0.237
	9	5167.70	5218.49	0.1421
	10	5266.99	5342.30	0.0852
	11	5404.90	5478.40	0.0511
	12	5501.60	5600.00	0.0306
	13	5629.99	5789.80	0.0184
	14	5819.10	6100.00	0.011
100 Hz	1	724.70	736.59	19.7686685
	2	928.70	940.59	16.7486
	3	1118.70	1130.54	14.1899
	4	1299.95	1310.95	12.0221
	5	1468.05	1479.87	10.1855
	6	1660.72	1672.66	8.6295
	7	1846.69	1860.51	7.3111
	8	2055.97	2068.56	6.1942
	9	2240.80	2254.71	5.2479
	10	2437.96	2449.77	4.4462
	11	2701.96	2713.78	3.767
	12	2891.97	2904.82	3.1915
	13	3120.96	3132.62	2.7039
	14	3312.03	3329.72	2.2908
	15	3578.15	3595.93	1.9407
	16	3853.99	3871.88	1.6444
	17	4124.80	4141.59	1.3931
	18	4400.80	4417.43	1.1803

Table 8.5: Split times and modulation frequencies for the EM fast and slow frequency loop OLTF experiment [32].
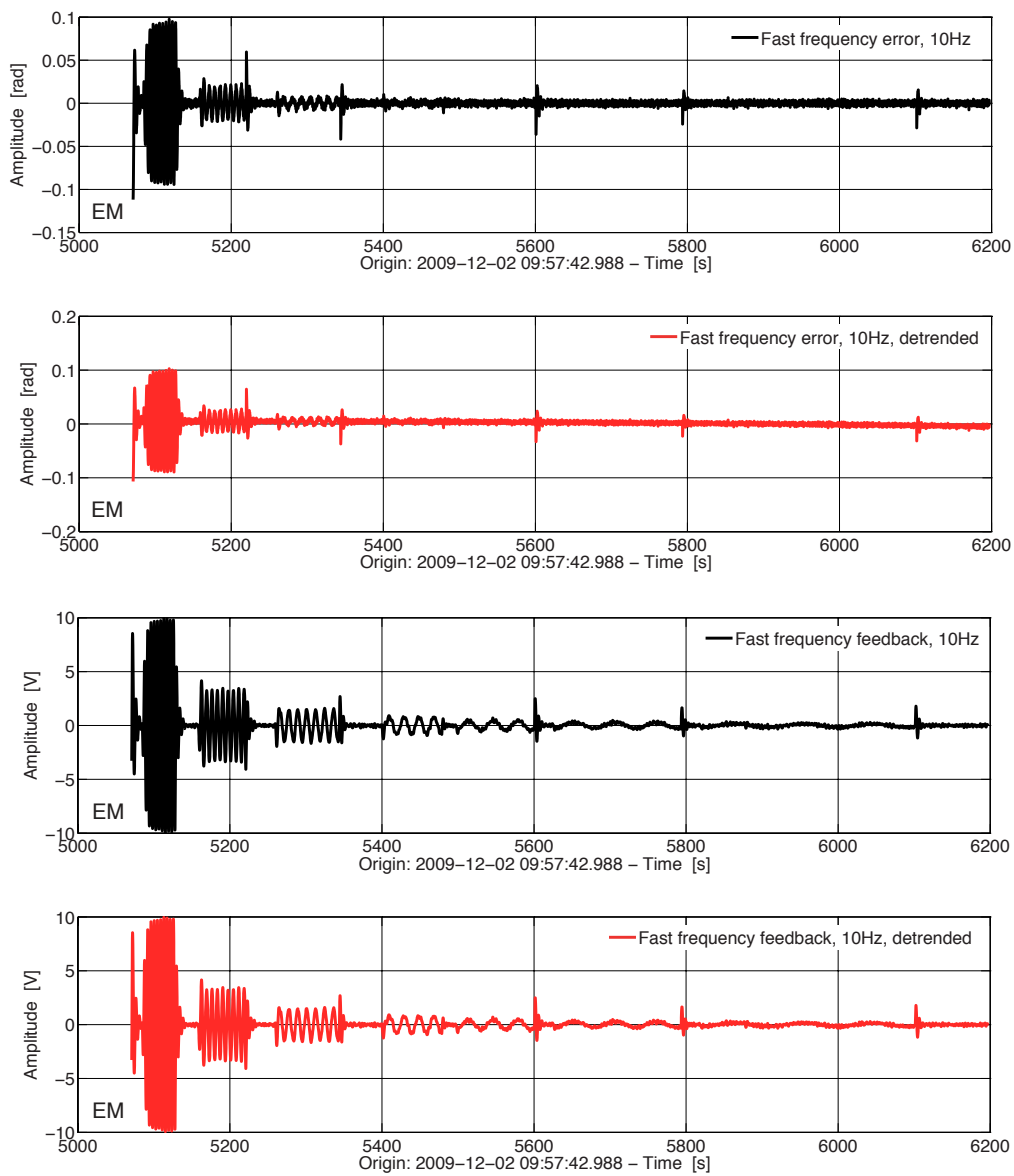
Figure 8.6: The timeseries of the fast frequency error and feedback signals used in the fast frequency controller calibration analysis using EM test campaign data. The original data is shown in black, and the detrended data in red.

Appendix
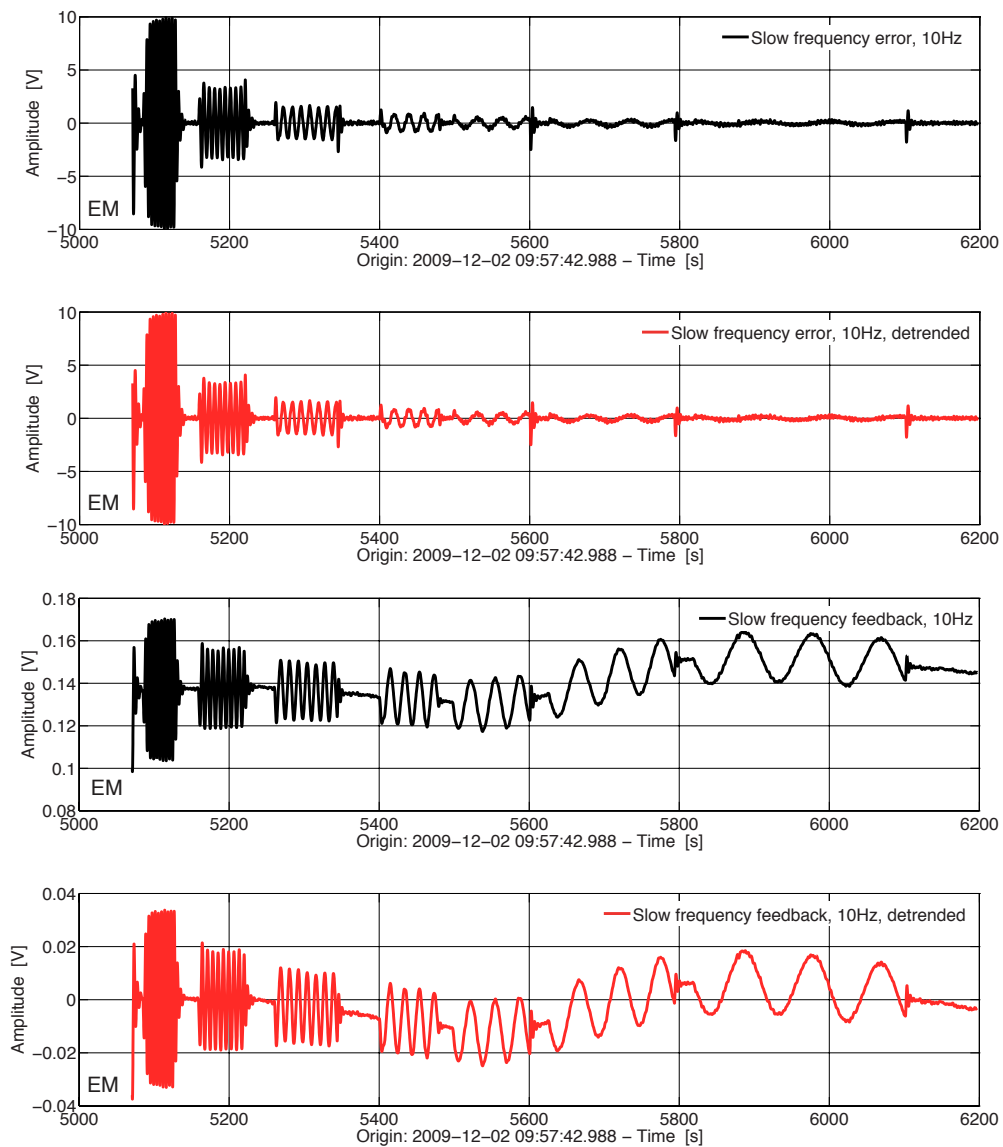
8 Appendix: Investigation information
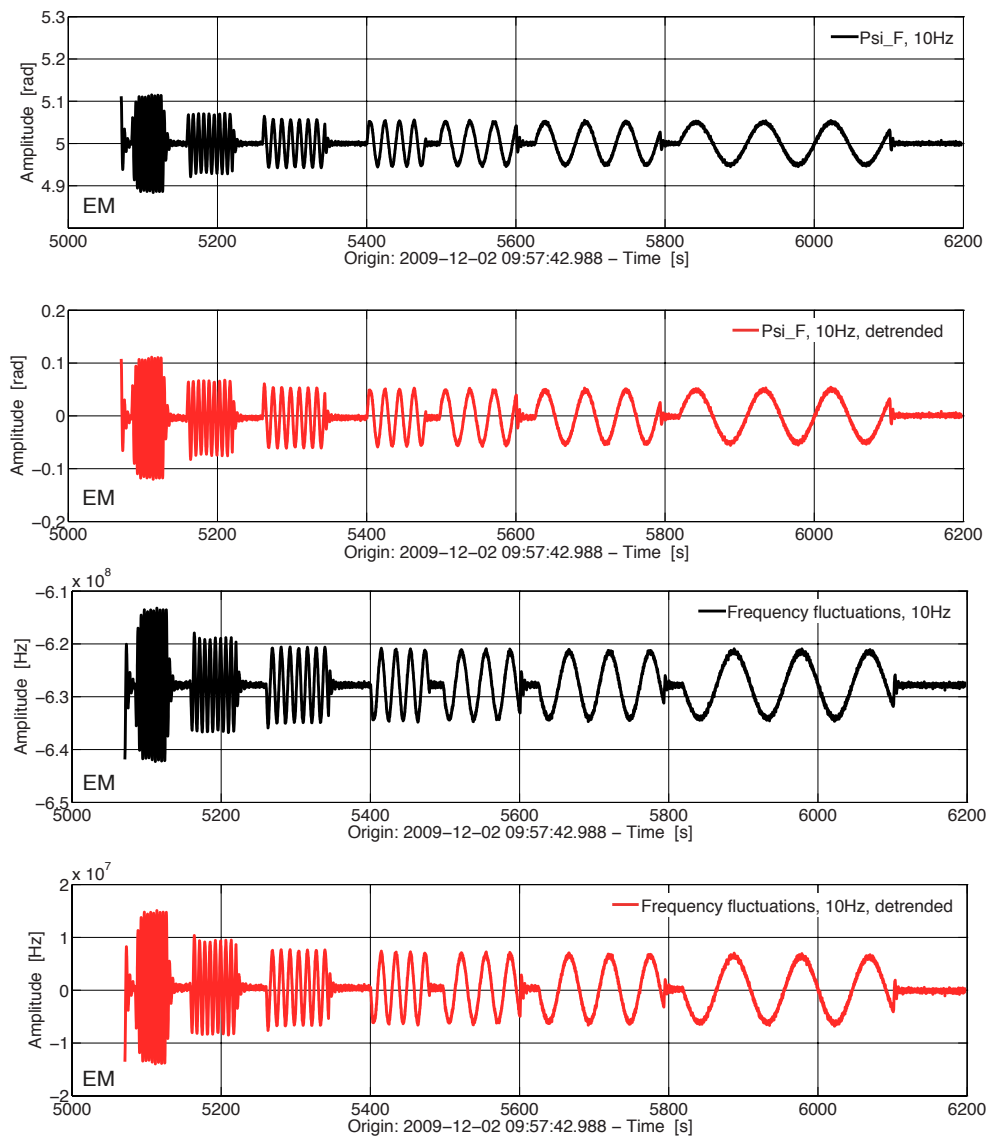

Figure 8.7: The timeseries of the slow frequency error and feedback signals used in the slow frequency controller calibration analysis using EM test campaign data. The original data is shown in black, and the detrended data in red.

Figure 8.8: The original and detrended timeseries of the EM test campaign Ψ_F channels, and the frequency fluctuations calculated from the Ψ_F data.
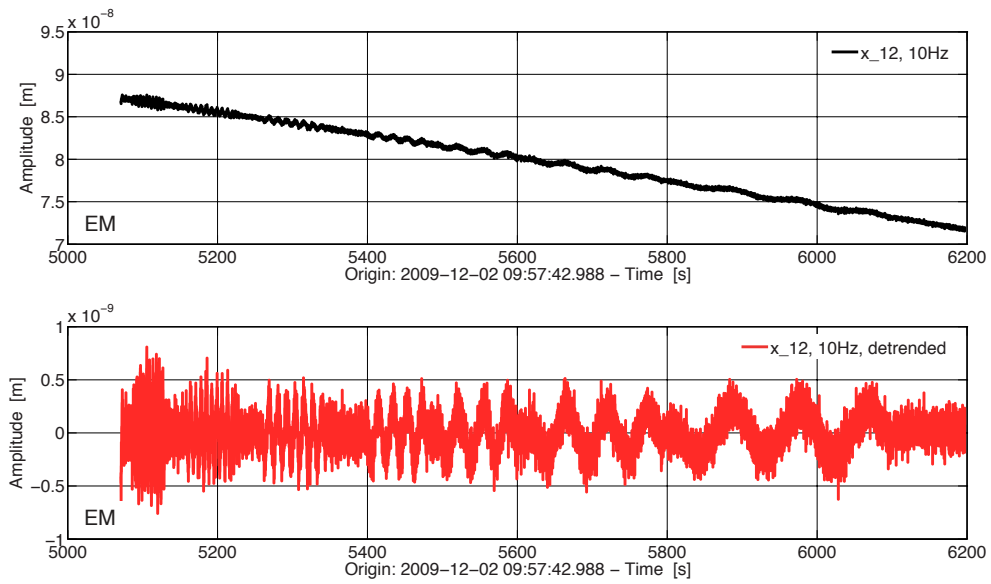
Figure 8.9: The original and detrended timeseries of the x_{12} channel from the EM test campaign OLTF investigation.

Investigation ref.	TC-OMS-L-SF-003/TC-OMS-FF-003		
Downloaded timespan	2010-08-20	Times	14:33:00
			16:12:00
Investigation info.	SF: nominal, feedback = varying (loop closed).		
	FF: nominal/testing offset Δx, feedback = varying.		
	OPD: fixed output y, feedback = 0 V.		
	SP: fixed output y, feedback = 0 V.		
	FP closed		
Transfer function method	10 Hz data	Split: 4293.71 to end.	

Table 8.6: Measurement details for the FM fast and slow frequency control loop OLTF experiment [43].

	Segment	Start time [s]	End time [s]	Frequency [Hz]
10 Hz data	1	4046.30	4088.21	1.1
	2	4330.31	4416.30	0.6594
	3	4481.20	4570.73	0.3943
	4	4596.80	4661.50	0.237
	5	4675.40	4750.00	0.1421
	6	4768.00	4907.80	0.0852
	7	4938.00	5047.00	0.0511
	8	5187.00	5334.00	0.0306
	9	5385.00	5614.20	0.0184
	10	5680.90	5930.00	0.011
100 Hz	1	231.00	246.86	23.3333
	2	522.20	535.30	19.7687
	3	730.21	744.03	14.1899
	4	916.30	934.14	12.0221
	5	1219.00	1236.89	8.6295
	6	1453.00	1467.64	7.3111
	7	1673.01	1688.89	6.1942
	8	1919.09	1934.71	5.2479
	9	2139.00	2154.73	4.4461
	10	2375.01	2390.13	3.767
	11	2800.20	2815.31	2.7039
	12	3015.00	3032.88	2.2908
	13	3281.01	3296.08	1.6444
	14	3502.20	3520.14	1.3931
	15	3840.20	3858.14	1.1803
	16	4114.21	4132.04	1.1

Table 8.7: Split times and modulation frequencies for the FM fast and slow frequency loop OLTF experiment [43].

8.2 Optical pathlength difference noise characterisation

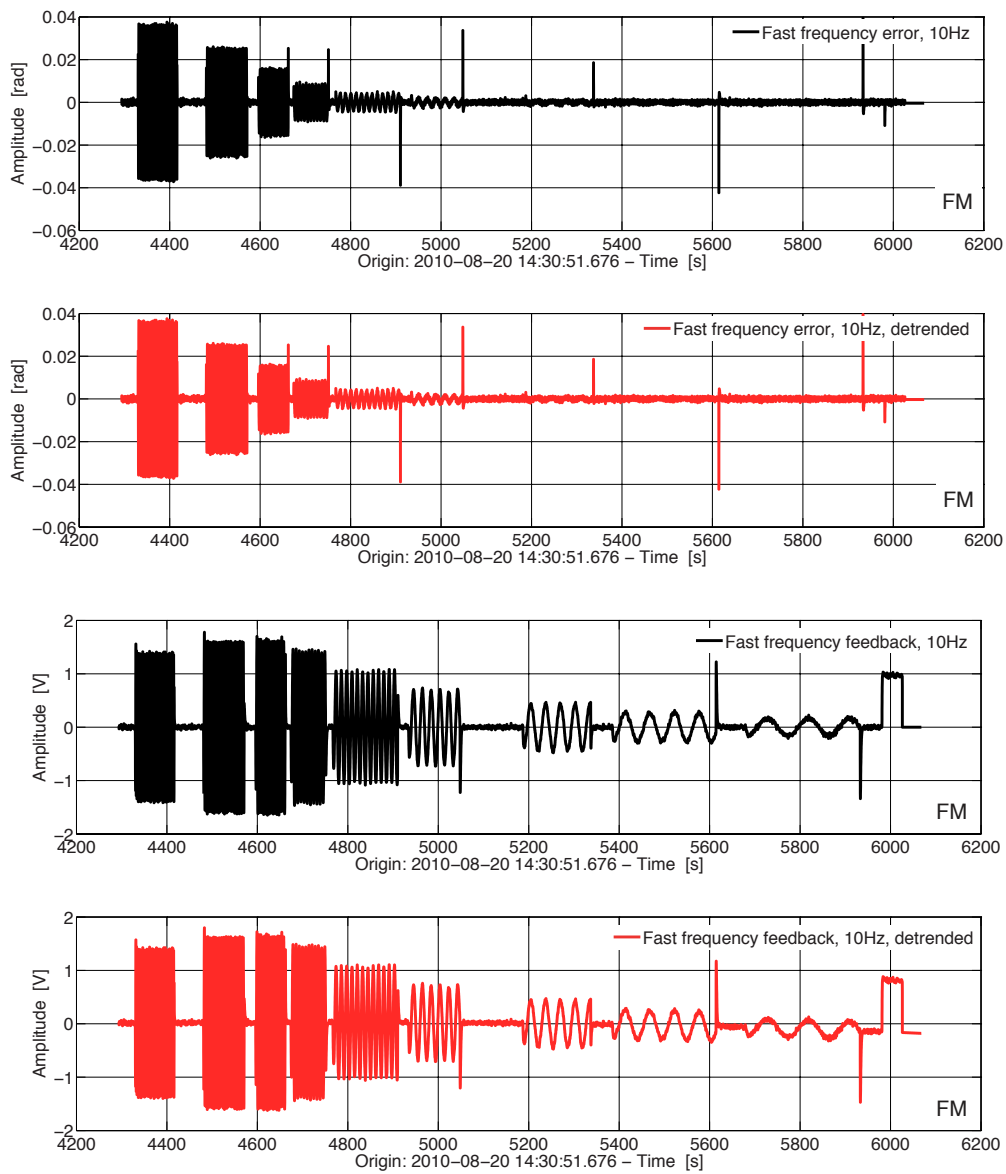### 8.2.1 Free-running optical pathlength difference noise

Figure 8.10: The timeseries of the fast frequency error and feedback signals used in the fast frequency controller calibration analysis using FM test campaign data. The original data is shown in black, and the detrended data in red.
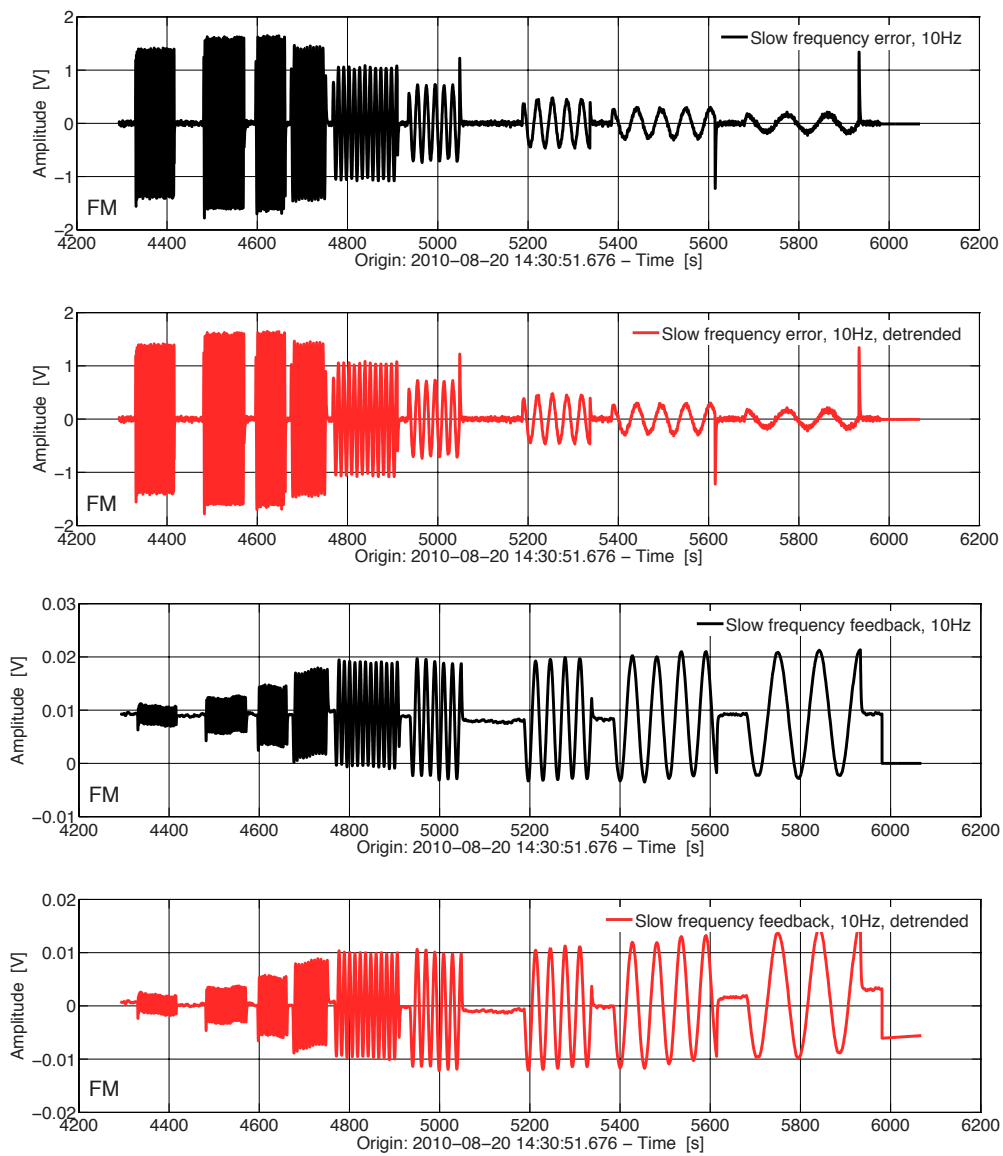
Appendix

8 Appendix: Investigation information

Figure 8.11: The timeseries of the slow frequency error signal and feedback signals used in the slow frequency controller calibration analysis using FM test campaign data. The original data is shown in black, and the detrended data in red.
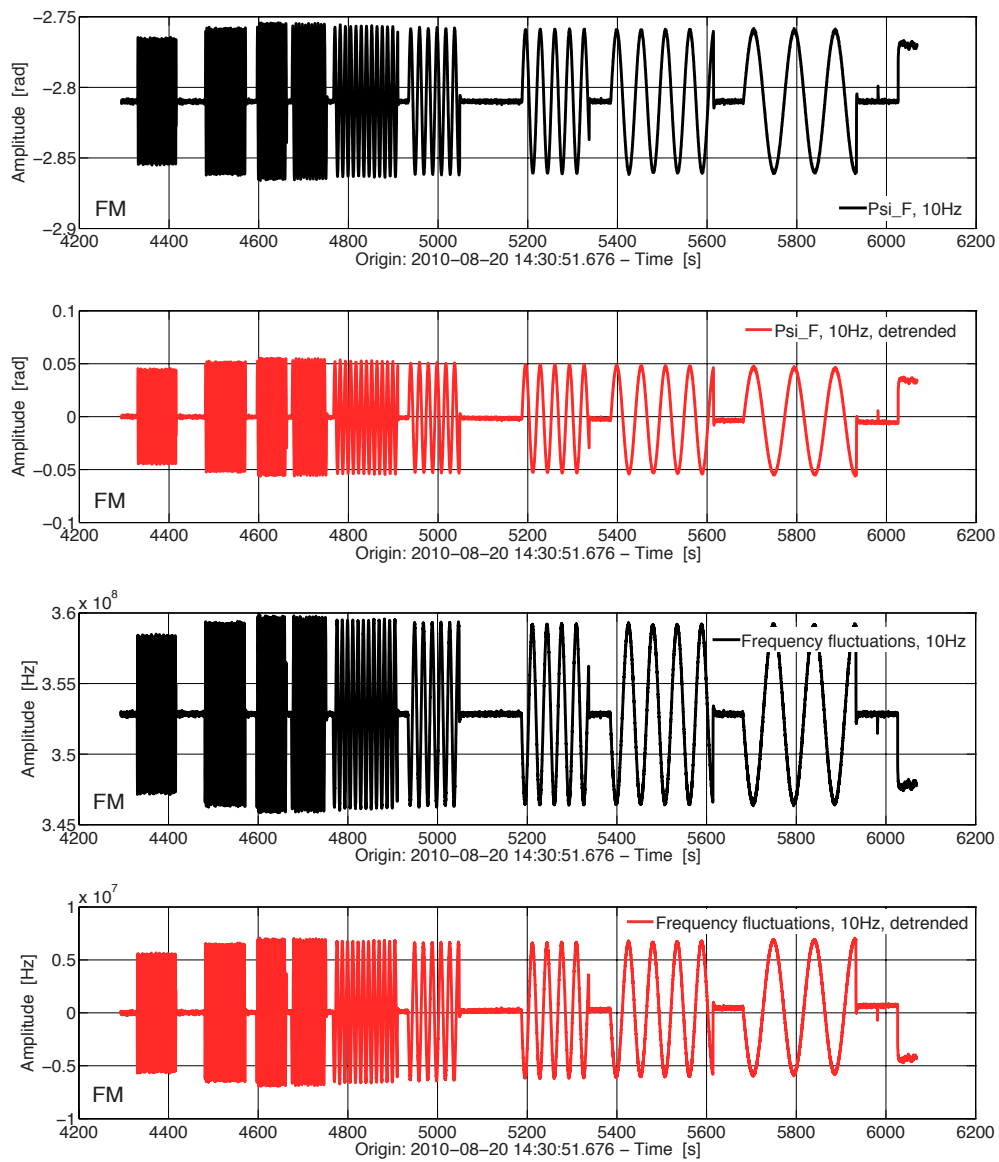
Figure 8.12: The original and detrended timeseries of the FM test campaign Ψ_F channels, and the frequency fluctuations calculated from the Ψ_F data.

Investigation ref.		TC-OMS-L-PO-001	
Downloaded timespan	2009-12-07	Times	00:01:00
			23:59:00
Investigation info.	SF: fixed output y, feedback = 0 V.		
	FF: fixed output y, feedback = 0 V.		
	OPD: fixed output y, feedback = 0 V.		
	SP: fixed output y, feedback = 0 V.		
Free-running freq. info.	Split for OPD state/feedback: 23925 s to 33558 s.		
	Split for other states: None.		
	Data quality issues: Gaps.		
	Data repaired: Yes.		
	Split due to data repair: None.		
	A glitch was identified between 27542 s and 27995 s.		
	The data was split into two segments.		
	Segment one:	Split for glitches: 23925 s to 27541 s.	
	Segment two:	Split for glitches: 27996 s to end.	
Free-running freq. coupling info.	Segment one:	Freqs. used for coupling coeff.: 0.0097046 Hz to 0.24051 Hz.	
	Segment two:	Freqs. used for coupling coeff.: 0.0029044 Hz to 0.033401 Hz.	

Table 8.8: Measurement details for the EM free-running OPD noise analyses [32].

Investigation ref.	TC-OMS-L-PO-001		
Downloaded timespan	2010-08-26	Times	21:00:00
	2010-08-28		08:00:00
Investigation info.	SF: nominal.		
	FF: nominal.		
	OPD: fixed output y, feedback = 0 V.		
	SP: nominal.		
Free-running freq. info.	Split for OPD state/feedback: 45951.14 s to 66500.35 s.		
	Split for other states: 46304 s to 60927.32 s.		
	Data quality issues: Gaps.		
	Duplicates.		
	Backward jumps in main channels.		
	Backward jumps in SSC.		
	Data repaired: Yes.		
	Split for glitches: 53113.99 s to 56917.09 s.		
Free-running freq. coupling info.	Freqs. used for coupling coeff.: 0.016565 Hz to 0.06212 Hz.		

Table 8.9: Measurement details for the FM free-running OPD noise analyses [43].

Appendix

341

Investigation ref.	Free-running noise measurements, Run 1		
Downloaded timespan	2011-10-28	Times	02:00:00
			13:30:00
Investigation info.	SF: nominal, feedback = varying (loop closed).		
	FF: nominal, feedback = varying (loop closed).		
	OPD: fixed output y, feedback = 0 V.		
	SP: fixed output y, feedback = 0 V.		
Free-running freq. info.	Split for OPD state/feedback: None.		
	Split for other states: None.		
	Data quality issues: Gaps.		
	Backward jumps in main channels.		
	Backward jumps in SSC.		
	Data repaired: Yes.		
	Split due to data repair: None.		
	Some glitches detected.		
	Split for glitches: 28132.40 s to 33532.40 s.		
Free-running freq. coupling info.	Freqs. used for coupling coeff.: 0.0022237 Hz to 0.031132 Hz.		

Table 8.10: Measurement details for the OSTT free-running OPD noise analyses, measurement one [44].

8.2.2 Control loop characterisation

Experiment ref.	TC-OMS-L-OPD-003	
Downloaded timespan	2010-11-26	Times
		18:37:00
		19:38:17
Investigation info.	SF: fixed output y, feedback = 0 V.	
	FF: fixed output y, feedback = 0 V.	
	OPD: nominal/testing offset Δx, feedback = varying.	
	SP: fixed output y, feedback = 0 V.	

Table 8.11: Measurement details for the EM OPD OLTF experiment [32].

	Segment	Start time [s]	End time [s]	Frequency [Hz]
10 Hz data	1	6445.80	6505.50	0.39532
	2	6527.20	6590.80	0.23699
	3	6612.41	6671.31	0.14207
	4	6688.41	6742.31	0.08517
	5	6763.20	6842.20	0.05106
	6	6868.40	6958.30	0.030608
	7	6973.30	7070.61	0.01835
	8	7101.30	7235.11	0.011
100 Hz	1	3658.53	3668.46	6.1942393253178
	2	3835.31	3845.19	5.24792301154682
	3	4072.50	4086.31	4.44619708571573
	4	4295.31	4305.16	3.76695094069231
	5	4492.54	4503.60	3.19147332338697
	6	4702.53	4715.23	2.70391150143802
	7	4921.41	4933.31	2.2908345666038
	8	5164.60	5176.50	1.94086345235627
	9	5377.42	5389.28	1.644357473738
	10	5591.41	5604.11	1.39314875456868
	11	5831.40	5843.29	1.18031722624415
	12	6049.42	6062.13	1.1
	13	6324.61	6334.56	0.659432

Table 8.12: Split times and modulation frequencies for the EM OPD OLTF experiment [32].

Experiment ref.	TC-OMS-L-OPD-003		
Downloaded timespan	2010-08-18	Times	14:29:50
			16:35:00
Investigation info.	SF: not available. FF: fixed output y, feedback = 0 V. OPD: nominal/testing offset Δx, feedback = varying. SP: not available.		
	Data quality issues: Gaps. Data repaired: No.		

Table 8.13: Measurement details for the FM OPD OLTF experiment [43].

	Segment	Start time [s]	End time [s]	Frequency [Hz]
10 Hz data	1	5516.30	5566.30	0.6594
	2	5683.40	5750.50	0.3953
	3	5791.40	5880.11	0.237
	4	6018.39	6167.80	0.0852
	5	6215.60	6359.60	0.0511
	6	6379.60	6534.40	0.0306
	7	6556.90	6958.89	0.0184
	8	6988.30	7527.30	0.011
100 Hz	1	804.30	811.49	19.7687
	2	1026.30	1043.39	16.7486
	3	1263.50	1278.66	14.1899
	4	1501.50	1518.53	12.0221
	5	1739.50	1755.40	10.1855
	6	1975.50	1990.57	8.6295
	7	2197.50	2215.32	7.3111
	8	2460.32	2475.38	6.1942
	9	2736.32	2753.01	4.4461
	10	2975.61	2993.48	3.767
	11	3208.31	3225.40	3.1915
	12	3464.32	3478.12	2.7039
	13	3926.31	3940.18	2.2908
	14	4182.35	4198.20	1.9409
	15	4431.52	4448.26	1.6444
	16	4698.42	4714.16	1.3931
	17	5268.59	5286.03	1.1803

Table 8.14: Split times and modulation frequencies for the FM OPD OLTF experiment [43].

8.3 Performance measurements

Experiment ref.		XX		
Downloaded timespan	2010-08-18	Times	14:29:50
			16:35:00
Investigation info.	SF: nominal. FF: nominal. OPD: nominal. SP: not available.			
	Data quality issues: Gaps. Data repaired: Yes.			

Table 8.15: Measurement details for the EM performance investigation [43].

Performance measurement		
Experiment ref.		
Downloaded timespan	2010-09-07	00:01:00
	2010-09-08	09:00:000
	Times	
Investigation info.	SF: nominal.	
	FF: nominal.	
	OPD: nominal.	
	SP: not available.	
	Split for other states: 23935.56 s to 37612.69 s.	
	Data quality issues: Gaps.	
	Backward jumps in main channels.	
	Backward jumps in SSC.	
	Data repaired: Yes.	
	Split due to data repair: None.	
	Some glitches detected.	
	Split for glitches: 0 s to 36086.40 s.	

Table 8.16: Measurement details for the FM performance investigation [43].

Appendix

349

Experiment ref.	Nominal performance measurement (hot case), Run 1		
Downloaded timespan		Times	
	2011-10-29		15:00:00
	2011-10-30		03:30:00
Investigation info.	SF: nominal.		
	FF: nominal.		
	OPD: nominal.		
	SP: not available.		
	Split for other states: 12123.95 s to end.		
	Data quality issues: Gaps.		
	Backward jumps.		
	Backward jumps in SSC.		
	Data repaired: Yes.		
	Split due to data repair: None.		
	Some glitches detected.		
	Split for glitches: 0 s to 36086.40 s.		

Table 8.17: Measurement details for the OSTT test campaign hot performance investigation [44].

Experiment ref.	Nominal performance measurement (cold case), Run 1		
Downloaded timespan	2011-11-05	Times	16:25:00
	2011-11-06		03:00:00
Investigation info.	SF: nominal.		
	FF: nominal.		
	OPD: nominal.		
	SP: not available.		
	Split for other states: None.		
	Data quality issues: Gaps.		
	Backward jumps.		
	Backward jumps in SSC.		
	Data repaired: Yes.		
	Split due to data repair: 0 s to 37182.80 s.		
	Some glitches detected.		
	Split for glitches: 19807 s to 32451 s.		

Table 8.18: Measurement details for the OSTT test campaign cold performance investigation [44].

8.4 Amplitude noise characterisation

8.4.1 Free-running amplitude noise

Experiment ref.	Nominal performance measurement (hot case), Run 3		
Downloaded timespan	2011-10-29	Times	15:00:00
	2011-10-30		03:30:00
Investigation info.	SF: nominal. FF: nominal. OPD: nominal. SP: fixed output y, feedback = -6 V. FP: fixed output y, feedback = ~ 2.39 V.		
	Split for other states: None. Data quality issues: Gaps. Backward jumps in 10 Hz data. Data repaired: Yes. Split due to data repair: none. Some glitches detected. Split for glitches: 18100 s to 31500 s.		

Table 8.19: Measurement details for the OSTT test campaign free-running amplitude noise investigation, performed during the hot measurement phase [44].

8.4.2 Closed-loop amplitude noise

Experiment ref.	Nominal performance measurement (hot case), Run 1		
Downloaded timespan		Times	
	2011-10-30		14:33:00
	2011-10-31		00:30:00
Investigation info.	SF: nominal.		
	FF: nominal.		
	OPD: nominal.		
	SP: variable output y, feedback = -6 V.		
	Split for states: 12123.95 s to end.		
	Data quality issues: Gaps.		
	Backward jumps in 10 Hz data.		
	Data repaired: Yes.		
	Split due to data repair: none.		
	Some glitches detected.		
	Split for glitches: 18100 s to 31500 s.		

Table 8.20: Measurement details for the OSTT test campaign closed-loop amplitude noise investigation, performed during the hot measurement phase [44].

9 Appendix: Data quality

Contents

During the analysis of the EM, FM, and OSTT test campaign data, some issues with the data were identified, these have been split into two types:

- Data quality issues:

    - Backwards jumps;

    - Duplicate samples;

    - Incorrect sampling frequencies;

    - Gaps.

- Glitches.

In this section the identification and resolution of these issues is discussed. The FM free-running frequency measurement has been used to illustrate the data quality issues discussed, as all of the above issues were observed.

9.1 Data quality issues

9.1.1 Backward jumps

A backward jump in the data describes a situation where there is a negative interval between two consecutive time stamps, i.e., the x-axis data of a time-series Analysis Object (ao). It should be noted, that in order to check the data for these errors the data must <u>not</u> be sorted when downloaded from the repository.

Backward jumps in the time-stamping are identified by calculating the difference between the consecutive x-samples in an ao, and then outputting if there are instances where this value is less than zero. In general, where this issue has been identified, it has been found in all channels of a particular packet.

In order to determine the cause of the issue, the Source Sequence Counter (SSC) is used. This is an extra channel associated with each telemetry packet. For each sample in the packet the SSC incrementally increases by two, beginning at zero and counting up to 16382 before resetting, as shown in Figure 9.1.

If the SSC data is correctly incremented, then the timestamping of the channel with the backwards jumps can be considered to be incorrect. In this case, a solution would be to delete the x-values of the data, and reallocate new x-values based on the original start time, t0, and the known sampling frequency of the data. It should be noted that other issues, such as duplicate samples and data gaps, should be repaired before reallocating the x-values. If the SSC is not correctly incremented, then the data is considered to be incorrectly ordered. It is therefore necessary to reorder the samples such that the SSC increments as expected.
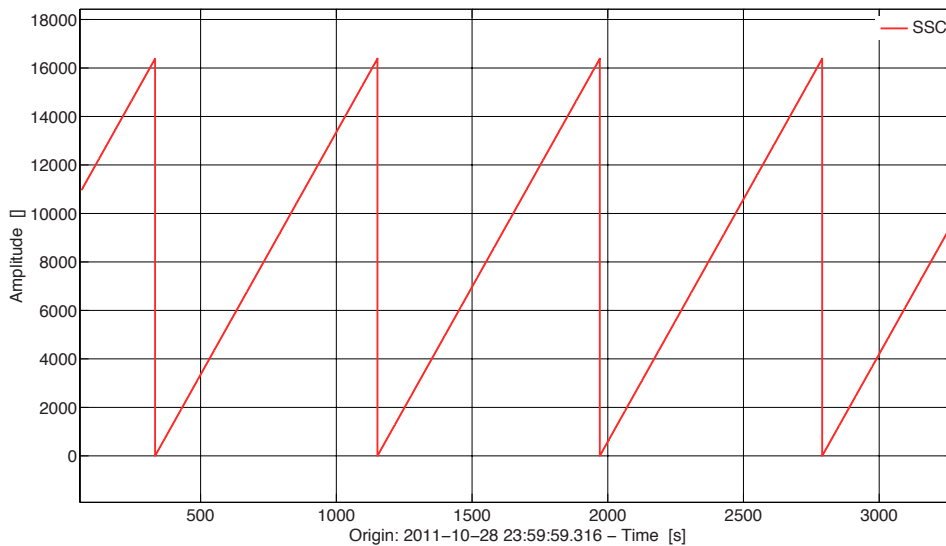
Figure 9.1: The source sequence counter for a correctly ordered data set. The counter starts at 0, and counts up to 16382 before resetting.

9.1.2 Duplicate samples

A duplicate sample describes the situation where there is zero interval between two consecutive time-stamps.

Duplicate samples are identified in the timeseries data by determining the difference between consecutive x-values, and determining if there are instances where this value is zero. In order to correct such errors, the LTPDA 'drop duplicates' method is used. This method identifies the index at which the difference between the consecutive samples is less than some defined tolerance and deletes the x and y values at that index.

9.1.3 Gaps

The data channels in the telemetry are created in the DMU with a defined sampling frequency. In terms of the telemetry required for the analyses in this thesis, the defined sampling frequencies are mostly 10 Hz, 1 Hz, and 100 Hz. Theoretically, the time between consecutive time samples should therefore be $1/10$ s, 1 s, or $1/100$ s. However, differently spaced gaps in the test campaign data can occur for a number of reasons:

Appendix

9 Appendix: Data quality

1. DMU sampling: The sampling accuracy of the DMU is limited by the accuracy of the clock. The result is that the actual sampling frequency of the data varies around the desired sampling frequency. For 10 Hz data, the actual sampling frequency is either ~9.85 Hz or 10.24 Hz [27].

2. DMU resets: The DMU clock periodically resets when the clock drift reaches 10 ms. This produces a regular decrease in the difference between consecutive x-samples [27].

3. Missing data: Any missing data will be seen as a gap in the data. Such gaps could potentially arise where some actual data has not been received or transmitted, or because the timespan of the retrieved data does not match the planned experiment timespan and there is no data.

Gaps in the data are identified by taking the difference between consecutive x-axis samples of the timeseries. The origin of the gap can be identified by creating some gap length criteria for each of the possible issues:

1. DMU sampling: $0.08983\,\text{s} <$ gap length $< 0.08985\,\text{s}$.

2. DMU resets: For 10 Hz data $0.0975 <$ gap length < 0.1017.

3. Missing data: any gap which does not meet either of the above criteria can be considered to be missing data.

The method of removing the gaps from the data depends upon the type of gap present. Firstly, large gaps in the data should be split out, such that these times are removed from the data set to be analysed. Smaller gaps due to missing samples are then interpolated using the 'interpmissing' method. At this point the data is then resampled to the frequency that we expect, either 10 Hz, 1 Hz, or 100 Hz for the OMS relevant channels. This is implemented by saving the toffset (the timestamp of the first sample) before deleting the x-values and replacing them with appropriately spaced timestamps. This removes the issues due to the DMU sampling inaccuracy, and the DMU clock resets.

In this thesis, gaps larger than 2 s were considered to require that section of data to be rejected. No appropriate statistical method for identifying the gap size limit for interpolating the data was determined.

9.1.4 Identification of artifacts

To aid identification of the aforementioned data artifacts the 'dataCheck' method was written. This method is intended to be used as a first step in the analysis of any time-series ao, it outputs an html file containing the information relating to any potential data issues. The output includes:

- data length;

- sampling frequency;

- whether the data is evenly sampled;

- the expected number of samples;

- the actual number of samples;

- the number of missing samples;

- the number of gaps;

- the number of backwards jumps;

- number of duplicates.

9.1.5 Solution algorithms

The previously described solutions of these data quality issues are relatively simple, and can be solved using existing LTPDA ao methods. Figure 9.2 shows a flowchart depicting the logic for their implementation. Question marks in the procedure indicate that the method for solving that issue is unknown, or is unlikely to be observed. For the step involving treating larger gaps, a method for determining the

361

Appendix

largest gap which can be interpolated is required. It is suggested that all data should first be evaluated using the dataCheck method, or similar, and then processed according to Figure 9.2. This could be implemented before the data is made available to the data analysis team, or implemented before each analysis is performed.

9.2 Glitches

Glitches, meaning spikes in the data, were identified using a band-pass filter and the 'spectrogram' method. Where large spikes were observed, the data was split to leave a segment without glitches.

Figure 9.2: A flow chart showing the data preparation algorithm.

Appendix

Bibliography

[1] A. Einstein. Die Grundlage der allgemeinen Relativitätstheorie [adp 49, 769 (1916)]. *Annalen der Physik*, 14(S1):517–571, 2005.

[2] B. Sathyaprakash and B. Schutz. Physics, astrophysics and cosmology with gravitational waves. *Living Reviews in relativity*, 12(2), 2009.

[3] J. Weber. Detection and generation of gravitational waves. *Phys. Rev.*, 117:306–313, Jan 1960.

[4] R. A. Hulse and J. H. Taylor. Discovery of a pulsar in a binary system. *Astrophysical Journal*, 195(2):L51–L53, January 1975.

[5] BICEP2 Collaboration et al. BICEP2 I: Detection of B-mode polarization at degree angular scales, 2014.

[6] P. R. Saulson. *Fundamentals of interferometric gravitational wave detectors*. World Scientific, 1994.

[7] B P Abbott et al. LIGO: the Laser Interferometer Gravitational-Wave Observatory. *Reports on Progress in Physics*, 72(7):076901, 2009.

[8] T Accadia et al. Virgo: a laser interferometer to detect gravitational waves. *Journal of Instrumentation*, 7(03):P03012, 2012.

[9] H. Grote et al. Methods and results of a search for gravitational waves associated with gamma-ray bursts using the GEO 600, LIGO, and Virgo detectors. *Classical and Quantum Gravity*, 25(1):4043, June 2008.

[10] A. Freise and K. Strain. Interferometer techniques for gravitational-wave detection. *Living Reviews in relativity*, 13(1), February 2010.

[11] eLISA Consortium. The Gravitational Universe: A science theme addressed by the eLISA mission observing the entire Universe.

[12] LISA Study Team. LISA: Laser Interferometer Space Antenna for the detection and observation of gravitational waves. Technical report, 1998.

[13] ESA. Laser Interferometer Space Antenna: a cornerstone mission for the observation of gravitational waves. Technical report, ESA, July 2000.

[14] P. Amaro-Seoane et al. Low-frequency gravitational-wave science with eLISA/NGO. *Classical and Quantum Gravity*, 29(12):124016, 2012.

[15] S. Vitale et al. The LISA Technology Package onboard SMART-2. Unitn-Int 10-2002/Rel 1.3, October 2002.

[16] K Danzmann et al. European LISA technology: Demonstration satellite for the LISA mission in ESA's Space Science Programme. Unpublished proposal, 1998.

[17] P. McNamara. Overview of LISA Pathfinder. Technical Report LISA-LPF-RP-0001, ESA, 2009.

[18] R. Wegener, R. Gerndt, N. Gradmann, and D. Kolbe. LTP user manual. Technical Report S2-ASD-MA-3004_LTP, ASD, 2014.

[19] S. Windisch. LTP RLU description of design changes from EM to PFM. Technical Report LTP-TESAT-TN-3088, TESAT, March 2007. LTP-TESAT-TN-0088.

[20] K. Wagner. Advanced optics laboratory notes, 2012.

[21] LM Team, K. Kudielka, C. Voland, E. Kamata, and M. Zollinger. Laser modulator (L21C0) assembly design synthesis report. Technical Report S2-CSZ-RP-3002_I2_R, Contraves Space AG, November 2005.

[22] E. Fitzsimmons and D. Robertson. Optical characterisation of 3OB. Technical Report S2-UGL-TN-3039, University of Glasgow, August 2013.

[23] U. Denskat, R. Gerndt, G. Link, and U. Johann. Phasemeter processing and laser control. Technical Report S2-ASD-RS-3018, ASD, September 2009.

[24] F. Guzman Cervantes. *Gravitational wave observation from space: optical measurement techniques for LISA and LISA Pathfinder.* PhD thesis, Max Planck Institute for Gravitational Physics, June 2009.

[25] F. Steier. *Interferometry techniques for spaceborne gravitational wave detectors.* PhD thesis, Leibniz Universitaet Hannover, 2008.

[26] M. Nofrarias. OMS geometric calibration. Technical report, AEI, 2009.

[27] H. E. Audley, I. Diepholz, A. Garcia Marin, A. Monsky, M. Nofrarias, and F. Steier. Report on the OMS FM phase 1 test campaign. Technical Report S2-AEI-TN-3068, AEI, May 2011.

[28] P. McNamara and G. Racca. Introduction to LISA Pathfinder. Technical Report LISA-LPF-RP-0002, ESA, March 2009.

[29] H. E. Audley, K. Danzmann, A. Garcia Marin, G. Heinzel, A. Monsky, M. Nofrarias, and F. Steier et al. The LISA Pathfinder interferometry - hardware and system testing. *Classical and Quantum Gravity*, 28, 2011.

[30] G. Vollmer. LTP OMS EM campaign: electrical and optical integration test report. Technical Report S2-ASD-TR-3066, ASD, October 2009.

[31] G. Geraldi, A. Garcia Marin, G. Hechenblaikner, R. Gerndt, F. Steier, K. Rogalla, H. Abele, D. Kolbe, and U. Johann. OMS EM functional fest plan and procedures. Technical Report S2-ASD-TP-3027, ASD, October 2009.

[32] V. Wand, G. Hechenblaikner, P. Luetzow-Wentzky, R. Gerndt, K. Rugalla, H. Abele, U. Johann, and D. Kolbe. OMS EM control loop and performance test report. Technical Report S2-ASD-TR-3075, ASD, April 2010.

[33] G. Geraldi, G. Hechenblaikner, V. Wand, R. Gerndt, K. Rogalla, H. Abele, D. Kolbe, and U. Johann. OMS EM functional test report. Technical Report S2-ASD-TR-3070, ASD, January 2010.

[34] G. Hechenblaikner, V. Wand, R. Gerndt, K. Rogalla, H. Abele, U. Johann, and D. Kolbe. OMS interferometer calibration and commissioning test report. Technical Report S2-ASD-TR-3072, ASD, February 2010.

[35] G. Hechenblaikner, R. Gerndt, U. Johann, P. Luetzow-Wentzky, V. Wand, H. Audley, K. Danzmann, A. Garcia-Marin, G. Heinzel, M. Nofrarias, and F. Steier. Coupling characterization and noise studies of the optical metrology system onboard the LISA Pathfinder mission. *Appl. Opt.*, 49(29):5665–5677, Oct 2010.

[36] H Audley, K Danzmann, A Garcia-Marin, and G Heinzel et al. LISA Pathfinder interferometry- hardware and system testing. *Classical and Quantum Gravity*, 28(9):094003, 2011.

[37] G. Geraldi, V. Wand, R. Gerndt, K. Rogalla, H. Abele, D. Kolbe, and U. Johann. OMS PFM campaign phase 1: functional test plan. Technical Report S2-ASD-TP-3060, ASD, June 2010.

[38] G. Hechenblaikner, V. Wand, R. Gerndt, K. Rogalla, H. Abele, U. Johann, and D. Kolbe. OMS interferometer calibration and commissioning FM phase 1. Technical Report S-ASD-TP-3061, ASD, July 2010.

[39] V. Wand, R. Gerndt, K. Rogalla, B. Barlage, U. Johann, and D. Kolbe. Control loop and performance test procedures - OMS PFM phase-1. Technical Report S2-ASD-TP-3062, ASD, June 2010.

[40] G. Vollmer, P. Luetzow-Wentzky, V. Wand, K. Rogalla, H. Abele, and D. Kolbe. LTP OMS PFM phase 1 integration test report. Technical Report S2-ASD-TR-3097, ASD, December 2010.

[41] G. Geraldi, V. Wand, R. Gerndt, K. Rogalla, H. Abele, D. Kolbe, and U. Johann. OMS PFM campaign phase 1: functional test report. Technical Report S2-ASD-TR-3110, ASD, February 2011.

[42] V. Wand, G. Hechenblaikner, D. Gerardi, R. Gerndt, K. Rogalla,

U. Johann, and D. Kolbe. OMS PFM phase 1 calibration and commissioning test report. Technical Report S2-ASD-TR-3111, ASD, March 2011.

[43] V. Wand, R. Gerndt, K. Rogalla, H. Abele, U. Johann, and D. Kolbe. Control loop and performance test report - OMS PFM phase-1. Technical Report S2-ASD-TR-3112, ASD, March 2011.

[44] D. Geraldi, R. Flatscher, J. Burkhardt, R. Gerndt, K. Rugalla, N. Gradmann, and D. Kolbe. TOQM OMS performance during the OSTT test campaign. Technical Report S2-ASD-TR-3152, ASD, March 2012.

[45] E. Fitzsimmons. DWS calibration procedure for the LTP OBI PFM, issue 2.2. Technical Report S2-UGL-PR-3018, University of Glasgow, April 2010. S2-UGL-PR-3018.

[46] F. Guzman Cervantes. OSTT LTP operator log. Technical report, AEI, November 2011.

[47] R. Flatscher, R. Gerndt, K. Rogalla, N. Gradmann, and D. Kolbe. Test report on OMS performance parameter characterisation during OSTT. Technical Report S2-ASD-TR-3155, ASD, March 2012.

[48] S. Vitale and K. Danzmann et al. Science requirements and top-level architecture definition for the LISA Technology Package (LTP) on board LISA Pathfinder (SMART 2). LTPA-UTN-ScRD-Iss003-Rev1, June 2005.

[49] N. Brandt, T. Ziegler, R. Schubert, M. Hirth, W. Fichter, D. Wealthy, R. Gerndt, N. Dunbar, U. Johann, and I. Honstvet. Experiment performance budget (M3 optical, FEEP). Technical Report S2-ASD-RP-3036, ASD, 2010.

[50] M. Kersten, V. Wand, G. Hechenblaikner, R. Gerndt, N. Gradmann, K. Rogalla, and U. Johann. OMS control loop stability analysis and filter design. Technical Report S2-ASD-TN-3017, ASD, 2011.

[51] A. Abramovici and J. Chapsky. *Feedback control systems: A fast-track guide for scientists and engineers.* Kluwer Academic

Publishers, 2000.

[52] G. Heinzel. SMART-2 interferometer. Technical Report S2-AEI-TN-3010, AEI, September 2002. S2-AEI-TN-3010.

[53] G. Heinzel, V. Wand, A. Garcia, F. Guzman, F. Steier, C. Killow, D. Robertson, H. Ward, and C. Braxmaier. Investigation of noise sources in the LTP interferometer. Technical Report S2-AEI-TN-3028, AEI, October 2005.

[54] A. Garcia Marin. *Minimisation of optical pathlength noise fro the detection of gravitational waves with the spaceborne laser interferometer LISA and LISA Pathfinder*. PhD thesis, Fakultät für Mathematik und Physik der Gottfried Wilhelm Leibniz Universität Hannover, 2007.

[55] A. Monsky. *Understanding interferometric drag-free sensors in space using intelligent data analysis tools*. PhD thesis, Leibniz Universitaet Hannover, 2010.

[56] M. Hewitson and A. García. Laser amplitude noise characterisation for LTP. Technical Report S2-AEI-TN-3055, AEI, January 2009.

[57] A. Freise. *The next generation of interferometry: multi-frequency optical modelling, control concepts and implementation*. PhD thesis, Leibniz Universitaet Hannover, 2003.

[58] F. Steier, A. Garcia Marin, V. Wand, and G. Heinzel. LTP extra mode definition. Technical Report S2-AEI-TN-3021, AEI, February 2005.

[59] M. Hewitson, A. Garcia Marin, and M. Nofrarias. Laser frequency noise characterisation for LTP. Technical Report S2-AEI-TN-3058, AEI, January 2009.

[60] M. Tröbs and G. Heinzel. Improved spectrum estimation from digitized time series on a logarithmic frequency axis. *Measurement*, 39:120–129, 2006.

[61] J. Bogenstahl and D. Robertson. Optical components- test report. Technical Report S2-UGL-TR-3010, University of Glasgow,

2008.

Acknowledgements

BIBLIOGRAPHY

Heather E. Audley

Address: Voßstraße 20
                 30161, Hannover
                 Germany
Phone: +49(0) 511 37038084
Email: heacheraudley@googlemail.com
Date of birth: 8th November 1986
Nationality: British

E D U C A T I O N

Dr.rer.nat, Max Planck Institute for Gravitational Physics/AEI — 2009-present

MSci. (Hons) Physics and Space Research, University of Birmingham, UK — 2005-2009

Sutton Coldfield Grammar School for Girls, Birmingham, UK — 1998-2005

Edgbaston High School for Girls, Birmingham, UK — 1990-1998

Publications:

Refereed journal articles:

L Ferraioli, E K Porter, M Armano, <u>H Audley</u>, G Congedo, I Diepholz, F Gibert, M Hewitson, M Hueller, N Karnesis, N Korsakova, M Nofrarias, E Plagnol, S Vitale, 2014, **Improving Bayesian analysis for LISA Pathfinder using an efficient Markov Chain Monte Carlo method**, Experimental Astronomy.

G. Hechenblaikner, R Gerndt, U Johann, P Luetzow-Wentzky, V Wand, <u>H Audley</u>, K Danzmann, A Garcia-Marin, G Heinzel, M Nofrarias, and F Steier, 2010, **Coupling characterization and noise studies of the optical metrology system onboard the LISA Pathfinder mission**, Applied Optics, Volume 49, Issue 29, pp. 5665-5677.

Published proceedings (refereed):

N Karnesis, M Nofrarias, C F Sopuerta, F Gibert, M Armano, <u>H Audley</u>, G Congedo, I Diepholz, L Ferraioli, M Hewitson, M Hueller, N Korsakova, E Plagnol, and S Vitale, 2012, **Bayesian Model Selection for LISA Pathfinder**, Astronomical Society of the Pacific conference series volumes, Volume 467, p. 337.

M Nofrarias, F Antonucci, M Armano, <u>H Audley</u>, G Auger et al, 2012, **State space modelling and data analysis exercises in LISA Pathfinder**, Astronomical Society of the Pacific conference series volumes, Volume 467, p. 161.

P McNamara, F Antonucci, M Armano, <u>H Audley</u>, G Auger et al, 2012, **The LISA Pathfinder mission**, Classical and Quantum Gravity, 29(12), 124014.

<u>H Audley</u>, K Danzmann, A Garcia-Marin, G Heinzel et al, 2011, **LISA Pathfinder interferometry- hardware and system testing**, Classical and Quantum Gravity, 28(9), 094003.

F Antonucci, M Armano, <u>H Audley</u>, G Auger et al, 2011, **LISA Pathfinder: mission and status**, Classical and Quantum Gravity, 28(9), 094001.

F Antonucci, M Armano, <u>H Audley</u>, G Auger et al, 2011, **From laboratory experiments to LISA Pathfinder: achieving LISA geodesic motion**, Classical and Quantum Gravity, 28 (9), 094002.

F Antonucci, M Armano, <u>H Audley</u>, G Auger et al, 2011, **LISA Pathfinder data analysis**, Classical and Quantum Gravity, 28(9), 094006.

Non-refereed articles, white papers:

The eLISA Consortium: P Amaro Seone, S Aoudia, <u>H Audley</u>, G Auger et al, 2013, **The Gravitational Universe**, submitted to the European Space Agency on May 24th 2013 for the L2/L3 selection of ESA's Cosmic Vision program, arXiv:1305.5720.